Contrast Agent Imaging Using An Optimized Table-top X-ray Fluorescence and Photon-Counting Computed Tomography Imaging System

by

Chelsea Amanda Saffron Dunning
B.Sc., University of British Columbia, 2015

A Dissertation Submitted in Partial Fulfillment of the
Requirements for the Degree of

DOCTOR OF PHILOSOPHY

in the Department of Physics and Astronomy



I acknowledge with respect the Lekwungen peoples on whose traditional territory the university stands and the Songhees, Esquimalt and W̱SÁNEĆ peoples whose historical relationships with the land continue to this day.

Contrast Agent Imaging Using An Optimized Table-top X-ray Fluorescence and Photon-Counting Computed Tomography Imaging System

by

Chelsea Amanda Saffron Dunning
B.Sc., University of British Columbia, 2015

Supervisory Committee

---

Dr. M. Bazalova-Carter, Supervisor
(Department of Physics & Astronomy)

---

Dr. C. Hoehr, Departmental Member
(Department of Physics & Astronomy)

---

Dr. F. C. J. M. van Veggel, Outside Member
(Department of Chemistry)

## ABSTRACT

Contrast agents are often crucial in medical imaging for disease diagnosis. Novel contrast agents, such as gold nanoparticles (AuNPs) and lanthanides, are being explored for a variety of clinical applications. Preclinical testing of these contrast agents is necessary before being approved for use in humans, which requires the use of small animal imaging techniques. Small animal imaging demands the detection of these contrast agents in trace amounts at acceptable imaging time and radiation dose. Two such imaging techniques include x-ray fluorescence computed tomography (XFCT) and photon-counting CT (PCCT). XFCT combines the principles of CT with x-ray fluorescence by detecting fluorescent x-rays from contrast agents at various projections to reconstruct contrast agent maps. XFCT can image trace amounts of AuNPs but is limited to small animal imaging due to fluorescent x-ray attenuation and scatter. PCCT uses photon-counting detectors that separate the CT data into energy bins. This enables contrast agent detection by recognizing the energy dependence of x-ray attenuation in different materials, independent of AuNP depth, and can provide anatomical information that XFCT cannot. To achieve the best of both worlds, we modeled and built a table-top x-ray imaging system capable of simultaneous XFCT and PCCT imaging.

We used Monte Carlo simulation software for the following work in XFCT imaging of AuNPs. We simulated XFCT induced by x-ray, electron, and proton beams scanning a small animal-sized object (phantom) containing AuNPs with Monte Carlo techniques. XFCT induced by x-rays resulted in the best image quality of AuNPs, however high-energy electron and medium-energy proton XFCT may be feasible for on-board x-ray fluorescence techniques during radiation therapy. We then simulated a scan of a phantom containing AuNPs on a table-top system to optimize the detector arrangement, size, and data acquisition strategy based on the resulting XFCT image quality and available detector equipment. To enable faster XFCT data acquisition, we separately simulated another AuNP phantom and determined the best collimator geometry for Au fluorescent x-ray detection.

We also performed experiments on our table-top x-ray imaging system in the lab. Phantoms containing multiples of three lanthanide contrast agents were scanned on our tabletop x-ray imaging system using a photon-counting detector capable of sustaining high x-ray fluxes that enabled PCCT. We used a novel subtraction algorithm for reconstructing separate contrast agent maps; all lanthanides were distinct at low

concentrations including gadolinium and holmium that are close in atomic number. Finally, we performed the first simultaneous XFCT and PCCT scan of a phantom and mice containing both gadolinium and gold based on the optimized parameters from our simulations.

This dissertation outlines the development of our tabletop x-ray imaging system and the optimization of the complex parameters necessary to obtain XFCT and PCCT images of multiple contrast agents at biologically-relevant concentrations.

# Contents

# Publications

PEER-REVIEWED MANUSCRIPTS

1. C. Curry, **C. A. S. Dunning**, M. Gauthier, H. G. Chou, F. Fluza, G. Glenn, Y. Tsui, M. Bazalova-Carter, and S. Glenzer (2020). Optimization of radiochromic film stacks to diagnose high-flux laser-accelerated proton beams. *Review of Scientific Instruments*, 91(9), 093303.

2. D. Richtsmeier, **C. A. S. Dunning**, K. Iniewski, and M. Bazalova-Carter (2020). Parameter optimization for multi-contrast imaging using photon-counting CT. *Journal of Instrumentation*, accepted 11 Sept 2020.

3. **C. A. S. Dunning** and M. Bazalova-Carter (2020). Design of a combined x-ray fluorescence computed tomography (CT) and photon-counting CT table-top imaging system. *Journal of Instrumentation*, **15** P06031.

4. **C. A. S. Dunning**, J. O'Connell, S. M. Robinson, K. J. Murphy, A. L. Frencken, F. C. J. M. van Veggel, K. Iniewski, and M. Bazalova-Carter (2020). Photon-counting computed tomography of lanthanide contrast agents with a high-flux 330 $\mu$m-pitch cadmium zinc telluride (CZT) detector on a table-top system. *Journal of Medical Imaging*, 7(3), 033502.

5. **C. A. S. Dunning** and M. Bazalova-Carter (2019). X-ray fluorescence computed tomography induced by photons, electrons, and protons. *IEEE Transactions on Medical Imaging*, *38*(12), 2735-2743.

6. **C. A. S. Dunning** and M. Bazalova-Carter (2018). Optimization of a table-top x-ray fluorescence computed tomography (XFCT) system. *Physics in Medicine and Biology*, *65*: 235013.

7. **C. A. S. Dunning** and M. Bazalova-Carter (2018). Sheet beam x-ray fluorescence computed tomography (XFCT) imaging of gold nanoparticles. *Medical Physics*, *45*(6): 2572-2582.

PEER-REVIEWED ABSTRACTS

1. **C. A. S. Dunning** and K. Iniewski (2020). Charge-sharing discrimination for K-edge imaging using CZT photon counting detectors. *IEEE Nuclear Science Symposium and Medical Imaging Conference 2020.*

2. **C. A. S. Dunning** and M. Bazalova-Carter (2020). Simultaneous x-ray fluorescence computed tomography (XFCT) and photon-counting CT (PCCT) imaging of phantoms and mice on a table-top x-ray system. *Joint AAPM—COMP Annual Meeting 2020*.

3. **C. A. S. Dunning**, D. Richtsmeier, and M. Bazalova-Carter (2019). Combined x-ray fluorescence and spectral computed tomography of multiple contrast agents. *Medical Physics*, *46*(11), Scientific Session 1: YIS–06.

4. **C. A. S. Dunning**, J. O'Connell, S. M. Robinson, K. J. Murphy, K. Iniewski, and M. Bazalova-Carter (2019). BEST IN PHYSICS (IMAGING): Multiplexed Spectral Computed Tomography (CT) Imaging of Three Contrast Agents. *Medical Physics*, *46*(6), E220.

5. **C. A. S. Dunning** and M. Bazalova-Carter (2018). BEST IN PHYSICS (IMAGING): Optimization of a Table-Top X-Ray Fluorescence Computed Tomography (XFCT) System. *Medical Physics*, *45*(6), E368-E369.

6. **C. A. S. Dunning** and M. Bazalova-Carter (2017). Alternative geometries for x-ray fluorescence CT (XFCT) imaging of gold nanoparticles. *Medical Physics*, *44*(8), Scientific Session 1: YIS–03.

7. **C. A. S. Dunning** and M. Bazalova-Carter (2017). Alternative geometries for x-ray fluorescence CT (XFCT) imaging of gold nanoparticles: TH-AB-708-02. *Medical Physics*, *44*(6), 3289-3290.

8. **C. Dunning**, C. Lindsay, N. Unick, V. Sossi, M. Martinez, and C. Hoehr (2016). Poster-40: Treatment verification of a 3D-printed eye phantom for proton therapy. *Medical Physics*, *43*(8Part2), 4945-4946.

# List of Tables

# List of Figures

# List of Abbreviations

**2D** Two-dimensional.

**3D** Three-dimensional.

**AAPM** American Association of Physicists in Medicine.

**ASIC** Application Specific Integrated Circuit.

**AuNP** Gold Nanoparticle.

**CdTe** Cadmium Telluride.

**CNR** Contrast-to-Noise Ratio.

**COMP** Canadian Organization of Medical Physicists.

**cps** Counts per second.

**CSD** Charge-Sharing Discrimination.

**CT** Computed Tomography.

**CZT** Cadmium Zinc Telluride.

**DECT** Dual-Energy Computed Tomography.

**EID** Energy-Integrating Detector.

**EPR** Enhanced Permeation and Retention.

**eV** Electron Volt.

**FBP** Filtered Backprojection.

**FDK** Feldkamp-Davis-Kress.

**FWHM** Full Width at Half Maximum.

**GUI** Graphical User Interface.

**Gy** Gray.

**HU** Hounsfield Unit.

**IAEA** International Atomic Energy Agency.

**IEC** International Electrotechnical Commission.

**IEEE** Institute of Electrical and Electronics Engineers.

**keV** Kilo Electron Volt.

**kVp** Peak Kilovoltage.

**MC** Monte Carlo.

**MCA** Multi-channel Analyzer.

**MLEM** Maximum Likelihood Expectation Maximization.

**MRI** Magnetic Resonance Imaging.

**NIST** National Institute of Standards and Technology.

**PCCT** Photon Counting Computed Tomography.

**PCD** Photon Counting Detector.

**PCDA** Pentacosa-10,12-diynoic acid.

**PIXE** Particle Induced X-ray Emission.

**PLA** Polylactic Acid.

**PMMA** Polymethylmethacrylate.

**ROI** Region Of Interest.

**SDD** Silicon Drift Detector.

**SNR** Signal-to-Noise Ratio.

**UVic** University of Victoria.

**VHEE** Very High Energy Electrons.

**XCITE** X-ray Cancer Imaging and Therapy Experimental.

**XFCT** X-ray Fluorescence Computed Tomography.

**XML** Extensible Markup Language.

**XRF** X-ray Fluorescence.

**Z** Atomic Number.

# Acknowledgements

I must say, I am one of the most luckiest and fortunate people ever. Without really knowing ahead of time, I started my Master's at the University of Victoria just two months after my supervisor, **Dr. Magdalena Bazalova-Carter**. After hearing a few testimonials about her energy and passion towards medical physics and her students, I knew I wanted her to be my supervisor. And what luck, she had an opening for a Master's student! I never did finish my Master's with her, however, because I enjoyed working with her so much that I transferred to a PhD program. I can't thank her enough for all the time she has poured into helping transform me from a baby Master's student who couldn't draw an x-ray tube spectrum to save her life into a PhD powerhouse ready for her next journey at the Mayo Clinic. I am so impressed with how the XCITE Lab has grown over the time since I joined, and I can't wait to see what the XCITE Lab does next.

Thank you to the members of the XCITE Lab whom I've had the pleasure of working with - **Spencer Robinson**, **Kevin Murphy**, **Nolan Esplen**, **Devon Richtsmeier**, and **Dr. Dylan Breitkreutz** to name a few, in no particular order. Thank you to our collaborators at Redlen Technologies, in particular **Dr. Kris Iniewski**, and at the UVic Chemistry Department, in particular **Dr. Frank van Veggel** and **Adriaan Frencken**. Thank you to **Dr. Cornelia Hoehr** for setting me up well to succeed in grad school, and for your guidance as a committee member.

When I started grad school in a new city, I found myself in a loving group of friends that felt like my grad school family. As most of you have all moved away to different corners of the world, just know you guys are awesome and I miss Thursday karaoke nights at Felicita's with y'all. An incomplete list of my grad school family: **Pramodh Yapa**, **Graeme Niedermayer**, **Kacie Williams**, **Zoey Warmerdam**, **Anne-Marie Lefebvre**, **Astara Light**, **Ildara Enríquez**, **Andrew Coathup** (medphys study buddy!), **Noa Hacohen**, **Juan Hernandez**, **Kate Taylor** (THEORY!!), **Ryan Kim**, **Lina Rotermund**, **John Coffey**, **Nolan Esplen** (hey you again), **Ayden Loughlin**, **Thomas Boerman**, and **Thor Tronrud**. Just the fact that this incomplete list is so long is a reflection of how blessed I truly am.

Throughout grad school I found many people who were kind enough to welcome me to their communities. For all the Astronomy grad students who let this random Medical Physics student drink with you at the Grad House every Friday – thank you. For the Victoria swing dancing community from whom I learned how to swing dance,

and among which I've met some of the most fun and interesting people – thank you. For all the people whom I've played volleyball with, whether during intramurals or messing around on the sand courts – thank you. For all the people who have lived in the Arbutus House who have formed a community and welcomed me with open arms – thank you. And to everyone else I have met along the way, I am so grateful!

For **Dr. Samantha van Nest** and **Dr. Christopher Johnstone**: you both are a huge inspiration to me and have made my time at UVic memorable. Thank you for the advice, the fun times, and the many memories we shared; I look up to you both immensely. And for **Clay Lindsay**: I like to credit you as the reason why I ended up here in the first place. Your mentorship and advice has been truly priceless.

Finally, for my partner, **Logan Francis**: you have loved and supported me so much throughout my journey, and I am thankful that we have grown so much together. Thank you for making me a better person.

# Dedication

For my parents, Scott and Denise Dunning, for encouraging and supporting me against all odds throughout my education and my entire life.

For all the friends I made along my journey, the adventures we had, and the beers I drank with them.

And for all the frontline workers around the world fighting the ongoing global pandemic, and for the people who continue to protest injustice and inequality. I stand with you.

# Frontispiece

*Kola and Roxy, who made accomplishing this degree possible.*

# Chapter 1

# Introduction

## 1.1 Motivation of the Use of Contrast Agents in Imaging and Radiation Therapy

Imaging techniques, which encompass x-ray radiography and computed tomography (CT), magnetic resonance imaging (MRI), ultrasound, and emission tomography, are widely applied for diagnosis of diseases and abnormalities. In particular, cancer is the leading cause of death in Canada, and the rate of cancer incidence in Canada is rising due to a growing and aging population[1]. CT is a widely applied form of x-ray imaging capable of reconstructing axial images that provide anatomical information for cancer detection and staging, and for a variety of other clinical applications.

X-ray contrast agents are solutions containing elements of high atomic number ($Z$), such as iodine and gadolinium, that are frequently used to enhance structures in diagnostic imaging. These contrast agents are usually injected intravenously into the patient. Iodine-based solution is a common contrast agent for diagnostic CT imaging that highlights areas of increased blood vasculature to diagnose a tumour[2], vascular disease[3], or a pulmonary embolism[4]. Gadolinium-based solution, due to its magnetic properties, is used in MRI scans to diagnose diseases such as atherosclerosis[5] and multiple sclerosis[6]. In addition, gadolinium can be used as an alternative for iodine-sensitive patients who require contrast for x-ray imaging[7, 8]. While high-contrast areas in CT images can be identified as iodine or gadolinium, CT imaging does not offer material-specific information free of anatomical noise.

Half of all patients who are diagnosed with cancer receive some form of radiation therapy treatment, whether it is via x-ray, electron, or proton beams. Radiation therapy requires medical imaging to provide the location of the tumour and other anatomical information needed for treatment planning. However, a common chal-

lenge is to reduce the amount of radiation to normal tissue during treatment. Gold nanoparticles (AuNPs) have been studied for the purposes of sensitizing tumours to radiation during cancer treatment in both *in vitro* and *in vivo* models[9, 10], and have only recently begun clinical trials[11]. Targeting AuNPs to tumour cells is enabled by the enhanced permeation and retention (EPR) effect, which allows for AuNPs to remain inside tumour cells without immediate excretion. Gold is a natural choice for NP-based radiosensitizers as it is non-toxic to biological systems in the small quantities needed. However, since gold atoms are capable of increased DNA damage to cells upon irradiation, it is crucial to verify that the AuNPs are indeed localized in tumour cells and not in normal tissue.

Verifying AuNP location is one application of preclinical imaging. X-ray imaging at the preclinical stage is often done on table-top imaging systems for the purpose of small animal imaging. Preclinical imaging systems are crucial for the development of novel contrast agents and their applications. For example, it must be demonstrated that the presence of AuNPs in a tumour corresponds to increased radiation damage and decreased normal tissue damage in a small animal model before this application is tested on humans. The biologically relevant concentration of AuNPs in small animal systems is very low, ranging between 0.001%[12] to 0.7%[10]. These trace amounts of AuNPs are undetectable in conventional CT imaging. The goal of this dissertation is to design such a table-top x-ray imaging system that can reconstruct maps of AuNPs and other contrast agents for small animal applications better than the current clinical CT methods.

## 1.2 The Atom and Radiation

Understanding the atomic structure and electromagnetic interactions with matter in the kilovoltage energy range is crucial to the theory behind the imaging techniques explored in this research. This section outlines the principles of photon and electron interactions which are relevant to contrast agent imaging in small animals. The relevant photon interactions include photoelectric effect, Rayleigh scattering, and Compton scattering. Pair production is another possible photon interaction in the field of medical physics, however this interaction only occurs above 1.022 MeV and is not relevant to this work. Electron interactions of note arise from the effects following photon interactions, which include the production of Meitner-Auger electrons and *bremsstrahlung* radiation. Finally, proton interactions are introduced.

### 1.2.1 Structure of the Atom

All matter is made up of atoms. The atom itself (Figure 1.1) is made up of a nucleus surrounded by orbital shells. The nucleus consists of positively-charged protons and neutrally-charged neutrons. The number of protons corresponds to the atomic number ($Z$) which denotes the element. Hydrogen, carbon, and oxygen have $Z = 1$, 6, and 8, while gadolinium and gold have $Z = 64$ and 79, respectively. The orbitals are a series of shells with a given energy level in which negatively-charged electrons reside in and surround the nucleus. Atoms or compounds that are neutral have an equal number of protons and electrons; an imbalance of protons and electrons will result in ions. The innermost orbital is known as the K-shell orbital, can only hold two electrons, and its energy level is the highest in magnitude because the electrons in this shell are tightly bound toward the nucleus. The next orbital level is called the L-shell orbital and can hold eight electrons. Successive orbital shells have energy levels of decreasing magnitude with decreasing proximity to the nucleus. The energy of each level is referred to as the binding energy of the orbital shell, which differs by element.

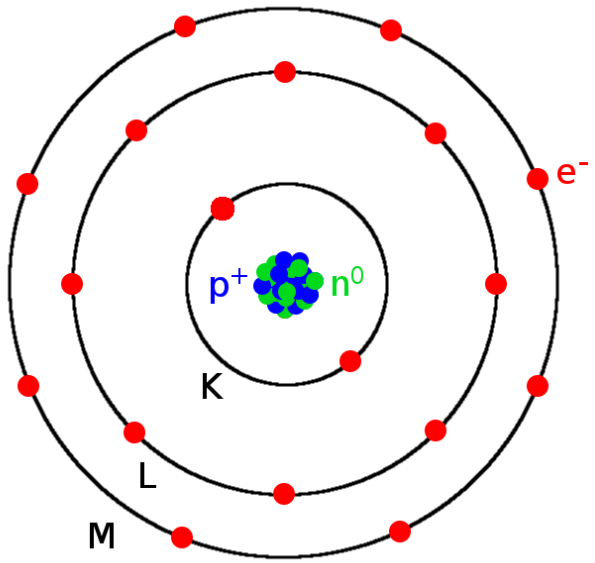


Figure 1.1: A simplistic diagram of an atom. The nucleus is composed of protons ($p^+$, blue) and neutrons ($n^0$, green). The K-shell, L-shell, and M-shell orbitals are labeled and are occupied by electrons ($e^-$, red).

Compounds such as water can be described as having an effective atomic number ($Z_{eff}$), which is of the following formula:

$$Z_{eff} = \sqrt[2.94]{\sum_i f_i Z_i^{2.94}} \tag{1.1}$$

where $Z_i$ is the atomic number of element $i$ and $f_i$ is the fraction of the total electrons for element $i$[13]. The $Z_{eff}$ for water ($H_2O$) and polylactic acid ($C_3H_4O_2$) is 7.42 and 6.82, respectively. Atoms with the same $Z$ but different number of neutrons are referred to as isotopes.

### 1.2.2 Photon Absorption

Consider a number of monochromatic x-ray photons $N_0$ incident on a uniform material. The number of photons $N$ that travel through a thickness of uniform material $t$ without interacting is governed by the following power law:

$$N(t) = N_0 \exp(-\mu t) \tag{1.2}$$

where $\mu$ is the linear attenuation coefficient, which is dependent on the material and the energy of the photons[14]. The linear attenuation coefficient governs how many of the incident photons are transmitted through material, and can be thought of as a probability. Incident photons which are not transmitted through the material are otherwise considered to have interacted with the material via any of the aforementioned types. Often $\mu$ is tabulated as a function of energy and is divided by the material density $\rho$; the value $\mu/\rho$ is know as the mass attenuation coefficient.

Figure 1.2 shows the total $\mu/\rho$ of gold and water, along with the partial mass attenuation coefficients $\tau/\rho$, $\sigma_{coh}\rho$, and $\sigma_{inc}\rho$ for photoelectric effect, Rayleigh scattering, and Compton scattering, respectively, in the energy range below 200 keV. The partial attenuation coefficients are cross sections that sum up to the total mass attenuation coefficient, such that $\tau + \sigma_{coh} + \sigma_{inc} = \mu$, and can be thought of as the probability of that particular photon interaction occurring in a material at a given energy.

### 1.2.3 Photoelectric Effect

A photon with a kinetic energy $h\nu$ that undergoes the photoelectric effect (Figure 1.3) ejects an electron from its atomic orbital, and renders the atom in an excited state. The ejected electron is known as a "photoelectron", and leaves behind a vacancy in the orbital shell it once occupied. If the electron was ejected from the innermost

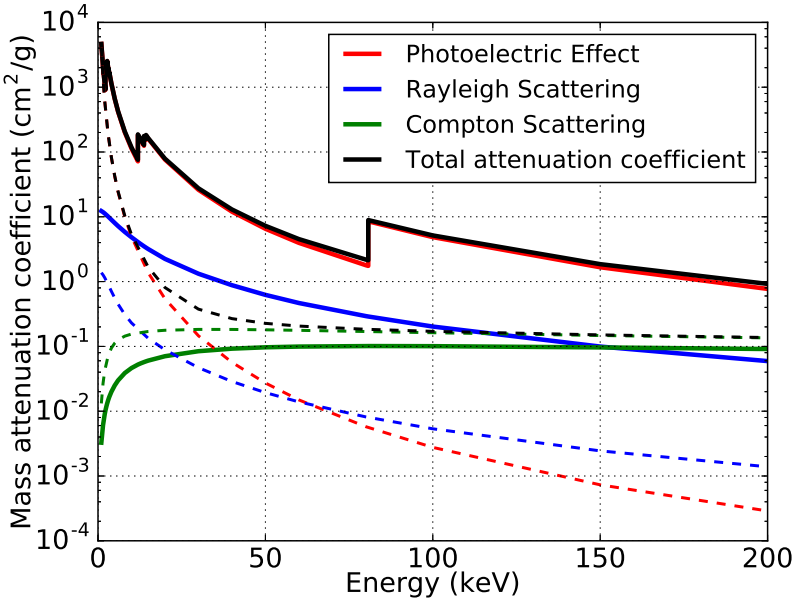


Figure 1.2: Total mass attenuation coefficients of gold (solid) and water (dashed), with contributions from each photon interaction type as a function of photon energy. Data from NIST "XCOM" tables[15].

K-shell orbital, the kinetic energy of the photoelectron is equal to $h\nu - E_K$, where $E_K$ is the binding energy of the K-shell orbital. The discontinuities in the total mass attenuation coefficient for gold in Figure 1.2 is due to the photoelectric effect; a photon needs to have a kinetic energy $h\nu$ that is greater than the binding energy of the orbital shell in order to eject a photoelectron. For example, the K-shell orbital of gold has a binding energy of 80.7 keV. This is the threshold energy an incident photon must have in order to eject a photoelectron from the K-shell orbital of a gold atom. In general, the probability of a photoelectric effect interaction occurring is proportional to $Z^4/(h\nu)^3$. In other words, the higher the $Z$ of the atom and the lower the kinetic energy $h\nu$ of the photon, the more likely the photon will undergo a photoelectric effect process.

In order for the atom to relax back to the ground state, the vacancy in the orbital shell is filled by another electron in a higher orbital shell. Energy is released from the atom to fill the vacancy in the form of fluorescent x-rays or Meitner-Auger electrons, which will be described later in this section.

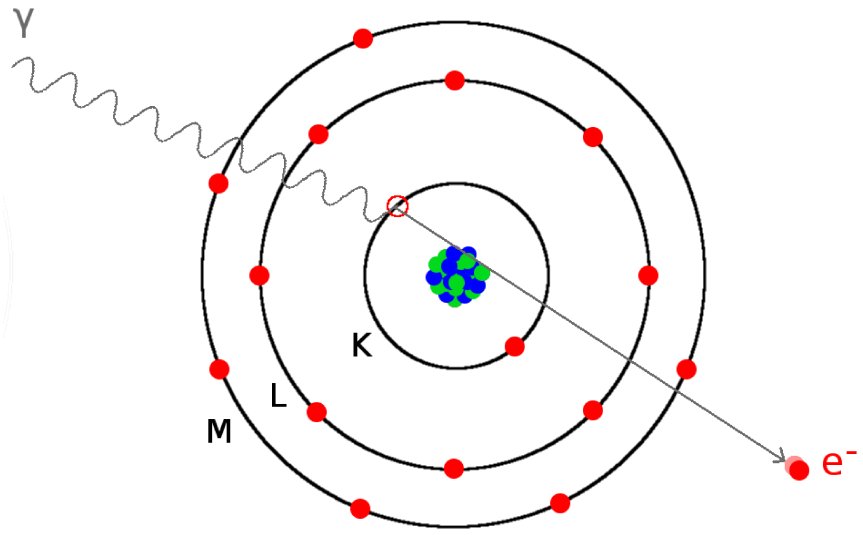


Figure 1.3: Diagram of photoelectric effect, where a photon ($\gamma$) ejects the photoelectron ($e^-$) from its innermost atomic orbital.

### 1.2.4 Rayleigh Scattering

A photon that undergoes Rayleigh, or coherent, scattering interacts with a bound electron in an atomic orbital. The angle at which this photon scatters is small, and there is no energy transfer from the photon to the electron leaving the atom unchanged. Therefore it is an elastic scattering, and it occurs with probability $\sigma_{inc}$. This type of interaction contributes a relative importance of at most 14% to the total attenuation coefficient of gold and water at energies below 200 keV.

### 1.2.5 Compton Scattering

A photon with kinetic energy $h\nu$ that undergoes Compton, or incoherent, scattering (Figure 1.4) interacts with an electron in an atomic orbital and transfers some energy to the electron, ejecting it. The photon and ejected electron scatter with angles $\theta$ and $\phi$, respectively, relative to the incident photon trajectory such that energy and momentum are conserved. The scattered photon has an energy $h\nu'$ that is dependent on its scattering angle $\theta$, defined in Equation 1.3 below:

$$h\nu' = h\nu \frac{1}{1 + \epsilon(1 - \cos\theta)} \tag{1.3}$$

where $\epsilon = \frac{h\nu}{m_e c^2}$ and $m_e c^2 = 511$ keV is the rest energy of an electron. As the photon scattering angle $\theta$ increases, the more energy it has lost and $h\nu'$ decreases.

The ejected electron's kinetic energy $E_k$ can be found with conservation of energy, $E_k = h\nu - h\nu'$, and its scattering angle $\phi$ is related to $\theta$ by Equation 1.4 below:

$$\cot\phi = (1+\epsilon)\tan\left(\frac{\theta}{2}\right) \tag{1.4}$$

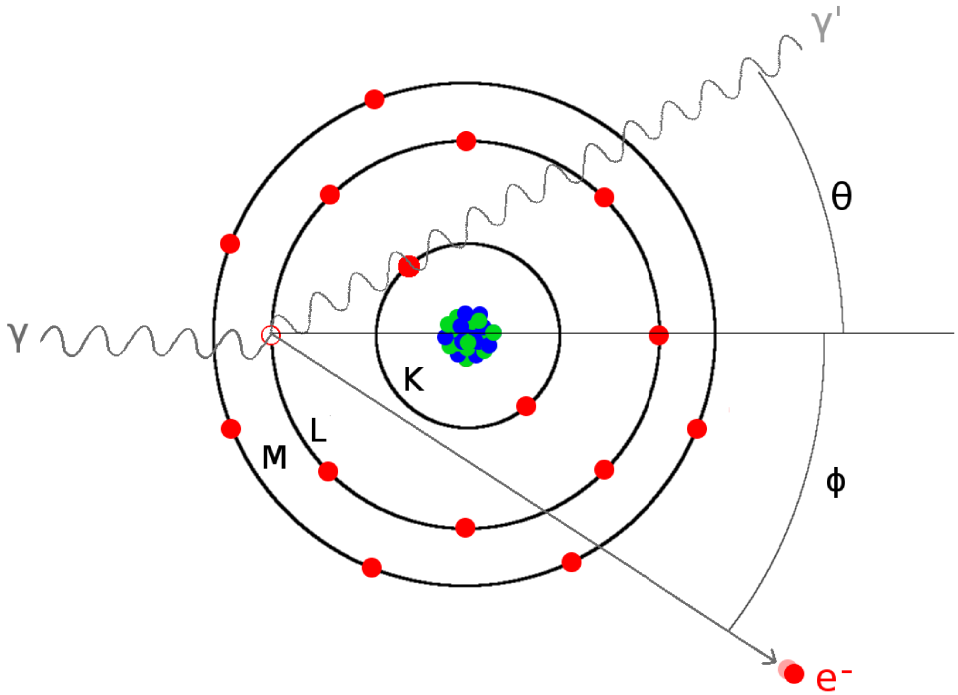


Figure 1.4: Diagram of a Compton scattering event, where a photon ($\gamma$) causes the ejection of an electron ($e^-$) while the photon loses kinetic energy ($\gamma'$). The photon and electron are scattered with angles $\theta$ and $\phi$, respectively, relative to the incident photon trajectory.

The probability of Compton scattering is dependent on $Z$, and strongly dependent on incident photon energy. The likelihood of Compton scattering relative to other photon interactions is greater than 80% above 50 keV in water, and less than 10% below 200 keV in gold.

The differential cross-section $\frac{d\sigma}{d\Omega}$ of Compton scattering per unit solid angle $\Omega$ as a function of photon energy $h\nu$ and scattering angle $\theta$ is defined in Equation 1.5 below:

$$\frac{d\sigma}{d\Omega} = \frac{r_e^2}{2}(1+\cos^2\theta)\left(\frac{1}{1+\epsilon(1-\cos\theta)}\right)^2\left(1+\frac{\epsilon^2(1-\cos\theta)^2}{[1+\epsilon(1-\cos\theta)](1+\cos^2\theta)}\right) \tag{1.5}$$

where $r_e = 2.818 \times 10^{-15}$ m$^2$ is the classical electron radius. Equation 1.5 is the Klein-Nishina formula[16], which is valid for photons scattering off of free electrons. To calculate the differential cross-section for Compton scattering off of bound electrons, $\frac{d\sigma}{d\Omega}$ is modified by a factor that depends on $\theta$, $h\nu$, and $Z$[14]. Based on the Klein-Nishina formula (Equation 1.5), lower energy incident photons ($< 100$ keV) tend to have a wide distribution of scattering angles whereas higher energy photons ($> 1$ MeV) tend to be more forward scattered.

### 1.2.6 Fluorescent X-rays and Meitner-Auger Electrons

The release of fluorescent x-rays or Meitner-Auger electrons from an atom is a consequence of an ejected electron from an inner orbital by any means. One of these two processes occurs when an outer orbital donates an electron to fill the vacancy left by the ejected electron. A vacancy in the K-shell orbital results in the emission of a K-shell fluorescent x-ray. The energy of the K-shell fluorescent x-ray is equal to $E_K - E_X$, where $E_K$ and $E_X$ are the binding energies of the K-shell orbital and the $X^{\text{th}}$-shell donor orbital, respectively. Similarly, the release of an L-shell fluorescent x-ray will result from the vacancy in an L-shell orbital. The distinction of an $\alpha$ or $\beta$ fluorescent x-ray depends on the specific donor orbital; for instance $K_\alpha$ or $K_\beta$ fluorescent x-rays are emitted when the donor orbital is the L-shell or M-shell, respectively. Fluorescent x-rays have characteristic energies that are specific to the element, making x-ray fluorescence an excellent tool for element identification. K-shell and L-shell fluorescent x-rays from high-$Z$ elements are important in this research.

The probability of a fluorescent x-ray emission event upon atom de-excitation is denoted by the fluorescent yield $\omega$; $\omega_K$ and $\omega_L$ represent the probability of a K-shell or L-shell fluorescent x-ray being released, respectively, depending on if the vacancy is in the K-shell or L-shell orbital. The emitted fluorescent x-ray has an energy equal to the difference between the binding energies of the inner and outer orbitals. An example of fluorescent x-ray emission is shown in Figure 1.5.

Electrons in any orbital will be ejected from the atom, leaving more vacancies. These subsequent ejected electrons are Meitner-Auger electrons, which were first discovered by Dr. Lise Meitner[17]. Other electrons in outer shells will continue to fill these vacancies, and this process repeats until all vacancies are in the outermost orbital. The probability of the release of Meitner-Auger electrons is equal to $1-\omega$. This Meitner-Auger effect occurs to help remove excess energy that may not be completely

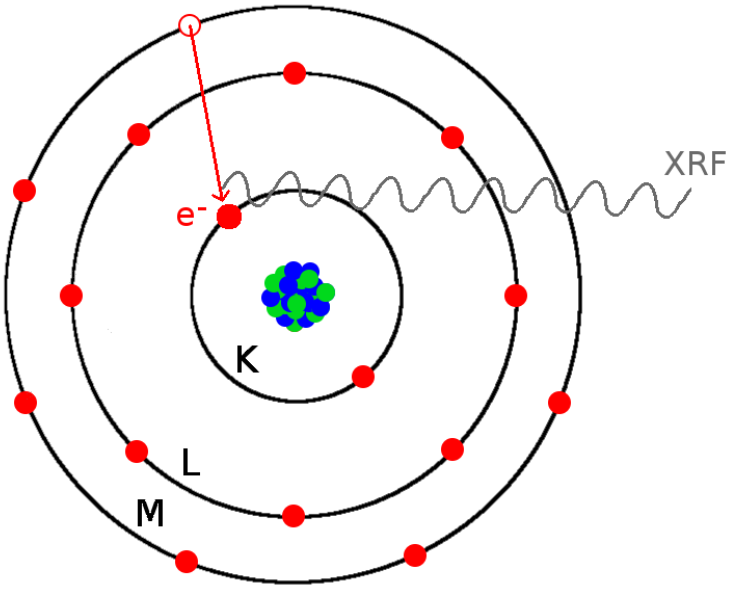


Figure 1.5: Diagram of K-shell fluorescent x-ray emission, in which an electron $e^-$ from the M-shell of the excited atom moves to the vacancy left in the K-shell. The excess energy is released in the form of a $K_\beta$ fluorescent x-ray (XRF) with energy $h\nu = E_K - E_M$ in this case.

accounted for from fluorescent x-ray emission to stabilize the excited atom[18].

The fluorescent yield $\omega_K$ for gold and water (effective $Z = 7.42$) is 0.95 and 0.00; when a K-shell orbital has a vacancy gold atoms predominantly undergo fluorescent x-ray emission while the hydrogen and oxygen atoms in water solely release Meitner-Auger electrons.

### Particle-Induced X-ray Emission

Particle-induced x-ray emission (PIXE) is the production of fluorescent x-rays that arise from charged particle interactions with atomic orbitals. A particle, such as an electron or proton, would need a kinetic energy greater than the binding energy of an atomic orbital shell to ionize an electron in the orbital, with the highest probability usually in the 1-3 MeV range for protons[19]. This ultimately results in the release of a fluorescent x-ray or Meitner-Auger electron when another electron in a higher orbital shell fills the vacancy in a similar manner to the photoelectric effect, except that the incident particle is not absorbed into the atom. While not strictly limited to kilovoltage energies, PIXE is a process that is relevant to this research.

### 1.2.7 *Bremsstrahlung* Radiation

As electrons travel through material, they experience collisional and radiative losses of energy. Collisional energy loss of a traveling electron is due to interactions of atomic electrons, which may be ejected from their orbitals and have enough kinetic energy to start traveling through the material on their own. These ejected electrons are known as delta rays. The majority of the electrons with energies $< 200$ keV that travel through material suffer from collisional losses, which lead to these delta rays and heat[14].

Radiative energy loss occurs when an electron closely approaches a nucleus of an atom and curves around the nucleus due to the electric field between its own negative electric charge and the positively-charged nucleus. Since this close approach causes the electron to slow down and change direction, its deceleration forces the release of energy in the form of a *bremsstrahlung* x-ray, a German word for "braking" radiation. This is depicted in Figure 1.6, in which the energy of the *bremsstrahlung* x-ray is equal to the energy lost by the traveling electron.

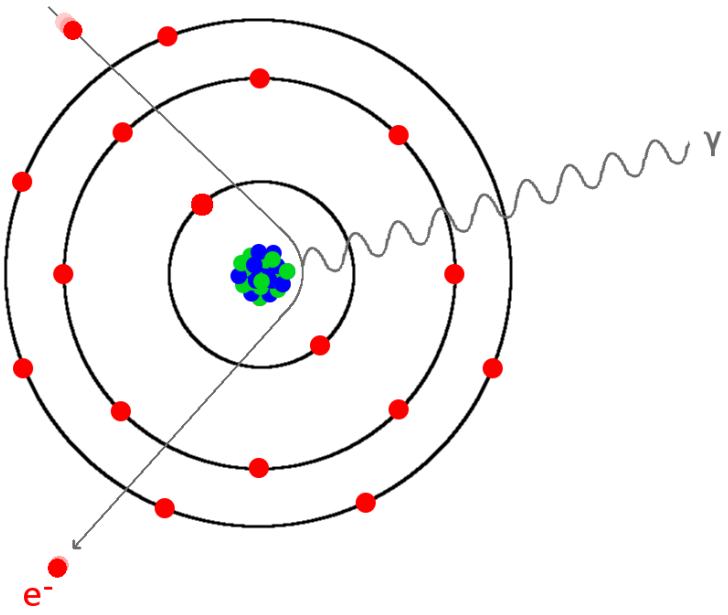


Figure 1.6: Diagram of a radiative loss, where a traveling electron ($e^-$) curves around the nucleus of an atom, slowing down and releasing excess energy as a *bremsstrahlung* x-ray ($\gamma$).

### 1.2.8 Proton Interactions

Protons interact with matter in three different methods – multiple Coulomb scattering, nuclear interactions, and collisions with atomic electrons[20]. Multiple Coulomb scattering is relatively rare and involves protons scattering off of atomic nuclei, resulting in small angular deflections that get stronger with increased $Z$. Nuclear interactions involve head-on inelastic collisions between protons and atomic nuclei, creating secondary particles. Protons slow down due to collisions with atomic electrons, and the rate of proton energy loss increases with decreasing energy until protons are completely stopped. This occurs because when a heavy proton collides with a light electron, it transfers more momentum to the electron; a proton with low kinetic energy will lose more of its energy when it spends more time interacting with an electron in its vicinity[20]. Note that protons with sufficient energy are able to knock out electrons from their orbitals. The proton mass stopping power $S = -\frac{1}{\rho}\frac{dE}{dx}$ is the rate of decreasing kinetic energy $E$ along a proton track $x$ in material with density $\rho$.

These three interactions contribute to the Bragg curve (Figure 1.7), which is the depth dose curve of protons in matter characterized by low entrance dose and a sharp Bragg peak at an energy-dependent depth with no exit dose. The dose is proportional to the number of protons and mass stopping power $S$[20].

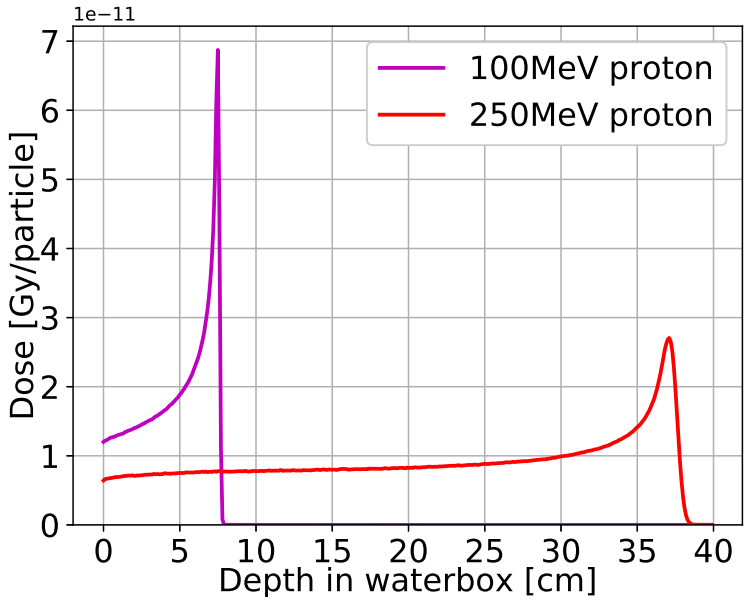


Figure 1.7: Depth dose curve of 100 MeV and 250 MeV proton beams simulated in water.

The Bethe equation below describes the energy loss of protons in material with atomic number and mass $Z$ and $A$:

$$S = -\frac{1}{\rho}\frac{dE}{dx} = 0.3072\frac{Z}{A}\frac{1}{\beta^2}(\log\frac{W_m}{I} - \beta^2) \tag{1.6}$$

$$W_m = \frac{2m_e c^2\beta^2}{1-\beta^2}$$

where $I$ is mean excitation energy of the material, the fraction $\beta = \frac{v}{c}$ is the ratio between the proton speed and speed of light, and $W_m$ is largest possible proton energy loss in a single collision with a free election of rest mass $m_e$[20]. When corrected for density, $S$ decreases with increasing $Z$[20].

## 1.3 Methods of Imaging Contrast Agents

### 1.3.1 X-ray Computed Tomography

X-ray Computed Tomography (CT) is a widely-used form of anatomical imaging which reconstructs axial slices of the patient from 2D projection images produced using x-ray beams at different angles and energy-integrating detectors. Since its invention in the 1970s[21], a lot of research and development has gone into CT imaging which has culminated into a powerful imaging modality that offers high-resolution and relatively high-contrast images today. In principle, the amount of x-ray attenuation differs by material and x-ray beam energy from Equation 1.2 and Figure 1.2, which translates into different amounts of contrast for each material that appears in the CT image. When CT became capable of perfusion imaging with fast continuous measurements, the use of contrast agents as described above became widespread[22]. However, with novel lanthanide-based contrast agents and AuNPs being rapidly developed to improve disease diagnosis, CT imaging by itself may not achieve the contrast resolution necessary for distinguishing these materials from each other and other higher-$Z$ materials such as bone and metal implants.

### 1.3.2 Dual-Energy Computed Tomography

Dual-energy CT (DECT) is an imaging technique that uses two diagnostic energy levels to highlight differences in x-ray attenuation between multiple materials. This can be achieved in a variety of ways, such as two filters at the x-ray tube or detector[23], rapid switching of x-ray tube voltages[24], or with two imaging chains operating at

different x-ray tube voltages[25]. DECT has widespread clinical use for reducing anatomical noise when imaging soft tissue and bone, and for imaging contrast agents such as iodine using techniques such as logarithmic weighted subtraction and K-edge subtraction, respectively[26]. However, the implementation of DECT needs further improvement with respect to reduction in imaging time and dose and improved material distinction[27].

### 1.3.3 Photon-Counting Computed Tomography

Energy-selective CT was proposed a few years after the first demonstration of CT[28], and was made possible with the advent of modern photon-counting detectors for the purpose of material quantification[29]. The energy-integrating detectors used in conventional CT and DECT can only store count information, however photon-counting detectors are sensitive to the energy of x-rays by sorting the pulse heights generated in the active layer into user-defined energy bins. The type of imaging enabled by photon-counting detectors is referred to as Photon-Counting CT (PCCT), however it is also known as spectral photon-counting CT, spectral CT, or even colour CT. DECT functionally has two energy bins, while the use of photon-counting detectors effectively increases the number of energy bins to anywhere from four to eight depending on the imaging system. Figure 1.8 illustrates the concept of CT, DECT, and PCCT.

For high-$Z$ materials, there is a general trend of decreased x-ray attenuation for increased x-ray energies in a material, except for sharp discontinuities at the K-edge energy from Figure 1.2. PCCT imaging paired with K-edge subtraction can be used to separate contrast agents in a CT image by setting the energy bin thresholds to coincide with the K-edge energies of these materials. The subtraction of reconstructed CT images at energy bins adjacent to the contrast agent's K-edge energy highlight the location of a particular contrast agent. While DECT is normally limited to discriminating one high-$Z$ contrast agent from patient anatomy, PCCT can discern multiple high-$Z$ contrast agents from structures such as bone or other contrast agents, which would be difficult to resolve in conventional CT images[30]. Photon-counting detectors, such as those bonded to the Medipix technology, have remained preclinical due to issues with pulse pileup at high photon count rates necessary for clinical x-ray imaging[31]. In addition, low energy resolution and low-dose reconstruction techniques are further issues currently preventing clinical translation of PCCT[32].

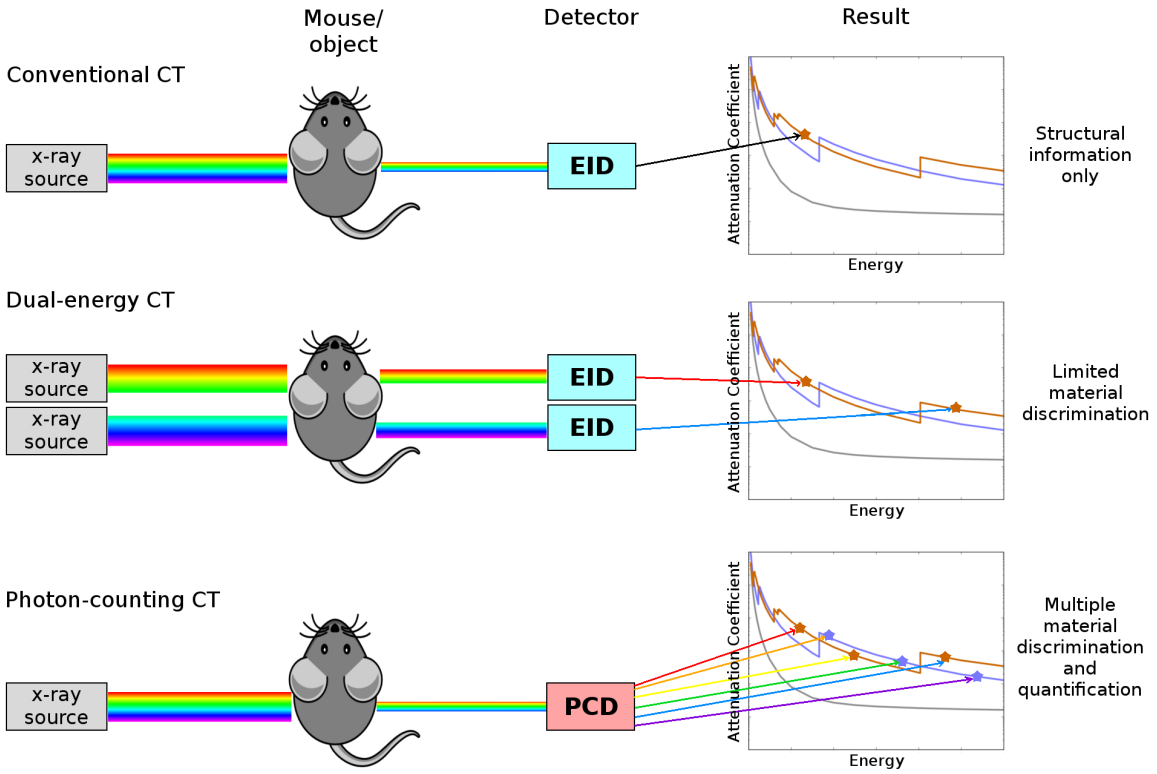


Figure 1.8: Diagram of conventional and dual-energy CT enabled by energy-integrating detectors (EID) and photon-counting CT enabled by photon-counting detectors (PCD).

The development of high-flux photon-counting detectors have caused PCCT to rapidly develop in recent years for clinical and non-destructive testing applications. However, photon-counting detector technology is still limited by charge-sharing at high fluxes of millions of counts per second and the cost of large-scale production for medical imaging purposes[33, 34]. PCCT is promising for diagnostic medicine due to its capability of multiple material discrimination and quantifying biologically-relevant concentrations of AuNPs[35].

### 1.3.4 X-ray Fluorescence Computed Tomography

Another method of x-ray imaging of contrast agents is x-ray fluorescence CT (XFCT). First demonstrated with a monoenergetic x-ray source in the late 1980s[36], XFCT combines CT with the spectroscopic technique of x-ray fluorescence to reconstruct axial images of high-$Z$ contrast agents. In XFCT imaging (Figure 1.9), maps of contrast agent solution are reconstructed by counting the number of fluorescent x-

rays from high-$Z$ atoms that are produced from atomic vacancies induced by incident x-ray radiation. Only incident x-rays with energies greater than the K-shell binding energy (or the K-edge) of an element can induce K-shell x-ray fluorescence in that element. Note that the highest probability of x-ray fluorescence occurs when the incident x-rays are monoenergetic with an energy just above the K-edge due to the photoelectric effect. XFCT has the potential to reconstruct very low concentrations of high-$Z$ elements as demonstrated using monoenergetic x-ray sources[37], however many XFCT systems use polyenergetic x-ray sources as they are more accessible[38, 39, 40]. Many XFCT systems have studied the detection of AuNPs in particular[41, 42, 43], but also of gadolinium[44, 40]. XFCT imaging for multiple contrast agents has been demonstrated for elements including gold, gadolinium, and barium[45].

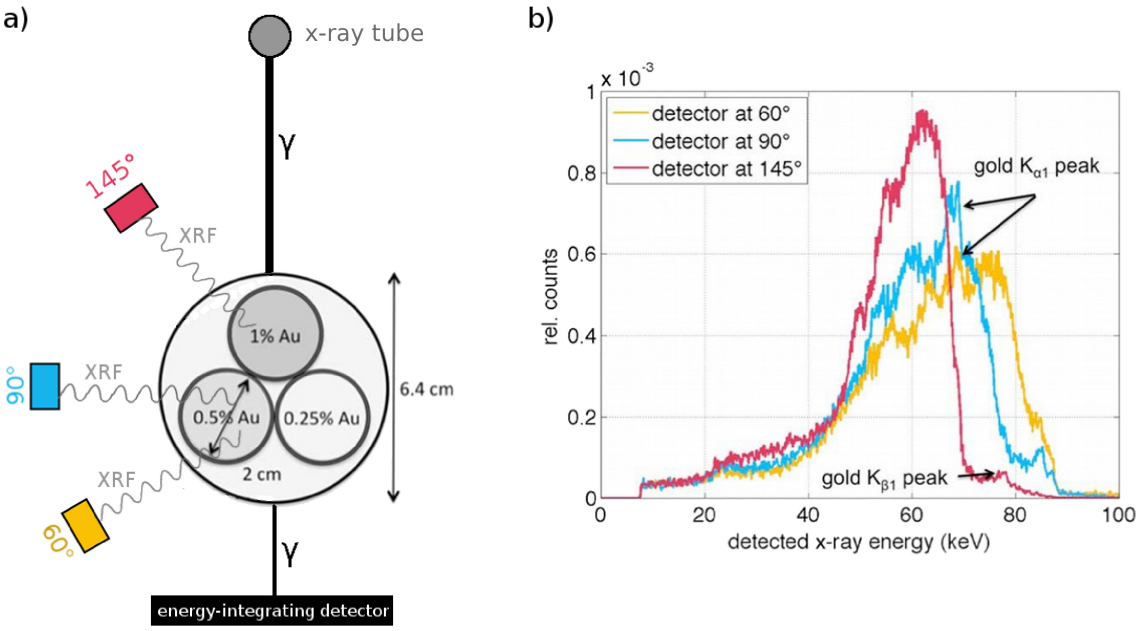


Figure 1.9: Diagram of a table-top XFCT imaging system (a), where the incident beam from the x-ray tube induces x-ray fluorescence (XRF) in the gold (Au) samples. Spectrometers placed at angles of 60°, 90°, and 145° relative to the outgoing beam detect x-ray spectra (b) with Au K-shell fluorescent x-ray peaks highlighted. The energy-integrating detector can simultaneously acquire CT data during XFCT acquisition to provide anatomical information. Figure adapted from Ahmad *et al.* (2015)[39].

XFCT is considered to be a quantitative method of imaging contrast agents, meaning that the number of detected fluorescent x-rays is proportional to the number of high-$Z$ atoms. Detecting the net number of fluorescent x-rays for image reconstruc-

tion is challenging due to factors such as fluorescent x-ray attenuation, Compton-scattered x-ray interference, and spectrometer resolution. Scatter and attenuation of fluorescent x-rays in material limit XFCT to small animal imaging; many scatter- and attenuation-correction algorithms were developed to overcome these problems[46, 43]. The placement of a spectrometer at higher scattering angles effectively shifted the Compton-scattered x-ray spectrum to lower energies (Equation 1.3) to reduce its interference with the gold K-shell fluorescent x-rays[47, 39], as shown in Figure 1.9. Although the 145° spectrometer placement improved the XFCT image quality, the imaging time resulting from the x-ray pencil beam setup was prohibitively long for small animal imaging. Many fan beam and cone beam XFCT system designs have been developed with a variety of collimator and detector geometries with the goal of faster imaging times[48, 49, 50, 51, 38]. And compared to K-edge CT, XFCT has better imaging sensitivity for gold concentrations below 0.4%[52, 53].

In addition, the detection of L-shell fluorescent x-rays has been studied to further improve imaging sensitivity of AuNPs compared to detection of K-shell fluorescent x-rays in table-top imaging systems[54, 55]. This is because lower energy x-ray beams can induce more L-shell fluorescent x-rays than K-shell fluorescent x-rays by higher energy x-ray beams. L-shell XFCT has the potential to increase AuNP imaging sensitivity, but the low energy of the L-shell fluorescent x-rays makes them extremely susceptible to attenuation[56].

## 1.4 Summary of Dissertation

It is important to note that the development of novel imaging modalities starts at the table-top imaging system. Just as how the development of contrast agents begins with small animal studies, the development of small animal imaging systems serves as a basis for future clinical translation and for improving small animal imaging used for other experiments.

This dissertation will focus on imaging contrast agents, such as AuNPs, using PCCT and XFCT within the scope of small animal imaging. In the first three simulation studies we investigated the K-shell and L-shell XFCT image quality of AuNPs as a function of radiation source type, collimation strategy, detector arrangement, and AuNP depth in the imaging subject, also known as a phantom. The first study not only compared XFCT image quality between monoenergetic and polyenergetic x-rays, but demonstrated the possibility of detecting AuNPs using x-ray fluorescence

for other applications involving electron or proton beams. The results from the latter studies served to benchmark the design of the XFCT portion of the table-top x-ray imaging system using multiple detectors. In the next experimental study, we used PCCT to image multiple novel contrast agents at once to determine the amount of cross contamination between elements in each image. In the final experiment, we present the first simultaneously-acquired XFCT and PCCT images of gold and gadolinium solutions in a phantom and in euthanized mice on our system, which was designed based on our previous XFCT simulations and PCCT experiments.

**Chapter 1** contains an introduction of the use of contrast agents in the contexts of both radiation therapy and imaging and the methods used for imaging, followed by an overview of the structure of the dissertation itself.

**Chapter 2** describes in detail the materials and methods that were used throughout the research discussed in this dissertation.

**Chapter 3** outlines the imaging workflow from phantom design and data acquisition to image reconstruction and analysis.

**Chapter 4** documents the expected XFCT image quality when imaging gold nanoparticles in small- and medium-sized phantoms using a variety of excitation beams including monoenergetic and polyenergetic x-rays, high- and low-energy electrons, and protons.

**Chapter 5** demonstrates the effect of different collimator geometries on image quality for sheet beam XFCT compared to pencil beam XFCT.

**Chapter 6** is a study which optimizes the arrangement of multiple spectrometers for Au K-shell and L-shell XFCT, and documents image quality based on spectrometer type, spectrometer distance from phantom, data acquisition strategy, and gold nanoparticle depth in the phantom.

**Chapter 7** introduces a novel K-edge subtraction CT imaging technique enabled by a photon-counting detector and experimentally investigates the ability to resolve multiple lanthanide contrast agents using PCCT.

**Chapter 8** is a culmination of the presented research with the design of a table-top x-ray system capable of simultaneous XFCT and PCCT imaging of Gd and Au contrast agents in a phantom and in euthanized mice.

**Chapter 9** contains a summary of conclusions drawn from the presented research, and offers future direction.

# Chapter 2

# Materials and Methods: Theory

This chapter describes the theory of the methods and the details of the materials used for the research projects in this dissertation. X-ray generation, detectors, Monte Carlo theory, and film dosimetry will be discussed.

## 2.1 Kilovoltage X-ray Beam Generation

X-rays are generated by keV-range electrons striking a material and converting their energy into x-rays. An x-ray tube is a device contained within a vacuum envelope that accelerates electrons from a cathode filament using a potential difference, referred to as the tube voltage, to hit an anode target to produce x-rays (Figure 2.1). The tube current is the amount of charge from electrons per second that travel to the anode, and a greater tube current results in greater x-ray output[26]. The definition of an eV is the energy required to move an electron across a 1 V potential difference, so a tube voltage of 90 kV results in 90 keV electrons incident on the target. Electrons convert some portion of their kinetic energy into *bremsstrahlung* x-rays, fluorescent x-rays, or heat.

Figure 2.2a shows an unfiltered *bremsstrahlung* x-ray spectrum that is output from the anode in vacuum. The closer the electron approaches to atomic nuclei, the greater the *bremsstrahlung* x-ray kinetic energy. The probability of producing a *bremsstrahlung* x-ray increases with increasing circumference around the nucleus; the circumference is dependent on the radial distance between the electron and the nucleus. This results in an inverse linear relationship between the *bremsstrahlung* x-ray output and energy. The filtered *bremsstrahlung* x-ray spectrum in Figure 2.2a is what actually leaves the x-ray tube because the vacuum-sealed glass and inherent filtration attenuate lower energy x-rays. While this reduces the x-ray output, the

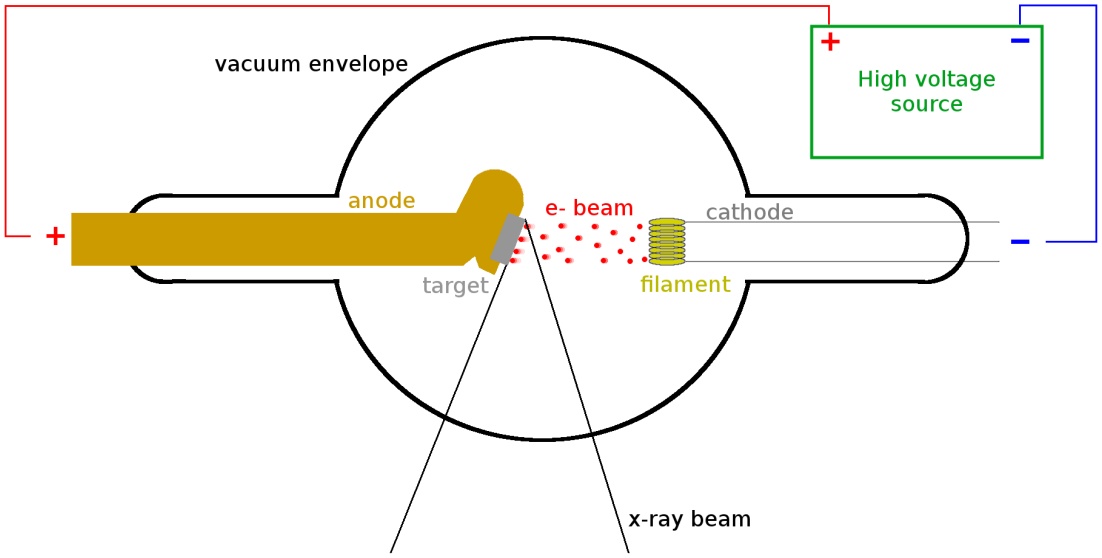


Figure 2.1: Diagram of an x-ray tube based on Bushberg *et al.* (2011)[26]. An electron beam ($e^-$) is produced by the cathode filament and is accelerated by the high voltage toward the anode. The electrons interact with the target to produce an x-ray beam.

removal of low energy x-rays is beneficial – low energy x-rays are not useful for CT imaging and only contribute to imaging dose. Adding extra filtration material such as Pb, Al, or Cu changes the shape of the *bremsstrahlung* x-ray spectrum and increases the mean x-ray energy by attenuating more low energy x-rays[26].

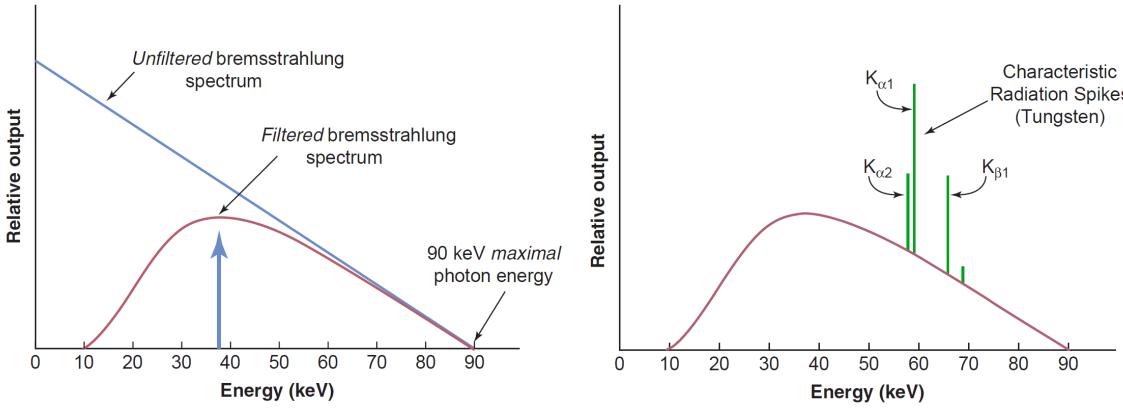


(a) *Bremsstrahlung* x-rays. (b) Characteristic x-rays.

Figure 2.2: Example of an x-ray tube spectrum with peak voltage of 90 kV and mean energy 38 keV incident on a tungsten target, composed of a) *bremsstrahlung* and b) characteristic fluorescent x-rays. Figure adapted from Bushberg *et al.* (2011)[26].

Fluorescent x-rays from the x-ray tube target are also produced from collisions of the electrons with atomic electrons in the target, provided the electrons have enough kinetic energy from the tube voltage to eject atomic electrons from their orbitals. Figure 2.2b shows characteristic K-shell fluorescent x-rays from electrons hitting the tungsten target superimposed on a filtered *bremsstrahlung* x-ray spectrum. The K-shell fluorescent x-rays of tungsten are 59.32 keV ($K_{\alpha 1}$), 57.98 keV ($K_{\alpha 2}$), and 67.24 keV ($K_{\beta 1}$)[57].

The x-ray tube that was used for experimental XFCT and PCCT imaging was the MRX-160/22 X-ray tube (Comet Technologies, Flamatt, Switzerland), which had a tungsten target and was capable of a maximum x-ray tube voltage of 160 kV. However, the maximum x-ray tube voltage used was 120 kV due to the amount of shielding in the lab room.

## 2.2 Detectors

In a perfect detector, the exact number of x-rays and their energies could be recorded. This is often modeled in simulations as a simple boundary crossing, in which an x-ray that crosses a surface has its energy recorded. The detection efficiency in the context of XFCT imaging is often described in terms of solid angle coverage of the detector, as fluorescent x-rays are emitted isotropically. So a perfect XFCT system would have a single spherical boundary around the phantom that could record every single fluorescent x-ray.

However, perfect detectors do not exist. The detection of x-rays is confounded by scatter, the detector response, the energy resolution, and the size of the active area. For multi-pixel detectors, the interference of a detection event between pixels from a single x-ray is an additional issue. This section will introduce two kinds of detectors used in this research – a spectrometer and a photon-counting detector for XFCT and PCCT imaging, respectively – and the methods of how the detector behaviour was modeled.

### 2.2.1 Spectrometers

A spectrometer is a detector device that is capable of detecting an energy histogram of the x-rays that are absorbed in the detection crystal. Spectrometers are particularly useful in XFCT imaging, as discrete fluorescent x-ray peaks often stand out in the detected x-ray spectra. The spectrometer types that were studied are the Amptek X-

123CdTe X-ray Spectrometer and X-123SDD X-ray Spectrometer with Silicon Drift Detector (SDD) (Amptek Inc., Bedford, MA, USA), pictured in Figure 2.3a. The X-123CdTe spectrometer, referred to simply as a CdTe spectrometer, was available in both $(3 \times 3)$ mm$^2$ and $(5 \times 5)$ mm$^2$ square CdTe crystal sizes with 1 mm thickness. It has a maximum x-ray energy detection limit of 150 keV, making the CdTe spectrometer appropriate for the detection of K-shell fluorescent x-rays from high-$Z$ elements. The X-123SDD spectrometer had a cylindrical Si crystal size of 25 mm$^2$ cross-sectional area and 1 mm thickness, and will be referred to as a Si spectrometer. With a maximum x-ray energy detection limit of only 30 keV, the Si spectrometer is appropriate for the detection of L-shell fluorescent x-rays. Our research lab has two $(3 \times 3)$ mm$^2$ CdTe spectrometers, two $(5 \times 5)$ mm$^2$ CdTe spectrometers, and four Si spectrometers. In addition, these spectrometers can sustain count rates of $2.0 \times 10^5$ counts per second (cps) maximum as specified by the manufacturer, which were appropriate for measuring scattered x-rays in XFCT imaging as typical x-ray count rates are approximately $1 \times 10^4$ cps.

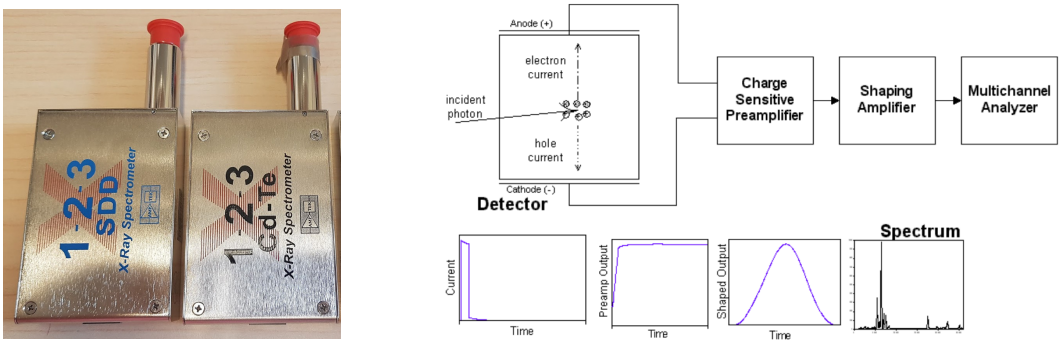


(a) Amptek X123 spectrometers.

(b) Diagram of the spectrometer and its electronics.

Figure 2.3: a) Photo of Amptek X123SDD (left) and Amptek X123CdTe (right) spectrometers. b) Diagram of the spectrometer operation and its electronics. The current $I(t)$ generated by electron-hole pairs in an electric field is integrated to a charge signal, and shaped into an analog signal[58].

Each of the Amptek X-123 spectrometers is a complete integrated system consisting of an XR-100 detector and preamplifier, a DP5 digital pulse processor and multi-channel analyzer (MCA), and a PC5 power supply. When ionizing radiation such as an x-ray deposits its energy in the crystal, it generates electron-hole pairs with its charge proportional to the energy deposited. In the presence of an electric

field generated by an applied voltage, the electron-hole pairs drift apart in the crystal towards the cathode and anode (Figure 2.3b) which in turn generates a current. The current is the time derivative of charge, so the preamplifier produces an output pulse that integrates the current into a signal that is proportional to the charge. A shaping amplifier then shapes the pulse to maximize the signal-to-noise ratio by reducing background noise. The MCA measures the amplitude of this pulse signal, which is directly proportional to the amount of energy deposited. The number of amplitudes that the MCA can measure are referred to as channels. The MCA outputs a histogram showing the number of pulses with amplitude measured within the range of each channel[58]. The default number of channels is 1024, and each channel was calibrated to characteristic gamma rays from known radioactive sources.

The Amptek DPPMCA software is available for installation on Windows operating systems and enabled real-time display of data acquisition via a direct 12 Mbps USB 2.0 connection. Figure 2.4 depicts the Amptek DPPMCA graphical user interface (GUI) software, which allowed for the adjustment of the spectrometer settings, monitoring of spectrometer conditions, and analysis of the acquired data.

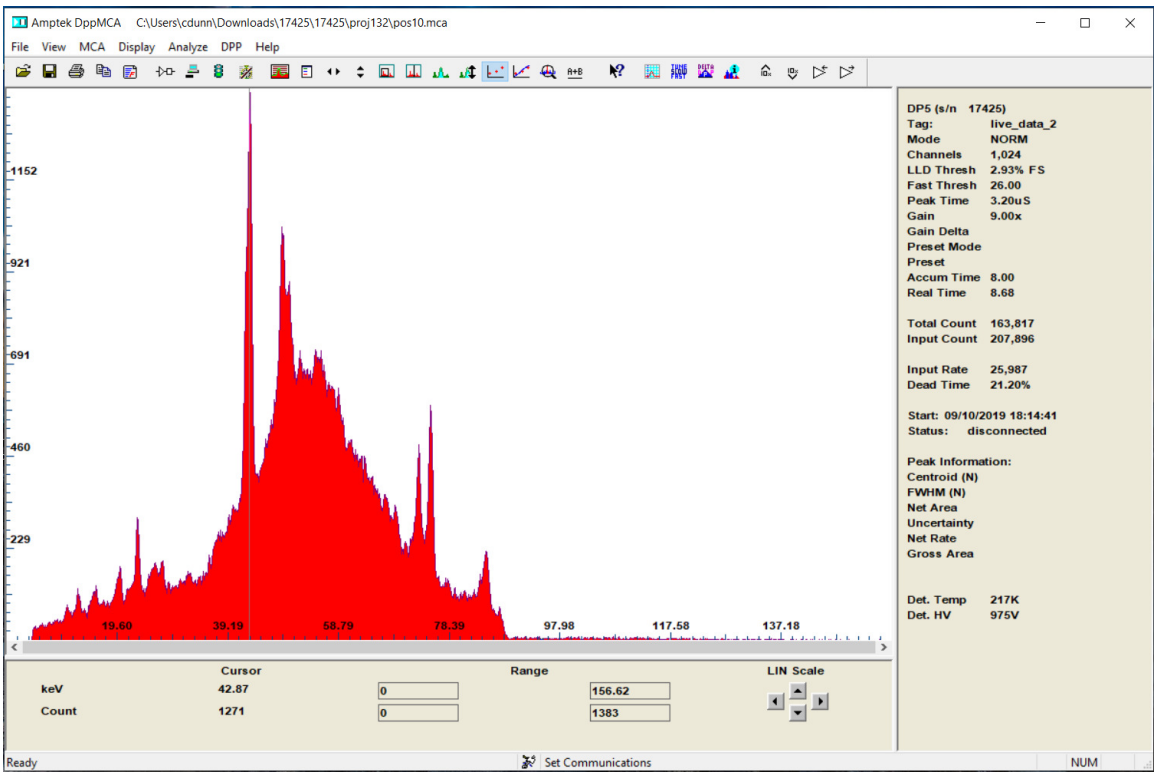


Figure 2.4: Amptek GUI showing an example of an acquired x-ray spectrum by the MCA.

When simulating energy deposition in the detector crystal, it is important to accurately model the surrounding materials in the x-ray path to the crystal. The geometry of each CdTe spectrometer is a CdTe block of dimensions 1 mm × 5 mm × 5 mm with a 0.2 $\mu$m-thick top layer of platinum, 1 $\mu$m-thick bottom layer of indium, and a 100 $\mu$m-thick beryllium window (Figure 2.5a). The geometry of each Si spectrometer is a Si cylinder of cross-sectional area 25 mm$^2$ and thickness 1 mm with a 12.5 $\mu$m-thick beryllium window. The Si layer sits directly below a multi-layer collimator with a 17 mm$^2$ opening and consists of a stack of the following materials from top to bottom: 100 $\mu$m tungsten, 35 $\mu$m chromium, 15 $\mu$m titanium, and 75 $\mu$m aluminum (Figure 2.5b). All spectrometer geometries were according to manufacturer's specifications and did not include the housing of the electronics.

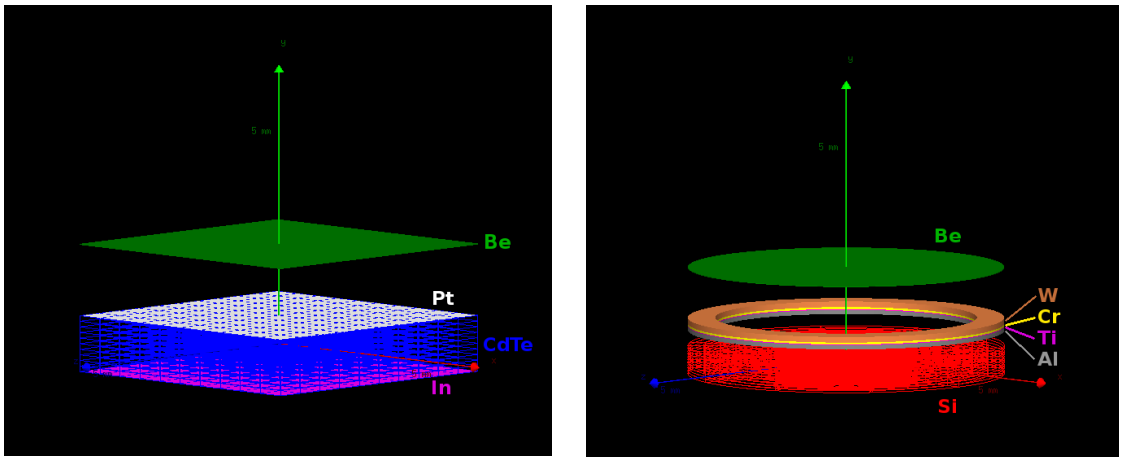


(a) 25 mm$^2$ CdTe spectrometer. (b) 25 mm$^2$ Si spectrometer.

Figure 2.5: a) Simulated geometry of the 25 mm$^2$ CdTe spectrometer with beryllium (Be) window, top contact of platinum (Pt), and bottom contact of indium (In). b) Simulated geometry of the 25 mm$^2$ Si spectrometer with Be window and multi-layer collimator consisting of tungsten (W), chromium (Cr), titanium (Ti), and aluminum (Al).

### Energy Calibration and Resolution

The energy resolution of each spectrometer type was verified experimentally with the use of calibration sources. The CdTe and Si spectrometers recorded a spectrum from $^{133}$Ba and $^{55}$Fe radioactive sources with relevant gamma ray energies of 80.99 keV and 5.89 keV, respectively, for 30 minutes each with the rise time discrimination setting turned off and a peak time of 3.2 $\mu$s and 11.2 $\mu$s, respectively. These calibration

sources were chosen based on the similarity of gamma ray energies and fluorescent x-ray energies of gold. Each source was placed as close as possible to the appropriate spectrometer without causing detector pile up. The channels corresponding to the 5.89 keV and 80.99 keV gamma ray peaks of the $^{55}$Fe and $^{133}$Ba spectra, respectively, were calibrated to those energies for a fixed gain, and channel 0 was calibrated to zero energy.

The energy resolution of each spectrometer was measured by fitting the following Gaussian function to the $E_0 = 5.89$ keV peak of $^{55}$Fe and the $E_0 = 80.99$ keV peak of $^{133}$Ba, shown in Figure 2.6:

$$N(E) = N_0 \exp\left(\frac{-(E - E_0)^2}{2\sigma^2}\right) \tag{2.1}$$

where $E$ is the detected photon energy, $N_0$ is the number of gamma ray counts at $E_0$, and $\sigma$ is the standard deviation. In particular for the $^{133}$Ba spectrum, most of the 80.99 keV peak was fit to the Gaussian due to the hole-tailing effect at the lower-energy end of the peak. The Gaussian fit was performed using the SciPy Optimize module in Python. The full width at half maximum (FWHM) $= 2\sqrt{2\ln 2}\sigma$ of each Gaussian was determined to be 125 eV, 902 eV, and 798 eV for the Si, 25 mm$^2$ CdTe, and 9 mm$^2$ CdTe spectrometers, respectively. The specifications of each spectrometer was quoted as 125 eV at the 5.89 keV $^{55}$Fe peak, <1.5 keV at the 122 keV $^{57}$Co peak, and <1.2 keV at the 122 keV $^{57}$Co peak for the Si, 25 mm$^2$ CdTe, and 9 mm$^2$ CdTe spectrometers, respectively. Since the measured energy resolution for each spectrometer was consistent with their specifications, the FWHM of the Gaussian representing the energy resolution of each spectrometer at the appropriate fluorescent x-ray energies was modeled as 200 eV, 900 eV, and 800 eV for the Si, 25 mm$^2$ CdTe, and 9 mm$^2$ CdTe spectrometers, respectively, in Figure 2.6[59].

The energy deposition in the crystal as a function of incident photon energy can be scored in XFCT simulations. To mimic realistic data acquisition, the energy deposition was mathematically convolved with a Gaussian function with a FWHM equal to that of the spectrometer energy resolution, as described above.

### Detector Response

In a perfect detector, a 67 keV Au K-$\alpha_2$ x-ray would be detected by an event where 67 keV of energy was deposited in the crystal by secondary electrons. However, this is not always the case depending on the x-ray interactions and the electron tracks relative to

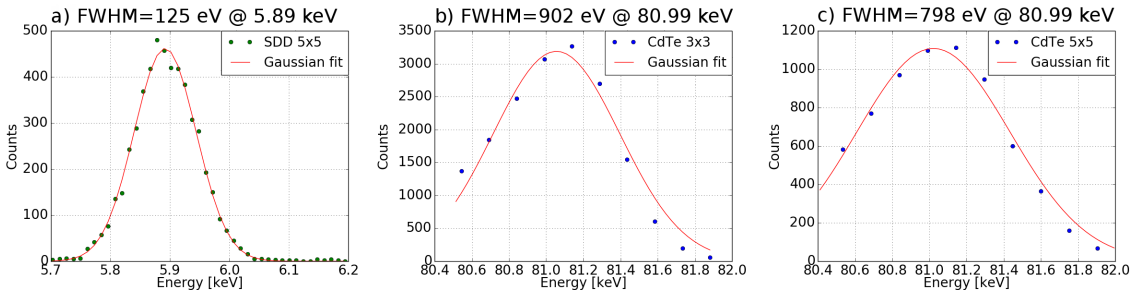


Figure 2.6: Measured counts of calibration source peaks detected by the Si, 25 mm$^2$ CdTe, and 9 mm$^2$ CdTe spectrometers. The calibration sources were $^{55}$Fe and $^{133}$Ba for the Si and CdTe spectrometers, respectively.

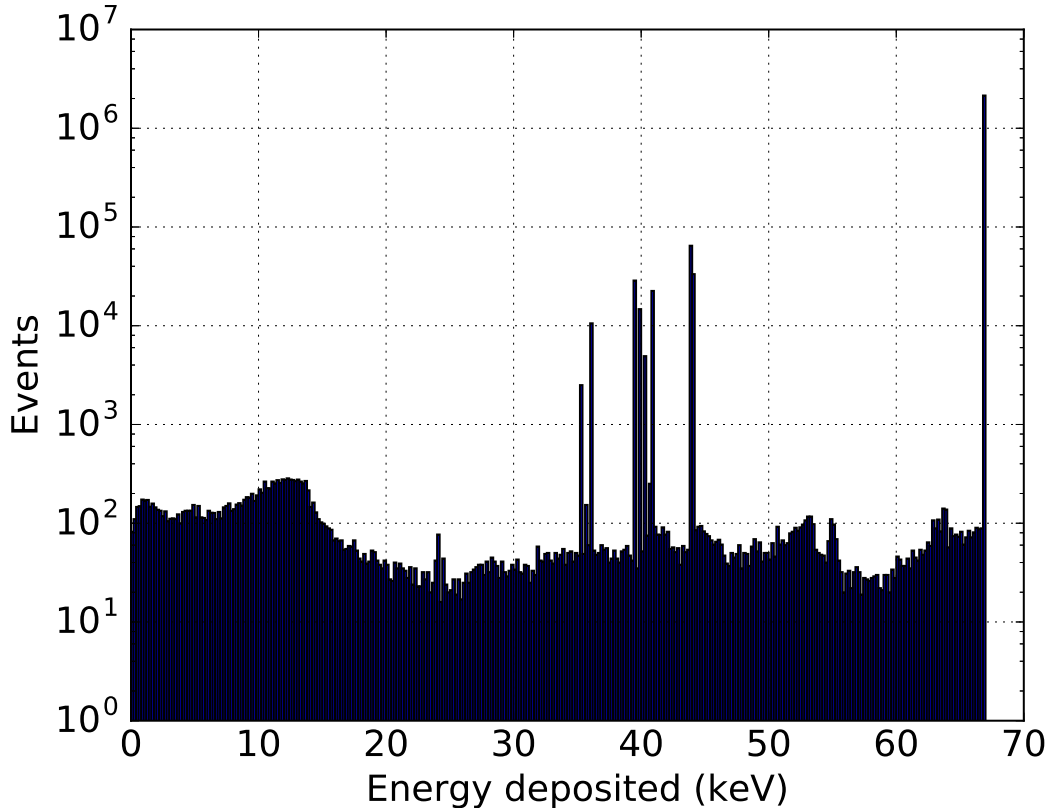


Figure 2.7: Simulated detector response of the 25 mm$^2$ CdTe spectrometer to 67 keV x-rays.

the spectrometer size and geometry; Figure 2.7 depicts the 25 mm$^2$ CdTe spectrometer response to a beam of 67 keV x-rays, for instance. The stripping method [60] is an algorithm that corrects for the detector energy response and detection efficiency of the detected x-ray spectrum $N_d(E)$:

$$N_t(E_0) = \frac{N_d(E_0) - \sum_{E=E_0+\Delta E}^{E_{\max}} R(E_0, E) N_t(E)}{R(E_0, E_0)} \tag{2.2}$$

where $N_t(E_0)$ is the true number of photons with energy $E_0$, $N_d(E_0)$ is the number of photons detected with $E_0$, $E_{\max}$ is the maximum energy in the detected spectrum, $R(E_0, E)$ is the monoenergetic response function (Figure 2.7 with $E_0 = 67$ keV), and $R(E_0, E_0)$ is the full-energy absorption peak efficiency. In other words, $R(E_0, E_0)$ is the proportion of $E_0 = 67$ keV x-rays that are detected as 67 keV x-rays. The monoenergetic response functions for each spectrometer type were obtained using a series of TOPAS Monte Carlo simulations by scoring the energy deposition in the crystal from 5.0 $\times 10^6$ monoenergetic x-rays with energy $E$ in steps of $\Delta E$. $E$ ranged from 3.0 keV to 50.0 keV in steps of $\Delta E = 0.1$ keV for the Si crystal, while $E$ ranged from 5.0 keV to 120.0 keV in steps of $\Delta E = 0.2$ keV for both CdTe crystal sizes. The cross-sectional area of the x-ray beam was double the size of the crystal. The simulated geometry for each spectrometer to generate the monoenergetic response functions were identical to the modeled spectrometers in the XFCT simulations[59].

### 2.2.2 Photon-Counting Detector

Semiconductor photon-counting detectors operate under a direct conversion principle, where the x-rays are converted directly into electrical signal in the form of electron-hole pairs upon interaction in the crystal, similar to as described in the previous section on spectrometers. The detector operates under a bias voltage which forces the electrons toward the anode to generate the electronic signals. The amount of signal generated in each detector pixel is proportional to the energy deposited by the incident x-ray. The ASIC sorts these electronic signals by pulse height and counts the number of signals that exceed the defined energy thresholds[34]. Each energy bin was defined by these thresholds which were adjustable in the 16-200 keV energy range. The basic operation of a photon-counting detector with two thresholds involves recording events with energy above the lowest threshold in one dataset, and events with energy above the highest threshold in another dataset, with a maximum threshold equal to the x-ray tube potential. The number of counts in the energy bin defined by these thresholds are calculated by the difference between the two datasets[34]. This can be expanded to six energy bins for the particular photon-counting detector in this work. The energy thresholds forming the six energy bins were set to coincide with

the K-edge energies of the studied contrast agents, which were in the available energy range.

The photon-counting detector used in this work (Redlen Technologies, Saanichton, BC Canada) consisted of two adjacent modules each 8 mm × 12 mm in size with a 2 mm-thick sensor made of a cadmium zinc telluride (CZT) semiconductor crystal. The modules were oriented such that the total active area of the detector was 8 mm× 24 mm. The CZT crystal was grown using the Traveler Heat Method (Redlen Technologies, Saanichton, BC), and had 864 individual pixels (24 × 36) with a 330$\mu$m pitch and a pixel count variability of <10%. The sensor operates under high-flux conditions at 250 $\times 10^6$ cps/mm$^2$ without any signs of polarization, which is necessary for CT applications when the detector is placed directly in the path of the x-ray beam[33]. The sensor was connected to the high-speed photon counting Application Specific Integrated Circuit (ASIC) that operated at rates up to 62.5 million cps per channel with six energy bin configuration.

### Energy Resolution

The energy resolution of the pixelated photon-counting detector can vary between pixels, with the specified values between 6-9 keV as quoted by the manufacturer. The manufacturer of the photon-counting detector performed a spectral sweep of an $^{241}$Am calibration source near the relevant gamma ray energy of 59.5 keV and computed the median spectrum across all pixels to measure the energy resolution. A spectral sweep consists of multiple acquisitions of gamma rays from the calibration source with incremental energy bin thresholds set on the photon-counting detector. The full width at half maximum (FWHM) of the 59.5 keV gamma ray peak of $^{241}$Am was measured to be 8.9 keV, as shown in Figure 2.8.

### Fluorescent Cross-talk and Charge Sharing

For pixelated semiconductor detectors such as the CZT photon-counting detector, fluorescent cross-talk and charge sharing are phenomena that can affect the total number of detected x-rays. Figure 2.9 illustrates fluorescent cross-talk and charge sharing[61].

The fluorescent cross-talk occurs when fluorescent x-rays from the Cd, Zn, or Te atoms are produced by the incident x-rays interacting with a particular pixel in the CZT sensor. Each fluorescent x-ray may subsequently migrate to another pixel and

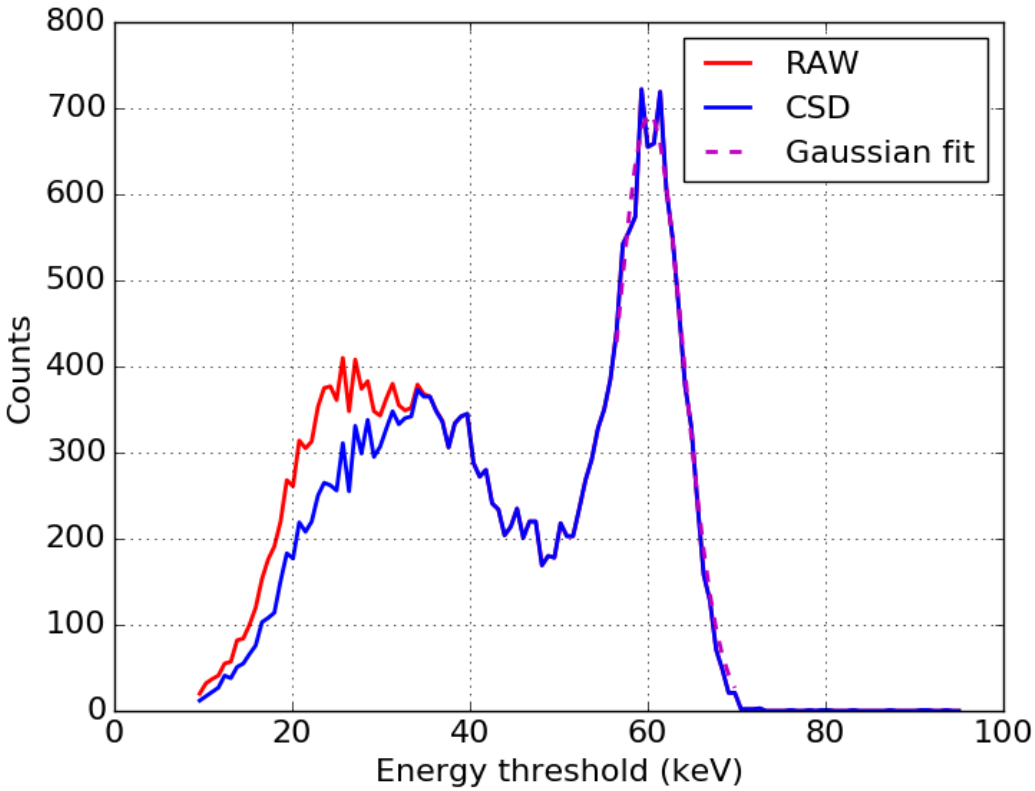


Figure 2.8: Spectral sweep of $^{241}$Am gamma ray spectrum measuring the Gaussian mean and FWHM of the 59.5 keV peak to be 60.2 keV and 8.9 keV, respectively. The acquisition was performed with and without charge-sharing discrimination (CSD). Data provided by Dr. Elmaddin Guliyev of Redlen Technologies Inc.

interact. This results in the appearance of two lower-energy events in two different pixels. Charge-sharing occurs when an incident x-ray deposits its energy in between two neighbouring detector pixels, and the resulting electronic signal is split between these pixels. In both cases, the image quality is degraded by the appearance of lower energy events across multiple pixels from one higher energy x-ray. The larger the pixel pitch, the less pronounced the effects of fluorescent cross-talk and charge sharing are in the resulting image quality. The CZT photon-counting detector has a charge-sharing discrimination (CSD) setting built into the detector electronics. The spectral sweep of $^{241}$Am in Figure 2.8 demonstrates the reduction of lower energy events when CSD is enabled.

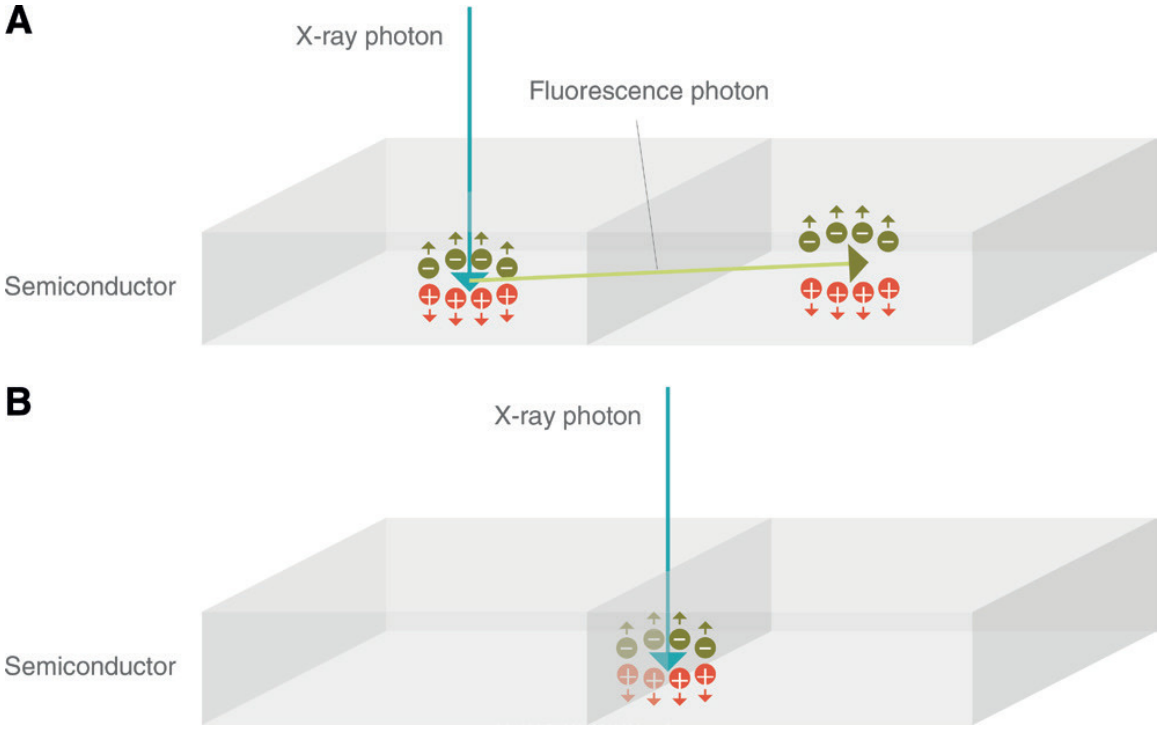


Figure 2.9: a) Detector pixel cross talk by fluorescence, where an incident x-ray photon induces fluorescence in the crystal. The fluorescent x-ray interacts with another detector pixel, depositing its energy there. b) Detector pixel cross talk by charge sharing, where the ionization of incident x-ray photon in the crystal produces a charge cloud on the boundary of two neighbouring detector pixels. The amount of energy corresponding to the event is split between the two pixels. Figure adapted from Willemink *et al.* (2018)[61]

## 2.3 Monte Carlo Simulations

The behaviour of particles in material is stochastic in nature, meaning that there is randomness associated with each particle's direction and method of interaction. As computational power increased over recent years, Monte Carlo simulations of particle transport played an increasingly important role in medical physics research and practice. In this research, Monte Carlo software was used to simulate XFCT imaging experiments and to calculate imaging dose. The following section will detail the basics of Monte Carlo modeling from random number generation to particle transport and interactions, considering only electromagnetic interactions for simplicity.

### 2.3.1 Monte Carlo Methods

#### Random Number Generation

Suppose a random number is sampled multiple times from a uniform distribution ranging from 0 to 1. A sequence of randomly computer-generated numbers is not truly random, however, since number generation algorithms tend to follow a pattern of periodicity. Many algorithms generate pseudo-random numbers, meaning that the pattern of generated numbers repeats extremely rarely and can be considered as random for all intents and purposes[62]. A random seed is a number used to initialize a pseudo-random number sequence.

#### Particle Transport

When simulating photon transport, the distance each photon travels before it interacts with matter must be randomly generated according to a probability distribution. The probability of a photon with energy $E$ traveling a distance $t$ through material with linear attenuation coefficient $\mu = \mu(E)$ is governed by an exponential function $\exp(-\mu t)$. A common method used to randomly sample photon distances is to equate the cumulative probability distribution of this exponential function with that of the uniform distribution with random variable $r$, then rearrange to solve for $t$:

$$\begin{aligned} \int_0^r \mathrm{d}r &= \int_0^t \exp(-\mu t) \\ r &= \frac{1}{\mu}\Big(1 - \exp(-\mu t)\Big) \\ \frac{-1}{\mu}\ln(1-\mu r) &= t \end{aligned}$$

This method randomly samples $r$ from a uniform distribution ranging from 0 to 1, and transforms the random number into a random photon distance $t$ as if it were sampled from an exponential distribution[62, 63].

Simulating electron transport requires the knowledge of the stopping power in the material an electron is in. Each electron is transported across a chosen step size, in which the continuous electron interactions of ionization and *bremsstrahlung* are condensed to save computation time. The mean energy loss over this chosen step size of the electron is computed, and the electron's kinetic energy is updated, along with position and direction based on the step size and deflections[63]. The simulation

of proton transport is similar to that of electron transport[63]. Note that proton deflections and stopping are the interactions most relevant for proton-induced XFCT simulation. The Bethe-Bloch formula introduced in Equation 1.6 is used to calculate the energy loss of protons in matter[64].

### Interaction Selection

After a photon is transported by a random distance, the type of interaction it undergoes must be chosen pseudo-randomly. This is usually decided by considering the fraction of the total linear attenuation coefficient for each possible photon interaction at its energy. For example, a 120 keV photon can undergo a photoelectric effect, Rayleigh scattering, or Compton scattering event with the respective partial attenuation coefficients of $\tau$, $\sigma_{coh}$, and $\sigma_{inc}$. If $\tau + \sigma_{coh} + \sigma_{inc} = \mu$, then the outcome of a uniform random number $r$ between 0 and 1 can decide what photon interaction occurs by the following method:

$$\text{if} \quad \begin{cases} 0 \leq r < \frac{\tau}{\mu} & \rightarrow \text{Photoelectric effect} \\ \frac{\tau}{\mu} \leq r < \frac{\sigma_{coh}+\tau}{\mu} & \rightarrow \text{Rayleigh scatter} \\ \frac{\sigma_{coh}+\tau}{\mu} \leq r < 1 & \rightarrow \text{Compton scatter} \end{cases}$$

Depending on the photon interaction selected, the photon track is either terminated, or its properties change. If a Compton scatter event occurs, for example, then the photon scattering angle must be pseudo-randomly sampled to change its direction, and subsequently its new energy is calculated according to Equation 1.3. Some interactions will give rise to new photon and electron tracks, such as secondary fluorescent x-rays or electrons from the Compton scatter process. Electrons can also give rise to *bremsstrahlung* x-rays, which then proceed according to the aforementioned photon transport and interaction methods. The terminology describing all of the subsequent interactions caused by a single incident photon is known as a particle history.

### Accept-Reject Method

For functions whose probability distribution functions are non-invertible, such that its cumulative distribution function cannot be matched to that of the uniform distribution, the accept-reject Monte Carlo method is a useful tool[65]. The accept-reject method can be used to sample the energy of the scattered photon after a Compton

event in the bound-electron version of Equation 1.5, for instance[66].

In the accept-reject method (Figure 2.10), the probability distribution function $f(x)$ of a random variable $x$ is bound by the rectangular area $[x_{min}, x_{max}]$ and $[y_{min}, y_{max}]$. In a single trial, a test point $(x_t, y_t)$ is uniformly sampled within this rectangular area. If $y_t < f(x_t)$, then $x_t$ is accepted as a random value, otherwise it is rejected. This process repeats until a sufficient amount of trials have been performed.

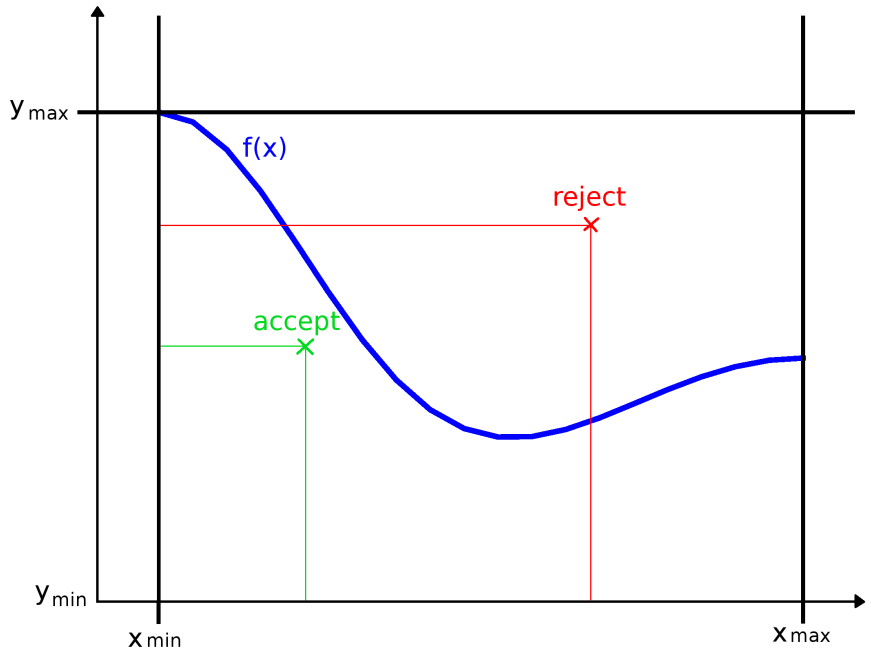


Figure 2.10: Diagram of the accept-reject method, showing an example of an accepted and rejected trial sampled relative to the probability distribution function $f(x)$.

The accept-reject method is a valuable algorithm when sampling based on complicated probability distribution functions, akin to throwing darts in the rectangle. However, it can be inefficient for a large amount of trials and is only valid for continuous functions over a finite range.

### Phase Space

A phase space is a collection of particle information that is saved when a particle travels across a geometric boundary. A phase space file contains information about each particle's type, energy, direction, position, and weight. The Monte Carlo simulation can also impose restrictions on what particles are saved in the phase space, such as

including only photons. Phase spaces are useful for storing particle information for later use; for example in x-ray tube simulations the photons that make up the x-ray beam are saved at the exit port of the x-ray tube to reduce computation time. It can also be used to score other parameters, such as particle fluence through a boundary or the photon energy spectrum. Phase space files can get quite large, so often they are stored in a binary IAEA format with complementary `ASCII` header files describing phase space characteristics such as the number of photons, maximum and minimum energy, and the number of histories in the original simulation.

### 2.3.2 Monte Carlo Software

Monte Carlo simulations are quite computationally intensive, requiring the knowledge of each individual particle and simulation geometry as well as random number generation to govern their behaviour. Several Monte Carlo software packages have been benchmarked for a variety of different applications. Three Monte Carlo software packages that have been used include FLUKA, TOPAS, and EGSnrc.

#### FLUKA

FLUKA (*FLUktuierende KAskade*, version 2011.2c-5)[67],[68] is a general purpose closed-source Monte Carlo package used to simulate x-ray fluorescence for sheet beam XFCT. FLUKA is based in FORTRAN77 code and can accurately model electrons and photons with energies ranging from 100 eV to thousands of TeV. FLUKA is typically used for high energy physics, nuclear activation, and shielding calculations, however it is capable of low-energy physics that are relevant to XFCT imaging. Detailed photoelectric edge treatment, fluorescence, Rayleigh scattering, and inelastic Compton scattering were included in all FLUKA simulations as part of the Precision default physics setting. The electron and photon transport cutoff was set to 5 keV, meaning that when the kinetic energy drops below 5 keV the particle is terminated and all of its energy is transferred to the medium.

Flair is the GUI for FLUKA based in Python and Tkinter, which enabled the visualization of the geometry. The method of combinatorial geometry was used; three-dimensional shapes known as "bodies" formed the imaging setup which included the phantom and collimators, and "regions" made of a specific material were assigned to areas relative to the bodies using boolean operators.

### TOPAS & Geant4

TOPAS (version 3.1.p2) is a wrapper and extension to the Geant4 Simulation toolkit to enable an easy-to-use simulation framework for medical physics applications[69, 63]. Geant4 (version 10.3.p01) is an established collaborative toolkit based in C++ code, with many physics packages suitable for a wide range of particle energies ranging from as low as 250 eV to TeV-scale. TOPAS uses a unique parameter control system to design the geometry, enable physics packages, and assemble other simulation parameters to communicate with the Geant4 backend. TOPAS is able to use IAEA format phase spaces as a particle source, and also uses OpenGL to visualize geometry and histories.

TOPAS was used to simulate x-ray fluorescence in gold and energy deposition in detectors. PIXE and fluorescent x-ray and Meitner-Auger electron generation options were enabled. The range cut for all particles was set to as low as 0.005 mm for photon-induced XFCT simulations, or as high as 1 mm for charged-particle induced XFCT simulations. This means that if a particle does not have enough energy to travel the distance specified by the range cut, it is terminated. The physics modules used for XFCT and dose calculation simulations include "g4em-standard_opt4", "g4decay", "g4ion-binarycascade", "g4stopping", and "g4em-extra". The "g4em-standard_opt4" package is the latest Geant4 standard physics package which governs electromagnetic interactions relevant to XFCT. The "g4ion-binarycascade" module contains inelastic hadronic models for ions, the "g4stopping" module encodes the capture of charged particles at rest, the "g4decay" module handles the decay of excited nuclei, and the "g4em-extra" module enables photonuclear interactions[69, 63, 70]. These latter four modules are more relevant for simulating heavy particles such as MeV-range protons.

### EGSnrc

The Electron-Gamma-Shower (EGSnrc) code[71], together with the BEAMnrc software component[72], was developed by the National Research Council of Canada as a Monte Carlo simulation toolkit. EGSnrc is open-source and is widely used for modeling electromagnetic interactions for medical physics purposes. The table-top x-ray system was simulated in EGSnrc[73], which recorded a photon phase space in IAEA format for use as an x-ray source in subsequent TOPAS simulations. A variance reduction technique known as directional *bremsstrahlung* splitting[74] was applied to the resulting photons in the x-ray tube simulation to improve the computational ef-

ficiency. In this technique, a *bremsstrahlung* x-ray is split into $N = 2000$ x-rays each with weight $\frac{1}{N}$. Only the x-rays whose direction is aimed toward a field interest was kept. The relative efficiency of directional *bremsstrahlung* splitting on photon fluence compared to no splitting is close to a factor of 500, when using a splitting factor $N = 2000$ for a 6 MV x-ray beam with a 10×10 cm$^2$ field size[74].

#### Computer Hardware for Monte Carlo Simulations

The WestGrid and Compute Canada networks of CPUs, available for academic researchers free of charge, were used to run Monte Carlo simulations in parallel on multiple cores. All FLUKA simulations were run on a SGI Altix XE cluster made up of Xeon X5675 and L5420 processors with 4160 cores, which is a part of the WestGrid network. All TOPAS simulations were run on a cluster of Intel E5-2683 v4 CPUs as part of the Compute Canada network. TOPAS Monte Carlo simulations for quick dose calculations were run on a local laptop with an AMD A10 processor.

### 2.4 Imaging Time & Dose Measurements

#### 2.4.1 Imaging Time

It is important to consider the imaging time. XFCT and PCCT imaging is primarily limited to small animal studies, during which the animals may be restrained or under anesthesia. Aside from considering animal welfare, a longer imaging time may render images prone to motion artifacts[75]. Small animal imaging should be no longer than 1.5 hours in duration[56]. The imaging time of an experimental PCCT or XFCT scan was measured using a stopwatch.

When simulating a fixed number of histories sampled from a specific x-ray beam spectrum in XFCT, the imaging time was estimated by first considering the typical electron current $I$ and *bremsstrahlung* yield from a table-top x-ray tube to estimate the x-ray output of the imaging beam. The *bremsstrahlung* yield $\gamma_e$ is the ratio of isotropic *bremsstrahlung* x-rays produced from electrons striking the anode target; typically this number is a function of $Z$ and electron energy and is tabulated[26, 76]. The useful x-ray output $\dot{\Phi}$ in x-rays per second at a distance $r$ from the focal spot of a hypothetical x-ray tube with an anode angle of $2\theta$ was estimated in the following equation:

$$\dot{\Phi} = I \times \frac{\gamma_e}{e} \times \frac{2\pi(1-\cos\theta)}{4\pi} \times \frac{A}{\pi r^2 \tan^2\theta} \tag{2.3}$$

where $A$ is the imaging beam area at the distance $r$, and $e = 1.602 \times 10^{-19}$ C is the elementary charge of the electron. This equation accounts for the anode angled at $2\theta$ by considering the fraction of solid angle that the x-ray beam would cover and the collimation of the conical beam to an area $A$.

Alternatively, if the simulated x-ray source is a phase space from a separate x-ray tube simulation, then the x-ray output can be estimated by the following equation:

$$\dot{\Phi} = \frac{N_\gamma I}{N_e e} \tag{2.4}$$

where $N_\gamma$ is the number of x-rays in the phase space and $N_e$ is the number of original electron histories from the x-ray tube simulation. This equation assumes that the x-rays have been collimated to the appropriate area in the x-ray tube simulation.

Next, the imaging time per acquisition $t_{acq}$ is estimated in the following equation:

$$t_{acq} = \frac{N_{sim}}{\dot{\Phi}} + t_{save} \tag{2.5}$$

where $N_{sim}$ is the number of primary x-rays used to simulate one acquisition and $t_{save} = 0.5$s is the time allowed between acquisitions for data-saving and repositioning during a hypothetical scan[39]. Multiplying $t_{acq}$ by the number of acquisitions in a full XFCT scan will give an estimate of the total imaging time.

### 2.4.2 Dose

The definition of dose in units of Gray (Gy) is the mean energy from ionizing radiation deposited per unit mass in a medium, equal to a joule per kilogram (J/kg). Since dose translates directly to living tissue damage, it is important to limit the amount of dose in XFCT and PCCT imaging. In clinical CT, the typical imaging doses range from 0.1 mGy to 100 mGy[26]; in particular, the brain dose from a head CT scan ranges from 50-60 mGy[77]. For preclinical mouse imaging, a standard imaging protocol of 60 kVp x-rays would result in approximately 40 mGy body dose[78]. In one study, 16 mGy was an average dose for mouse imaging, with no noticeable effect on mice after a 200 mGy total dose after a four-week period[79]. The mechanism of dose deposition for x-ray based imaging is by secondary electrons that are produced via photon interactions, which transfer kinetic energy to its medium along its path.

For simulated XFCT images, the total dose to the phantom was calculated by scoring the dose in the phantom volume in FLUKA and TOPAS. For the PCCT and

XFCT images obtained on the table-top x-ray system, the total dose was calculated in TOPAS using a phase space generated by the Monte Carlo model of the x-ray tube in EGSnrc. The phase space consisted of a number of 120 kVp x-rays filtered with 1 mm Al that were produced by a number of electrons $N_e$. The total Monte Carlo dose $D_{MC}$ was scored in a central 270 $\mu$m-thick slice of a cylindrical water phantom, then converted to a useful imaging dose $D_{img}$ using the following equation:

$$D_{img} = D_{MC} \times \frac{I N_{acq} t_{acq}}{N_e e} \tag{2.6}$$

where $I$ is the x-ray tube current, $N_{acq}$ is the number of detector acquisitions, $t_{acq}$ is the time for a single acquisition, and $e$ is the elementary charge of an electron. In addition, $D_{MC}$ can also be converted to the total dose for a complete 360° scan $D_{scan}$ by the following equation:

$$D_{scan} = D_{MC} \times \frac{360^\circ I}{\omega N_e e} \tag{2.7}$$

where $\omega$ is the angular speed of the phantom during acquisition in °/s.

### 2.4.3 Film Dosimetry

Gafchromic® EBT3 film (Ashland Advanced Materials, Bridgewater, NJ) is a common type of radiochromic film that is self-developing. It is composed of a 28 $\mu$m-thick active layer of pentacosa-10,12-diynoic acid (PCDA) between two 125 $\mu$m-thick layers of clear polyester coatings[80]. PCDA is a clear monomer that turns dark blue due to polymerization upon radiation exposure; the amount of darkening is proportional to the dose. The optical density is a measure of this amount of darkening based on the light exposure from a flatbed scanner, which will correspond to a unique value of dose for calibration[81].

The following film calibration procedure of the x-ray tube was performed in separate research[73]. A PTW Farmer® TN30013 ionization chamber (PTW, Freiburg, Germany) was irradiated by 120 kVp x-rays filtered with 1 mm Al for 1 minute at 13 mA to determine the dose rate at a 2 cm depth in solid water (CIRS, Norfolk, VA) with a 5 cm-thick slab of solid water underneath the ion chamber to provide backscattered radiation. Using the same setup, ten films were then irradiated to doses between 0.2 Gy and 8 Gy, and then scanned with an EPSON 10000XL flatbed scanner at a 200 dots per inch resolution. A control film with 0 Gy dose was also scanned. The optical density of each film was calculated by analyzing the pixel value of the film region

in the FilmQA pro® computer program (Ashland Advanced Materials, Bridgewater, NJ), using the encoded red channel in the scanned film colour image. This results in an optical density vs. dose curve, shown in Figure 2.11, for the specific x-ray beam energy and filtration for each channel for the purposes of calibration.

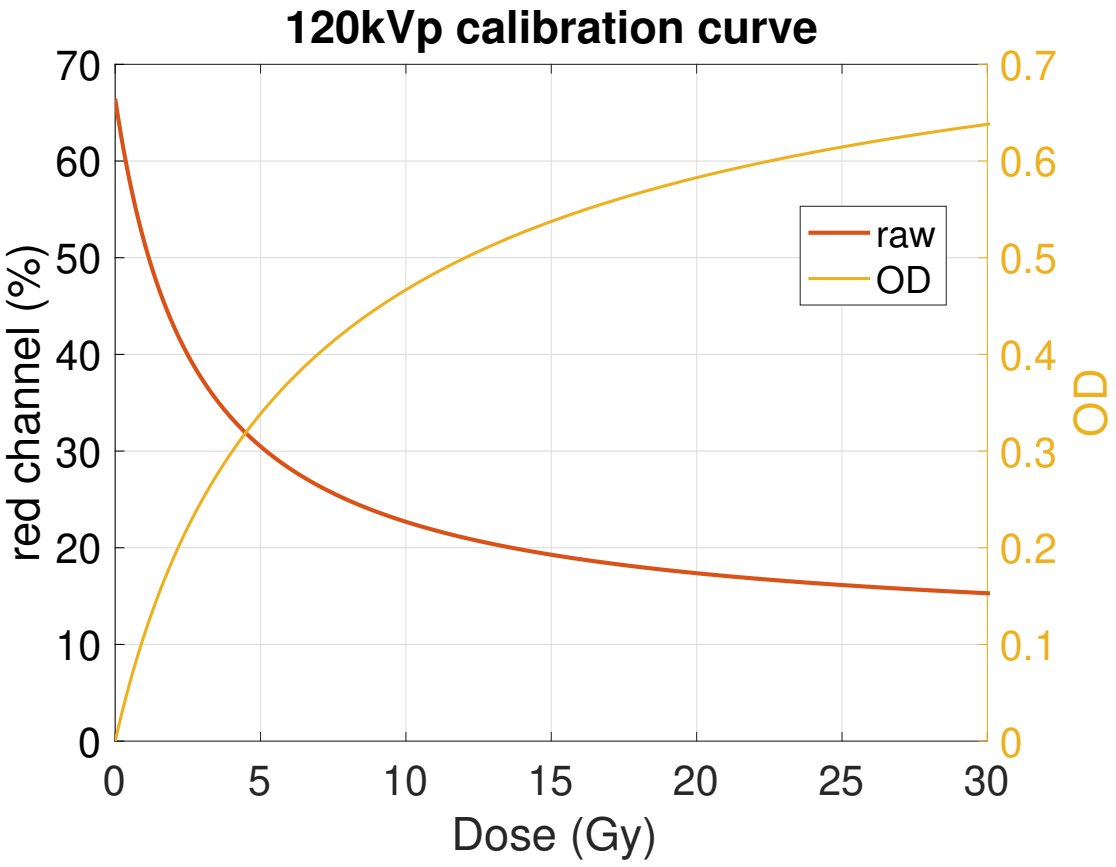


Figure 2.11: Film calibration curve of the raw pixel value of the red channel and optical density (OD) vs. dose from 120 kVp x-rays filtered with 1 mm Al. Plot provided courtesy of Nolan Esplen.

The Monte Carlo-derived phantom dose was experimentally verified using film dosimetry. A 3 cm-diameter circle was cut from a sheet of Gafchromic® EBT3 film and was placed at isocentre between two 3D-printed phantoms. The film was irradiated by a 120 kVp x-ray beam filtered with 1 mm Al over a 720° rotation, and left to rest for 24 hours. The film was then scanned with an EPSON® 10000XL flatbed scanner (Epson America, Long Beach, CA) at a resolution of 200 dots per inch, and its optical density was calculated in a 2 cm × 2 cm middle region of the film. This optical density value was then compared to a previously-generated calibration curve of optical density vs. dose (Figure 2.11). This process was repeated over three films

to obtain an average dose value.

A film batch will darken over time due to environmental effects such as natural background radiation or temperature fluctuations, causing an offset in the optical density which affects the dose reading. An unirradiated circle of film cut from the same sheet as the irradiated circular film was scanned separately. The calculated dose of this unirradiated film was subtracted from the irradiated film dose to account for the offset. The average dose from the three irradiated films was divided by two to find the average dose over a 360° rotation. This dose differed by 6.6% compared to $D_{scan}$ from Equation 2.7.

# Chapter 3

# Materials and Methods: Imaging Workflow

This chapter describes all the materials and methods used for the acquisition of XFCT and PCCT images. Both XFCT and PCCT imaging use a similar framework for data acquisition, image reconstruction, and image quality evaluation as conventional CT. The imaging subjects are introduced first, followed by the workflow of conventional CT; keeping in mind PCCT has extra information regarding x-ray energy and that there are modifications for XFCT application.

## 3.1 Imaging Subjects

A phantom, such as the one illustrated in Figure 3.2, is a well-defined object manufactured out of known materials. It is used as an imaging subject to evaluate the performance of an imaging system. Often the phantom is made out of water, plastic, or other tissue-equivalent material. The term tissue-equivalent refers to the similarity of radiological properties of a material compared to biological tissue, such as chemical composition and density.

For table-top x-ray imaging systems used in XFCT and PCCT, the important image quality characteristics to measure are the detectability of contrast agents in a phantom and accuracy of the reconstructed concentration. Often a cylindrical phantom, made of water or other hard plastic, containing holes filled with water-diluted contrast agents of varying concentrations is used to evaluate the minimum concentration of a contrast agent detectable. The size of these holes are chosen to mimic regions of accumulated contrast agent in biological systems, such as in blood vessels or in a tumour. These holes are arranged with radial symmetry at uniform depth in the phantom. The phantom design can also feature holes with varying depths to evaluate the change in image quality. The image quality assessment of XFCT and

PCCT phantom images is expanded upon in Section 3.4.

Phantom size is similar to the size of small animals, since table-top x-ray systems are used for small animal imaging and therapy purposes. Small animals such as mice contain anatomical structures that may impact the image quality of internal contrast agents.

### 3.1.1 Physical Phantom

A 3D-printed phantom (Figure 3.1a) made of uniform polylactic acid (PLA) was used for the experimental XFCT and PCCT studies. The cylindrical phantom had a density of 1.25 g/cm$^3$, a diameter of 3 cm, and a height of 2.5 cm. Seven 6 mm-diameter holes were built into the phantom to allow for insertion of 0.2 mL Flat Cap Eppendorf tubes (Fisher Scientific, Ottawa, ON Canada). These tubes held various solutions of contrast agents for XFCT and PCCT imaging studies. Iodine, lanthanum, gadolinium, holmium, lutetium, and gold-based solutions were all of the contrast agents studied.

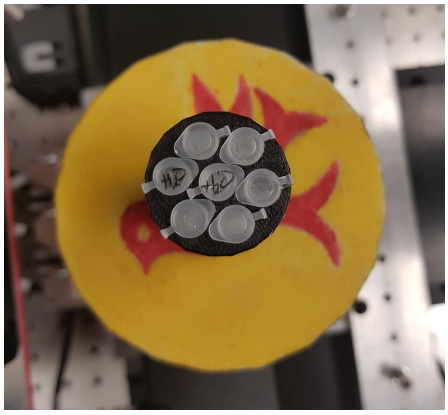

(a) 3D-printed phantom.

(b) Three contrast-filled mice of mass 20 g, 26 g, and 32 g from left to right.

Figure 3.1: Imaging subjects used for experimental XFCT and PCCT studies filled or injected with contrast agent solution.

### 3.1.2 Mice

Three euthanized mice (Figure 3.1b) were used for a preliminary XFCT and PCCT imaging study. Each mouse weighed 20 g, 26 g, and 32 g, and was euthanized after unrelated research. One day after euthanasia, the 26 g and 32 g mouse were each injected with 0.2 mL of 5% Au and 5% Gd solution, respectively, in the upper thoracic

region where the solution collected in the lungs. The 20 g mouse was injected with a mixture of 0.1 mL 5% Gd and 0.1 mL 5% Au solution also in the upper thoracic region, but the solution collected in the heart due to the smaller size of the mouse. All mice fit snugly into 50 mL plastic test tubes (Fisher Scientific, Ottawa, ON Canada) which had a diameter of 2.5 cm.

## 3.2 Data Acquisition

CT has several generations of data acquisition geometries. At the table-top imaging stage, CT data can be acquired with pencil beam, fan beam, sheet beam, or cone beam geometries. Instead of detecting the number of transmission x-rays in conventional CT, the data acquisition can be applied to XFCT by detecting fluorescent x-rays, and to PCCT with the extra step of sorting the energies of transmission x-rays into bins. The below explanation of the data acquisition is general and in the context of conventional CT for small animal imaging, keeping in mind this work is both simulated and experimental.

### 3.2.1 The Sinogram

The acquired data is collected in the form of a sinogram. The sinogram is an array with at least two dimensions – position of transmission x-rays through the phantom and the angle of the transmission x-rays relative to the phantom. A diagram of sinogram formation is shown in Figure 3.2. A three-dimensional sinogram would include a second position dimension in the case of a cone beam geometry. Each sinogram entry $j$ encodes the number of transmission x-rays $N_j$ for a specific position and angle, which is converted into projections $p_j$ by the following equation:

$$p_j = -\ln\left(\frac{N_j}{N_{0j}}\right) \tag{3.1}$$

where $N_{0j}$ is the number of transmission x-rays detected with no phantom present. The number of transmission x-rays $N$ through a material with linear attenuation coefficient $\mu$ and thickness $t$ can be found using Beer's law $N = N_0 \exp(-\mu t)$, presented in Equation 1.2.

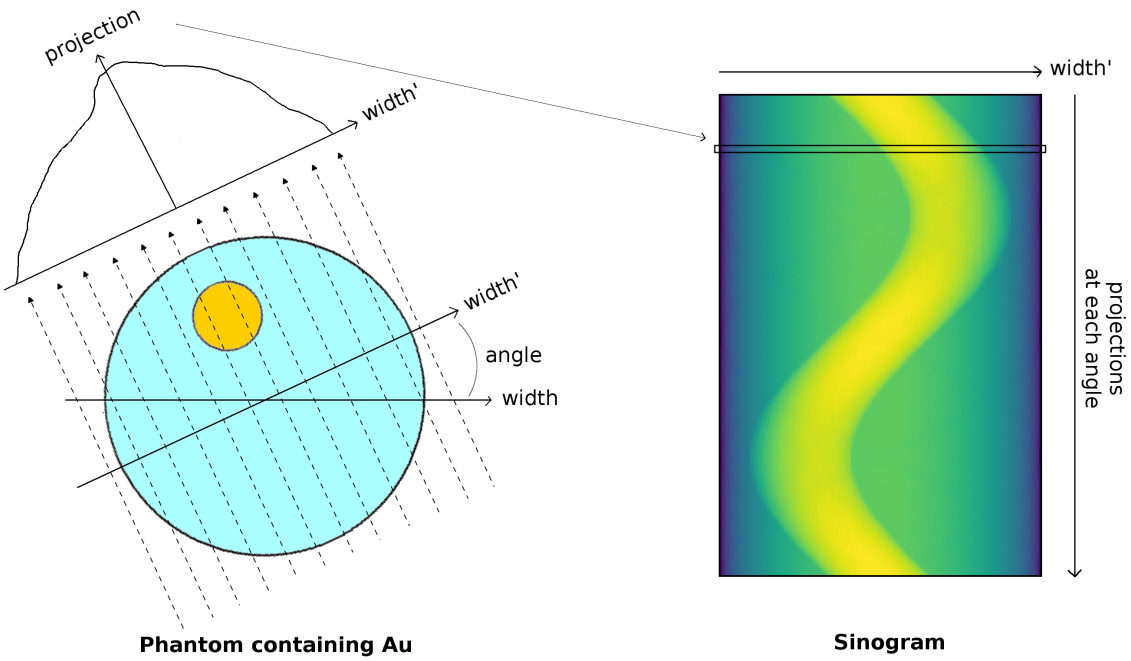


Figure 3.2: Sinogram formation from x-ray data at different positions and angles.

### 3.2.2 Pencil Beam

The pencil beam geometry (Figure 3.3) is perhaps the most straightforward geometry, which will be referenced to understand CT data acquisition. The x-ray beam from the x-ray tube is millimetre-sized with minimal beam divergence, similar in shape to a pencil. The x-ray tube and detector move across the phantom and save the data acquired over each position. Then, the x-ray tube and detector rotate at a fixed angle relative to the phantom, and the translation is repeated again. This process leads to the pencil beam geometry being known as the "rotate-translate" first CT generation[26].

The data acquisition in the pencil beam geometry results in a two-dimensional sinogram; the position and rotation are each represented by the x-ray tube/detector movements. Each sinogram entry directly translates to the path length of the pencil beam through the phantom body from Equation 3.1. The spatial resolution of the resulting CT image is controlled by the size of the pencil beam and the number of translation and rotation steps. Pencil beam CT images are less prone to scattered x-rays because only x-rays in the path of the incident beam are used for reconstruction. The ability to block scattered x-rays by means of collimation in pencil beam CT can

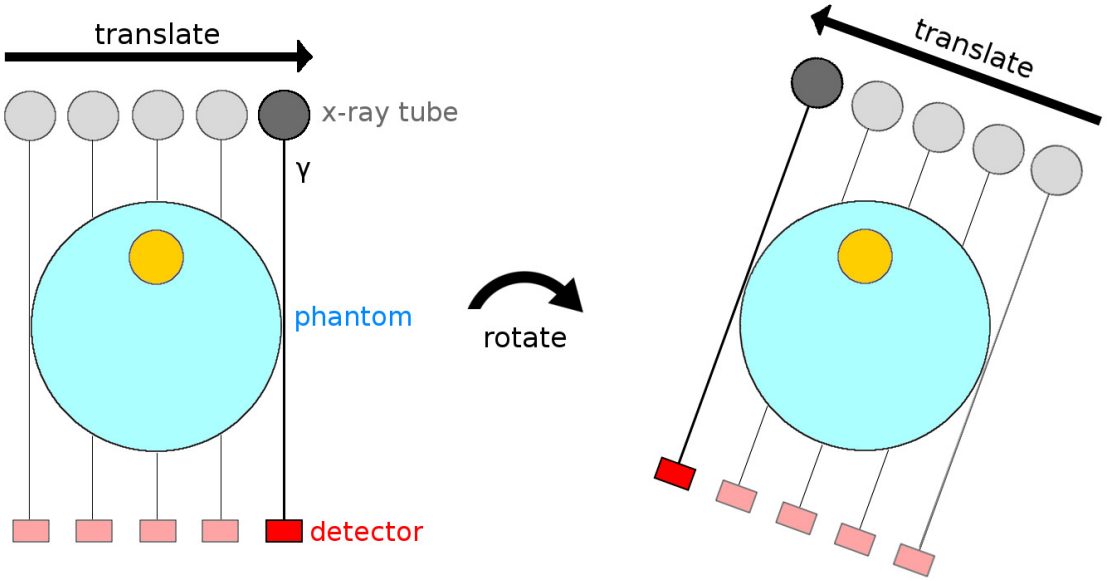


Figure 3.3: Pencil beam CT geometry. The x-ray tube and detector translate across the phantom body, rotate, then translate across the phantom body again. This repeats over a full rotation. The x-ray beam ($\gamma$) is small.

offer good spatial resolution, but at the expense of prohibitively long imaging times in practice.

### 3.2.3 Fan or Sheet Beam

The fan beam geometry (Figure 3.4) is characterized by a wide triangular-shaped beam and a row of individual detector elements spanning the field of view of the beam. The sheet beam geometry is similar to that of the fan beam geometry except that the beam is non-divergent and rectangular in shape, and perpendicular to the row of detector elements. The fan and sheet beam geometries are faster implementations of CT compared to pencil beam geometry by a factor of the number of detector elements. The x-ray tube and detector row rotates around the phantom as shown in Figure 3.4, so the fan beam geometry is known as the "rotate-rotate" third generation CT[26].

The data acquisition for fan and sheet beam geometries result in a two-dimensional sinogram. The position dimension is represented by each of the detector elements, and the rotation dimension by the x-ray tube/detector rotations. The spatial resolution is controlled by the number of elements along the row detector, the size of each detector element, the number of rotations around the phantom, and the x-ray tube focal spot

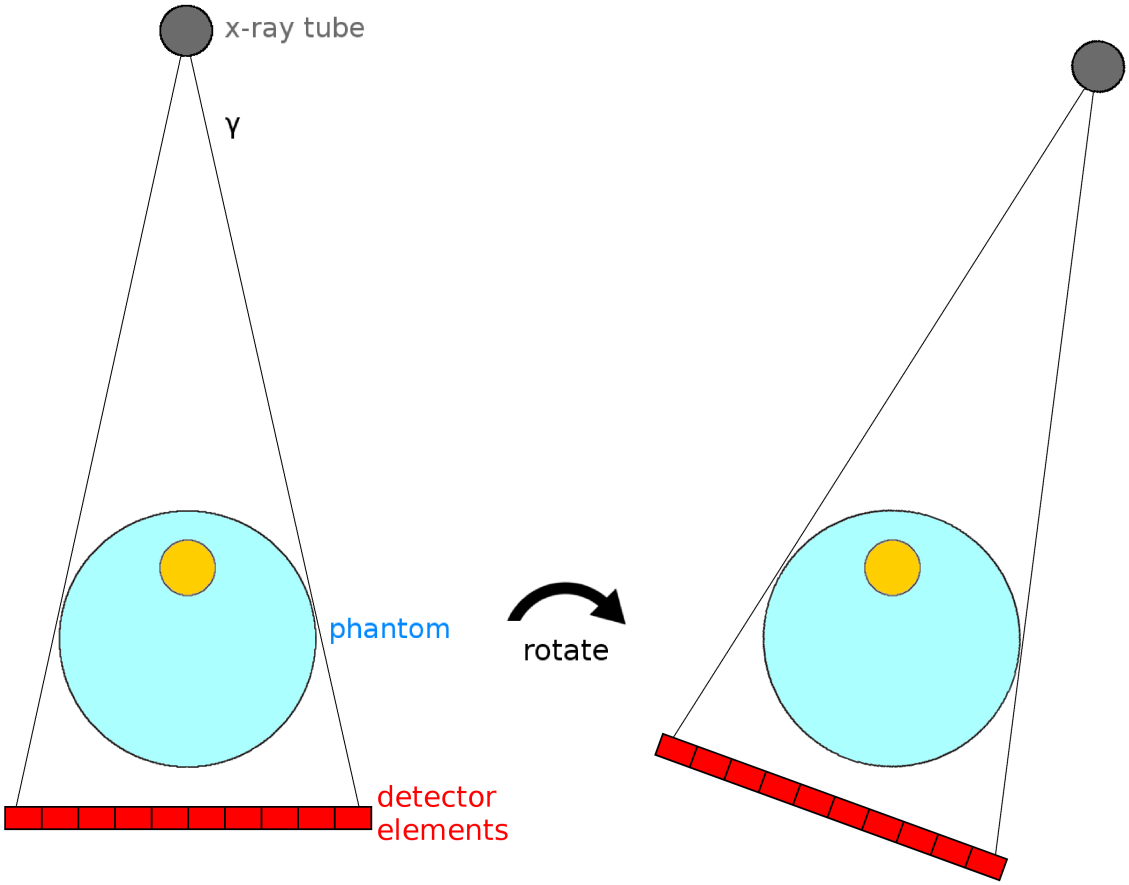


Figure 3.4: Fan beam CT geometry. The x-ray tube and detector rotate over a full rotation. The x-ray beam ($\gamma$) is fan-shaped, and the detector elements provide spatial discrimination. A sheet beam CT geometry is similar except the x-ray beam is rectangular-shaped with no beam divergence.

size. Modern CT scanners have detector elements with sub-millimetre pixel sizes. However, this CT geometry is limited to imaging one slice at a time to form a two-dimensional CT image. In addition, the wider beam increases the amount of scattered x-rays, which can reach other detector elements and be misattributed to the wrong position.

### 3.2.4 Cone Beam

The cone beam geometry (Figure 3.5), or multi-slice CT, was adopted in CT scanners in the early 2000s[22] and expands the fan beam geometry to a multi-slice acquisition enabled by a grid of individual detector elements. The beam is cone- or pyramid-shaped whose field of view covers the entire detector grid. To image the entire phan-

tom, using a cone beam CT geometry would decrease the acquisition time by a factor of the number of columns in the detector grid compared to the fan beam geometry.

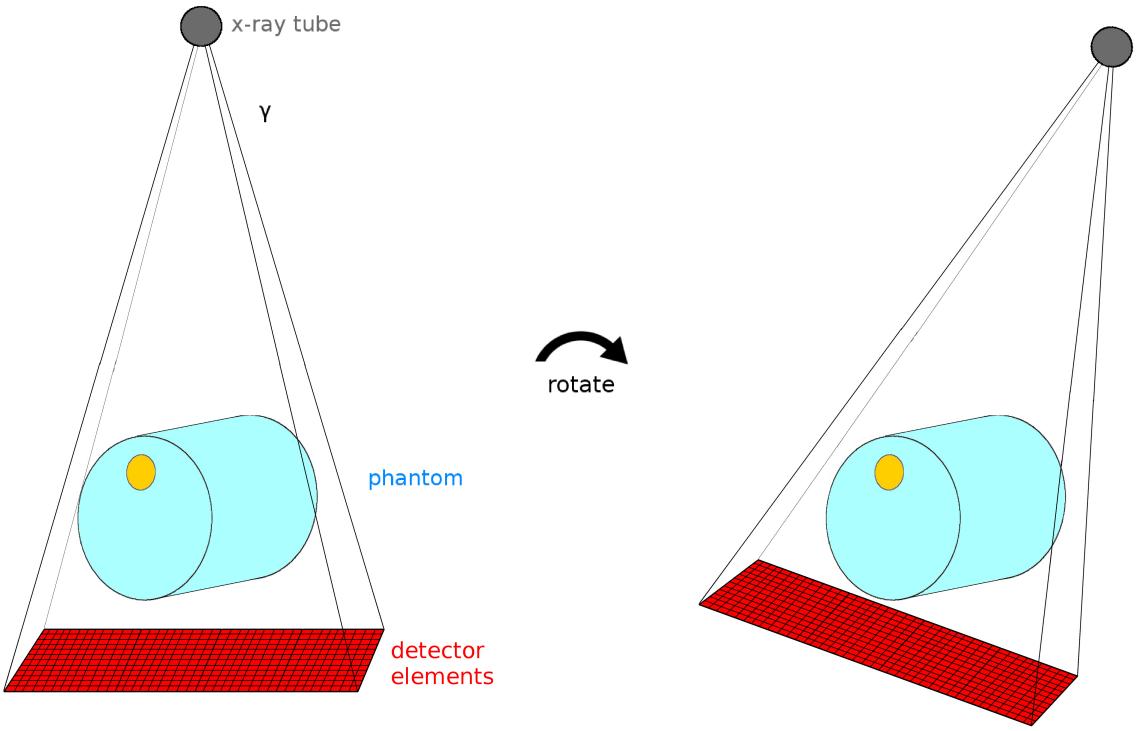


Figure 3.5: Cone beam CT geometry. The x-ray tube and detector rotate over a full rotation. The x-ray beam ($\gamma$) is cone-shaped or pyramid-shaped to provide full coverage of the phantom. The detector elements provide spatial discrimination in two dimensions, resulting in a three-dimensional image.

The data acquisition for the cone beam geometry results in a three-dimensional sinogram due to the rows and columns of the detector grid in addition to the x-ray tube/detector rotations. Similar to that of fan beam CT images, the spatial resolution of cone beam CT images is controlled by the number of elements in the grid detector, the size of each detector element, the number of rotations around the phantom, and the x-ray tube focal spot size. The cone beam geometry is widely available in modern CT scanners, as fast acquisition time is important for patient imaging.

### 3.2.5 XFCT Geometries

Pencil beam XFCT data acquisition (Figure 3.6a) is similar to that of conventional CT. Instead of an energy-integrating detector, an energy-resolving detector such as a spectrometer is placed away from the incident x-ray beam, ideally at high-scattering

angles[47, 39], to collect a spectrum of scattered x-rays. The net number of fluorescent x-rays is extracted from the spectrum for each translation and rotation step to form a sinogram, with negative values set equal to zero because it is not physical to have a negative number of fluorescent x-rays. Fluorescent x-ray emission is isotropic, so a single-pixel spectrometer that covers a $4\pi$ solid angle around the phantom could detect the most fluorescent x-rays. However, such a spectrometer would be prohibitively expensive and geometrically infeasible to implement on a real x-ray imaging system.

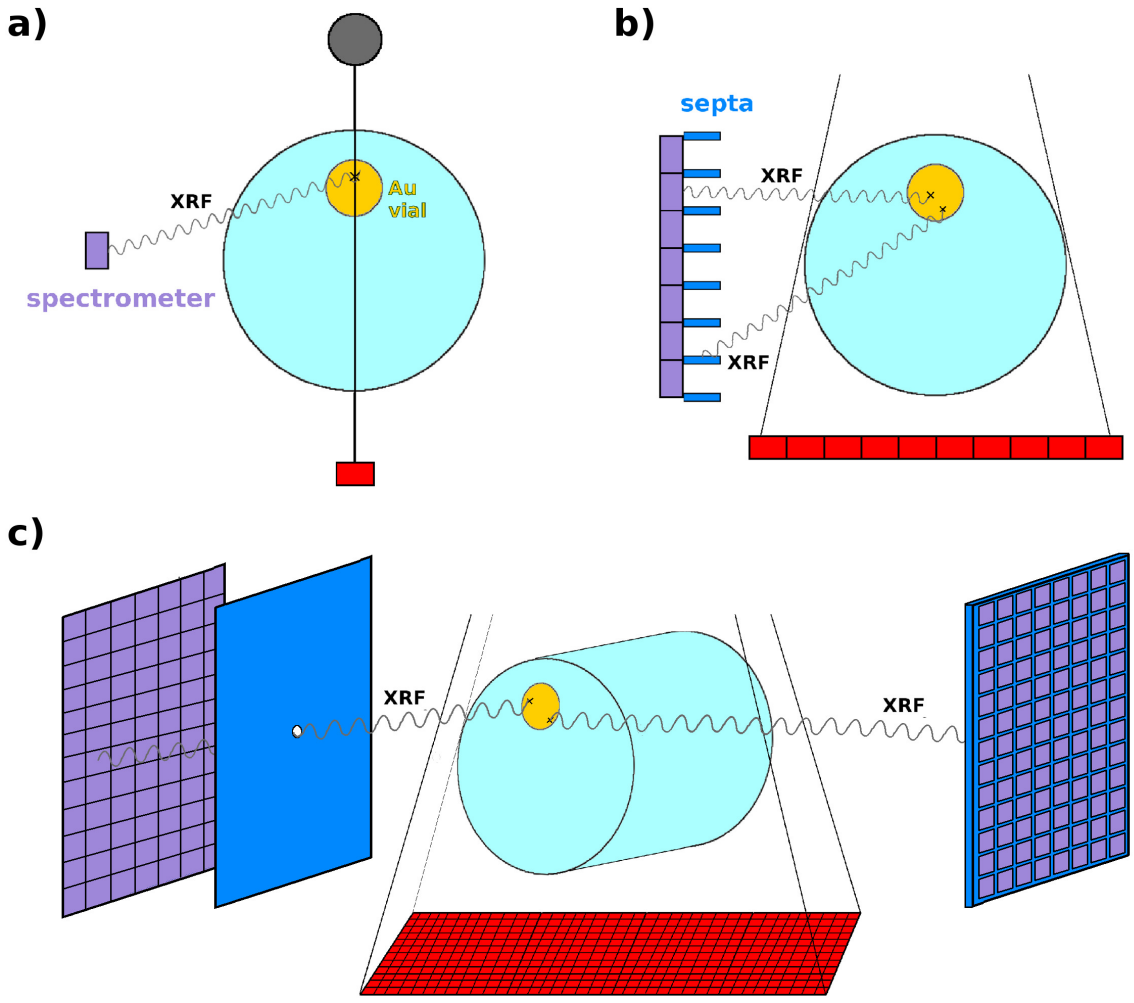


Figure 3.6: Modified XFCT geometries for a) pencil beam, b) fan and sheet beam, and c) cone beam CT geometries showing example acquisition of fluorescent x-rays (XRF). Pinhole and parallel-hole collimator configurations are shown for the c) cone beam CT geometry on the left and right sides, respectively.

Fan, sheet, and cone beam XFCT data acquisition (Figures 3.6b,c) require the use

of collimators between each detector element to determine the paths of fluorescent x-rays from the phantom. The collimators must be designed with acceptance angle and absorption of scattered x-rays in mind, with septal thickness, width, length, and material as parameters. Usually an acceptable amount of x-ray penetration through the collimator material is 5%, so choosing a high-$Z$ material is best to minimize the septal thickness that obstructs the active area of the detector[82]. For XFCT scans, the energy-resolving detector is placed perpendicular to the fan or sheet beam as shown in Figures 3.6b,c. Different collimation strategies exist that impact XFCT image quality. Two collimator designs commonly used in cone beam XFCT systems[44, 38] are pinhole and parallel-hole collimators, shown in Figure 3.6c. The pinhole acts as a lens aperature for forming XFCT projections onto a spectrometer grid, but its small size rejects a lot of otherwise useful fluorescent x-rays. Each individual spectrometer in the parallel-hole collimator design detects parallel fluorescent x-rays, but requires each spectrometer element to be individually collimated. The pinhole and parallel-hole collimators can also be applied to fan and sheet beam XFCT. Note that each individual detector element would need to be capable of energy discrimination to identify the fluorescent x-ray energies, which limits the size of the fan or cone beam XFCT systems due to the cost of such detectors.

## 3.3 Image Reconstruction

This section describes the image reconstruction and normalization methods used to reconstruct XFCT and PCCT images in this dissertation. An algorithm developed to correct for fluorescent x-ray attenuation in the phantom is presented later in this section.

### 3.3.1 Filtered Backprojection

Simple backprojection and filtered backprojection (FBP) are fast reconstruction algorithms based on the mathematical inverse Radon transform[83]. FBP is a modified version of simple backprojection and is used to reconstruct parallel beam geometries such as pencil beam or sheet beam CT images. The basic principle of simple backprojection (Figure 3.7a) involves "smearing" the projection for a given angle, or a "view", back across the image plane at that angle. This is done over many views, where the projections add up to solve for what the imaging subject looks like in the image. The more views at different angles, the better the reconstruction accuracy. However,

simple backprojection results in a characteristic $1/r$ blurring especially around highly attenuating features in the resulting CT image[26]. In FBP, a filter function is convolved with each view to improve the sharpness of these features. The mathematical nature of FBP is Fourier-based, so in order to remove the $1/r$ blurring the filter function must be defined such that its Fourier transform undoes this effect. The ramp filter, which is linear in the Fourier domain, achieves the desired outcome as shown in Figure 3.7b [26, 84]. The inverse Radon transform with the ramp filter is available in Python's scikit-image package[85], which was used for FBP reconstruction in this work.

#### Feldkamp-Davis-Kress Algorithm

The Feldkamp-Davis-Kress (FDK) reconstruction algorithm is a modification to the FBP algorithm described above[86]. This modification is required to reconstruct cone beam CT images, in which the scanning x-ray beams are not parallel. To account for the beam divergence in image reconstruction, the source to isocentre distance and the source to detector distance are used to fix distortions of the image shape. A FDK image reconstruction package available in Matlab was used to reconstruct cone beam images in this work[87].

### 3.3.2 Maximum Likelihood Expectation Maximization

Iterative reconstruction algorithms are an alternative method for CT reconstruction. The general principle of an iterative reconstruction algorithm (Figure 3.8) is forward projecting an approximate image into its projections, then comparing these to the acquired projections in the sinogram. Over a series of iterations, a good estimate of the image is reconstructed based on the acquired projections. The iterative reconstruction algorithm used to reconstruct simulated pencil and sheet beam XFCT images was the Maximum Likelihood Expectation Maximization (MLEM) algorithm, which is described below[88].

The relationship between the acquired projections $p$ along projection lines $j$ and the image $a$ with $i$ pixels is the following:

$$p_j = \sum_i M_{ij} a_i \tag{3.2}$$

in which $M_{ij}$ is a size $i \times j$ matrix. The entries of $M_{ij}$ represent the contribution of

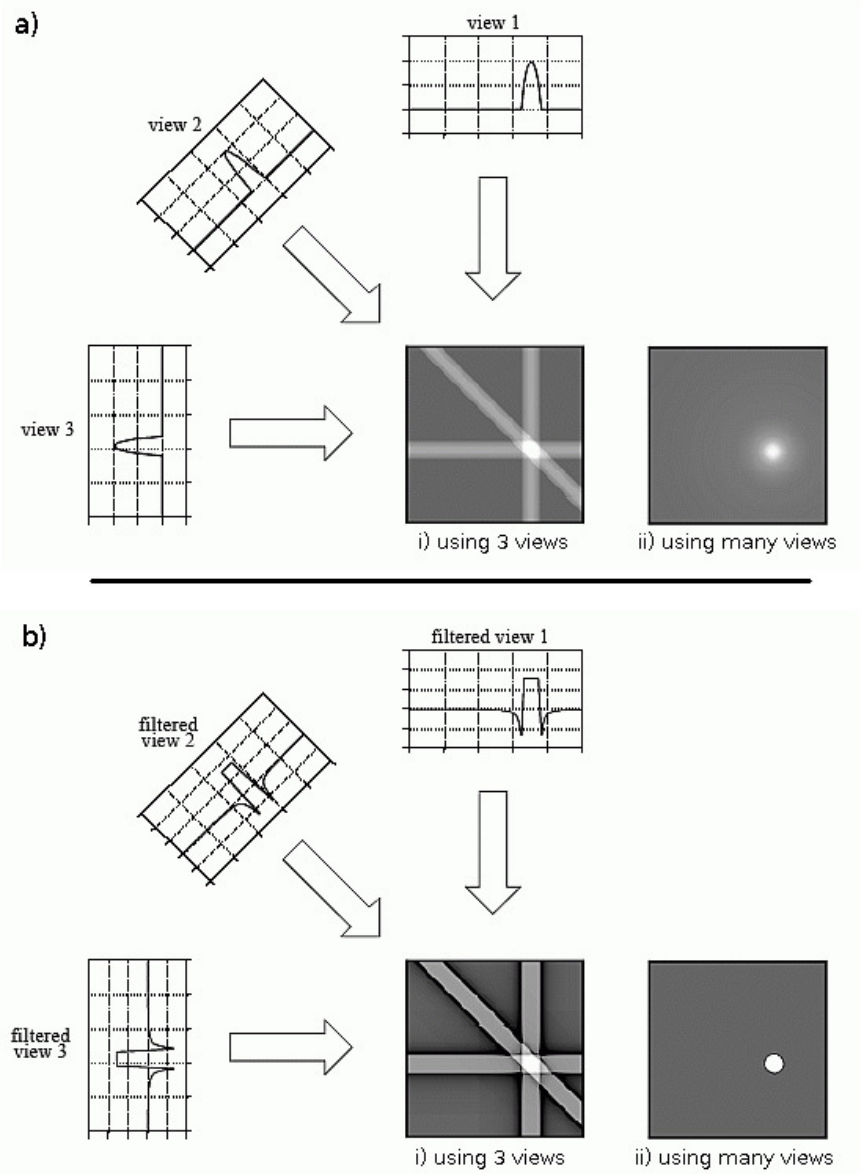


Figure 3.7: a) Simple and b) filtered backprojection reconstruction algorithms. Figure adapted from Smith (1997)[84].

projection lines $j$ through each image pixel $i$ in forward projection, normalized to the case where the projection line intersects with the pixel centre so that $0 <= M_{ij} <= 1$. Therefore, solving for $a_i$ is a matrix inversion problem, which is a difficult if not impossible task for modern CT datasets. Hence, iterative reconstruction algorithms offer approximate solutions for $a$. The general form of the MLEM algorithm used to estimate an image $a$ after the $k^{\text{th}}$ iteration is the following:

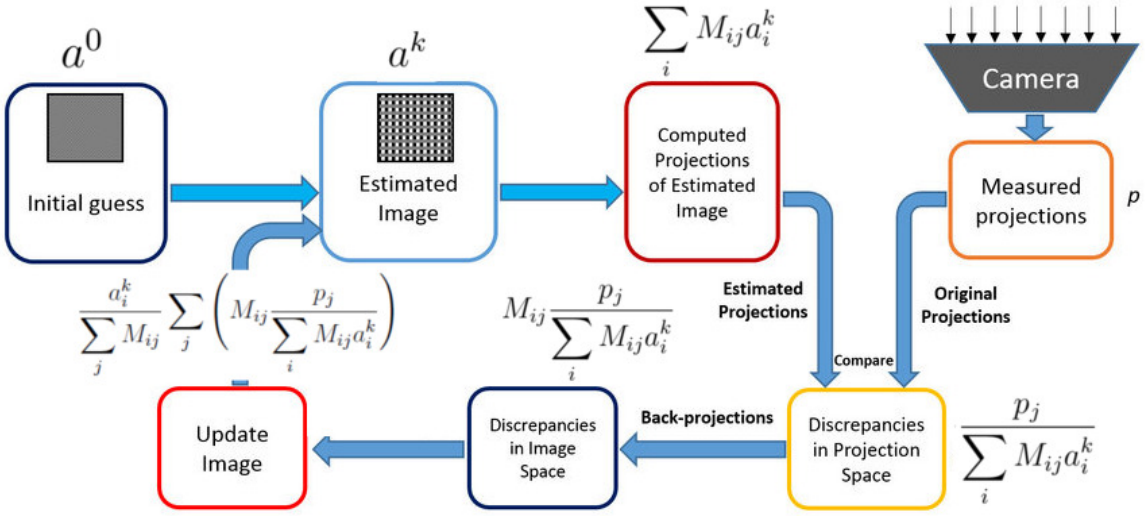


Figure 3.8: Flowchart of the MLEM iterative reconstruction algorithm principle. Figure adapted from Ravi *et al.* (2019)[89].

$$a_i^{k+1} = \frac{a_i^k}{\sum_j M_{ij}} \sum_j \left( M_{ij} \frac{p_j}{\sum_i M_{ij} a_i^k} \right) \tag{3.3}$$

Referring to the flowchart in Figure 3.8, the MLEM algorithm starts with an initial guess $a^0$. The $\sum_i M_{ij} a_i^k$ term is the forward projection of the current image estimate $a^k$, which is compared to the measured projections $p_j$ by taking a ratio between the two terms. The closer this ratio is to 1, the smaller the discrepancy in the measured vs. estimated projections. The summation over $j$ of $M_{ij}$ multiplied by this ratio is a backprojection of the discrepancies in the image space, which is normalized by the $\sum_j M_{ij}$ term. These terms are used to correct the old image $a^k$ to update it to $a^{k+1}$[89].

### Attenuation Correction

In XFCT, attenuation of fluorescent x-rays is a limitation for detecting low concentrations of contrast agents. For instance, the energy of the highest yield K-shell and L-shell fluorescent x-rays from Au are 68.8 keV and 9.71 keV, respectively. The fluorescent x-ray fluence at these energies is reduced to 10% of their original value through thicknesses of 12 cm and 4 mm of water, respectively, highlighting the need for fluorescent x-ray attenuation correction especially for L-shell XFCT. The method

of attenuation correction done in this work is based on Beer's law and was achieved by modifying the MLEM algorithm that was introduced above.

The primary x-ray beam requires an attenuation correction especially if the tube voltage is set at a lower value to enable L-shell XFCT imaging. Considering a pencil beam geometry for simplicity, the primary x-ray beam attenuation correction factor $c_{ij}^{p}$ was calculated for an image pixel $i$ along a projection $j$ by the following:

$$c_{ij}^{p} = \exp\left(-\mu_p d_{ij}\right) \tag{3.4}$$

where $\mu_p$ is the linear attenuation coefficient of the primary x-ray beam in the phantom material, and $d_{ij}$ is the distance the primary x-ray beam travels from the phantom entrance to pixel $i$ along the projection $j$ for a particular beam position and angle. On Figure 3.9, $d_{ij}$ is represented by the distance between points A and B, where point B resides in pixel $i$. For polyenergetic primary x-ray beams, the value of $\mu_p$ was chosen for the mean beam energy.

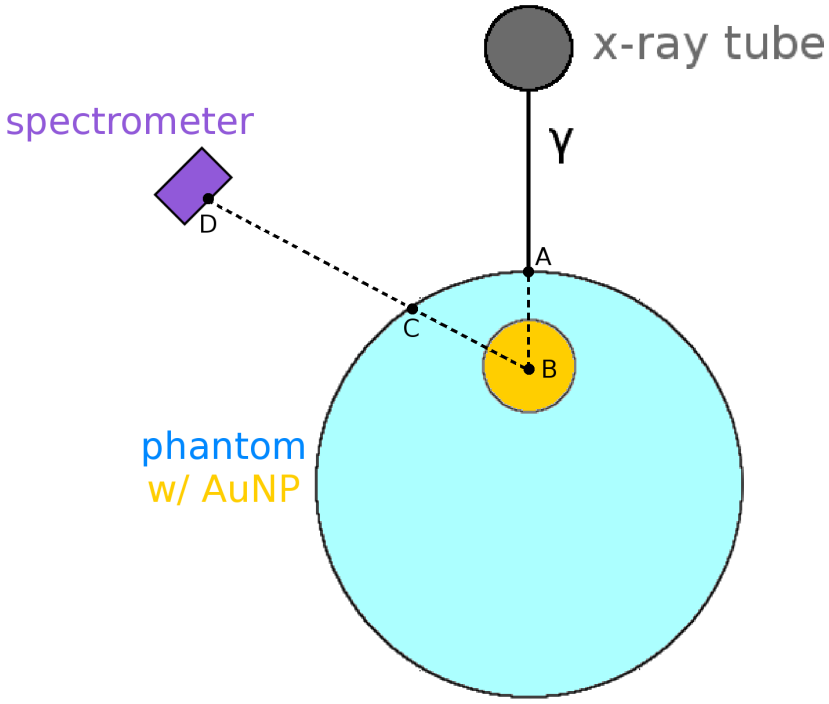


Figure 3.9: Diagram of attenuation correction for pencil beam XFCT.

The fluorescent x-ray attenuation correction factor $c_{ij}^{f}$ was calculated for the same image pixel $i$ at a projection $j$ by the following:

$$c_{ij}^{f} = \sum_{f} \omega_f \exp(-\mu_f t_{ij}) \tag{3.5}$$

where $\omega_f$ is the fluorescent yield for a particular K-shell or L-shell fluorescent x-ray $f$, $\mu_f$ is the linear attenuation coefficient of the fluorescent x-ray at its particular energy in the phantom material, and $t_{ij}$ is the distance the fluorescent x-ray originating at pixel $i$ travels through the phantom toward the spectrometer. On Figure 3.9, $t_{ij}$ is represented by the distance between points B and C, with the spectrometer located at point D.

Combining Equations 3.4 and 3.5, we can modify the matrix $M_{ij}$ from Equation 3.2 into $M'_{ij}$ by the following correction:

$$M'_{ij} = M_{ij} \frac{c_{ij}^{p}}{c_{ij}^{f}} \tag{3.6}$$

and replace all instances of $M_{ij}$ with $M'_{ij}$ in Equation 3.3 to perform XFCT image reconstruction using this attenuation-corrected MLEM algorithm. This application of attenuation correction for MLEM image reconstruction has been done in other XFCT studies[41, 90, 40].

In the water phantoms designed throughout this work, often the concentrations of AuNPs in the phantom are low enough to approximate the value of $\mu_p$ and $\mu_f$ as being in water. This was the assumption made for water phantoms with AuNP concentrations of less than 2%. For larger concentrations, or for a more accurate reconstruction, the mathematical argument in the exponential term of Equation 3.5 can be modified in the following manner:

$$c_{ij}^{f} = \sum_{f} \omega_f \left( \prod^{m} \exp(-\mu_f^m t_{ij}^m) \right) \tag{3.7}$$

where $\mu_f^m$ is the linear attenuation coefficient of material $m$ at the energy of fluorescent x-ray $f$ and $t_{ij}^m$ is the distance a fluorescent x-ray travels from image pixel $i$ through material $m$, such that $\sum_{m} t_{ij}^m = t_{ij}$. Note that Equation 3.7 reduces to Equation 3.5 in the case where the phantom is of uniform material, or where $\mu_f^m$ is similar for all $m$.

### 3.3.3 Image Normalization

Reconstructed CT images are attenuation maps often presented in greyscale, with darker values corresponding to materials of low attenuation and lighter values to high attenuation from Equation 3.1. The CT number of a pixel in a CT image is a contrast value relative to air and water useful for material identification, and is measured in Hounsfield Units (HU). Attenuation maps were normalized to CT number, defined below for each pixel $i$ in the resulting CT image:

$$\text{CT number}_\text{i} = 1000\frac{\mu_i - \mu_{\text{H}_2\text{O}}}{\mu_{\text{H}_2\text{O}} - \mu_{\text{air}}} \tag{3.8}$$

where $\mu$ is the attenuation value in pixel $i$, and $\mu_{\text{H}_2\text{O}}$ and $\mu_{\text{air}}$ are the attenuation values of water and air, respectively, in the attenuation map. The CT numbers by definition of water and air are 0 and -1000, respectively. The attenuation values of $\mu_{\text{H}_2\text{O}}$ and $\mu_{\text{air}}$ can be found empirically, but is a formidable task with polyenergetic x-ray CT. In this research $\mu_{\text{H}_2\text{O}}$ and $\mu_{\text{air}}$ were simply found in a region of interest (ROI) made up of exclusively water and air, respectively.

XFCT and K-edge PCCT images of a contrast agent in a phantom were calibrated to the region with the highest concentration of contrast agent. This was done by dividing the entire image by the mean pixel value in this region and multiplying by the actual concentration of the contrast agent. Negative values in the XFCT and K-edge PCCT images were set equal to zero.

## 3.4 Image Analysis

This section details the metrics used for image analysis throughout the research in this dissertation. The following metrics assessed image quality in terms of contrast agent detection limit and signal linearity.

### 3.4.1 Contrast-to-Noise Ratio and Signal-to-Noise Ratio

The Contrast-to-Noise Ratio (CNR) is a useful image quality parameter to optimize that measures the signal and background levels relative to the noise level of an x-ray imaging system. The CNR of a ROI in an image relative to the background is defined as the following:

$$\text{CNR} = \frac{\mu_{\text{ROI}} - \mu_{\text{BG}}}{\sigma_{\text{BG}}} \tag{3.9}$$

where $\mu_{\text{ROI}}$ is the mean of the pixel values in the ROI and $\mu_{\text{BG}}$ and $\sigma_{\text{BG}}$ are the mean and standard deviation of the pixel values in the background, respectively[26]. In the context of XFCT and K-edge PCCT contrast-only images, the various ROIs were vials containing different contrast agents of varying concentrations. The background ROIs were chosen as a water vial in the phantom containing zero contrast or as the entire phantom body, depending on the study. The CNR for this research was calculated to find the imaging sensitivity of the contrast agents in XFCT and PCCT images.

The Signal-to-Noise Ratio (SNR) is similar to the CNR except that the size and shape of the ROIs does not alter the SNR[26]. A definition of the SNR is below:

$$\text{SNR} = \frac{\sum_i \mu_{\text{i}} - \mu_{\text{BG}}}{\sigma_{\text{BG}}} \tag{3.10}$$

where $\mu_{\text{i}}$ is the signal in pixel $i$ of an ROI[26]. Since the background is close to zero in XFCT and PCCT contrast-only images, the CNR is expected to be similar to the SNR in these images provided the ROIs are coincident with the locations of each vial.

### 3.4.2 Imaging Sensitivity

The imaging sensitivity of a particular XFCT or PCCT imaging setup is defined as the minimum concentration of contrast agent detectable in the resulting images for a given imaging dose. In this dissertation, this was achieved by imaging a cylindrical phantom consisting of equal-diameter vials at equal depths containing different concentrations of contrast agent, and computing the CNR of each vial. A linear fit of CNR vs. concentration was performed to find the imaging sensitivity, defined as the concentration at which CNR is equal to 4 or 5. This is based on the Rose criterion[91], which was defined as the limit in which an object is detectable in most cases. In CT imaging, the Rose criterion defines the detection limit as SNR = 5[91, 26]. However in XFCT imaging, the choice of CNR value to define the detection limit is subjective. XFCT studies have used CNR = 4 in the past[52, 47, 92], as well as CNR = 3[38]. The linear fit was computed using SciPy's curve fit function to a defined linear function in which the y-intercept was fixed at zero[93].

### 3.4.3 Reconstruction Accuracy

The reconstruction accuracy for a contrast agent-only XFCT or PCCT image was evaluated as a comparison between the reconstructed concentration and the actual concentration of a contrast agent in a vial. The reconstructed concentration in a vial was evaluated by computing the mean in a ROI that coincided with this vial in a XFCT or PCCT image. The particular reconstructed concentration of a contrast agent was considered accurate if it was within one standard deviation of the actual concentration in the vial. Note that images with high amounts of noise would result in accurate concentration evaluation due to the large standard deviation.

The reconstructed and actual concentration values were plotted against each other to verify signal linearity in the presented images. This was done by fitting a line to this plot and computing the coefficient of determination $R^2$, the slope, and its associated error. The formula for $R^2$, a metric used to assess the goodness of linear fits, is the following:

$$R^2 = 1 - \frac{\sum_i (\mu_i - c_i)^2}{\sum_i (\mu_i - \bar{\mu})^2} \tag{3.11}$$

where $\mu_i$ is the reconstructed concentration in vial $i$, $c_i$ is the actual concentration of the contrast agent in vial $i$, and $\bar{\mu}$ is the mean of all reconstructed concentration values in the phantom data set. Signal linearity was achieved when the slope and its error was consistent with being equal to 1, and the $R^2$ value was as close to 1 as possible with 0.99 typically considered to be a good $R^2$ value. The linear fit was computed using SciPy's curve fit function to a defined linear function in which the $y$-intercept was fixed at zero [93].

# Chapter 4

# X-Ray Fluorescence Computed Tomography Induced by Photon, Electron, and Proton Beams

## 4.1 Summary

In table-top XFCT systems incident photons interact with high-$Z$ atoms to induce fluorescent x-rays for XFCT imaging. Charged particles can also induce fluorescent x-rays via the mechanism of colliding with atomic electrons to create vacancies. Compared to x-rays which don't have a range, charged particles at treatment energies can reach high-$Z$ atoms at depth. Proton, electron, and megavoltage photon-induced XFCT could be used for the purpose of range verification during treatment in combination with contrast agent administration. This simulation study documents the image quality achievable for K-shell and L-shell XFCT induced by a variety of different incident particles and energies in two different phantom sizes[94].

## 4.2 Introduction

X-ray Fluorescence Computed Tomography (XFCT) is an emerging molecular imaging modality which combines x-ray spectroscopy with the principles of computed tomography. XFCT can image high atomic number ($Z$) materials, such as gold nanoparticles (AuNP), in mouse-sized objects at high sensitivity. The excitation source most commonly used in XFCT imaging are photons, which originate from x-ray tubes or synchrotrons. X-ray tubes produce polychromatic photon beams, which results in increased scatter which degrades the XFCT imaging sensitivity. The development of Compton scatter removal and scatter correction techniques have made XFCT imaging feasible with preclinical table-top systems[47, 39, 59, 46]. Synchrotron photon beams offer reduced Compton scatter background in the resulting XFCT images due to the

narrow beam energy spread, however the availability of synchrotron facilities limits widespread use. In addition, the detection of lower-energy L-shell fluorescent x-rays have also been shown to improve XFCT imaging sensitivity in both simulations and experiments due to the higher interaction cross-section[48, 56, 95, 55, 90]. Another way to reduce the Compton scatter background involves the use of particle beams as excitation sources, in particular protons and electrons.

Proton-induced XFCT builds upon the existing Particle-Induced X-ray Emission (PIXE) technique, in which lower-energy proton beams of order 2-6 MeV excite trace high-$Z$ metals in thin samples, which then emit material-specific fluorescent x-rays for analysis[96]. The use of higher-energy proton beams enables PIXE at depth and potential range verification during proton therapy. Proton-induced XFCT has already been simulated and demonstrated experimentally using 220 MeV protons to irradiate a 7 cm-diameter water phantom containing 3%-5% gold solutions, whose K-shell fluorescent x-rays were detected using a cadmium telluride (CdTe) spectrometer[97]. AuNPs have been shown to increase the relative biological effectiveness of protons locally in a tumour[98], which highlights a need to develop *in vivo* XFCT imaging to guide nanoparticle-enhanced proton radiotherapy applications. Clinical electron beams, which range in energy from 6 MeV to 20 MeV, and very-high energy electron (VHEE) beams, which are of order 100 MeV, can induce x-ray fluorescence in high-$Z$ atoms. In addition, VHEE beams from linear accelerators are promising for treatment of cancer in specific cases, such as in pediatric, lung, and prostate patients[99, 100]. However, electron-induced XFCT has been seldom investigated to date.

Both electrons and protons induce x-ray fluorescence in high-$Z$ atoms by colliding with inner-shell electrons. Photons induce x-ray fluorescence primarily by the photoelectric effect. In all cases the inner-shell electron is freed which causes an outer-shell electron to fill the vacancy, releasing an Auger electron or a fluorescent x-ray. Depending on the particular transition, the probability that the emitted particle is a fluorescent x-ray rather than an Auger electron is governed by the fluorescent yield $\omega_k$. In this paper, we will compare XFCT images induced by kilovoltage and megavoltage photon beams, clinical electron energy and VHEE beams, and 100 MeV and 250 MeV proton beams to explore the potential feasibility of XFCT for different excitation beams due to the widespread use of proton therapy and the growing interest in VHEE radiation therapy. The 81 keV kilovoltage photon beam represents a monoenergetic beam produced by a synchrotron, while the 5 MeV megavoltage photon beam represents an approximate 15 MV clinical photon beam used for treatment.

The 220 kVp photon beam represents a polyenergetic treatment beam from a typical small animal irradiator, while the 6 MV photon beam represents a polyenergetic beam that is commonly used in megavoltage radiotherapy[101]. The 10 MeV and 100 MeV electron beams each represent a clinical electron beam and a VHEE beam from a linear accelerator. The 100 MeV and 250 MeV proton beams are typical of proton radiotherapy in patients. In addition, we will explore the effect of K-shell versus L-shell XFCT, as well as the effect of a larger phantom size on the imaging sensitivity of gold.

## 4.3 Materials and Methods

### 4.3.1 XFCT imaging

#### Phantoms

Two cylindrical water phantoms, 2.5 cm and 5 cm in diameter and in height, were modeled in this study and are shown in Figures 4.1a and 4.1b, respectively. Each cylindrical water phantom contained vials with AuNP concentrations of 0.1% - 2% by weight in water. The vials were 5 mm and 10 mm in diameter and in height for the 2.5 cm and 5 cm diameter phantom, respectively. The centres of each vial were located 5 mm and 7.5 mm from the surface of the 2.5 cm and 5.0 cm diameter phantom, respectively. The AuNP solutions were modeled as being a mixture of water and gold rather than individual nanoparticles, which would have a minimal impact on the generation and transport of x-ray fluorescence. The entire geometry was in air.

#### Imaging geometry

For all images, a 0.5 mm-thick slice of the phantom was irradiated by a monoenergetic square beam of 81 keV and 5 MeV x-rays, 10 MeV and 100 MeV electrons, and 100 MeV and 250 MeV protons seperately. The phantom was also imaged with a polyenergetic square beam of 220 kVp and 6 MV x-rays. These excitation sources caused the release of both K-shell and L-shell fluorescent x-rays, respectively, from the AuNPs in the phantom. The pencil beam XFCT scan consisted of 180 2-degree phantom rotations and 50 and 100 translations over the 2.5 cm and 5 cm diameter phantoms in 0.5 mm steps, respectively. The dose to the phantom for each beam source type was calculated by scoring the total energy deposited in the water in the

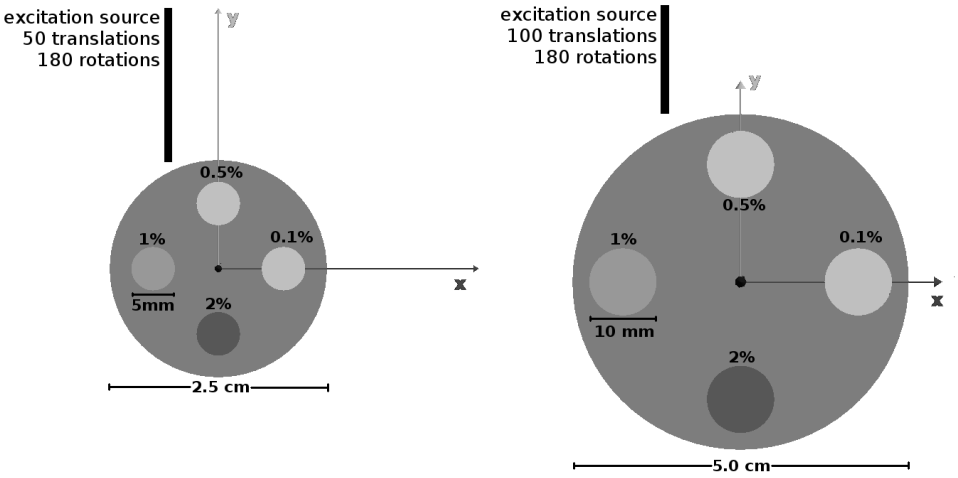


(a) 2.5 cm diameter phantom. (b) 5 cm diameter phantom.

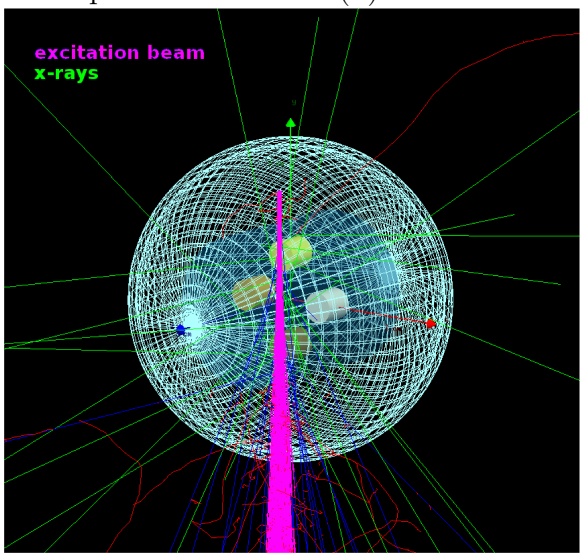


(c) Excitation beam and x-rays captured by spherical detector surrounding a phantom.

Figure 4.1: Cross-section of a) 2.5 cm and b) 5.0 cm diameter cylindrical water phantoms. c) Snapshot of Monte Carlo simulation depicting the excitation beam inducing fluorescent x-rays from AuNP in the phantom, which reach the spherical detector. The excitation beam originates from within the spherical detector.

0.5 mm-wide slice over the entire pencil beam scan. The total imaging dose for each beam source type and the corresponding total number of particles is summarized in Table 4.1. A non-pixelated detector surrounding the phantom was simulated as a spherical boundary with ideal detection efficiency to score all x-rays that crossed the detector's surface. This detector, shown in Figure 4.1c, was modeled as a sphere of

Table 4.1: Complete list of all excitation sources and phantom sizes for each XFCT image, with the total number of incident particles used to yield the total imaging dose.

| **Pencil beam source** | **Phantom size (cm)** | **Total # of particles** | **Mean dose (mGy)** |
|---|---|---|---|
| 81 keV x-rays | 2.5 | $6.71 \times 10^8$ | 2 |
| 81 keV x-rays | 5 | $1.36 \times 10^9$ | 2 |
| 220 kVp x-rays | 2.5 | $6.71 \times 10^8$ | 2.5 |
| 220 kVp x-rays | 5 | $1.38 \times 10^9$ | 2.5 |
| 5 MeV x-rays | 2.5 | $6.71 \times 10^8$ | 49 |
| 5 MeV x-rays | 5 | $1.03 \times 10^9$ | 49 |
| 6 MV x-rays | 2.5 | $6.71 \times 10^8$ | 33 |
| 6 MV x-rays | 5 | $1.25 \times 10^9$ | 33 |
| 10 MeV electrons | 2.5 | $6.71 \times 10^8$ | 1720 |
| 10 MeV electrons | 5 | $1.36 \times 10^9$ | 1710 |
| 100 MeV electrons | 2.5 | $6.71 \times 10^8$ | 1700 |
| 100 MeV electrons | 5 | $1.30 \times 10^9$ | 1700 |
| 100 MeV protons | 2.5 | $6.71 \times 10^8$ | 6990 |
| 100 MeV protons | 5 | $1.22 \times 10^9$ | 6980 |
| 250 MeV protons | 2.5 | $6.71 \times 10^8$ | 3630 |
| 250 MeV protons | 5 | $1.28 \times 10^9$ | 3590 |

diameter double than that of each phantom and has full $4\pi$ coverage.

### 4.3.2 Monte Carlo simulations

The TOPAS Monte Carlo (MC) code (version 3.1.p2) [69], was used to simulate XFCT induced in gold solution. TOPAS is a wrapper for the Geant4 (version 10.3.p01) [63] simulation toolkit, which allows flexibility for a variety of energy ranges and particle types. The physics modules `"g4em-standard_opt4"`, `"g4h-phy_QGSP_BERT_HP"`, `"g4decay"`, `"g4ion-binarycascade"`, `"g4h-elastic_HP"`, `"g4stopping"`, and `"g4em-extra"` were selected. They include hadronic interactions necessary for proton transport as well as the relevant photon interaction physics such as Rayleigh scattering, Compton scattering, and photoelectric effect. X-ray fluorescence, Meitner-Auger electron generation, and PIXE settings[96] were turned on, and the range cut for all particles was set to 1 mm. All TOPAS simulations were run on a cluster of Intel E5-2683 v4 CPUs as part of the Compute Canada network.

For each of the simulations involving the 2.5 cm diameter phantom, the total

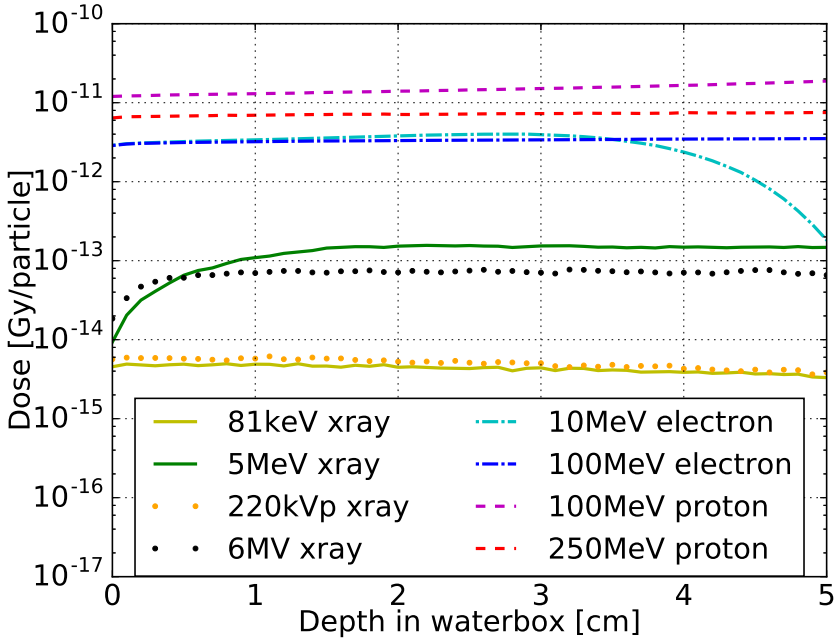


Figure 4.2: Depth dose profiles generated in TOPAS normalized to Gy per particle for each excitation source in a water box. The Bragg peaks for each of the 100 MeV and 250 MeV proton beams are beyond the depth of the largest water phantom.

number of incident particles was fixed between excitation sources. The number of incident particles was chosen such that the phantom would receive a total of 2 mGy dose when irradiated with 81 keV x-rays. For the 5 cm diameter phantom, the number of incident particles was chosen such that the same total dose was delivered as to the 2.5 cm diameter phantom for each excitation source. The doses and number of incident particles used are summarized in Table 4.1. In addition, the depth dose profiles in a water box for each excitation source was simulated in TOPAS and are shown in Figure 4.2 to show beam attenuation in depth. To simulate each pencil beam XFCT scan, there were a total of 180 rotations $\times$ 50 translations $=$ 9000 simulations for the 2.5 cm diameter phantom and 180 rotations $\times$ 100 translations $=$ 18000 simulations for the 5 cm diameter phantom.

### 4.3.3 Image reconstruction

Histograms of the x-rays crossing the detector boundary were recorded in 0.5 keV and 0.2 keV energy bins for K-shell and L-shell XFCT images, respectively. The chosen energy bin size was based on the energy resolution of the Amptek X-123CdTe

Table 4.2: L-shell and K-shell fluorescent x-ray energies of gold which contributed to each XFCT image and their fluorescent yield [57].

| **Fluorescent x-ray** | **Energy (keV)** | **Yield (%)** | **Fluorescent x-ray** | **Energy (keV)** | **Yield (%)** |
|---|---|---|---|---|---|
| L$\alpha_1$ | 9.71 | 100 | K$\alpha_1$ | 68.80 | 100 |
| L$\alpha_2$ | 9.63 | 11 | K$\alpha_2$ | 66.99 | 59 |
| L$\beta_1$ | 11.44 | 67 | K$\beta_1$ | 77.98 | 23 |
| L$\beta_2$ | 11.58 | 23 | K$\beta_2$ | 80.15 | 8 |
| L$\gamma_1$ | 13.38 | 13 | K$\beta_3$ | 77.58 | 12 |

X-ray Spectrometer and X-123SDD X-ray Spectrometer with Silicon Drift Detector (Amptek Inc., Bedford, MA, USA) to resolve K-shell and L-shell fluorescent x-rays, respectively[59]. The histograms were generated by recording a phase space in binary format of x-rays that crossed the detector boundary, then reading in their energies. The fluorescent x-rays used for K-shell and L-shell XFCT reconstructions are listed in Table 4.2. All data was analyzed using Python.

### Reconstruction algorithm

All XFCT images were reconstructed using the maximum-likelihood expectation maximization (MLEM) algorithm [88]. The general form of the MLEM algorithm is the following:

$$a_i^{k+1} = \frac{a_i^k}{\sum_j M_{ij}} \sum_j \left( M_{ij} \frac{p_j}{\sum_i M_{ij} a_i^k} \right) \tag{3.3}$$

where $a_i$ is the relative concentration of AuNP solution in image pixel $i$ and $M_{ij}$ is the contribution of image pixel $i$ to the projection line $j$ normalized to the case in which the projection line intersects the centre of the pixel, such that $0 \leq M_{ij} \leq 1$. The sinogram entry $p_j$ represents the total counts from projection $j$, which indicates the rotation angle of the projection line and the position of the incident pencil beam. The iteration number is denoted by $k$, which varies with each XFCT image. These numbers were optimized to reduce the image noise, thereby decreasing the sensitivity limit, as higher iteration numbers can introduce more noise[102]. The chosen iteration number also ensures the signal is sufficiently linear ($R^2 > 0.95$) with AuNP concentration when possible. The image noise was defined as the standard deviation in the water region of interest, which was taken to be four circles of diameter

5 mm and 10 mm in between each vial at equal phantom depth for the 2.5 cm and 5 cm diameter phantoms, respectively.

The excitation beam attenuation correction factor $c_{ij}^{e}$ for photons and charged particles was calculated by the following:

$$c_{ij}^{e} = \begin{cases} \exp(-\mu_e d_{ij}) & \text{for photons} \\ \text{PDD}(d_{ij}) & \text{for charged particles} \end{cases} \tag{4.1}$$

where $\mu_e$ is the linear attenuation coefficient of water, respectively, for the mean energy of the photon beam and $d_{ij}$ is the distance through water a photon travels to reach pixel $i$ for a projection $j$ (from Equation 3.4). The depth dose plot in Figure 4.2 was converted to percent depth dose (PDD) to perform the excitation beam correction for charged particles.

Fluorescent x-ray attenuation correction was performed for both K-shell and L-shell XFCT imaging. Due to the lower energy x-rays in L-shell XFCT imaging, fluorescent photon attenuation must be accounted for in the generation of L-shell XFCT images for objects greater than 1 mm in size [90]. To perform the fluorescent x-ray attenuation correction, an attenuation map $b$ for K-shell and L-shell XFCT for each phantom, shown in Figure 4.3, was generated by the following equation based on Equations 3.5 and 3.7:

$$b_i = \sum_f \omega_f \left[ \frac{\sum_{\rho=1}^{N} \exp(-r_{\rho i f})}{N} \right] \tag{4.2}$$

$$r_{\rho i f} = \sum_m \mu_{mf} t_m \tag{4.3}$$

where $\omega_f$ and $\mu_{mf}$ are the fluorescent yield and linear attenuation coefficient of material $m$, respectively, for each fluorescent x-ray energy $f$ in Table 4.2. A series of $N$ rays, represented by $r_{\rho i}$, isotropically emitted from image pixel $i$ is the dot product of the proportion of path length $t_m$ that a fluorescent photon along a ray would travel. The linear attenuation coefficients $\mu_m f$ for each material were assumed to be based on *a priori* knowledge of the AuNP concentrations and vial locations, which could be approximately obtained from a CT scan. The total number of rays $N$ was chosen to be 2,500 and 10,000 for the 2.5 cm and 5.0 cm diameter phantom, respectively, to

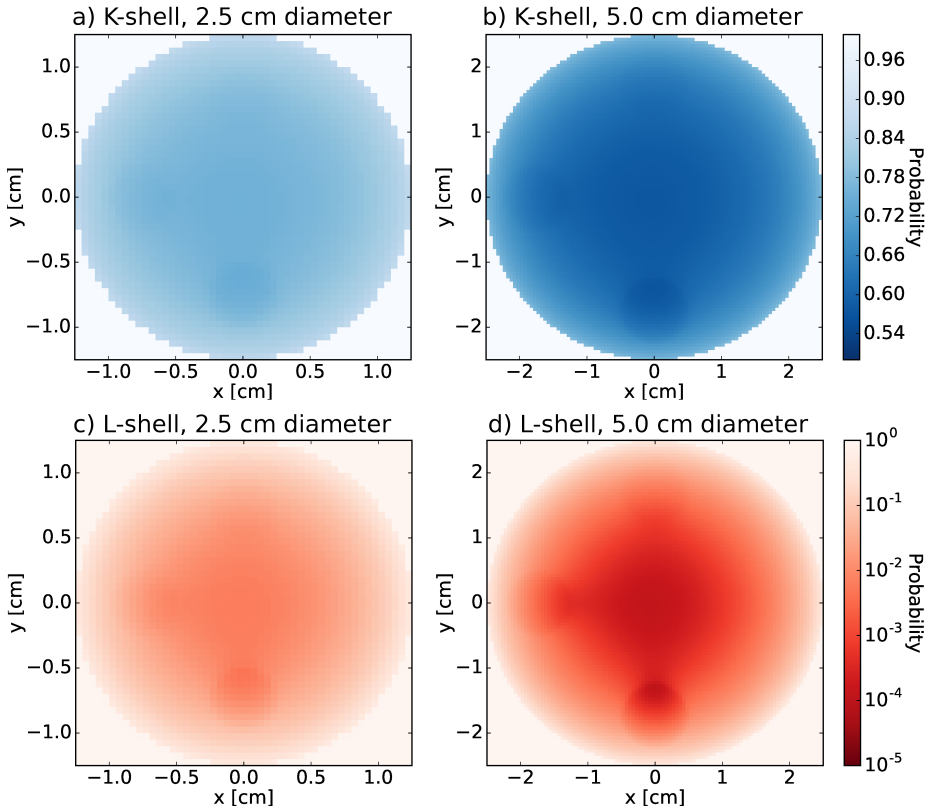


Figure 4.3: Attenuation maps showing the probability of K-shell fluorescent x-rays escaping the a) 2.5 cm and b) 5.0 cm diameter phantom, and L-shell fluorescent x-rays escaping the c) 2.5 cm and d) 5.0 cm diameter phantom.

approximate fluorescent detection with the spherical detector.

The attenuation-corrected imaging matrix $M'_{ij}$ was calculated from the original $M_{ij}$ as:

$$M'_{ij} = M_{ij} c^{e}_{ij} \tag{4.4}$$

where $c^{e}_{ij}$ is defined in Equation 4.1. $M'_{ij}$ in Equation 4.4 will differ for each phantom size because the summation indices $i$ and $j$ will change. Finally, after $k$ iterations of the MLEM algorithm, the XFCT image is then divided by the attenuation map $b$ from Equation 4.2. The reconstructed XFCT images were then normalized to the known highest AuNP concentration in the phantom. The normalization factor was calculated as the mean signal of the vial containing the 2% AuNP solution.

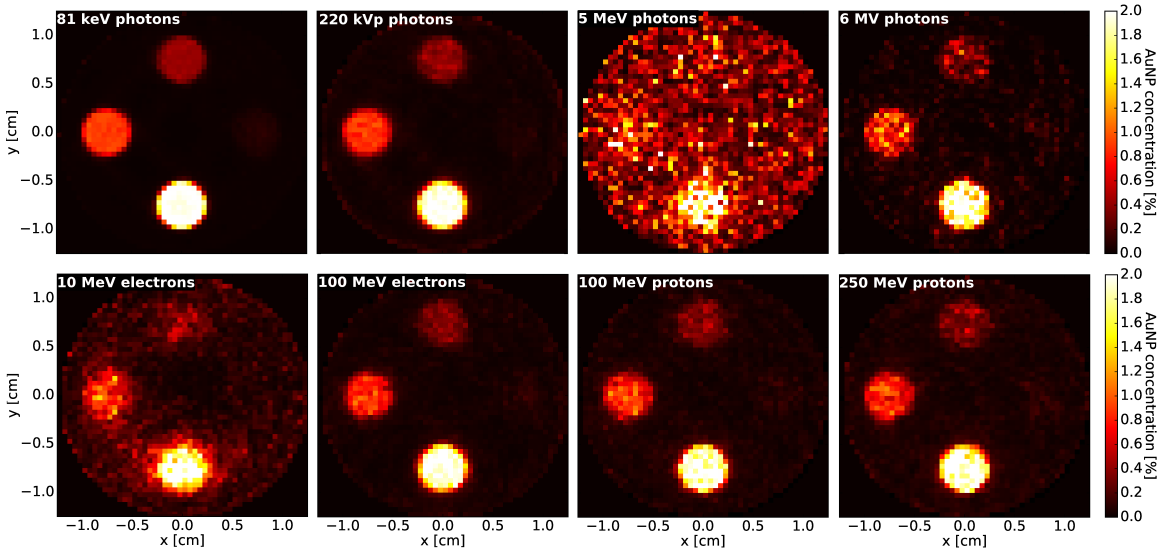


Figure 4.4: K-shell XFCT images of 2.5 cm diameter phantom.

### 4.3.4 Image quality evaluation

The CNR was the metric used to evaluate the AuNP sensitivity for each XFCT image, and was calculated as the following:

$$\mathrm{CNR} = \frac{\mu_{\mathrm{vial}} - \mu_{\mathrm{water}}}{\sigma_{\mathrm{water}}} \tag{3.9}$$

where $\mu_{\mathrm{vial}}$ and $\mu_{\mathrm{water}}$ are the mean values of the signal of the vial and water regions of interest, respectively, and $\sigma_{\mathrm{water}}$ is the standard deviation of the signal from the water region of interest. The image noise was taken to be equal to $\sigma_{\mathrm{water}}$. To evaluate the uncertainty in the CNR, the numerator in Equation 3.9 was replaced with $\sigma_{\mathrm{vial}}$.

The AuNP imaging sensitivity for each XFCT image was estimated by normalizing the CNR data to an imaging dose of 30 mGy using the fact that the CNR scales with the square root of dose. The CNR data was fit to a line with a forced y-intercept of 0, and then interpolated to the concentration value of AuNP solution corresponding to the Rose criterion of CNR = 4 [91]. This was taken to be the AuNP imaging sensitivity limit.

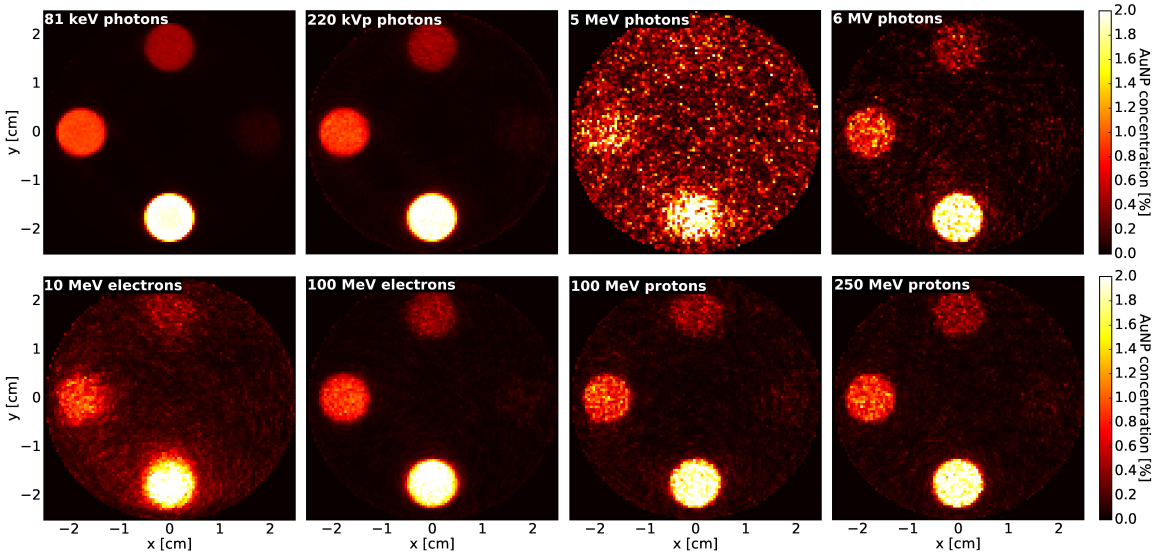


Figure 4.5: K-shell XFCT images of 5.0 cm diameter phantom.

## 4.4 Results and Discussion

### 4.4.1 Reconstructed XFCT images

K-shell XFCT images from the eight excitation sources are shown in Figure 4.4 for the 2.5 cm diameter phantom and Figure 4.5 for the 5.0 cm diameter phantom. For the 2.5 cm diameter phantom, the noise in the 81 keV photon XFCT image was the lowest overall, followed by the 220 kVp photon and 100 MeV electron XFCT images. Both proton XFCT images have low noise but at the expense of high imaging doses. However, the noise in the 5 MeV photon XFCT image was the highest overall due to the build-up region within 2 cm in the depth-dose profile (Figure 4.2) for 5 MeV photons and the reduced probability of photoelectric effect interactions. Some noise was present in the 6 MV photon XFCT image, however lower energy photons at a mean of approximately 2 MeV meant a higher probability of photoelectric interactions compared to 5 MeV photons. The 10 MeV electron XFCT image also suffers from high noise due to very little interactions causing inner shell vacancies. The relative noise amount is also apparent in the K-shell XFCT images for the 5.0 cm diameter phantom.

L-shell XFCT images from the eight excitation sources are shown in Figure 4.6 for the 2.5 cm diameter phantom and Figure 4.7 for the 5.0 cm diameter phantom. For both phantom sizes, the 81 keV photon XFCT image had the lowest amount of noise, followed by the 100 MeV proton, 220 kVp photon, and 250 MeV proton XFCT images

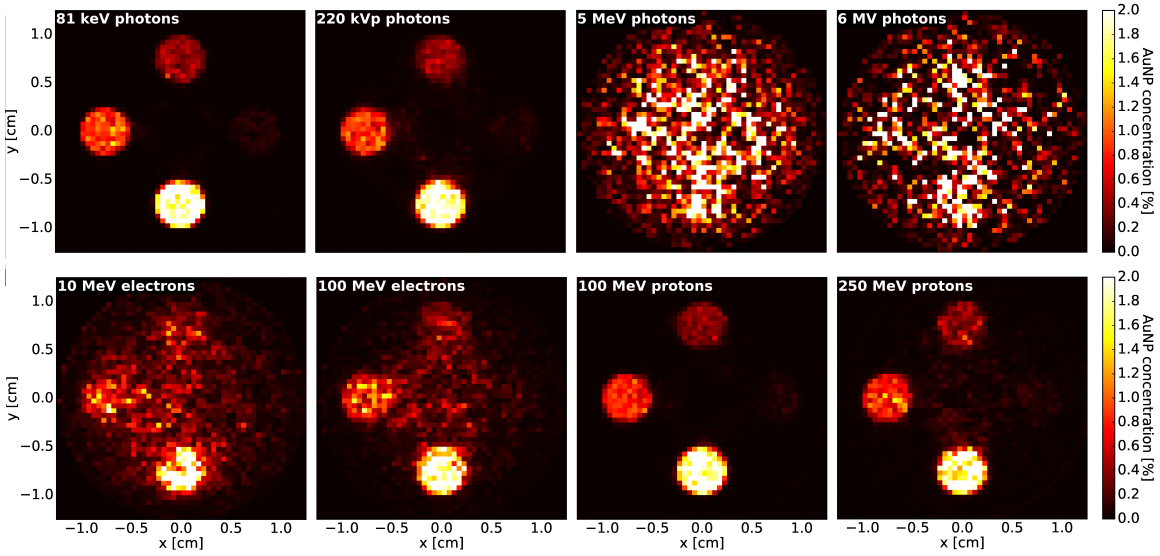


Figure 4.6: L-shell XFCT images of 2.5 cm diameter phantom.

in that order. However, the 5 MeV and 6 MV photon XFCT images had the highest amount of noise; no vials were visible in these images. The noise was prevalent in the electron-induced XFCT images; most of the noise was likely due to the lack of fluorescent x-rays. Other factors including the known problem of increased noise with increasing number of iterations for emission tomography images and the approximate attenuation correction algorithm will have also contributed to the amount of noise. A lower number of counts in L-shell XFCT due to attenuation in the phantom and within the vial also contributed to the increase in noise, especially for the 5.0 cm diameter phantom. Self-attenuation in the vials due to the approximation of $\mu_f$ to be for pure water is likely to have contributed to non-uniform vials in the L-shell XFCT images. This effect becomes more apparent in the 5.0 cm diameter phantom since the vials are double in size compared to the vials in the 2.5 cm diameter phantom. Using the value of $\mu_f$ for 9.71 keV $L\alpha_1$ x-rays for both pure water ($\mu_f = 6.888\,\mathrm{cm}^{-1}$) and for a 2% gold solution by weight ($\mu_f = 11.25\,\mathrm{cm}^{-1}$), the expected x-ray intensity transmitted through a 5 mm and 10 mm vial is 3% and 0.1% for pure water and 0.36% and 0.001% for 2% gold solution, respectively. The amount of fluorescent photon attenuation when approximating the $\mu_f$ to be for pure water is underestimated by an order of magnitude at worst, which can account for the signal non-uniformity in the vials.

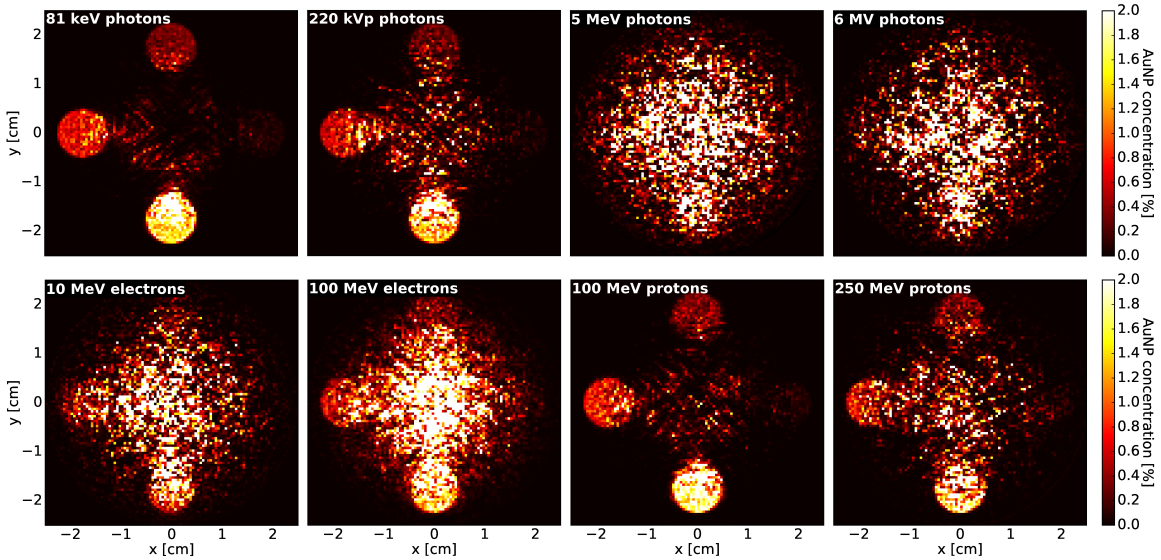


Figure 4.7: L-shell XFCT images of 5.0 cm diameter phantom.

### 4.4.2 Contrast-to-noise ratio

The CNR normalized to 1 mGy for the K-shell and L-shell XFCT images of the 2.5 cm and 5.0 cm diameter phantoms are shown in Figures 4.8a and 4.8b, respectively. Normalization to 1 mGy was done to maintain dose independence between all XFCT images with different excitation sources and for ease of scaling to other imaging doses. For some of the K-shell XFCT images, the CNR was higher for the 5.0 cm diameter phantom due to the higher total number of particles simulated in the excitation beam. However, this effect was not seen for the L-shell XFCT images, likely due to the increased effect of attenuation.

For equal imaging dose, the CNR of the 81 keV photon K-shell XFCT images was at least two orders of magnitude higher than the other XFCT images for both phantom sizes, except for the 220 kVp and 6 MV images. The 10 MeV electron XFCT image of the 2.5 cm diameter phantom had the lowest CNR, about two times less than the CNR of the 5 MeV photon and 100 MeV proton XFCT image. The CNR tripled between the 100 MeV proton XFCT image and the 100 MeV electron XFCT image, with the CNR of the 250 MeV proton XFCT image being intermediate. A similar relative trend of the CNR was evident among the XFCT images of the 5.0 cm diameter phantom, however the CNR of the 100 MeV and 250 MeV proton XFCT images were found to be similar to that of the 10 MeV electron and 5 MeV photon XFCT image. The CNR of the 100 MeV electron XFCT image of the 5.0 cm diameter

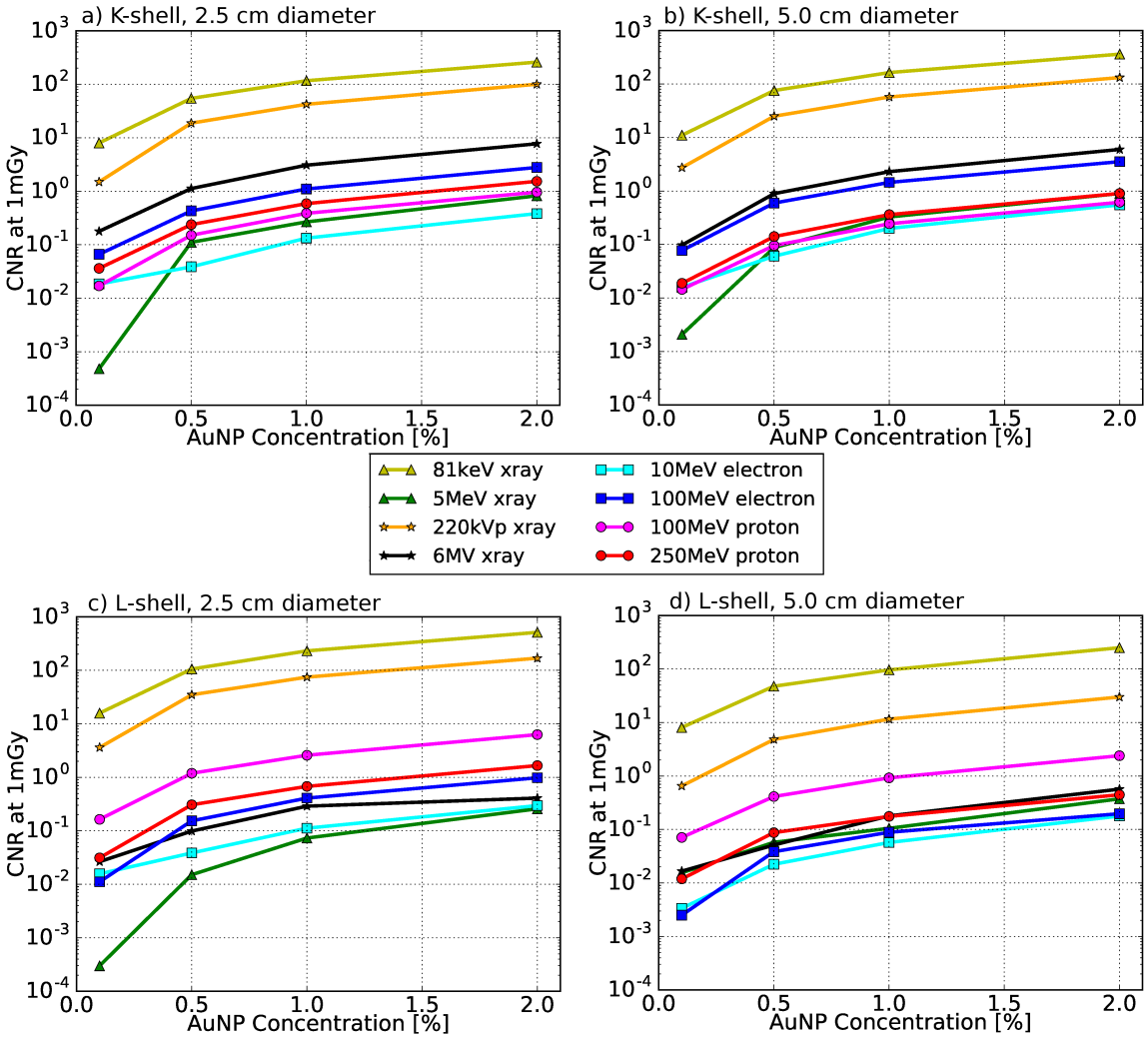


Figure 4.8: Normalized CNR at 1 mGy for the K-shell a) 2.5 cm and b) 5.0 cm diameter XFCT images and L-shell c) 2.5 cm and d) 5.0 cm diameter XFCT images.

phantom nearly doubled likely due to less noise from scatter in between the AuNP vials where the water region of interest was defined, as a result of the larger vial separation.

For L-shell XFCT, the CNR of the 81 keV photon XFCT image was also at least two orders of magnitude higher than the other XFCT images for the 5.0 cm diameter phantom. However the difference in the CNR between the 81 keV photon and 220 kVp photon-induced XFCT images for the 2.5 cm and 5.0 cm diameter phantom is about a factor of 3 and 10, respectively.

Table 4.3: Summary of AuNP sensitivity for each MLEM-generated K-shell XFCT image and its corresponding number of iterations normalized to 30 mGy.

| **Beam source** | **81 keV x-rays** | | **220 kVp x-rays** | | **5 MeV x-rays** | | **6 MV x-rays** | |
|---|---|---|---|---|---|---|---|---|
| **Phantom diameter** | 2.5 cm | 5 cm | 2.5 cm | 5 cm | 2.5 cm | 5 cm | 2.5 cm | 5 cm |
| **AuNP sensitivity @ 30 mGy** | 0.006% | 0.004% | 0.02% | 0.01% | 2.28% | 2.08% | 0.22% | 0.29% |
| **Number of iterations** | 17 | 13 | 11 | 11 | 18 | 20 | 22 | 23 |
| **Beam source** | **10 MeV electrons** | | **100 MeV electrons** | | **100 MeV protons** | | **250 MeV protons** | |
| **Phantom diameter** | 2.5 cm | 5 cm | 2.5 cm | 5 cm | 2.5 cm | 5 cm | 2.5 cm | 5 cm |
| **AuNP sensitivity @ 30 mGy** | 4.85% | 3.42% | 0.62% | 0.49% | 1.79% | 2.81% | 1.11% | 1.91% |
| **Number of iterations** | 21 | 17 | 14 | 18 | 14 | 20 | 13 | 20 |

### 4.4.3 AuNP imaging sensitivity

The imaging sensitivity for each XFCT image was defined to be the AuNP concentration at the Rose criterion limit for an imaging dose of 30 mGy, which does not exceed typical doses used in small animal imaging[103]. A summary of the AuNP imaging sensitivity for the K-shell XFCT images in Figures 4.4 and 4.5 for each of the eight excitation sources is shown in Table 4.3. A similar summary of the AuNP imaging sensitivity for the L-shell XFCT images in Figures 4.6 and 4.7 is shown in Table 4.4.

For small animal studies, the biologically relevant concentration of AuNPs ranges from 0.001%[12] to 0.7%[10] by weight. The AuNP sensitivity limit for K-shell XFCT images induced by 81 keV photons in the 2.5 cm and 5.0 cm diameter phantom was 0.006% and 0.004%, respectively. These AuNP sensitivity limits for each phantom size increase to 0.02% and 0.01%, 0.22% and 0.29%, and 0.62% and 0.49%, respectively, for the 220 kVp photon-, 6 MV photon-, and 100 MeV electron-induced K-shell XFCT images. The AuNP sensitivity limit for L-shell XFCT images induced by 81 keV photons in the 2.5 cm and 5.0 cm diameter phantom was 0.003% and 0.007%, respectively. These AuNP sensitivity limits for each phantom size increase to 0.01% and 0.07%, and 0.28% and 0.81%, respectively, for the 220 kVp photon- and 100 MeV proton-induced K-shell XFCT images. For both K-shell and L-shell XFCT images of the 2.5 cm and 5 cm diameter phantoms, the 81 keV photon excitation source

Table 4.4: Summary of AuNP sensitivity for each MLEM-generated L-shell XFCT image and its corresponding number of iterations normalized to 30 mGy.

| **Beam source** | **81 keV x-rays** | | **220 kVp x-rays** | | **5 MeV x-rays** | | **6 MV x-rays** | |
|---|---|---|---|---|---|---|---|---|
| **Phantom diameter** | 2.5 cm | 5 cm | 2.5 cm | 5 cm | 2.5 cm | 5 cm | 2.5 cm | 5 cm |
| **AuNP sensitivity @ 30 mGy** | 0.003% | 0.007% | 0.01% | 0.07% | 7.11% | 5.63% | 3.30% | 4.35% |
| **Number of iterations** | 19 | 20 | 12 | 26 | 23 | 27 | 20 | 19 |
| **Beam source** | **10 MeV electrons** | | **100 MeV electrons** | | **100 MeV protons** | | **250 MeV protons** | |
| **Phantom diameter** | 2.5 cm | 5 cm | 2.5 cm | 5 cm | 2.5 cm | 5 cm | 2.5 cm | 5 cm |
| **AuNP sensitivity @ 30 mGy** | 6.04% | 12.7% | 1.89% | 8.33% | 0.28% | 0.81% | 1.14% | 4.07% |
| **Number of iterations** | 15 | 37 | 17 | 22 | 13 | 22 | 16 | 31 |

resulted in the highest AuNP sensitivity. While not as good as 81 keV or 220 kVp photons, these results suggest that 100 MeV electron beams could be suitable for K-shell XFCT imaging of AuNPs in both phantom sizes, and 100 MeV protons could be suitable for L-shell XFCT imaging of AuNPs for the 2.5 cm diameter phantom at small animal imaging doses.

The Bazalova-Carter *et al.* 2015 study[55] for a table-top L-shell XFCT system could achieve a AuNP sensitivity of 0.007% in 4 mm diameter vials for a 2.8 cm diameter phantom. This is on par compared to 0.003% and 0.01% for our L-shell XFCT images of a 2.5 cm diameter phantom induced by 81 keV and 220 kVp photon beams, respectively. The 50 kVp beam used in the Bazalova-Carter *et al.* 2015 study was chosen to maximize the photoelectric effect interaction probability to produce more L-shell fluorescent x-rays, which will decrease the AuNP detection limit. In addition, the chosen gold solution concentrations of 0.06% to 0.1% in the Bazalova-Carter *et al.* 2015 study will result in less attenuation of L-shell fluorescent x-rays within the 4 mm vials compared to our 5 mm vials filled with 0.1% to 2% of gold solution. In addition, the 4 mm vials have a vial edge depth of 2 mm, which are shallower than our 5 mm vials at a vial edge depth of 2.5 mm.

The AuNP sensitivity quoted in the Ahmad *et al.* 2014 MC study[47] was 0.001% for an imaging dose of 20 mGy to reconstruct a K-shell XFCT image of a 2.25 cm diameter phantom. When compared to our AuNP sensitivity of 0.006% for 81 keV

photon-induced K-shell XFCT images, the difference can be explained by the following reasons. The scanning resolution of the XFCT image in the Ahmad *et al.* 2014 study was 120 translations over 2.25 cm and 360 rotations. The increased resolution in pencil beam spacing and angular rotations over a smaller phantom would increase the AuNP sensitivity. In addition, real AuNPs were simulated in 0.001%-0.1% concentrations by weight. We approximated the AuNPs in our simulation as a gold solution in higher concentrations, which may result in some fluorescent x-ray attenuation.

The experimental AuNP sensitivity of 1.7% quoted in another Bazalova-Carter *et al.* 2015 study[97] for a K-shell XFCT of a 7 cm diameter phantom induced by 220 MeV protons was for an imaging dose of 580 Gy using a single spectrometer or 92 mGy using a 2 cm-wide detector ring. Compared to our AuNP sensitivity of 1.91% for 250 MeV protons of a 5 cm diameter phantom, our sensitivity is similar, however will increase with higher dose. For similar imaging dose our sensitivity is better due to the spherical detector increasing the efficiency of fluorescent x-ray detection compared to a single spectrometer or 2 cm-wide detector ring. In addition, the vials used in this Bazalova-Carter *et al.* 2015 study were 3%-5% concentration by weight of gold chloride solution, which would cause attenuation of the fluorescent x-rays within the vial.

There were several factors to consider in our simulation design that may have affected our results. First, our MC simulations assumed no geometrical uncertainty, which would be a factor in typical imaging experiments. We used a spherical detector with ideal detection efficiency in that it captured each fluorescent x-ray that escaped the phantom in a single pixel. This spherical detector was used to decrease the simulation time, and should not affect relative results if a more realistic geometry were used. In practice, detectors that encompass the entire phantom are not feasible to implement due to cost and geometric constraints. Reducing the detection area would increase the AuNP sensitivity limit for each image. For instance, the 2D array detector in another study had an active area of 6.22 $cm^2$[30]. When placed at the same distance as the spherical detectors in our study, the solid angle coverage offered by the 2D array detector decreases by a factor of 5 and 10, respectively. This corresponds to a decrease in the number of fluorescent x-rays detected, which in turn reduces the CNR by a factor of $\sqrt{5}$ and $\sqrt{10}$. Increasing the imaging dose by the factor of 5 and 10 would mitigate the effect of the reduced solid angle coverage, however the scan time would increase by the same amount. Alternatively in this case, the scan time could be kept the same if the beam current would increase, however this could increase

signal pile-up in the detector array. Due to Compton scattered photons interfering with the fluorescent x-ray detection, the placement of the 2D detector array would be an important geometry consideration and could change the imaging sensitivity by up to an order of magnitude[47],[39]. In addition, the response of the spherical detector is assuming to be perfect, since every fluorescent x-ray that escapes the phantom crosses the detector boundary. The x-ray spectra recorded by typical spectrometers, such as the Amptek X-123CdTe or X-123SDD, are not ideal and must be corrected for detector response[104].

Most of the excitation beams in the present study were modelled as monoenergetic, however all beams had zero beam divergence. Apart from synchrotron sources, it is difficult to achieve a monoenergetic photon beam. Kilovoltage and megavoltage photon beams from x-ray tubes are polyenergetic, and can be approximated as monoenergetic beams with excess filtration at the expense of output. It is easier to produce monoenergetic charged particle beams, however a small beam-energy spread is unavoidable in practice. Using a polyenergetic beam increases the scatter and reduces the gold photoelectric effect cross-section, which decreases the AuNP imaging sensitivity as evidenced by the XFCT images induced by 220 kVp and 6 MV photons.

The imaging doses for the proton-induced XFCT images are quite high for routine small animal imaging. These doses are typical of fractionated radiotherapy, which lends the possibility of using x-ray fluorescence techniques for on-line range verification using gold seeds or dose-enhancement mapping during charged-particle therapy. To verify the proton range for each treatment fraction, a 2D collimated detector array could be placed perpendicular to the incident proton beam to detect the origin of gold x-ray fluorescence along the proton beam path. Due to these high imaging doses, proton beams might also be feasible for *ex vivo* XFCT imaging. However, we have only demonstrated small-animal imaging with electron- and proton-induced XFCT; expansion to larger-sized phantoms would compromise the signal of L-shell fluorescent x-rays due to more attenuation. For depths where the percent depth dose of 100 MeV electrons is higher compared to 81 keV as shown in Figure 4.2, XFCT induced by 100 MeV electrons has the potential to image larger objects than XFCT induced by 81 keV photons. The choice of 2.5 cm and 5.0 cm diameter phantoms was to study the effect of imaging different sizes of small animals using XFCT, since there may be excitation beam attenuation. The effect of fluorescent x-ray attenuation was controlled for in the phantom design by keeping the distance between the edge of the vial and the surface of the phantom constant between phantom sizes. Changing this

distance will impact the CNR in L-shell XFCT images. In our previous study, we showed that L-shell XFCT images induced by 15 keV photons have a higher CNR than K-shell XFCT images induced by 81 keV photons when the depth of the vial edge is less than 3 mm[59].

In addition, the equipment used for proton therapy, VHEE beam therapy, and kilovoltage x-ray imaging are fitted to perform pencil beam scans suitable for XFCT imaging purposes; this is not necessarily the case for clinical megavoltage x-ray and electron beams. 10 MeV electron beams were found to not be suitable for XFCT imaging, however the use of small gold seeds instead of AuNPs for x-ray fluorescence studies would increase the number of fluorescent x-rays produced, which in turn would increase the signal. 6 MV photon beams are better than 5 MeV photon beams, as the mean energy of 6 MV photons have a higher probability of photoelectric effect interaction. 81 keV photon beams have the highest probability of photoelectric effect interaction, followed by 220 kVp photon beams. This is reflected in the images where XFCT induced by 81 keV photon beams results in the highest CNR. 5 MeV photon beams were found to be not appropriate for XFCT imaging.

Finally, the imaging time required to complete a pencil beam XFCT scan in practice would need to be considered. To prevent harmful effects of anesthesia on a small animal, scan time should not exceed 1 hour. For a single spectrometer XFCT scan using 120 kVp x-rays to image a 6.4 cm diameter phantom, the imaging time was 87 minutes at a 14 mGy dose[39]. The imaging time for a 220 MeV proton beam scan of a 7 cm diameter phantom using a single spectrometer to detect fluorescent x-rays was 252 minutes for a 580 Gy dose[97], however the amount of pileup for a detector prevented its placement close to the phantom and resulted in long imaging time. The use of multiple spectrometers or a detector ring could reduce the dose and imaging time of each scan to an acceptable level suitable for small animal imaging. We will consider clinical x-ray and electron beams produced by a linear accelerator such as the Truebeam (Varian Medical Systems, Palo Alto, CA). The nominal dose rate at $d_{max}$ is calibrated to 1 cGy/MU, with the maximum output being 600 MU/min for 6 MV and 15 MV photons and 1000 MU/min for 10 MeV electrons. Even when collimated to a 0.5 mm $\times$ 0.5 mm pencil beam for XFCT imaging, the imaging time would be at least 1 minute since the gantry and couch could rotate and translate. However, detector pileup may result in longer imaging times. A linear accelerator producing VHEE beams, such as the Next Linear Collider Test Accelerator at SLAC National Accelerator Laboratory, would be capable of fast electromagnetic scanning

due to the high dose rates of up to 9.0 Gy/s[105]. Considering the dose per particle for 100 MeV electrons is approximately $2.5\times10^{-12}$ Gy/particle from Figure 4.2, the imaging time on this linear accelerator for a 30 mGy scan would be very short at $2.5\times10^{-12}$ Gy/particle $\times 1.30\times10^{9}$ electrons $\times$ (30 mGy / 1700 mGy) $\div$ 9.0 Gy/s = 6.4 $\times10^{-6}$ seconds. However, the rotational geometry necessary for XFCT imaging would limit the imaging time. This calculation also assumes no detector pileup.

X-ray tube pencil beam scan times for the 2.5 cm and 5.0 cm diameter phantoms imaged to a dose of 30 mGy are estimated to be 162 minutes and 324 minutes, respectively[95]. A fan beam would decrease the scan time by a factor of 50 and 100, respectively, to 3.24 minutes per slice in each case. A cone beam imaging geometry would result in a further reduction of the imaging time by producing multiple images simultaneously. The use of fan beam or cone beam geometry would decrease the imaging time by removing the need for translational steps, however it would necessitate the use of a detector collimator, which would decrease imaging sensitivity by up to an order of magnitude for summarizes these imaging times for the XFCT geometries scanning a hypothetical 1 cm slice of each phantom. According to this calculation, fan beam and cone beam XFCT would result in an acceptable imaging time. Collimator design has been shown to affect the detectable concentration of AuNP solution in sheet beam XFCT.[95] A pencil beam was used to remove the effect of collimation for each XFCT image, as the focus was on the relative XFCT image quality for each excitation source.

Table 4.5: Estimated scan time for pencil, fan, and cone beam XFCT geometry imaging a hypothetical 1 cm slice using kilovoltage photons.

| CT geometry | Scan time per 0.5 mm slice | | Total scan time of 1 cm slice | |
|---|---|---|---|---|
| Phantom size | 2.5 cm | 5.0 cm | 2.5 cm | 5.0 cm |
| Pencil beam | 162 min | 324 min | 3240 min | 6480 min |
| Fan beam | 3.24 min | 3.24 min | 64.8 min | 64.8 min |
| Cone beam | 3.24 min | 3.24 min | 3.24 min | 3.24 min |

## 4.5 Conclusions

We have used Monte Carlo simulations to generate pencil beam K-shell and L-shell XFCT images of two different sized water phantoms induced by 81 keV and 5 MeV photons, 220 kVp and 6 MV photons, 10 MeV and 100 MeV electrons, and 100

MeV and 250 MeV protons. 81 keV photon beams produce the best XFCT images of AuNP solutions overall for both K-shell and L-shell XFCT images of the 2.5 cm and 5.0 cm diameter phantom, followed closely by 220 kVp photon beams. However, 100 MeV electron beams and 100 MeV proton beams may be suitable for small animal imaging of AuNPs using K-shell and L-shell XFCT, respectively. Due to high imaging dose, these results suggest electron-induced and proton-induced x-ray fluorescence technique might be feasible for guiding AuNP-enhanced VHEE or proton radiotherapy.

# Chapter 5

# Sheet Beam X-ray Fluorescence Computed Tomography Imaging of Gold Nanoparticles

## 5.1 Summary

The use of collimators is necessary for spatial discrimination of fluorescent x-rays when imaging high-$Z$ elements using fan or sheet beam CT geometry. However, several collimation strategies are possible for implementation on a table-top imaging system. In this chapter we investigated the impact of the collimator design on the XFCT image quality compared to the case of pencil beam XFCT where no collimation is necessary in a Monte Carlo study. This was done for both K-shell and L-shell fluorescent x-rays originating from AuNPs in a small water phantom[95].

## 5.2 Introduction

Early detection of cancer is key for the prevention of metastasis and better prognosis for patient survival. Imaging modalities, which include computed tomography (CT), are used to diagnose cancerous tumours and assess further steps for treatment. CT is a common, sophisticated form of imaging which employs the use of keV-range x-rays for reconstructing high-contrast 3D image slices. Several generations of CT scanners since the 1970s have been developed for a wide range of clinical applications. In particular, the first generation of CT scanners feature a pencil beam geometry, while the third generation of CT scanners introduced the fan beam geometry.

In order to achieve contrast resolution at the molecular level, one can combine the well-studied CT concept with x-ray fluorescence, known as x-ray fluorescence CT (XFCT). In XFCT imaging, nanoparticles with high atomic number ($Z$) such as gold are injected into the region of interest, such as a tumour volume, before

the scan. Upon x-ray irradiation, the nanoparticles produce characteristic, or fluorescent, x-rays. Knowing the energy of the fluorescent x-rays after scattering, an image of the x-ray production sites at the region of interest can be reconstructed. XFCT was first exhibited using 7 keV synchrotron x-rays incident on small iron and titanium fibres[36]; later a first attempt at high resolution was achieved using a focused 20 keV x-ray beam incident on quartz capillaries containing high-$Z$ material solutions[37]. Recent advancements in detector efficiency and computational resources have prompted further investigation into the achievable resolution and sensitivity of XFCT imaging.

Simulations and experimental demonstrations of XFCT imaging of high-$Z$ nanoparticles in a small animal phantom show promising results[45],[47],[39]. It has also been shown that XFCT can outperform conventional CT when objects are imaged containing high-$Z$ material solutions at low, sub-percentage concentrations[52]. However, a persistent problem is the Compton background drowning out the magnitude of the K-shell fluorescence signal in the x-ray energy spectrum perceived by the detector. Since the energy of the Compton-scattered x-rays depend on the scattering angle, the Compton background can be shifted apart from the fluorescence signal to improve the imaging sensitivity[47],[39]. XFCT imaging using the L-shell fluorescence signal from high-$Z$ based Cisplatin has also been shown to improve imaging sensitivity due to the lower energy of the fluorescent x-rays being separated out from the Compton background[90] and better detector energy resolution. However, with lower energy x-rays, there is the tradeoff of increased attenuation through material. L-shell XFCT imaging has been experimentally demonstrated on a 12 mm-diameter phantom[54] and a 28 mm-diameter phantom[55] using bench-top XFCT imaging systems.

Another persistent problem is the prolonged imaging time for pencil beam geometries as compared to fan beam, sheet beam, or cone beam geometries. Collimators have also been investigated for their use in XFCT imaging in an effort to decrease the imaging time; a pair of staggered multi-pinhole lead collimators each in front of opposing planar detectors was used in a Monte Carlo model of a small animal phantom loaded with vials of AuNPs which generated cone beam XFCT images[41]. Recently, a multi-pinhole collimator with holes arranged in a grid was designed for volumetric XFCT imaging of iodine solutions and can image down to biologically relevant concentrations of 0.004%[51]. In particular, sheet beam XFCT imaging has been simulated and experimentally demonstrated with polyenergetic x-rays, which can detect AuNP concentrations down to as low as 0.2% in a 2 cm diameter wa-

ter phantom and 0.6% in a 6.4 cm diameter PMMA phantom[49],[106]. Sheet beam XFCT imaging has also been demonstrated with 37 keV synchrotron x-rays to detect iodine concentrations as low as 0.0005% in a 1 cm diameter acrylic phantom[107]. We have explored several alternative collimator designs for both K-shell and L-shell sheet beam XFCT which evaluate the lowest possible AuNP concentration detectable to determine which collimator is the optimal imaging geometry.

## 5.3 Materials and Methods

### 5.3.1 Phantom and imaging geometry

A cylindrical water phantom 2 cm in diameter and 3 cm in height containing 0.5mm - 2mm diameter vials with AuNP concentrations of 0.4% - 1.6% by weight in water is shown in Figure 5.1. The vials extend the entire length of the phantom, and the centres of each of the vials was located 3.3 mm from the surface of the phantom. The size of the phantom was chosen to mimic the size of a typical mouse, while the vial sizes were chosen to resemble typical structures and organs in a mouse[103]. Two opposing square detector planes which measured 3.2 cm $\times$ 3.2 cm were placed 1 cm away from the edge of the phantom perpendicular to the incident beam. Each detector plane was modeled as an air region which scored every K-shell and L-shell fluorescent x-ray that crossed the plane with an energy resolution of 0.5 keV and 0.2 keV, respectively. The chosen energy resolution was based on the specifications of the Amptek X-123CdTe X-ray Spectrometer and X-123SDD X-ray Spectrometer with Silicon Drift Detector (Amptek Inc., Bedford, MA, USA) for use in resolving K-shell and L-shell fluorescent x-rays, respectively. The phantom and imaging geometry were represented by combinatorial geometry, with the material being set to each region. The AuNP solutions were modeled as being a mixture of water and gold rather than individual nanoparticles, which should not affect the property of x-ray fluorescence crucial for image generation. The entire geometry was in air.

In the sheet beam geometry, a slice of the phantom was irradiated to a mean dose of 30 mGy to water separately by a 15 keV and 81 keV monoenergetic rectangular photon sheet beam of 0.4 mm in width and 2.2 cm in length with 360 1-degree phantom rotations to yield L-shell and K-shell fluorescent x-rays, respectively, by the presence of AuNPs. These energies of incident photons were chosen because they are situated just above the $L_I$-edge (14.35 keV) and K-edge (80.73 keV) of gold to maximize the probability of photoelectric interactions with gold atoms in the vials.

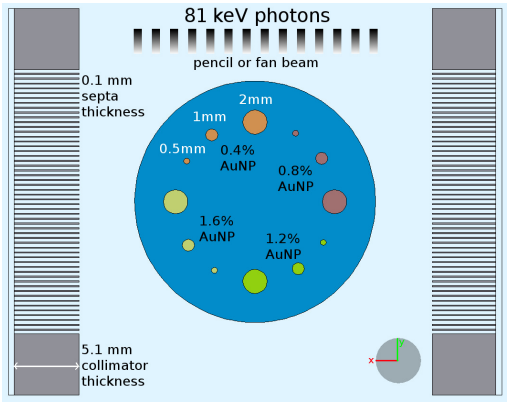


(a) K-shell, 81 keV x-ray beam, collimator thickness 5.1 mm.

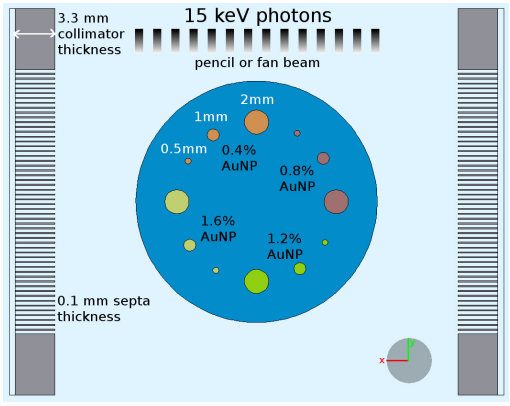


(b) L-shell, 15 keV x-ray beam, collimator thickness 3.3 mm.

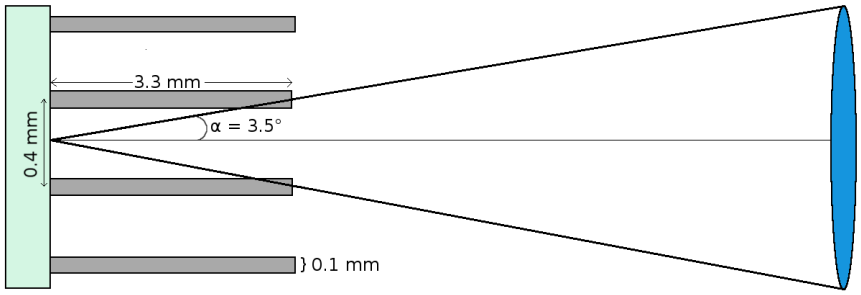


(c) Zoomed-in diagram of L-shell collimator. Diagram is not to scale.

Figure 5.1: Geometry of water phantom showing difference in collimator thickness and photon beam energy for a) K-shell versus b) L-shell imaging. c) Detailed L-shell collimator geometry illustrating the conical acceptance angle.

The 30 mGy dose to the phantom was verified in each simulation by scoring the total energy deposited in the water. The pencil beam geometry differed from the sheet beam geometry in that it consisted of 55 translations which scan transversely across the phantom over 2.2 cm in 0.4 mm-wide steps, and lacked the presence of collimators necessary for sheet beam geometry data acquisition. The pencil beam geometry images served as the ideal case when compared against sheet beam geometry images in order to assess the feasibility of each collimator geometry.

The total number of incident photons in the 15 keV and 81 keV beam for each imaging geometry was set to $6.6 \times 10^{10}$ and $1.72 \times 10^{10}$ respectively. For each XFCT imaging geometry, there were a total of 360 simulations for each rotation angle in the sheet beam geometry and 360 rotations $\times$ 55 translations = 19800 simulations in the pencil beam geometry.

### 5.3.2 Collimator geometries

Three types of collimators were considered for the sheet beam geometry: multi-pinhole, parallel, and converging, all of which resulted in 2D images with dimensions of 55 × 55 pixels with a resolution of 0.4 mm. The active area of the collimated detector on each side measures 3.2 cm × 2.2 cm for the parallel collimator, 2.2 cm × 3.2 cm for the converging collimator, and 0.04 cm × 2.2 cm for the pinhole collimator. The multi-pinhole collimator, shown in Figure 5.2a, was based on geometry presented in the cone-beam XFCT paper by Jones and Cho[41]; it had 55 0.3 mm-wide square holes separated by 0.1 mm-wide septa arranged in a column and was situated in the cross-sectional plane of the incident beam. The parallel collimator, shown in Figure 5.2b, was an elongated version of the multi-pinhole collimator, where each of the 55 slits is 32 mm × 0.3 mm, in an effort to increase the amount of fluorescent signal. Finally, the converging collimator, shown in Figure 5.2c, had double the amount of septa and was oriented perpendicular to the septa of the parallel and multi-pinhole collimator geometries. To accommodate the extra septa, each of the 110 slits was 32 mm × 0.1 mm and each septa was symmetrically focused onto the imaging slice of the phantom. A top-down view of the converging collimator is shown in Figure 5.2d. As the middle slit of the converging collimator was in the plane of the imaging slice, it was not useful for data acquisition. However, this middle slit accommodated the multi-pinhole collimator in the simulated geometry, allowing for simultaneous data acquisition for both collimator geometries. Each collimator was made out of lead, and the septa thickness was 0.1 mm. The collimator thickness for K-shell XFCT images was set to 5.1 mm to allow at most 5% photon transmission through lead[82]. Transmission of lower-energy fluorescent x-rays through lead is less pronounced, so for L-shell XFCT images the collimator thickness was set to 3.3 mm to allow a conical acceptance angle of 3.5°; this is illustrated in Figure 5.1c.

### 5.3.3 Monte Carlo simulations

The FLUKA[67],[68] Monte Carlo code, version 2011.2c-5, was used to simulate x-ray fluorescence. The appropriate electron and photon physics, including detailed photoelectric edge treatment, fluorescence, Rayleigh scattering, and inelastic Compton scattering were selected as part of the Precision default settings. Electron and photon transport cutoff was set to 5 keV. Since FLUKA is typically used for high energy applications, the fluorescent energies that are modeled by FLUKA are shown in Table

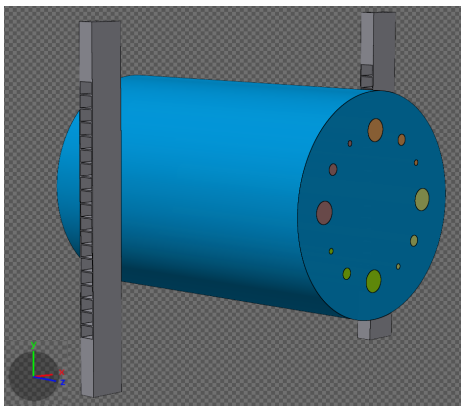

(a) Multi-pinhole collimator.

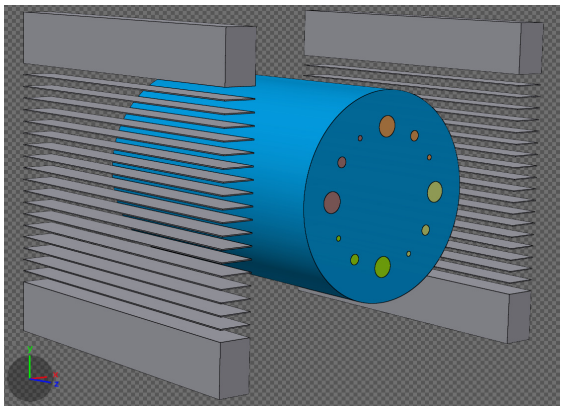

(b) Parallel collimator.

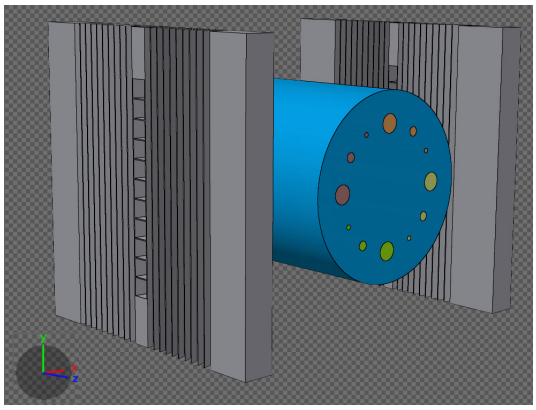

(c) Converging collimator.

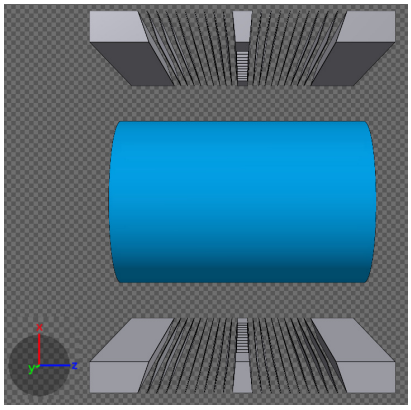

(d) Converging collimator (top view).

Figure 5.2: Lead collimator geometries for fan beam XFCT. The primary photon beam is incident on top of the phantom, ie. traveling in the -y direction. The number of septa have been reduced for better visualization.

5.1 and compared with the experimentally-based literature values[57]. Flair is the graphical user interface for FLUKA, which was helpful for visualizing all geometries. All simulations were run on a SGI Altix XE cluster made up of Xeon X5675 and L5420 processors with 4160 cores, which is a part of the Compute Canada/WestGrid network.

### 5.3.4 Image reconstruction

In each simulation, whenever an x-ray crossed a boundary into the planar detector, its energy, direction, and position were written into a binary phase space file. A sinogram for each side of the phantom and imaging geometry was generated by counting the number of K-shell or L-shell fluorescent x-rays that crossed the boundary with the

| Fluorescent x-ray | Intensity $\omega$ (%) | Experimental (keV) | FLUKA (keV) | % Difference |
|---|---|---|---|---|
| $L\alpha_2$ | 11% | 9.628 | 9.625 | -0.03% |
| $L\alpha_1$ | 100% | 9.713 | 9.705 | -0.08% |
| $L\beta_1$ | 67% | 11.44 | 11.47 | +0.35% |
| $L\beta_2$ | 23% | 11.58 | 11.58 | 0% |
| $K\alpha_2$ | 59% | 66.99 | 67.18 | +0.28% |
| $K\alpha_1$ | 100% | 68.80 | 69.03 | +0.33% |

Table 5.1: K-shell and L-shell fluorescent x-ray energies for Au and their fluorescent yield $\omega$[57], compared with FLUKA.

appropriate energy resolution. The number of background x-rays was estimated by linearly interpolating the background energy spectrum and approximating the contribution of the two nearest neighbouring energy bins separated by 0.5 keV for K-shell XFCT images and 0.2 keV for L-shell XFCT images. Due to the L-shell energy resolution, some of the L-shell fluorescent energies were too close together to resolve. Therefore, when generating sinograms from the fluorescent signal, the average energy of $L\alpha_2$ and $L\alpha_1$ (9.67 keV) was used, as well as the average energy of $L\beta_2$ and $L\beta_1$ (11.55 keV). The position axis of each sinogram was distinguished by the collimator shape in the sheet beam geometry XFCT images and the translational step of the incident beam in the pencil beam geometry XFCT images.

Each XFCT image was reconstructed using 50 iterations of the maximum-likelihood expectation maximization (MLEM) algorithm[88] with an applied attenuation correction. The general form of the MLEM algorithm is the following:

$$a_i^{k+1} = \frac{a_i^k}{\sum_j M_{ij}} \sum_j \left( M_{ij} \frac{p_j}{\sum_i M_{ij} a_i^k} \right) \tag{3.3}$$

where $a$ is the relative concentration of AuNP solution in image pixel $i$ and $M_{ij}$ is the contribution of image pixel $i$ to the projection line $j$ normalized to the case in which the projection line intersects the centre of the pixel with the largest line distance such that $0 \leq M_{ij} \leq 1$. The sinogram entry $p_j$ represents the total counts from projection $j$, indicating the rotation angle of the projection line and the position of the pencil beam or within the collimator array. The iteration number is denoted by $k$.

While it is not as important for higher energy K-shell XFCT images, primary and fluorescent photon attenuation must be accounted for in the generation of lower

energy L-shell XFCT images for objects greater than 1 mm in size[90]. The primary beam attenuation correction factor $c_{ij}^{p}$ was calculated by the following:

$$c_{ij}^{p} = \exp(-\mu_p d_{ij}) \tag{3.4}$$

where $\mu_p$ is the linear attenuation coefficient of water at the primary photon energy of 15 keV or 81 keV and $d_{ij}$ is the distance through water the primary photon beam travels to pixel $i$. The fluorescent photon attenuation correction factor $c_{ij}^{f}$ was calculated by the following:

$$c_{ij}^{f} = \sum_{f} \omega_f \exp(-\mu_f t_{ij}) \tag{3.5}$$

where $\mu_f$ is the linear attenuation coefficient of water at the fluorescent photon energy $f$ and $t_{ij}$ is the mean distance through water a fluorescent photon originating from pixel $i$ travels toward the detector plane. In the case of sheet beam geometries, the fluorescent photon trajectory is along projection $j$, whereas for pencil beam geometries the photon trajectory is averaged over the entire detector plane. All of the distances were estimated by mathematical geometry, and the linear attenuation coefficients $\mu_p$ and $\mu_f$ were assumed to be for pure water due to the low concentration of the AuNP solutions and small diameters of the vials.

Finally, the attenuation-corrected imaging matrix $M'_{ij}$ was calculated from the original $M_{ij}$ as:

$$M'_{ij} = M_{ij} \frac{c_{ij}^{p}}{c_{ij}^{f}} \tag{3.6}$$

where $c_{ij}^{p}$ and $c_{ij}^{f}$ are defined in Equations 3.4 and 3.5 respectively.

It is important to note that $M'_{ij}$ in Equation 3.6 is different depending on which detector is being considered, as $t_{ij}$ will change. Two sinograms were generated per imaging geometry; one representing signal from the detector on the left side of the phantom and the other from the detector on the right side. Hence, two images were reconstructed using the left-side and the right-side sinogram separately, then added together. The summed XFCT image was then normalized to the actual AuNP concentration by using *a priori* knowledge of the highest concentration and the largest vial in the phantom. The normalization factor was calculated as the mean signal of the 2 mm-diameter 1.6% AuNP concentration vial.

### 5.3.5 Image quality evaluation

The image quality metric used in this study is the contrast-to-noise ratio (CNR), which was calculated as the difference in mean value of the signal of each vial $\mu_{\text{vial}}$ and the surrounding water $\mu_{\text{water}}$ divided by the standard deviation of the signal from the surrounding water $\sigma_{\text{water}}$:

$$\text{CNR} = \frac{\mu_{\text{vial}} - \mu_{\text{water}}}{\sigma_{\text{water}}} \tag{3.9}$$

The uncertainty in the CNR was evaluated by replacing $\mu_{\text{vial}}$ with $\sigma_{\text{vial}}$ in Equation 3.9.

The imaging sensitivity for each vial size and imaging geometry was estimated by applying a linear fit to the AuNP concentration versus CNR data and interpolating the concentration value of AuNP solution corresponding to the Rose criterion of CNR = 4[91]. The linear fit was performed using the SciPy Optimize module[93] in Python.

## 5.4 Results

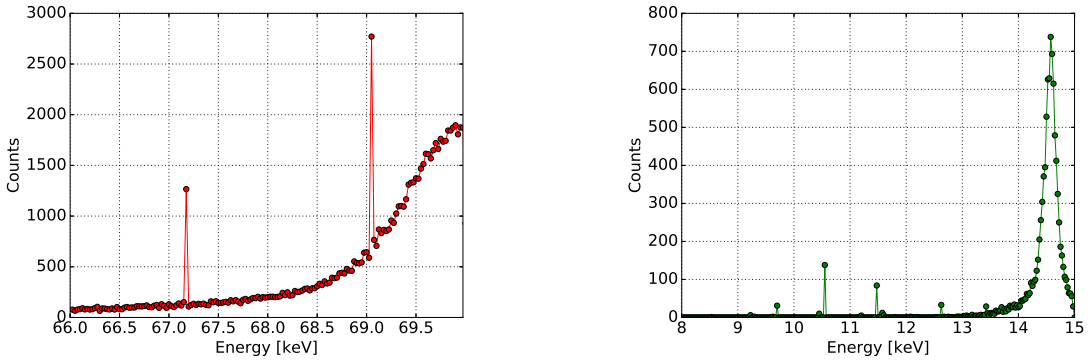


(a) K-shell (b) L-shell

Figure 5.3: X-ray energy spectrum for a lead parallel collimator scored by the left detector plane for a single phantom rotation.

### 5.4.1 Reconstructed XFCT images

The x-ray energy spectra resulting from the incident 81 keV and 15 keV photon sheet beam on the water phantom are shown in Figure 5.3. Simulated sheet beam XFCT images reconstructed by attenuation-corrected MLEM for the three collimator

geometries are shown in Figure 5.4. Among the K-shell XFCT images, the parallel and converging collimator geometries are similar in image quality. However, among the L-shell XFCT images there was excess noise introduced in the converging collimator compared to the parallel collimator, in part due to the extra amount of water in the phantom that the L-shell fluorescent x-rays must travel through in order to reach the detector. The number of L-shell fluorescent x-rays going through only 5 mm, 2 mm, or 1 mm of water will be reduced to approximately 11%, 41%, or 64% of the original amount. For both K-shell and L-shell XFCT images, the multi-pinhole geometry has the lowest image quality in part due to the lower active area of the detector, so it is prone to statistical error.

Simulated pencil beam XFCT images reconstructed by attenuation-corrected MLEM are shown in Figure 5.5. All vials are visible in both pencil beam images.

### 5.4.2 Contrast-to-noise ratio

The CNR for the sheet beam XFCT images as a function of the AuNP concentration is shown in Figure 5.6. Sample data for the CNR calculation of the 1.6% AuNP vials for the L-shell parallel collimator XFCT image is shown in Table 5.2. As a consequence of the excess water that fluorescent photons must travel through to reach the collimator, the CNR values for the converging collimator XFCT images were lower than that of the parallel collimator XFCT images as predicted by the presence of increased noise. This effect is magnified when considering the mean free path ($\approx$ 2.3 mm) of the lower-energy L-shell fluorescent x-rays. As expected, the CNR values for the multi-pinhole collimator XFCT images had a high statistical error. As the standard deviation of the vial signal was used to calculate the error in the CNR values, the error bars were largely in part due to the limited vial size in the phantom and some self-attenuation within the vials containing higher AuNP concentrations that the L-shell XFCT images are especially susceptible to. Note that it was not appropriate to compare the CNR values between K-shell and L-shell XFCT images for a given collimator geometry because the collimator thickness was different between K-shell (5.1 mm) and L-shell (3.3 mm) sheet beam XFCT.

The CNR for the pencil beam XFCT images as a function of the AuNP is shown in Figure 5.7. Considering the largest vial with the highest concentration of AuNP, the K-shell pencil beam XFCT image had an order of magnitude higher CNR than the K-shell parallel collimator XFCT image. Meanwhile, the L-shell pencil beam XFCT

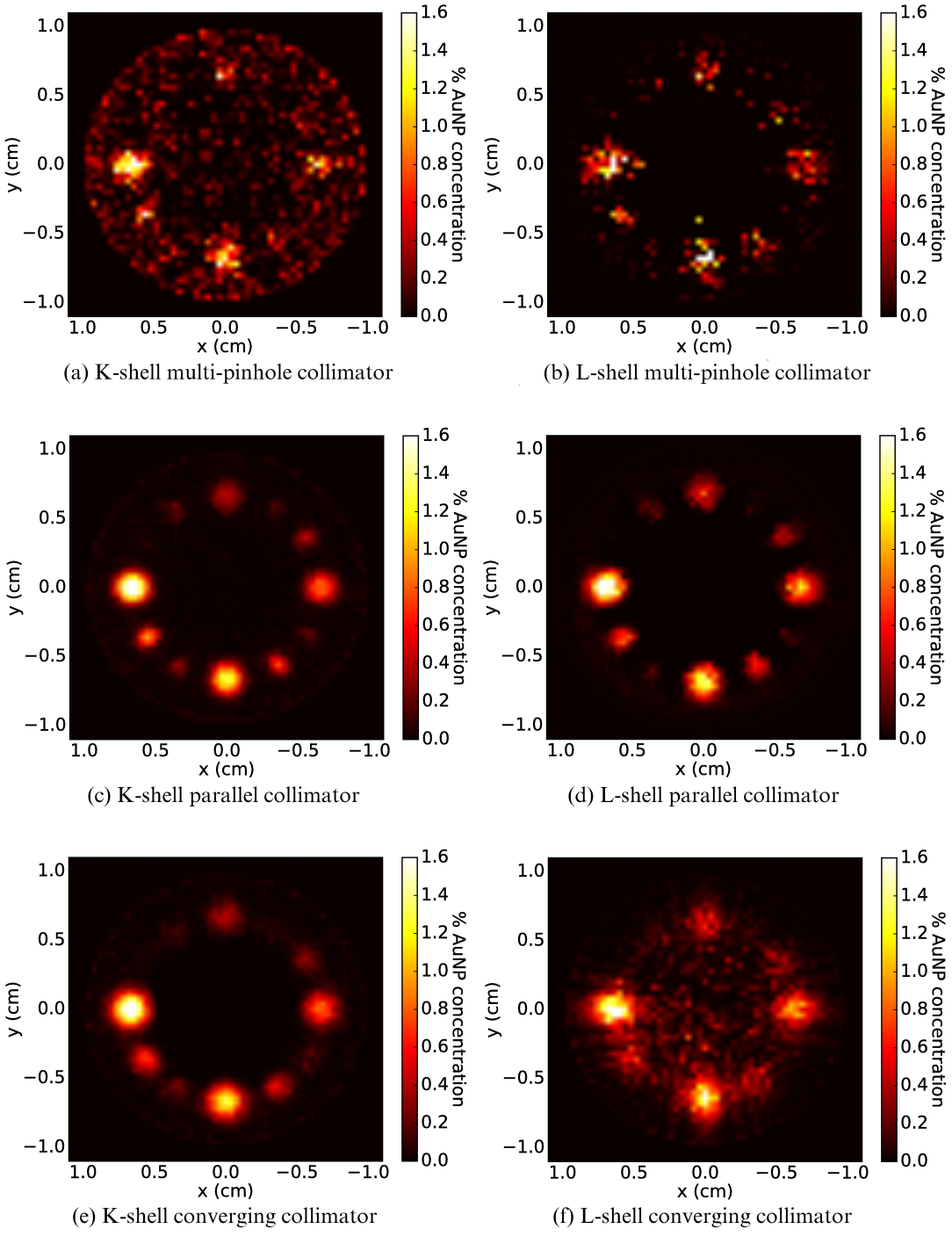


(a) K-shell multi-pinhole collimator

(b) L-shell multi-pinhole collimator

(c) K-shell parallel collimator

(d) L-shell parallel collimator

(e) K-shell converging collimator

(f) L-shell converging collimator

Figure 5.4: Sheet beam K-shell (a,c,e) and L-shell (b,d,f) XFCT images generated using the attenuation-corrected MLEM algorithm for the multi-pinhole (a-b), parallel (c-d) and converging (e-f) collimators.

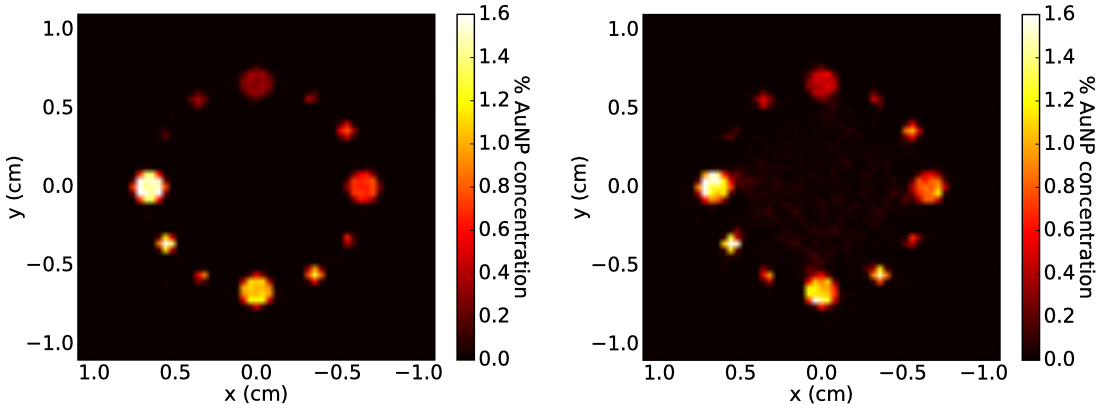


(a) K-shell pencil beam geometry

(b) L-shell pencil beam geometry

Figure 5.5: Pencil beam a) K-shell and b) L-shell XFCT images generated using the attenuation-corrected MLEM algorithm.

| Vial size | $\mu_{vial}$ | $\mu_{water}$ | $\sigma_{water}$ | CNR |
|---|---|---|---|---|
| 2 mm | 1.6 | 0.012 | 0.022 | 72.2 |
| 1 mm | 0.735 | 0.012 | 0.022 | 32.9 |
| 0.5 mm | 0.053 | 0.012 | 0.022 | 1.86 |

Table 5.2: Sample calculation of CNR for detection of 1.6% AuNP vials for L-shell parallel collimator.

image had roughly the same order of magnitude CNR value as the L-shell parallel collimator XFCT image.

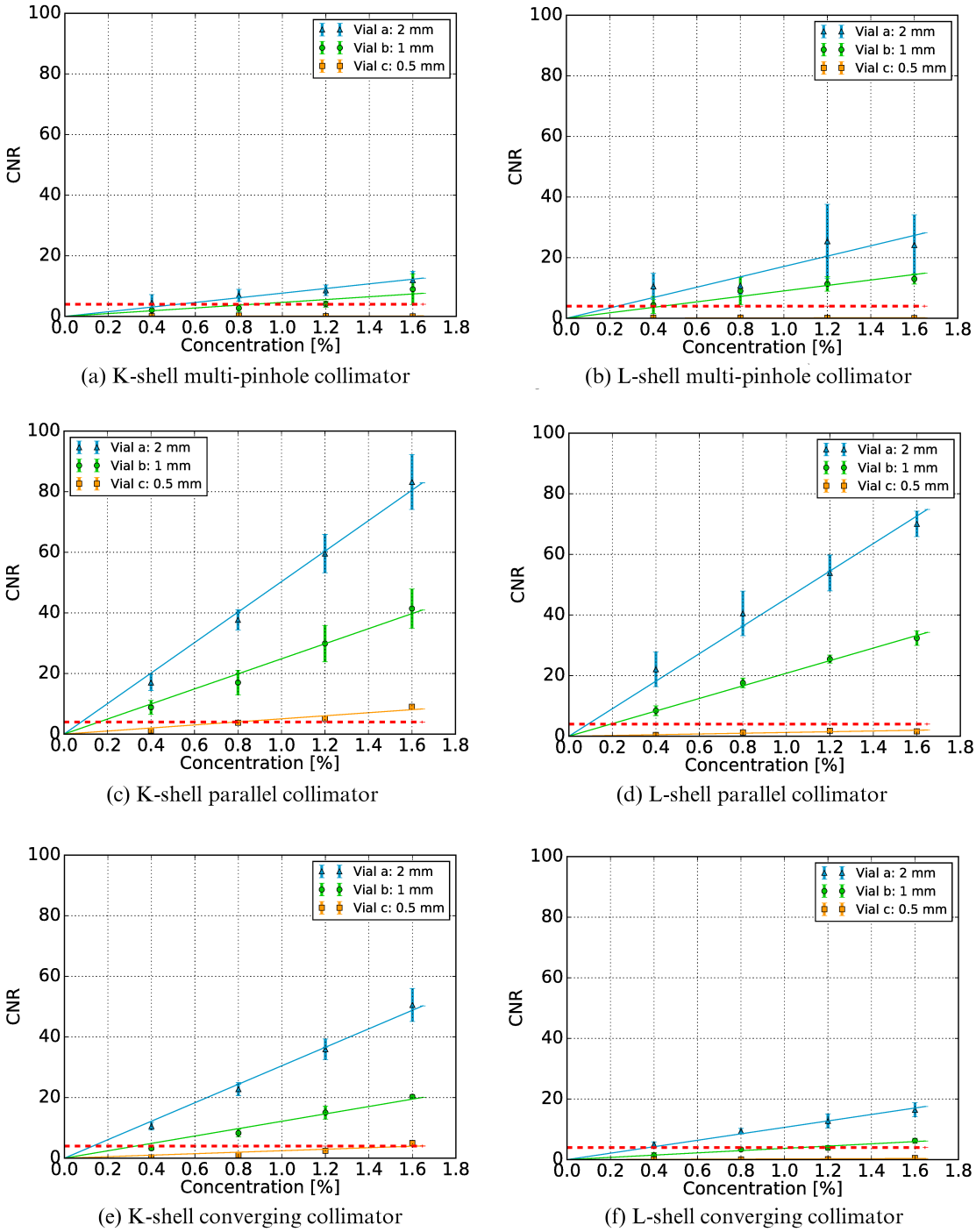


(a) K-shell multi-pinhole collimator

(b) L-shell multi-pinhole collimator

(c) K-shell parallel collimator

(d) L-shell parallel collimator

(e) K-shell converging collimator

(f) L-shell converging collimator

Figure 5.6: CNR versus AuNP concentration plots for the sheet beam K-shell (a,c,e) and L-shell (b,d,f) XFCT images for the multi-pinhole (a-b), parallel (c-d) and converging (e-f) collimators, irradiated to a dose of 30 mGy. The Rose criterion is shown as a red dashed line.

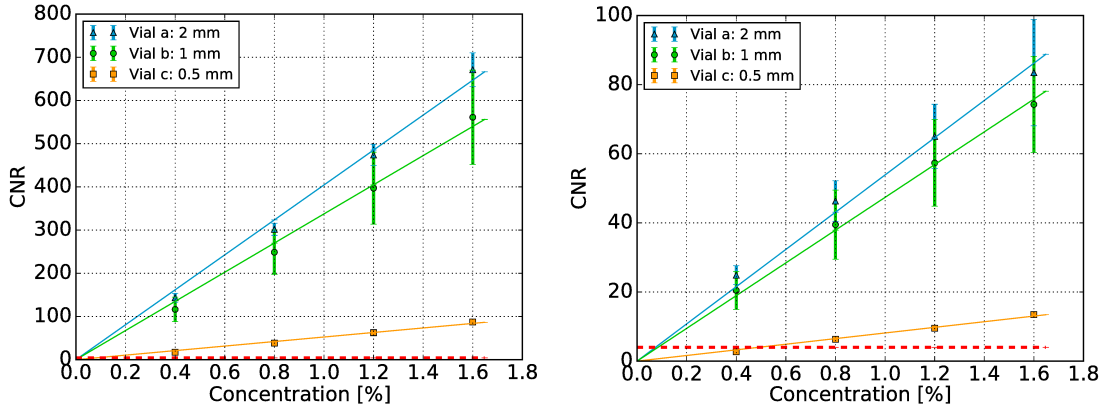


(a) K-shell pencil beam geometry

(b) L-shell pencil beam geometry

Figure 5.7: CNR versus AuNP concentration plots for the pencil beam a) K-shell and b) L-shell XFCT images. The Rose criterion is shown as a red dashed line.

### 5.4.3 Lowest concentration of AuNP detectable

The K-shell and L-shell XFCT imaging detection limits for AuNP are summarized in Table 5.3 for each of the sheet beam collimator geometries and the pencil beam geometry. Out of the three collimators for K-shell XFCT, the parallel collimator had the best imaging sensitivity of 0.08% being the minimum detectable AuNP concentration for a 2 mm diameter vial and 0.16% being the minimum for a 1 mm diameter vial. Out of the three collimators for L-shell XFCT, the parallel collimator could detect the lowest concentration of AuNP at 0.09% for the 2 mm diameter vial and 0.19% for the 1 mm diameter vial. Visibility issues of the 0.5 mm vial were present for all XFCT sheet beam images, which led to artificially high imaging detection limits. However, due to partial volume effects, the results for the 0.5 mm vial were not representative of the true CNR.

## 5.5 Discussion

### 5.5.1 Simulation results

We have showcased three different collimator geometries for sheet beam K-shell and L-shell XFCT imaging and compared these simulated images with pencil beam XFCT imaging. The AuNP imaging sensitivity limits were 0.01%, 0.01%, and 0.08% for the 2 mm, 1 mm, and 0.5 mm vial sizes, respectively, for the K-shell XFCT pencil beam

| | *K-shell* | *XFCT* | *L-shell* | *XFCT* |
|---|---|---|---|---|
| | **2mm** | **1mm** | **2mm** | **1mm** |
| **multi-pinhole** | 0.52% | 0.86% | 0.23% | 0.44% |
| **parallel** | 0.08% | 0.16% | 0.09% | 0.19% |
| **converging** | 0.13% | 0.33% | 0.38% | 1.07% |
| | | | | |
| **pencil beam** | 0.01% | 0.01% | 0.07% | 0.08% |

Table 5.3: Lowest concentration of AuNP solution detectable by pencil beam and sheet beam K-shell and L-shell XFCT imaging for collimator thicknesses of 5.1 mm and 3.3 mm, respectively. The data for the 0.5 mm vial are not shown.

images. For the L-shell XFCT pencil beam images, the AuNP imaging sensitivity limits were 0.07%, 0.08%, and 0.45% for the 2 mm, 1 mm, and 0.5 mm vial sizes, respectively. These sensitivity limits were quoted based on a dose of 30 mGy to water and for an incident monoenergetic photon beam of 81 keV or 15 keV. The AuNP sensitivity limits were included for the 0.5 mm vials as they were visible in the pencil beam XFCT images. The visibility issues present in the sheet beam XFCT images for the 0.5 mm vial was a drawback to the sheet beam data acquisition. Considering the 2 mm diameter vial, the AuNP imaging sensitivity for the K-shell XFCT parallel collimator geometry of 0.08% is about an order of magnitude higher than the AuNP imaging sensitivity for the K-shell pencil beam geometry of 0.01%. For L-shell XFCT, the AuNP imaging sensitivity of 0.09% for the parallel collimator geometry is quite comparable to that of the pencil beam geometry of 0.07%. For small animal studies, the biologically relevant concentration of AuNP ranges from as low as 0.001%[12] to as high as 0.7%[10] by weight.

The polychromatic cone beam K-shell XFCT Monte Carlo study done by Jones and Cho (2011) quoted the detection limit as 0.1% AuNP for 5 mm vials in a 5 cm PMMA phantom, for a dose of 30 cGy[41]. The collimator used in the Jones and Cho study was similar in shape to our multi-pinhole collimator; our higher AuNP detection limit for K-shell multi-pinhole sheet beam geometry can be explained in part by the lower imaging dose and smaller vial size. The grid-arranged multi-pinhole collimator proposed in the study by Sasaya et al. (2017) quoted the detection limit of iodine solutions as 38 $\mu$g/mL, or 0.0038%, for 3D tomographic XFCT images generated by a monochromatic photon beam[51]. While this collimator was optimized for its geometry, the imaging time of 90 minutes is quite long and is similar to how long data acquisition would take for a pencil beam XFCT image based on previous studies[39].

The Ahmad et al. study (2014) reported a AuNP sensitivity of 0.001% for pencil beam K-shell XFCT at 20 mGy dose[47]. This imaging sensitivity is lower than our result due to the collection of fluorescent x-rays at an increased detection angle, which is optimal for separating out the Compton scatter background from the fluorescent x-rays. The active detection area is 65% greater in the Ahmad et al. study, so more fluorescent x-rays would be recorded. Finally, the diameter of the AuNP vials in our study were less than half the size of the vials in the Ahmad et al. study, which would increase the AuNP sensitivity.

The choice of AuNP concentrations in our present study was used to reliably evaluate the limit of detection, as this is the basis to determine the optimal collimator geometry for sheet beam XFCT imaging. To help mitigate the self-attenuation effect of L-shell fluorescent x-rays produced in higher AuNP concentration vials, the vial sizes were purposely chosen to be small. However, with a vial diameter range of 0.5 mm to 2 mm, the image resolution of 0.4 mm introduced partial volume effects when reconstructing the accurate AuNP concentration at the periphery of the vials.

Various arrangements of collimator geometries have been previously investigated, such as multi-slit collimators paired with pencil beam geometry and single pinhole collimators paired with sheet beam geometry, for use with x-ray fluorescence emission tomography (XFET) applications[108],[50],[109]. The single pinhole collimator in particular enables direct imaging, bypassing the need for image reconstruction which can add additional noise[50]. However, the single pinhole collimator blocks a large portion of fluorescent x-rays that would otherwise reach the detectors if the collimator geometries presented in Figure 5.2 were utilized. While the multi-slit collimator geometry offers spatial resolutions as low as 50 $\mu$m for imaging trace elements such as bromine and copper in a 5 mm-sized object[108], the imaging time of 2 hours and high doses are prohibitive for small animal imaging applications.

To evaluate the effect of scattered incident x-rays causing fluorescence, we ran a quick simulation of a monoenergetic 15 keV photon sheet beam incident on the 2-cm diameter water phantom containing no AuNP vials. A phase space file was recorded on the other side of the phantom across a 2.3 cm x 2.3 cm air region. We found that the ratio of photons that scatter outside the path of the sheet beam which have an energy capable of producing fluorescent x-rays in gold to the number of incident 15 keV photons is less than 1%. Based on this result, we believe that the attenuation correction factor from Equation 3.5 is minimally affected by these scattered photons.

### 5.5.2 Setup feasibility

Synchrotrons, which are used to generate monoenergetic photon beams such as the ones simulated in this study, are not often widely available for ease of use. However, a monoenergetic photon beam can be approximated by excess filtering of a polychromatic photon beam. Since our XFCT images were simulated by a monoenergetic beam, assumed an ideal detector efficiency, and had no geometric uncertainty, the AuNP imaging sensitivity limits quoted in Table 5.3 were lower than may be realistically achieved. Manufacturing collimators out of lead may be a cumbersome task at sub-millimetre precision, however lead is a malleable material that could be pressed down into sheets. Tungsten is also a feasible option for collimator material, though it should be noted the fluorescent signal from the tungsten collimator can interfere with the fluorescent signal from the AuNPs as their energies are similar. Figure 5.8a illustrates the extra fluorescent x-ray energies due to the presence of tungsten in the range of the K-shell fluorescent x-rays. The K-shell XFCT image for the parallel collimator geometry is shown in Figure 5.8b, which has increased background due to the extra fluorescent signal from the tungsten. A more sophisticated background subtraction algorithm would be necessary when using tungsten as a possible collimator material.

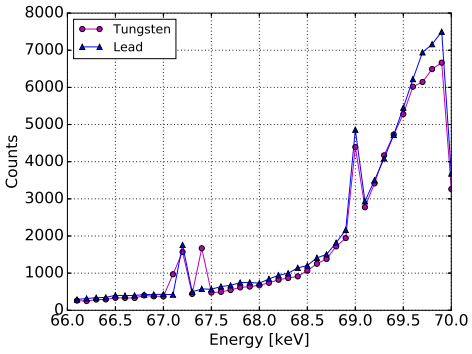


(a) X-ray energy spectra for single phantom rotation, compared with lead.

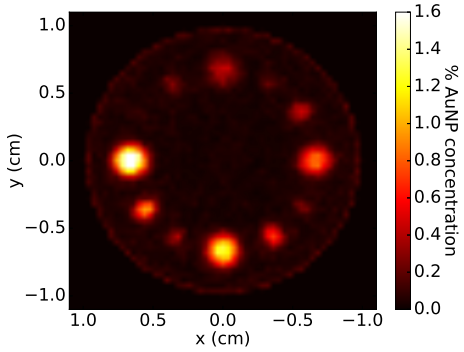


(b) MLEM-reconstructed XFCT image.

Figure 5.8: X-ray energy spectrum and K-shell XFCT image for a theoretical tungsten parallel collimator.

In addition, it is important to consider the imaging time and detector count rate to assess the feasibility of implementing the proposed imaging setup experimentally. To estimate the imaging time of the proposed setup, the output of a microfocus x-ray source (L9631, Hamamatsu Photonics Inc.) of 800 $\mu$A, used in Manohar *et al*

(2013) was considered[54]. The *bremsstrahlung* yield of 81 keV and 15 keV electrons striking a tungsten target was approximately 0.0123 and 0.0032 x-rays per electron, respectively[76]. Using an x-ray beam angle of 62° and assuming it reaches a beam area of 2.2 cm × 0.4 mm at a distance of 32 cm, the total useful x-ray output coming from this source was calculated from Equation 2.3 to be $3.32 \times 10^8$ x-rays per second for a fan beam area and $2.33 \times 10^9$ x-rays per second for a pencil beam area. For K-shell XFCT, $6.60 \times 10^{10}$ primary x-rays in total were used to deliver 30 mGy to water, which worked out to $6.60 \times 10^{10} \div 360$ rotations $= 1.83 \times 10^8$ x-rays per projection for a fan beam geometry and $6.60 \times 10^{10} \div (360$ rotations $\times 55$ translations $) = 3.33 \times 10^6$ x-rays per projection for a pencil beam geometry. The division of the number of x-rays per projection by the useful x-ray output in both beam geometries gave 0.552 seconds per projection, but does not include an extra 0.5-second allowance per projection for data-saving and stage-moving as quoted in Ahmad *et al* (2015)[39]. For pencil beam geometry, the multiplication of $0.552 + 0.500$ seconds per projection with $360 \times 55$ projections would result in an estimated imaging time of 347 minutes, or 5.8 hours. This is way too long for small animal imaging, as the scan time should not exceed 1 hour to prevent adverse effects of anesthesia. However, assuming similar imaging times between fan beam and sheet beam geometries, a sheet beam geometry with only 360 projections would result in a 6.3-minute imaging time. This is a much more reasonable imaging time, which emphasizes the need for a well-designed collimator geometry. The number of primary x-rays for L-shell XFCT imaging is reduced by about a factor of 4 to yield the same imaging dose of 30 mGy as for K-shell XFCT, but the *bremsstrahlung* yield of 15 keV electrons compared to 81 keV electrons is also reduced by a factor of 4. Thus the imaging time for L-shell XFCT is expected to be about the same as for K-shell XFCT.

The detector count rate must be considered in XFCT imaging. The parallel collimator geometry, due to its larger sensitive area than the other two collimator geometries, would see the most x-rays per detector element. The maximum number of x-rays that would reach a given detector element was estimated to be 1850 x-rays per projection. With an active imaging time of 0.583 seconds per projection as calculated above, the count rate was calculated to be roughly 3170 counts per second. For the Amptek X-123CdTe X-ray Spectrometer, the maximum count rate ranges from $1.2 \times 10^4$ to $1.2 \times 10^5$ counts per second, which is well above our estimated value. The smallest active area of this spectrometer is 9 $mm^2$, whose side length of 3 mm is larger than the parallel collimator slit width of 0.3 mm. Therefore, this

particular spectrometer is not suitable for the desired image resolution. The Medipix 3 detector array[110], containing a matrix of $256 \times 256$ detector chips with side length of 55 $\mu$m each, is an example of a suitable detector small enough for our desired image resolution. This chip has no dead time, however the energy resolution is quite poor and the detector array is quite expensive at this time. This work presents the need for detector characteristics enabling high-resolution high-sensitivity XFCT imaging of small animals.

## 5.6 Conclusions

Three lead collimator geometries have been proposed for sheet beam XFCT imaging for detecting both K-shell and L-shell fluorescent x-rays. This simulated Monte Carlo study showed that out of the three, the parallel collimator was able to detect the lowest minimum concentration of AuNP solution at 0.08% and 0.09% for K-shell and L-shell XFCT imaging, respectively, for a AuNP-loaded diameter vial of 2 mm and an imaging dose of 30 mGy. These AuNP detection limits for sheet beam XFCT approach the level of pencil beam XFCT, however the sheet beam geometry would reduce the imaging time by a factor of the number of translations in the pencil beam geometry due to the larger incident beam area. Examining the optimal collimator orientation for sheet beam XFCT imaging, when combined with other strategies to improve image quality, is important to be able to detect biologically relevant AuNP concentrations for many AuNP applications.

# Chapter 6

# Optimization of a Table-Top X-ray Fluorescence Computed Tomography System

## 6.1 Summary

The placement of a single spectrometer at high scattering angles has been shown to improve the sensitivity to K-shell fluorescent x-rays from AuNPs. This is an important result for the future design of table-top XFCT imaging systems. This Monte Carlo study proposes the use of multiple spectrometers to further improve imaging time and decrease imaging dose with an increased active area. However, further parameter optimization is required for multi-spectrometer systems which include the orientation, acquisition strategy, and the tradeoff between spectrometer crystal size and energy resolution. In addition, this study explores the effect of spectrometer orientation and AuNP depth in phantom for K-shell and L-shell fluorescent x-ray detection[59].

## 6.2 Introduction

X-ray Fluorescence Computed Tomography (XFCT) is a high-sensitivity molecular imaging modality which can image high atomic number ($Z$) materials, such as gold nanoparticles (AuNP), embedded in small animal-sized objects. This is achieved by the detection of fluorescent x-rays induced in the high-$Z$ atoms during a tomographic scan. The concept of XFCT was first demonstrated by Boisseau and Grodzins [36] before the advancement of modern detector technology. XFCT can produce better quality images than K-edge CT, for example, of objects containing high-$Z$ material solutions at clinically-relevant concentrations [52].

A persistent problem in K-shell XFCT imaging is the Compton background interfering with the fluorescence signal in the detected x-ray spectrum. Since the energy of

the Compton-scattered x-rays decreases with increasing scattering angle, the Compton background can be separated apart from the fluorescence signal by changing the spectrometer position. Detecting fluorescent x-rays at high scattering angles (or "backscattered" angles) relative to the incident pencil beam improved contrast-to-noise ratio (CNR) of K-shell XFCT images compared to isotropic fluorescent x-rays [47], however the single-detector imaging time when this concept was experimentally demonstrated was prohibitively long for small animal imaging[39].

L-shell XFCT can achieve higher CNR when imaging low concentrations of high-Z nanoparticles compared to K-shell XFCT at shallow depths due to the increased cross-section of heavy metals at lower energies [90], as well as the reduced Compton-scatter x-ray interference and better energy resolution of detection at lower energies. However, with lower energy x-rays, there is the tradeoff of increased attenuation through material. L-shell XFCT imaging of small objects has been experimentally demonstrated before using a synchrotron source [42] and a table-top XFCT system [54, 55]. To circumvent the interference of the Compton-scattered x-rays with the fluorescent x-rays in the detected x-ray spectrum during an XFCT scan, careful thought must be put into detector arrangement when imaging AuNP solutions at low concentrations.

Another persistent problem is the prolonged imaging time for pencil beam XFCT. Alternative collimator arrangements have been investigated in reducing XFCT imaging time for sheet beam XFCT [95], cone-beam XFCT [41], and full-field XFCT [51] while preserving image quality that is typical of pencil beam XFCT. In addition, the use of Compton cameras to detect fluorescent x-rays have been studied to reduce the imaging time [111], however these types of detectors are presently expensive. Pencil beam imaging thus far is often done with a single spectrometer. We propose the use of eight spectrometers which can theoretically achieve the same image quality in typical single-spectrometer scans with an eight-fold reduction in the imaging time.

We are designing a table-top XFCT system that can image AuNP solutions in small animal-sized objects using four cadmium telluride (CdTe) and four silicon drift diode (SDD) spectrometers to detect K-shell and L-shell fluorescent x-rays, respectively. While the CdTe spectrometers are appropriate for detecting K-shell fluorescent x-rays, they are also capable of detecting L-shell fluorescent x-rays at the expense of AuNP sensitivity compared to the SDD spectrometers [55]. Other design factors to account for include the area of the CdTe crystal and the scanning technique of moving or stationary spectrometers. The goal of this study is to find the optimal configuration of these spectrometers, and explore the effect of these other design factors on

the CNR of our imaging system. In addition, the vial-edge depth limit at which the image quality of L-shell XFCT is superior to K-shell XFCT will be investigated to assess when L-shell XFCT is appropriate for imaging small animal-sized objects with the system.

## 6.3 Materials and Methods

### 6.3.1 XFCT imaging

#### Phantoms

A cylindrical water phantom with AuNP mimicking a mouse was used in our Monte Carlo study[112]. The cylindrical water phantom (Figure 6.1a) was 2.5 cm in diameter and 8 cm in height containing 4 mm diameter vials with AuNP concentrations of 0.1% - 2% by weight in water. The vials were 4 mm in height, and the centres of each vial was located 6 mm from the surface of the phantom. To investigate the effect of x-ray beam attenuation on the K-shell and L-shell XFCT image quality, four more cylindrical water phantoms were modeled similarly to the phantom shown in Figure 6.1a, except the vial-edge depth was set at 0 mm, 1 mm, 2 mm, and 3 mm. The AuNP solutions were modeled as being a mixture of water and gold rather than individual nanoparticles, which should not affect the property of x-ray fluorescence crucial for image generation. The entire geometry was in air.

#### Imaging geometry

For all images, a 1 mm-thick slice of the phantom was irradiated to a mean dose of 30 mGy to water separately by a 0.5 mm Pb-filtered 120 kVp and 1 mm Al-filtered 30 kVp pencil beam (Figure 6.1b) to yield K-shell and L-shell fluorescent x-rays, respectively, by the presence of AuNPs. The pencil beam XFCT scan consisted of 50 translations in 0.5 mm steps over 2.5 cm and 180 2-degree phantom rotations. The pencil beam propagated in the $-y$ direction in the simulation geometry. The 30 mGy dose to the phantom was calculated in each simulation by scoring the total energy deposited in the water in the 1 mm-wide slice. In order to ensure full phantom coverage for vial-edge depths from 0 mm to 3 mm, the pencil beam scanned over 3.0 cm in 0.5 mm-wide steps, for a total of 60 translations. The mean dose to each phantom was also 30 mGy. Eight spectrometers were placed in the imaging plane of the phantom to collect the scattered x-rays. The CdTe spectrometer, appropriate

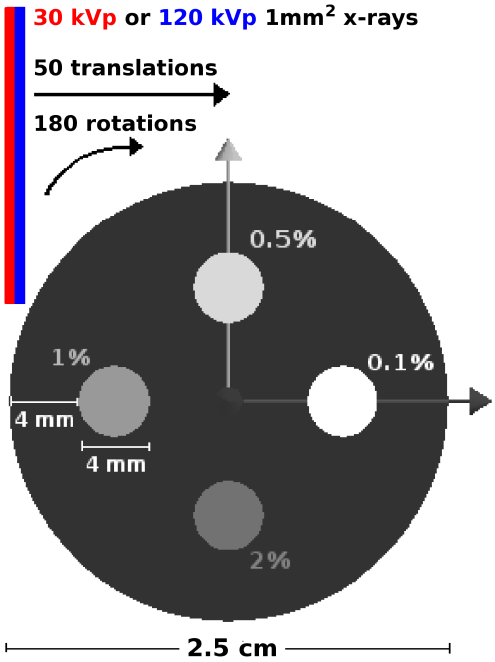


(a) Small animal phantom.

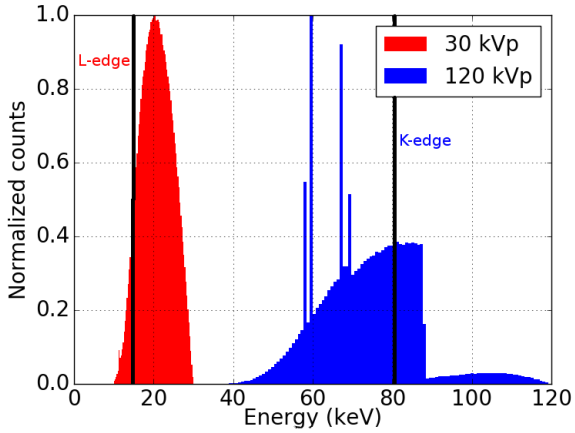


(b) Simulated primary photon beam spectra.

Figure 6.1: Geometry of water phantom containing AuNP-loaded vials with a vial-edge depth of 4 mm with varying concentrations. The simulated pencil beam spectra of 1 mm Al-filtered 30 kVp and 0.5 mm Pb-filtered 120 kVp x-rays were used to scan the phantom to generate respective L-shell and K-shell XFCT images of the AuNP distribution.

for the detection of K-shell fluorescent x-rays, was modeled as a CdTe crystal of dimensions 1 mm × 5 mm × 5 mm with a 0.2 $\mu$m-thick top layer of platinum, 1 $\mu$m-thick bottom layer of indium, and a 100 $\mu$m-thick beryllium window. The Si spectrometer, used to detect L-shell fluorescent x-rays, was modeled as a cylindrical Si crystal of cross-sectional area 25 mm$^2$ and thickness 1 mm with a 12.5 $\mu$m-thick beryllium window. The Si crystal is directly underneath a multi-layer collimator whose opening is 17 mm$^2$ in area and is made up of a stack of 100 $\mu$m tungsten, 35 $\mu$m chromium, 15 $\mu$m titanium, and 75 $\mu$m aluminum from top to bottom.

### 6.3.2 Spectrometers

The spectrometers used in this study were based on the Amptek X-123CdTe X-ray Spectrometer and X-123SDD X-ray Spectrometer with Silicon Drift Detector (Amptek Inc., Bedford, MA, USA). The CdTe spectrometer was available in two

crystal sizes: 9 mm$^2$ and 25 mm$^2$. The 9 mm$^2$ CdTe crystal was quoted to offer a superior energy resolution compared to the 25 mm$^2$ CdTe crystal at the compromise of a smaller active crystal area. We have four Si spectrometers, two 9 mm$^2$ CdTe spectrometers, and two 25 mm$^2$ CdTe spectrometers available in our lab.

### Spectrometer arrangement

Three possible arrangements were considered for orienting eight 25 mm$^2$ Si or CdTe spectrometers for XFCT imaging: isotropic, backscattered grid, and backscattered row (Figure 6.2).

In the isotropic arrangement, each crystal is placed 2.95 cm away from the phantom centre at angles of 45°, 75°, 105°, and 135° relative to the $y$ axis on either side of the phantom. These positions were chosen to place the spectrometers as close as possible to the phantom while still being able to detect x-rays with a wide range of scattering angles within the geometric constraints of the imaging geometry.

In the backscattered grid arrangement, four spectrometers were grouped into a 2×2 grid spaced 1 inch apart on either side of the phantom. The spacing was to allow enough room for the spectrometer housing, which was not modeled in the simulations. The centre of each group was placed 2.25 cm away from the phantom centre, at an angle of 120° relative to the $-y$ axis to collect x-rays that are backscattered relative to the direction of the incident pencil beam.

Alternatively in the backscattered row arrangement, four spectrometers were symmetrically arranged about the $x$ axis in a line spaced 1 inch apart on either side of the phantom. They were placed 2.25 cm away from the $z$ axis at an angle of 130° relative to the $-y$ axis. The main benefit to this arrangement would be the increased backscattered angle, however the spectrometers at the extreme ends of the phantom would be further away from the imaging plane and x-rays that reach these spectrometers would be more prone to attenuation.

For K-shell XFCT imaging, two other parameters were investigated for the CdTe spectrometer orientation. We explored the effect of swapping the eight 25 mm$^2$ CdTe crystals for the 9 mm$^2$ CdTe crystals and an alternative scanning technique where the eight 25 mm$^2$ CdTe spectrometers are stationary as opposed to translating with the phantom. These imaging geometries are shown in Figure 6.3, which assume the backscattered grid spectrometer arrangement. The aim was to explore the tradeoff of image quality should only 9 mm$^2$ CdTe spectrometers be available or if it was not

feasible to translate the spectrometers. In the scanning technique with stationary spectrometers, the centre of the spectrometer group was placed 7.25 cm away from the phantom isocentre, at an angle of 120° relative to the $-y$ axis. This distance was chosen to allow the phantom space to translate while still leveraging the benefit of the backscattered angle at all phantom positions. It should be noted, as illustrated in Figure 6.3c and 6.3d, that the naming of the scanning techniques are referring to the movement of the spectrometers relative to the pencil beam. The geometry was simulated such that the pencil beam translated while the spectrometers and phantom were held fixed in place for the moving spectrometer scanning technique, and the phantom translated while the spectrometers and pencil beam were held fixed in place for the stationary spectrometer scanning technique.

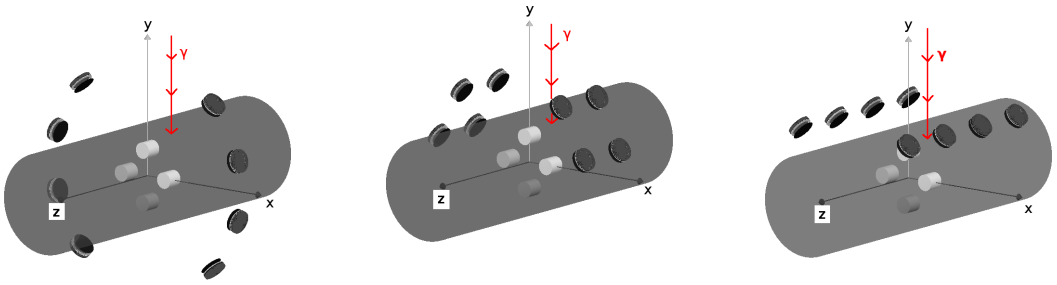


(a) Isotropic arrangement.

(b) Backscattered grid arrangement.

(c) Backscattered row arrangement.

Figure 6.2: Possible arrangements of eight 25 mm$^2$ Si spectrometers in the a) isotropic, b) backscattered grid, and c) backscattered row orientation. Eight 25 mm$^2$ CdTe spectrometers (not pictured) were also arranged similarly in these possible orientations. The primary pencil beam was incident on the phantom from the top.

For the vial edge depth study, eight 25 mm$^2$ CdTe or Si spectrometers were arranged in the backscattered grid arrangement with the moving spectrometer scanning technique for all K-shell or L-shell images, respectively.

Tables 6.1 and 6.2 summarize the parameters for each XFCT image presented in the study.

### 6.3.3 Monte Carlo simulations

#### X-ray tube simulations

The EGSnrc [71]/BEAMnrc [72] Monte Carlo (MC) code was used to simulate an x-ray tube which generated phase space files for the 120 kVp and 30 kVp beams. The

| **K-shell XFCT images** | | | |
|---|---|---|---|
| **Spectrometer type** | **Crystal size ($mm^3$)** | **Spectrometer arrangement** | **Scanning technique** |
| CdTe | 25 | Isotropic | Moving |
| CdTe | 25 | Backscattered grid | Moving |
| CdTe | 25 | Backscattered row | Moving |
| CdTe | 9 | Backscattered grid | Moving |
| CdTe | 25 | Backscattered grid | Stationary |
| **L-shell XFCT images** | | | |
| **Spectrometer type** | **Crystal size ($mm^3$)** | **Spectrometer arrangement** | **Scanning technique** |
| SDD | 25 | Isotropic | Moving |
| SDD | 25 | Backscattered grid | Moving |
| SDD | 25 | Backscattered row | Moving |

Table 6.1: Complete list of XFCT images and their parameters to investigate the optimal spectrometer orientation. The vial edge depth was 4 mm and the image size was 50×50 pixels.

| **K-shell XFCT images** | | | |
|---|---|---|---|
| **Spectrometer type** | **Crystal size ($mm^3$)** | **Spectrometer arrangement** | **Vial-edge depth (mm)** |
| CdTe | 25 | Backscattered grid | 0,1,2,3 |
| **L-shell XFCT images** | | | |
| **Spectrometer type** | **Crystal size ($mm^3$)** | **Spectrometer arrangement** | **Vial-edge depth (mm)** |
| SDD | 25 | Backscattered grid | 0,1,2,3 |

Table 6.2: Complete list of XFCT images and their parameters to investigate the effect of the vial-edge depth on CNR. The moving spectrometer scanning technique was used and the image size was 60×60 pixels.

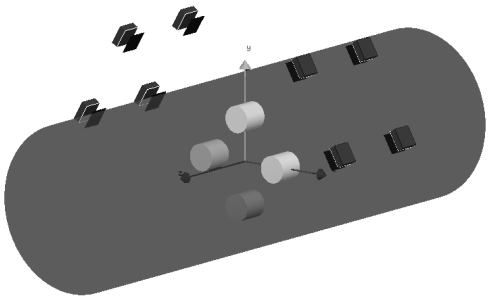

(a) 9 mm$^2$ CdTe crystal size.

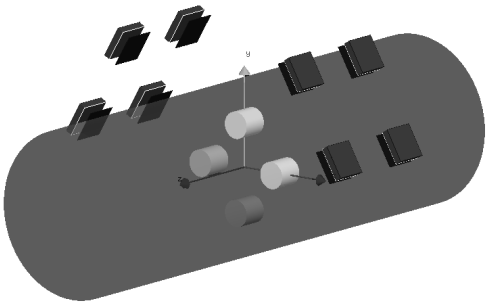

(b) 25 mm$^2$ CdTe crystal size.

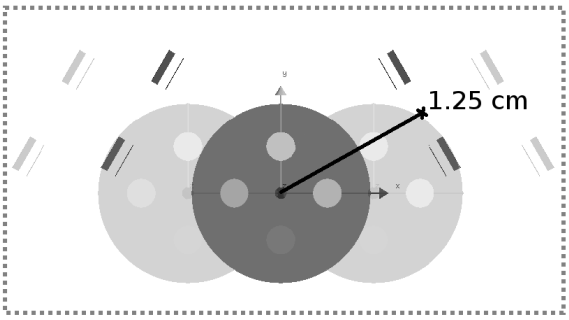


(c) Moving spectrometers.

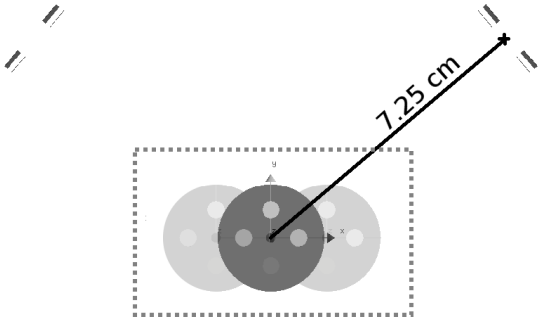


(d) Stationary spectrometers.

Figure 6.3: Eight CdTe spectrometers in the backscattered grid arrangement showing the difference in CdTe crystal size of a) 9 mm$^2$ and b) 25 mm$^2$ with the moving spectrometer scanning technique, and in scanning technique with c) moving and d) stationary 25 mm$^2$ CdTe spectrometers. Objects contained in the grey dashed box in c) and d) would rest on a translation stage. Diagrams are to scale.

x-ray tube was modeled as a tungsten anode angled at 20° with a 0.3 mm-diameter focal spot and a beryllium window of 0.8 mm thickness as part of inherent x-ray filtration. Additional filtration included 0.5 mm of lead and 1 mm of aluminum for the 120 kVp and 30 kVp x-ray beams, respectively. The x-ray beams were collimated with 5 mm of lead to form a 1 mm$^2$ square beam. The kinetic energy cutoff was set at 5 keV for electrons and photons. To save on simulation runtime, directional *bremsstrahlung* splitting with splitting number $N = 2000$ was used. The number of x-rays in the 120 kVp and 30 kVp phase space files were 1.430 $\times 10^6$ and 1.035 $\times 10^6$, respectively.

#### XFCT simulations

The TOPAS Monte Carlo code (version 3.1.p2) [69], was used to simulate x-ray fluorescence in gold solution and energy deposition in CdTe and Si. TOPAS is a wrapper for the Geant4 (version 10.3.p01) [63] simulation toolkit, which allows flexibility for a variety of energy ranges and particle types. The physics modules `"g4em-standard_opt4"`, `"g4h-phy_QGSP_BERT_HP"`, `"g4decay"`, `"g4ion-binarycascade"`, `"g4h-elastic_HP"`, `"g4h-inelastic_QBBC"`, `"g4stopping"`, and `"g4em-extra"` were selected and include the relevant photon interaction physics such as Rayleigh scattering, Compton scattering, and photoelectric effect. X-ray fluorescence, Meitner-Auger electron generation, and PIXE settings[96] were turned on, and the range cut for all particles was set to 0.005 mm. All TOPAS simulations were run on a cluster of Intel E5-2683 v4 CPUs as part of the Compute Canada network.

The total number of incident photons in the 120 kVp and 30 kVp beam for each image was set to $2.07 \times 10^{11}$ and $7.41 \times 10^{9}$, respectively. To simulate each pencil beam XFCT scan of the phantom shown in Figure 6.1a, there were a total of 180 rotations $\times$ 50 translations = 9000 simulations. For the vial-edge depth study, there were a total of 180 rotations $\times$ 60 translations = 10800 simulations.

### 6.3.4 Image reconstruction

Histograms of the energy deposited in the crystal of each spectrometer by each x-ray that impinged the crystal were recorded in 0.2 keV and 0.1 keV energy bins for K-shell and L-shell XFCT images, respectively. The histograms were generated by TOPAS and recorded in XML format as the raw data. All data was manipulated and analyzed using Python.

#### Spectrum convolution

To approximate the data the spectrometer would detect, the Monte Carlo-generated histogram of energy deposition was convolved with a Gaussian function from Equation 2.1 whose FWHM was the energy resolution of the appropriate spectrometer. As experimentally determined, the FWHM used was 200 eV, 900 eV, and 800 eV for the Si, 25 $mm^2$ CdTe, and 9 $mm^2$ CdTe spectrometers. The convoluted signal was then normalized to have the same total number of counts as the histogram.

### Stripping method

The x-ray spectrum must be corrected for the detector energy response and detection efficiency using the stripping method. The stripping method [60] is a developed algorithm that has been used in various detector studies [113, 114, 104], and is of the following form:

$$N_t(E_0) = \frac{N_d(E_0) - \sum_{E=E_0+\Delta E}^{E_{\max}} R(E_0, E) N_t(E)}{R(E_0, E_0)} \tag{2.2}$$

where $N_t(E_0)$ is the true number of photons with energy $E_0$, $N_d(E_0)$ is the number of photons detected with $E_0$, $E_{\max}$ is the maximum energy in the detected spectrum, $R(E_0, E)$ is the monoenergetic response function, and $R(E_0, E_0)$ is the full-energy absorption peak efficiency. The monoenergetic response functions were obtained using a series of TOPAS Monte Carlo simulations by scoring the energy deposition in the 25 mm$^2 \times 1$ mm Si or CdTe crystal, and 9 mm$^2 \times 1$ mm CdTe crystal from a monoenergetic beam with energy $E$ in steps of $\Delta E$ as described above for the appropriate crystal. $E$ ranged from 3.0 keV to 50.0 keV in steps of $\Delta E = 0.1$ keV for the Si crystal, while $E$ ranged from 5.0 keV to 120.0 keV in steps of $\Delta E = 0.2$ keV for both CdTe crystal sizes. The monoenergetic square beam in each simulation had a cross-sectional area that was double the size of the crystal to approximate a broad beam and consisted of 5.0 $\times 10^6$ photons. The full crystal geometry for all spectrometer types, which included the beryllium window, metallic contacts for the CdTe crystals, and multi-layer collimator for the Si crystal, were included as per manufacturer specifications and as they appeared in the XFCT simulation geometry. The full-energy absorption peak efficiency curve of each spectrometer, which was calculated from the monoenergetic response functions, is shown in Figure 6.4. The 9 mm$^2$ CdTe curve was found to be in good agreement with the curve calculated with EGSnrc/BEAMnrc [114], while the Si and 25 mm$^2$ CdTe data agreed with the curves calculated with PENELOPE code [104].

Once the x-ray spectrum is generated after convolution and stripping, the background is interpolated in the x-ray fluorescence regions on the energy spectrum, as shown in Figure 6.5. The difference in counts between the background and x-ray fluorescence for all K-shell or L-shell fluorescent x-ray energies was summed and taken to be the sinogram entry for the particular translation and rotation step for each spectrometer. Because of the energy resolution of each spectrometer, some of the

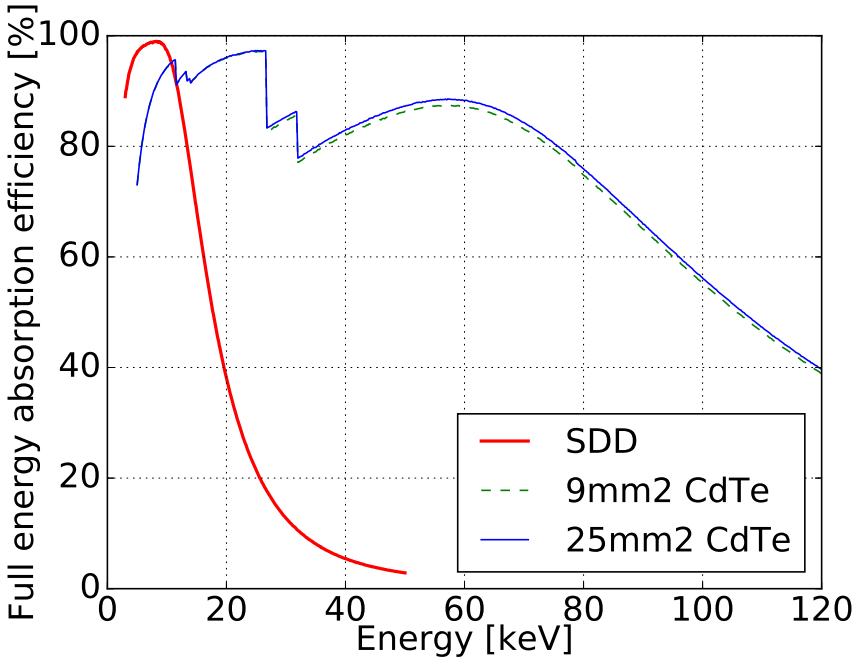


Figure 6.4: Full-energy absorption peak efficiency $R(E_0, E_0)$ for the Si, 9 mm$^2$ CdTe, and 25 mm$^2$ CdTe spectrometers.

fluorescent x-ray energies shown in Table 6.3, namely L$\beta_1$/L$\beta_2$ and K$\beta_1$/K$\beta_3$, appear as one consolidated peak.

### Reconstruction algorithm

Each XFCT image was reconstructed using the maximum-likelihood expectation maximization (MLEM) algorithm [88]. The general form of the MLEM algorithm is the following:

$$a_i^{k+1} = \frac{a_i^k}{\sum_j M_{ij}} \sum_j \left( M_{ij} \frac{p_j}{\sum_i M_{ij} a_i^k} \right) \tag{3.3}$$

where $a_i$ is the relative concentration of AuNP solution in image pixel $i$ and $M_{ij}$ is the contribution of image pixel $i$ to the projection line $j$ normalized to the case in which the projection line intersects the centre of the pixel such that $0 \leq M_{ij} \leq 1$. The sinogram entry $p_j$ represents the total counts from projection $j$, indicating the rotation angle of the projection line and the position of the incident pencil beam. The iteration number is denoted by $k$, and was chosen to be 25 iterations for K-shell XFCT

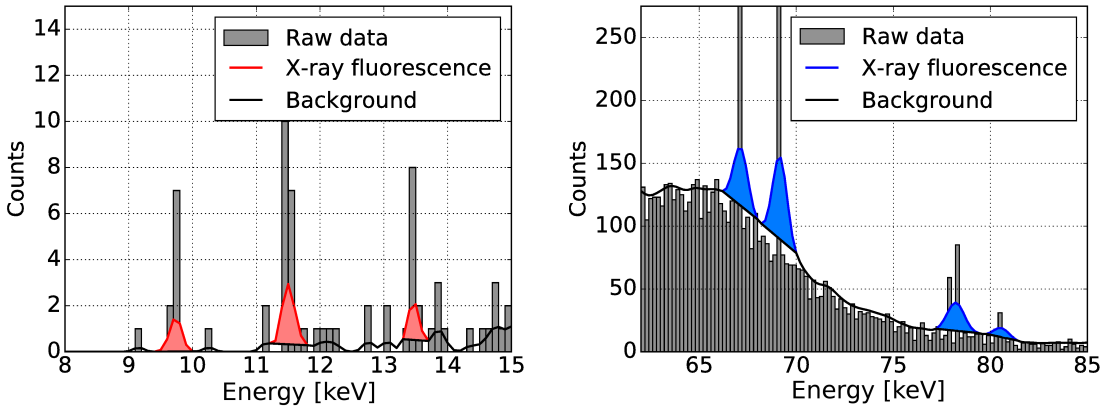


(a) L-shell fluorescent signal.

(b) K-shell fluorescent signal.

Figure 6.5: Sample detected spectra from a) 30 kVp and b) 120 kVp x-rays incident on the phantom. The Monte Carlo-generated histogram of photon counts in a) 0.1 keV bins and b) 0.2 keV bins scored the energy deposits in the Si or CdTe crystal, respectively. The x-ray fluorescence curve in each spectrum was the result of convolving the histogram with a Gaussian whose FWHM is the energy resolution of the appropriate spectrometer, normalizing, and then applying the stripping method.

images and 10 iterations for L-shell XFCT images. These numbers were optimized to reduce the image noise while ensuring signal linearity with AuNP concentration.

Due to the lower energy x-rays in L-shell XFCT imaging, primary and fluorescent photon attenuation must be accounted for in the generation of L-shell XFCT images for objects greater than 1 mm in size [90]. The primary beam attenuation correction factor $c_{ij}^{p}$ was calculated by the following:

$$c_{ij}^{p} = \exp(-\mu_p d_{ij}) \tag{3.4}$$

where $\mu_p$ is the linear attenuation coefficient of water at the average primary photon energy of 21.1 keV for 30 kVp 1 mm Al-filtered x-rays above the L-edge and $d_{ij}$ is the distance through water the primary photon beam travels to pixel $i$. The fluorescent photon attenuation correction factor $c_{ij}^{f}$ was calculated by the following:

$$c_{ij}^{f} = \sum_{f} \omega_f \exp(-\mu_f t_{ij}) \tag{3.5}$$

where $\omega_f$ and $\mu_f$ are the fluorescent yield and linear attenuation coefficient of water, respectively, for each L-shell fluorescent x-ray energy $f$ in Table 6.3 and $t_{ij}$ is the distance through water a fluorescent photon originating from pixel $i$ travels toward

| Fluorescent x-ray | Energy (keV) | Yield (%) | Fluorescent x-ray | Energy (keV) | Yield (%) |
|---|---|---|---|---|---|
| L$\alpha_1$ | 9.713 | 100 | K$\alpha_1$ | 68.80 | 100 |
| L$\alpha_2$ | 9.628 | 11 | K$\alpha_2$ | 66.99 | 59 |
| L$\beta_1$ | 11.44 | 67 | K$\beta_1$ | 77.98 | 23 |
| L$\beta_2$ | 11.58 | 23 | K$\beta_2$ | 80.15 | 8 |
| L$\gamma_1$ | 13.38 | 13 | K$\beta_3$ | 77.58 | 12 |

Table 6.3: L-shell and K-shell fluorescent x-ray energies of gold which contributed to each XFCT image and their fluorescent yield [57].

the centre of the Si crystal. All of the distances were calculated by mathematical geometry, and the linear attenuation coefficients $\mu_p$ and $\mu_f$ were assumed to be for pure water due to the low concentration of the AuNP solutions. No attenuation correction was performed for the K-shell XFCT images. For a real animal scan, the values of $\mu_p$ and $\mu_f$ can be approximated from a CT scan.

Finally, the attenuation-corrected imaging matrix $M'_{ij}$ was calculated from the original $M_{ij}$ as:

$$M'_{ij} = M_{ij} \frac{c^p_{ij}}{c^f_{ij}} \tag{3.6}$$

where $c^p_{ij}$ and $c^f_{ij}$ are defined in Equations 3.4 and 3.5 respectively.

It should be noted that $M'_{ij}$ in Equation 3.6 will differ for each spectrometer because $t_{ij}$ will change. Eight sinograms were generated per spectrometer; hence, eight images were reconstructed using each sinogram separately, then added together to generate a L-shell XFCT image. Because no attenuation correction was used for K-shell XFCT, eight sinograms from each CdTe spectrometer was summed into one sinogram, which was used to reconstruct each K-shell XFCT image. The summed XFCT image was then normalized to the known highest AuNP concentration in the phantom. The normalization factor was calculated as the mean signal of the vial containing the 2% AuNP solution.

### 6.3.5 Image quality evaluation

The CNR was the metric used to evaluate the image quality of each XFCT image, and was calculated as the following:

$$\text{CNR} = \frac{\mu_{\text{vial}} - \mu_{\text{water}}}{\sigma_{\text{water}}} \tag{3.9}$$

where $\mu_{\text{vial}}$ and $\mu_{\text{water}}$ are the mean values of the signal of a particular vial and water region, respectively, and $\sigma_{\text{water}}$ is the standard deviation of the signal from the water region. The water region was taken to be the background region of interest and was defined as a circle of diameter 6 mm in the centre of the phantom. The uncertainty in the CNR $\Delta_{\text{CNR}}$ was evaluated by replacing the whole numerator with $\sigma_{\text{vial}}$ in Equation 3.9, and is shown below in Equation 6.1.

$$\Delta_{\text{CNR}} = \frac{\sigma_{\text{vial}}}{\sigma_{\text{water}}} \tag{6.1}$$

The AuNP imaging sensitivity for each spectrometer orientation was estimated by fitting the AuNP concentration versus CNR data to a line with a forced y-intercept of 0 and interpolating the concentration value of AuNP solution corresponding to the Rose criterion of CNR = 4 [91].

## 6.4 Results

### 6.4.1 Reconstructed XFCT images

#### Spectrometer arrangement and CdTe crystal size

K-shell XFCT images for the three arrangements of eight 25 mm$^2$ CdTe spectrometers, one arrangement of eight 9 mm$^2$ CdTe spectrometers, and one arrangement of eight stationary 25 mm$^2$ CdTe spectrometers are shown in Figure 6.6. The noise in the image with the backscattered grid spectrometer arrangement in Figure 6.6b was the lowest overall. Despite the tighter energy resolution of the 9 mm$^2$ CdTe crystal size of 800 eV compared to 900 eV, the noise of the image shown in Figure 6.6d is worse due to the smaller active area. However, the noise in the image with the stationary spectrometers in Figure 6.6e was the highest overall due to the larger distance between the phantom edge and the spectrometers.

L-shell XFCT images for the three arrangements of eight 25 mm$^2$ Si spectrometers are shown in Figure 6.7. There is approximately the same amount of noise level between the three Si spectrometer arrangements, as there is not much background in the x-ray spectra interfering with the L-shell fluorescent signal.

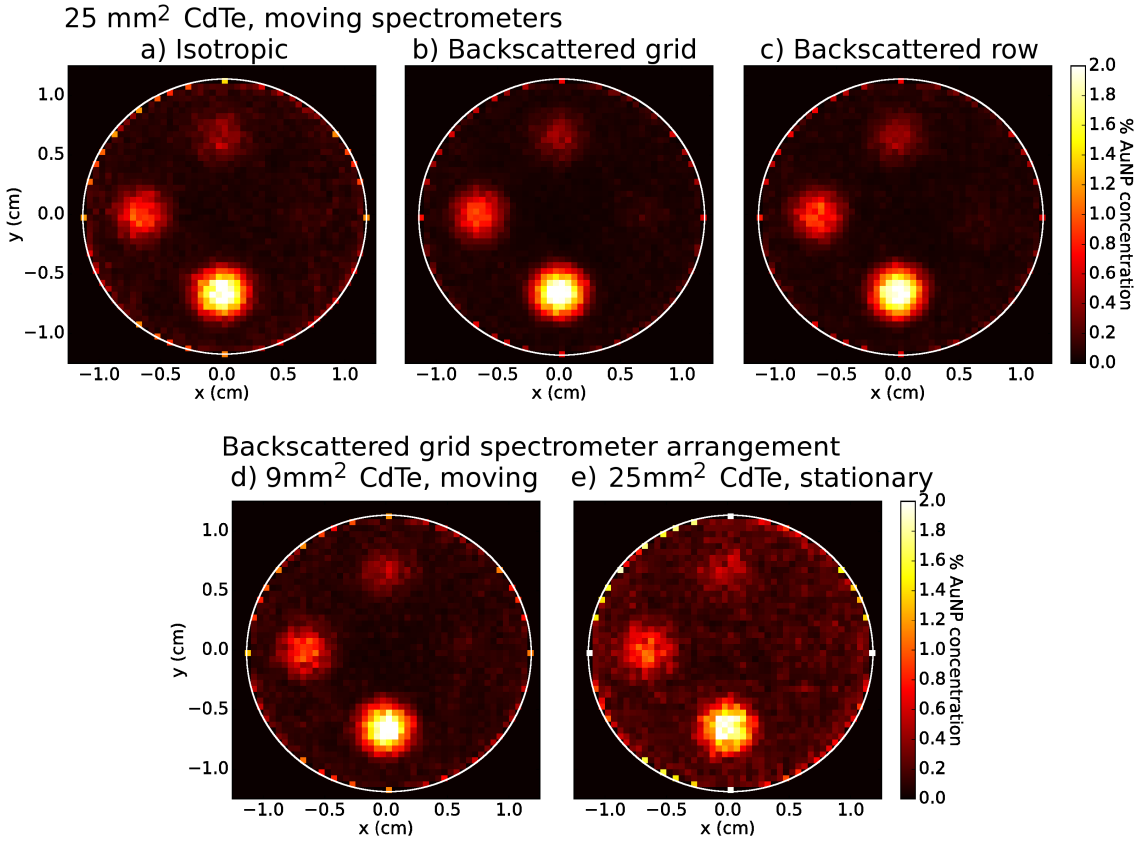


Figure 6.6: K-shell XFCT images generated using the MLEM algorithm for the 25 $mm^2$ CdTe crystal size and the moving spectrometer scanning technique in the a) isotropic, b) backscattered grid, and c) backscattered row spectrometer arrangements. In the backscattered grid spectrometer arrangement, K-shell XFCT images were generated using the MLEM algorithm for the d) 9 $mm^2$ CdTe crystal size and moving spectrometer scanning technique, and for the e) 25 $mm^2$ CdTe crystal size and stationary spectrometer scanning technique.

### AuNP vial edge depth

K-shell and L-shell XFCT images with varying vial-edge depth are shown in Figure 6.8. Among the K-shell XFCT images, the noise appears to be constant. However, among the L-shell XFCT images, the noise increases dramatically with increasing vial-edge depth. In some of the images in Figure 6.8, especially at shallow vial-edge depths, some of the vial signal appears to originate from outside the phantom. This in part can be attributed to scattered x-rays within the incident pencil beam.

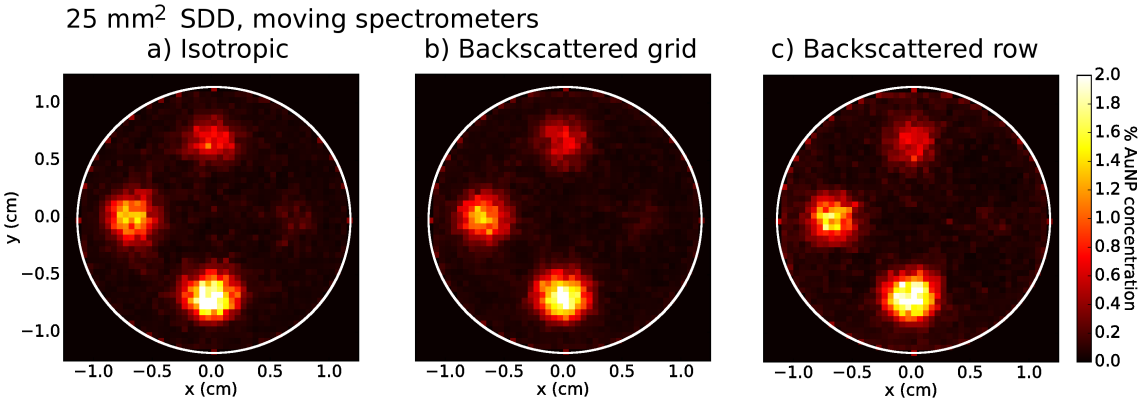


Figure 6.7: L-shell XFCT images generated using the attenuation-corrected MLEM algorithm for the 25 mm$^2$ Si crystal size and the moving spectrometer scanning technique in the a) isotropic, b) backscattered grid, and c) backscattered row spectrometer arrangements.

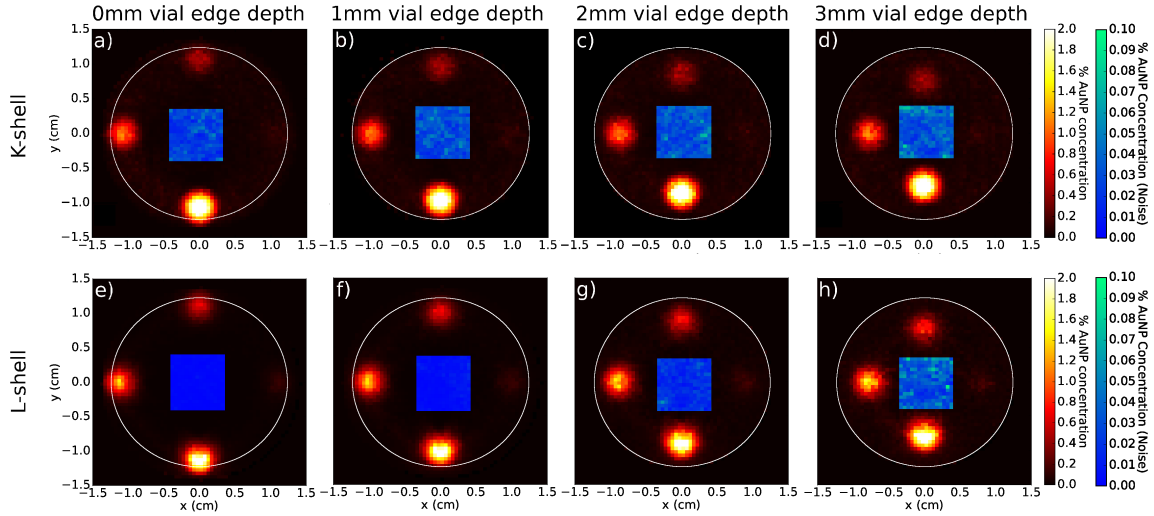


Figure 6.8: (a-d) K-shell and (e-h) attenuation-corrected L-shell XFCT images generated using MLEM for the backscattered grid spectrometer arrangement, moving spectrometer scanning technique, and the 25 mm$^2$ CdTe and Si crystal sizes, respectively. The vial edge depths were (a,e) 0 mm, (b,f) 1 mm, (c,g) 2 mm, and (d,h) 3 mm from the surface of the phantom. The inset in each XFCT image is plotted with a narrower window to better visualize image noise.

### 6.4.2 Contrast-to-noise ratio

The CNR for K-shell and L-shell XFCT images is presented in Figure 6.9. Figure 6.9a demonstrates that the CNR of the backscattered grid spectrometer arrangement was double the CNR of the isotropic spectrometer arrangement. Meanwhile, the CNR

of the backscattered row spectrometer arrangement is in the middle. Figure 6.9b demonstrates that the CNR of the 9 mm$^2$ CdTe crystal size XFCT image was lower than the CNR of the 25 mm$^2$ CdTe crystal size by a factor of 2. The difference in area between the two crystal sizes was almost a factor of 3, however the smaller energy resolution of the 9 mm$^2$ CdTe crystal size made up some of this difference. However, Figure 6.9b also shows the marked difference in the CNR between the two scanning techniques. Keeping the spectrometers as close as possible to the phantom by simultaneous translation improved the CNR by a factor of 5 for our setup. Figure 6.9c demonstrates that the CNR of the backscattered grid spectrometer arrangement improves by about half compared to the isotropic and backscattered row arrangements, which were found to be about equal in CNR.

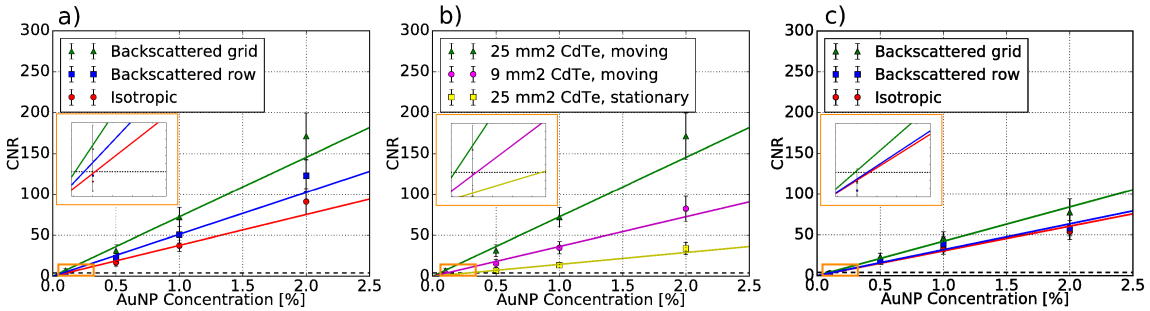


Figure 6.9: CNR vs. AuNP concentration plots comparing a) CdTe spectrometer arrangement, b) CdTe spectrometer crystal size and scanning technique, and c) Si spectrometer arrangement for the images shown in Figs. 6.6 & 6.7, respectively. The Rose criterion (CNR = 4) is shown as a dashed line. Inset: zoomed-in plot of relative AuNP sensitivity limits.

Figures 6.10a and 6.10b show the CNR as a function of vial-edge depth for the K-shell and L-shell XFCT images, respectively, when oriented with moving spectrometers in the backscattered grid arrangement. Among the K-shell XFCT images, the CNR does not change significantly with decreasing vial-edge depth. However, among the L-shell XFCT images, the CNR increases dramatically with decreasing vial-edge depth. The effect of attenuation of L-shell fluorescent x-rays is quite significant, as only 17% of the original fluorescent x-rays pass through 4 mm of water.

### 6.4.3 AuNP imaging sensitivity

The imaging sensitivity was defined to be the AuNP concentration at the Rose criterion limit. A summary of the AuNP imaging sensitivity for the K-shell XFCT images

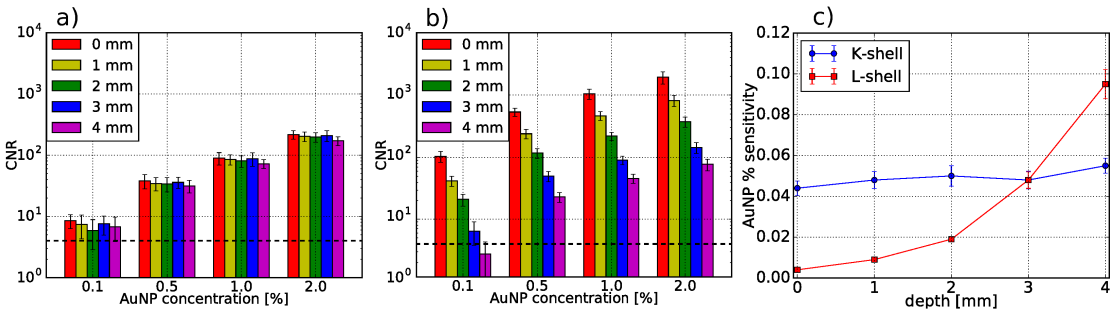


Figure 6.10: CNR vs. AuNP concentration bar plots comparing a) K-shell XFCT and b) L-shell XFCT as a function of vial-edge depth for the images shown in Fig. 6.8. The Rose criteron (CNR = 4) is shown as a dashed line. c) Vial-edge depth vs. AuNP sensitivity plot for K-shell and L-shell XFCT.

in Figure 6.6 for each CdTe spectrometer orientation is shown in Table 6.4. Among the three arrangements, eight 25 mm$^2$ CdTe spectrometers oriented in the backscattered grid arrangement detected the lowest concentration of AuNP at 0.055%, which was half the concentration of AuNP detectable for the isotropic arrangement. Reducing the CdTe crystal size to 9 mm$^2$ and using the stationary spectrometer scanning technique increased the concentration of AuNP detectable by a factor of 2 and 5, respectively.

| **K-shell XFCT imaging with CdTe spectrometers** | | | | | |
|---|---|---|---|---|---|
| **Arrangement** | Isotropic | Backscattered row | Backscattered grid | | |
| **Scanning technique** | Moving | | | | Stationary |
| **CdTe crystal size** | 25 mm$^2$ | 25 mm$^2$ | 25 mm$^2$ | 9 mm$^2$ | 25 mm$^2$ |
| **AuNP sensitivity** | 0.106% | 0.078% | **0.055%** | 0.110% | 0.275% |

Table 6.4: Summary of lowest detectable AuNP concentration for K-shell XFCT with eight CdTe spectrometers with different arrangements, scanning technique, and crystal size.

A summary of the AuNP imaging sensitivity for the L-shell XFCT images in Figure 6.7 for each Si spectrometer arrangement is shown in Table 6.5. Among the three arrangements, eight Si spectrometers oriented in the backscattered grid arrangement detected the lowest concentration of AuNP at 0.095%. This arrangement saw a modest improvement in AuNP imaging sensitivity compared to the isotropic and backscattered row arrangements at values of 0.132% and 0.126%, respectively.

| L-shell XFCT imaging with Si spectrometers | | | |
|---|---|---|---|
| **Arrangement** | Isotropic | Backscattered row | Backscattered grid |
| **Scanning technique** | Moving | | |
| **Si crystal size** | 25 $mm^2$ | | |
| **AuNP sensitivity** | 0.132% | 0.126% | **0.095%** |

Table 6.5: Summary of lowest detectable AuNP concentration for L-shell XFCT with eight Si spectrometers with different arrangements.

A plot of the AuNP imaging sensitivity as a function of vial-edge depth for both K-shell and L-shell XFCT is shown in Figure 6.10c. The detectable AuNP concentration is constant for the K-shell XFCT images but increases exponentially for the L-shell XFCT images with increasing vial-edge depth. The vial-edge depth at which the AuNP sensitivity are equal for both K-shell and L-shell XFCT in the backscattered grid spectrometer arrangement is 3.0 mm for our setup.

## 6.5 Discussion

Only incident photons whose energy was situated just above the K-edge (80.73 keV) and $L_I$-edge (14.35 keV) of gold were capable of inducing x-ray fluorescence in the gold atoms.

### 6.5.1 Simulation results

#### Spectrometer orientation and CdTe crystal size

We have showcased three arrangements of arranging eight CdTe and eight Si spectrometers and their relative effect on the AuNP imaging sensitivity for the resulting K-shell and L-shell XFCT images, respectively. These AuNP sensitivity limits calculated in this study were for imaging 4 mm-diameter objects at a 4 mm vial-edge depth with a dose of 30 mGy using the 0.5 mm Pb-filtered 120 kVp or 1 mm Al-filtered 30 kVp beam. The concentration of AuNP detectable for all images are still within the clinically relevant range from 0.001% [12] to 0.7% [10]. For both K-shell and L-shell XFCT imaging, placing the appropriate spectrometers in the backscattered grid orientation will improve the AuNP sensitivity; however the effect of attenuation and inverse square law does not offer this amount of image quality improvement in the

case of the backscattered row orientation. The Ahmad *et al.* (2014)[47] Monte Carlo study reported a AuNP imaging sensitivity of 0.002% for a 680 $\mu$m Pb-filtered 110 kVp pencil beam which scanned a phantom using backscattered K-shell fluorescent x-rays at 20 mGy dose. This imaging sensitivity is lower than our result of 0.055% mainly due to the order of magnitude difference in detection area (33% coverage for all x-rays with scattering angles greater than 110°versus 3% coverage offered by eight 25 mm$^2$ CdTe spectrometers placed 2.25 cm from the isocentre). In addition, the collection of K-shell fluorescent x-rays 1 keV windows that cross a boundary was quite idealized. Finally, the water phantom in the Ahmad *et al.* (2014)[47] study was 2.25 cm in diameter and the 5 mm-diameter vials contained much lower concentrations of AuNP (0.001% to 0.1%), which would be more forgiving of x-ray attenuation and scatter. The Ahmad *et al.* (2015) [39] experimental demonstration had an XFCT imaging limit of 0.25% AuNP in a 6.4 cm diameter water phantom. This was achieved using a single 9 mm$^2$ CdTe spectrometer placed at 145° relative to the incident 120 kVp 1 mm-Pb filtered pencil beam, which scanned this large phantom in 20 translations and 18 rotations and delivered a dose of 14 mGy. This number of translations and rotations would be a compromise in spatial resolution compared to our scanning protocol of 50 translations and 180 rotations.

The present study is the first comparison of the effect of different Si spectrometer arrangements on the CNR of the resulting L-shell XFCT images. The tabletop L-shell XFCT system as described in Bazalova-Carter *et al.* (2015) [55] consisted of a 9 mm$^2$ CdTe spectrometer and a Si spectrometer which detected x-rays at scattering angles of 120°. The SDD spectrometer could detect AuNP concentrations as low as 0.007% at a vial-edge depth of 2 mm. This is better than our quoted AuNP sensitivity of 0.019% for our L-shell XFCT image at the same vial-edge depth, however this difference can be attributed to the larger experimental dose of 400 mGy for an 18 hour scan and the lack of external beam filtration. The use of eight Si spectrometers for our tabletop system can theoretically reduce this imaging time by a factor of 8, which would in turn reduce the dose while preserving the CNR.

### Vial-edge depth study

We explored the effect of vial-edge depth on the resulting AuNP sensitivity of K-shell and L-shell XFCT images. The AuNP sensitivities of K-shell XFCT images ranged from 0.044% to 0.055% over a vial-edge depth of 0 mm to 4 mm. Meanwhile,

the AuNP sensitivities of L-shell XFCT images ranged from 0.004% to 0.095% with increasing vial depth. There was an order of magnitude difference in CNR between the K-shell and L-shell XFCT images at the shallowest vial depths, showcasing the improved sensitivity of L-shell over K-shell XFCT for imaging heavy $Z$ nanoparticles [56]. The vial-edge depth at which K-shell and L-shell XFCT have equal image quality is 3.0 mm, with a AuNP imaging sensitivity of 0.048%. Adding in the CNR data for K-shell and L-shell XFCT at vial-edge depth of 4 mm for the backscattered grid spectrometer orientation to Figure 6.10 confirmed the effect of attenuation on the AuNP sensitivity degradation.

It should be noted that attenuation correction in the image reconstruction was only applied to L-shell XFCT images. While the attenuation of K-shell fluorescent x-rays from Au is non-negligible for a small animal phantom, the transmission of a 66.99 keV $K\alpha_2$ x-ray is 61% through 2.5 cm of water. This is quite high compared to the transmission of 0.000034% of a 9.628 keV $L\alpha_2$ x-ray through 2.5 cm of water, which is why attenuation correction for L-shell fluorescence was necessary. Attenuation correction could be performed on K-shell XFCT images, however it is not expected to significantly improve the CNR.

### 6.5.2 Setup feasibility

Our results were based on Monte Carlo simulations of the proposed tabletop XFCT system, in which an effort was made to mimic realistic conditions during a scan. However, a few of the following points can be identified in which our model did not account for during data collection. The measured energy resolution of the CdTe spectrometers was 800 eV and 900 eV for the 9 mm$^2$ and 25 mm$^2$ crystal sizes, respectively. One factor that may have degraded the energy resolution was the hole tailing effect in the measured x-ray spectrum that resulted in partial Gaussians shown in Figure 2.6. The Si energy resolution of 125 eV was for an x-ray energy of 5.89 keV, and the L-shell fluorescence energies range from 9.713 keV to 13.38 keV. The energy resolution scales up with increasing x-ray energy according to manufacturer specifications, so the 200 eV energy resolution was appropriate for detecting L-shell fluorescence. No electronic noise was modeled in the simulated x-ray spectrum, and the simulation assumed no geometric error.

The XFCT images presented in this study assumed all eight spectrometers were homogeneous. In reality, our lab has four Si, two 9 mm$^2$ CdTe and two 25 mm$^2$

CdTe spectrometers. As a result of using mixed spectrometer types, the experimental AuNP sensitivities would be a factor of $\sqrt{2}$ worse that what is quoted for K-shell and L-shell XFCT. The main benefit of the moving spectrometer scanning technique is the significant improvement of the CNR compared to the stationary spectrometer scanning technique due to the minimization of distance from the phantom. However, one benefit of the stationary spectrometers is the reduction in dead time of the spectrometer. Placing the spectrometers as close as possible to the phantom may improve the signal from the fluorescent x-rays, however the maximum count rate of the spectrometer may be exceeded for high x-ray beam currents. In addition, it may not be feasible to place all eight spectrometers on a moving stage due to physical limitations of the electronics or the stage itself, which remains to be verified experimentally.

The imaging time during a pencil beam scan can potentially be quite long with a single spectrometer. Introducing eight spectrometers, as stated previously, can reduce the imaging time and dose by a factor of $\sqrt{8}$ while keeping the CNR constant. To generalize for $N$ spectrometers, the imaging time per projection and dose would be reduced by a factor of $\sqrt{N}$ for constant CNR. As calculated in our previous study[95] for a 2 cm-diameter phantom irradiated to 30 mGy, the imaging time for a 55 $\times$ 55 pencil beam XFCT image with 360 rotations was almost 6 hours. To estimate the imaging time of our setup, we considered the output of a stationary anode x-ray tube model NDI-160-22 (Varian Medical Systems, Palo Alto, CA) of 5 mA at 120 kVp and 15 mA for 30 kVp operating at 640 W. Using the fraction of x-rays in the phase space produced from the original electron histories, the total useful x-ray output coming from this source was calculated from Equation 2.4 to be $1.92 \times 10^{12}$ x-rays per second for the 120 kVp beam and $4.46 \times 10^{12}$ x-rays per second for the 30 kVp beam. For K-shell and L-shell XFCT, $2.07 \times 10^{11}$ and $7.41 \times 10^{9}$ primary x-rays in total were used to deliver 30 mGy to water, respectively, which worked out to $2.07 \times 10^{11} \div (180 \text{ rotations} \times 50 \text{ translations}) = 2.30 \times 10^{7}$ x-rays per projection for K-shell XFCT and $7.41 \times 10^{9} \div (180 \text{ rotations} \times 50 \text{ translations}) = 8.23 \times 10^{5}$ x-rays per projection for L-shell XFCT. The division of the number of x-rays per projection by the useful x-ray output for both beam energies gave $1.20 \times 10^{-5}$ and $1.84 \times 10^{-7}$ seconds per projection for K-shell and L-shell XFCT, respectively. However, these time intervals do not include an extra 0.5-second allowance per projection for data-saving and stage-moving, as mentioned in the Ahmad *et al.* (2015) study[39], and are negligible in comparison. Multiplying the time per per projection with the included 0.5-second allowance with $180 \times 50$ projections would result in an estimated imaging

time of 1.25 hours for both K-shell and L-shell XFCT. This is approaching the limit of a 1 hour scan time for small animal imaging. Reducing the number of projections is possible to reduce the imaging time, however there will be a compromise in spatial resolution which in turn would reduce the AuNP sensitivity.

The present study examines pencil beam XFCT imaging with multiple spectrometers. The advantage of this imaging geometry compared to fan beam or cone beam XFCT with 2D detector arrays is the improved spatial resolution that comes with pencil beam geometry while leveraging the benefit of reduced imaging time that comes with fan beam or cone beam geometry. In addition, the cost of the multiple spectrometers is less than a 2D detector array. The bench-top cone beam XFCT system presented in Manohar *et al.* (2018)[38] can achieve a AuNP imaging sensitivity of 0.03% for a 629 cGy dose to a 3 cm diameter PMMA phantom with a scan time of less than an hour. This is on the same order of magnitude to the achievable AuNP imaging sensitivity of our table-top XFCT system at a much higher imaging dose and slightly lower imaging time.

## 6.6 Conclusions

We have used MC to optimize the imaging system based on our available equipment. Using eight CdTe or Si spectrometers, the backscattered grid spectrometer arrangement was found to be the optimal arrangement with the lowest minimum concentration of AuNP detectable of 0.055% for K-shell XFCT and 0.095% for L-shell XFCT. The result of the vial-edge study suggests our table-top system will be able to use L-shell XFCT for imaging subcutaneous objects and K-shell XFCT for orthotopic objects.

These simulated results will guide the design for our new bench-top XFCT imaging system at the University of Victoria using the spectrometers we have available, which will enable faster imaging of high-$Z$ nanoparticles loaded in small animal-sized objects.

# Chapter 7

# Photon-Counting Computed Tomography of Lanthanide Contrast Agents with a High-Flux 330-$\mu$m Pitch Cadmium Zinc Telluride Detector on a Table-top System

## 7.1 Summary

On our table-top x-ray imaging system, we imaged multiple lanthanide contrast agents, which have been gaining recent attention in medicine, using K-edge subtraction imaging enabled by PCCT. While the use of multiple contrast agents has benefits in diagnostic medicine, a challenge with imaging multiple contrast agents is the energy resolution of the photon-counting detector. As lanthanide contrast agents are similar in atomic number and K-edge energy, this study examines the ability to resolve multiple lanthanide contrast agents using a novel form of K-edge subtraction[115].

## 7.2 Introduction

The use of energy-selective x-ray computed tomography (CT) for material analysis was proposed in the 1970s [28]. Energy-selective CT imaging is widely applied in the form of dual-energy CT (DECT) imaging, in which the effective atomic number ($Z$) of each material can be reconstructed and used for a more accurate material analysis compared to conventional x-ray CT that only offers attenuation information. DECT, like conventional CT imaging, uses energy-integrated detectors that measure photon flux. Many studies have employed DECT for the purpose of distinguishing contrast material, such as iodine, from a wide range of organs [25] and to aid in diagnoses of anomalies such as urinary stones, pulmonary embolisms, and thyroid

lesions [116, 117, 23]. Clinical DECT can be performed by either scanning with two different x-ray tube voltages to create two separate images or by scanning with a single tube voltage to create two images from energies above and below the K-edge of the material, which are then post-processed to enhance the material of interest. These two methods present a number of challenges in terms of imaging setup, scatter, and/or imaging dose. In addition, DECT is often limited to distinguishing materials with very different attenuation curves, such as bone and soft-tissue [118]. Thanks to the recent advancements in photon-counting detector development, multi-energy x-ray imaging, or photon-counting CT (PCCT), has become possible. Photon-counting detectors are based on the concept that incoming photons are counted and spectrally binned by analyzing the pulse heights generated in a semiconductor detection layer. PCCT imaging is capable of distinguishing multiple high-$Z$ materials by selecting appropriate energy bins above and below the K-edges of each material on a detector capable of energy discrimination. In DECT imaging, a similar effect is achieved by selecting appropriate x-ray beam energies on either side of a K-edge for one material [119]. The main advantage of PCCT when combined with K-edge imaging is the ability to discern high-$Z$ materials from structures such as bone, which would be difficult to resolve in a conventional energy-integrated CT image. As demonstrated in the Bazalova *et al.* (2012)[52] Monte Carlo study, gold and platinum were easily separated independently from two types of bone material with similar CT numbers in a K-edge subtracted image using a pencil beam of 110 kVp x-rays. K-edge subtracted imaging is also simpler to implement compared to basis material decomposition.

Previously, a photon-counting detector was used to image the abdominal area in humans containing iodine (I) without compromising image quality in the CT image offered by a conventional energy-integrating detector, which demonstrated the ease of translating PCCT to the clinic [120]. Further use of photon-counting detectors in PCCT imaging for large animal and human subjects[121, 122] also demonstrates this clinical translation. PCCT creates a paradigm shift in the clinical routine as it enables differentiation between two or more contrast agents in a single CT acquisition via K-edge imaging. In the case of CT colonography, for example, one contrast agent could be administered intravenously for enhancement of polyps and a second contrast agent could be administered orally for tagging of the fecal material and residual fluid in the bowel. In this example, the feasibility of using PCCT to differentiate between gadolinium (Gd) and I-based contrast material in a colon phantom was investigated by using the characteristic K-edge of Gd [123]. Imaging three contrast agents could

enable the diagnosis of inflammatory diseases, as well as monitoring drug delivery and the immune response to the drug in cancer treatment, in the same scan[124]. However, the ability of photon-counting detectors to sustain high photon fluxes cause PCCT to lag behind conventional photon-integrating x-ray CT imaging.

One goal of this study was to simultaneously image three high-$Z$ contrast agents with a novel high-flux photon-counting detector using K-edge subtraction techniques, and to explore the limitation of PCCT when imaging contrast agents that are similar in $Z$. Two of the five elements considered, namely I and Gd, are used clinically. I is a routinely used contrast agent for many clinical DECT scans to diagnose a wide range of diseases [125, 119], however its low K-edge energy of 33.2 keV makes it difficult for K-edge imaging. Gd, while typically used as a contrast agent in magnetic resonance imaging (MRI) scans, also has been shown to enhance lung and kidney vasculature in CT imaging [7], and has been used as a contrast agent for other PCCT studies [126, 127, 128, 129]. The group of elements known as the lanthanides, which include Gd, lanthanum (La), lutetium (Lu), and holmium (Ho), are being recognized as alternative contrast agents. Lanthanum carbonate, in particular, is effective as a way to lower excessive phosphate levels in kidney disease [130]. Lu has shown promise as a sensitizer for photodynamic therapy of prostate cancer [131]. Ho, while not commonly used in biological applications, may be a candidate as a high-field MRI contrast agent [132]. Elements with $Z$ between 56-73, which include the lanthanides, were demonstrated to have the best contrast enhancement for CT images using energies between 80-140 kVp[133]. PCCT experiments and simulations imaging ytterbium, hafnium, and other nearby elements such as osmium, europium, and thallium have been successful in identifying these elements [134, 135, 136]. However, as far as we know, PCCT imaging of La, Lu, and Ho have never been investigated.

PCCT imaging has been successfully used to simultaneously image Gd and I contrast agents using the Medipix silicon spectral detector [127] and a cadmium telluride (CdTe) detector array [30]. Simultaneous PCCT imaging of three contrast agents was achieved using four optimized energy bins on a MARS camera with a CdTe sensor [137, 138]. However, due to the lower absorption efficiency of silicon at higher x-ray energies compared to CdTe and cadmium zinc telluride (CdZnTe, hereon referred to as CZT), the silicon-based detector may struggle to image higher-$Z$ materials with similar detector thicknesses. CdTe detectors, compared to CZT, have a narrower bandgap which leads to a lower resistivity and higher leakage current noise [139]. The most recent PCCT prototype scanners use CZT as a sensor material for this rea-

son. Si-Mohamed *et al.* (2019)[140] used PCCT to simultaneously generate I and Gd maps *in vivo* for a tumour model in a rabbit liver. The present study used a high-flux, photon-counting CZT detector on a table-top cone beam system. We demonstrate the first simultaneous PCCT of three elements similar in $Z$ using K-edge subtraction inside a small phantom.

## 7.3 Materials and Methods

### 7.3.1 Imaging Setup and Phantom

The imaging setup consisted of an x-ray tube, a CZT detector, linear motion stages, a rotation stage, and the phantom (Figure 7.1a). The CZT detector (Redlen Technologies, Saanichton, BC Canada) consisted of two adjacent modules each 8 mm $\times$12 mm in size with a 2 mm thick, 330$\mu$m pitch high-flux sensor. The modules were oriented such that the total active area of the detector was 8 mm$\times$24 mm. The sensor was capable of operating at 250 Mcps/mm$^2$ rates without any signs of polarization [33]. The MRX-160/22 X-ray tube (Comet Technologies, Flamatt, Switzerland) and the CZT detector were mounted on the M-IMS300V and M-IMS600LM motion stages, and the phantom rested on a RVS80CC rotation stage on an optical table (Newport Corporation, Irvine, CA USA).

The 3D-printed cylindrical phantoms used in this study were 3 cm in diameter and 2.5 cm in height, and made of solid polyactic acid (PLA) of density 1.25 g/cm$^3$ (Conceptualize CAD & Print, Victoria, BC Canada). Seven holes of diameter 0.6 cm were built into the phantom to allow a snug fit for inserting 0.2 mL Flat Cap PCR tubes (Fisher Scientific, Ottawa, ON Canada). One hole was at the phantom centre and the other six were located on a 9 mm-radius circle concentric with the phantom. These tubes, hereon referred to as vials, contained various triplet combinations of contrast agents whose concentrations by weight were arranged as shown in Figure 7.1b-e to form four distinct phantoms. The phantoms containing 1% - 5% and 0.5% - 3% La, Gd, and Lu solutions are referred to as the high concentration (HC) and low concentration (LC) La-Gd-Lu phantom, respectively, and are depicted in Figures 7.1b-c. Figures 7.1d-e illustrate the phantoms containing 1% - 5% and 0.5% - 3% I, Gd, and Ho solutions and are referred to as the HC and LC I-Gd-Ho phantoms, respectively. The I solution used was iodine-based Omnipaque 300 (iohexol, GE Health-care, Princeton, NJ USA) diluted in deionized water. The La, Gd, Lu, and Ho contrast agents for the La-Gd-Lu and I-Gd-Ho phantoms were in the form

of lanthanum (III) chloride heptahydrate (>= 99.999%), gadolinium (III) chloride hexahydrate (99.999%), holmium (III) chloride hexahydrate (99.9%), and lutetium (III) chloride hexahydrate (>= 99.99%) dissolved in deionized water, respectively (Sigma-Aldrich, Oakville, ON Canada).

Each phantom was imaged using a cone beam CT geometry, with setup shown in Figure 7.1f. The x-ray beam was collimated with lead such that the beam area at the isocentre was 36.6 mm in width and 13.7 mm in height. The beam spectrum shown in Figure 7.2a was simulated using an existing Monte Carlo model of the x-ray tube [73].

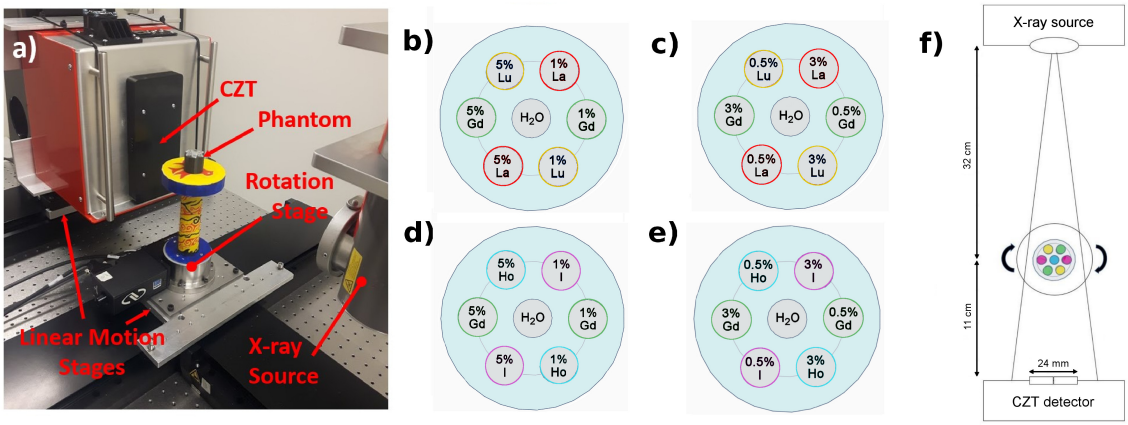


Figure 7.1: a) Lab setup for PCCT data acquisitions, with components labeled. Contrast phantom depicting layout of concentrations for b) HC and c) LC La, Gd, and Lu, and d) HC and e) LC I, Gd, and Ho in each vial. f) Schematic diagram showing the PCCT imaging setup.

### 7.3.2 Photon-counting Detector

The detector consisted of integrated readout electronics with a CZT sensor. The CZT crystal was grown using the Traveler Heat Method (Redlen Technologies, Saanichton, BC), and was chosen over CdTe due to its superior quantum efficiency. The CZT sensor had 864 individual pixels (24 × 36) with a pixel count variability of <10% and an individual pixel energy resolution of 6-9 keV. As specified by the manufacturer, the CZT detector performed a spectral sweep of $^{241}$Am to measure the energy resolution. The full width at half maximum (FWHM) of the 59.5 keV gamma ray peak of $^{241}$Am was 8.9 keV. The sensor was connected to the high-speed photon counting Application Specific Integrated Circuit (ASIC) that operated at rates up to 62.5 million counts

per second per channel with six energy bin configuration. The ASIC communicated through high-speed low-voltage differential signaling input/outputs to the external computer via a field-programmable gate array. The energy of photons incident onto the detector were sorted into six energy bins, which were adjustable in the 16-200 keV energy range. The choice of thresholds forming the six energy bins to coincide with the K-edges of the each contrast agent in each phantom enabled simultaneous, multiplexed K-edge imaging. The mass attenuation coefficients of each contrast agent, including their K-edge energy values, and the energy bin thresholds for each phantom scan are shown in Figure 7.2b-c.

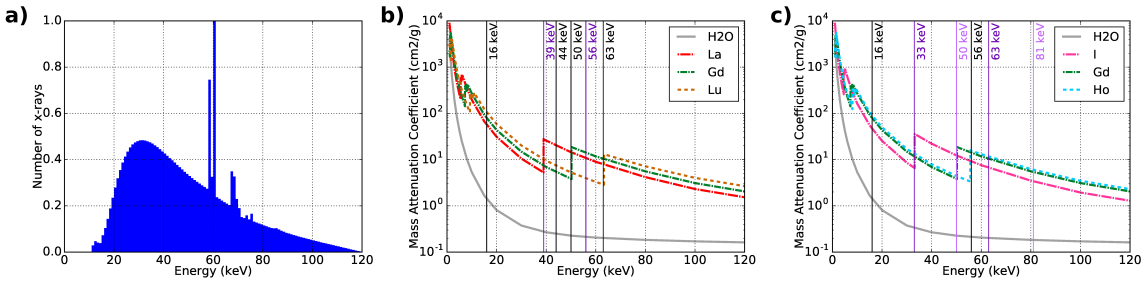


Figure 7.2: a) Spectrum of 120 kVp x-ray beam filtered with 1 mm Al and collimated by lead, which adds features including increased attenuation below the L-edges of lead and K-shell fluorescence x-rays from lead. Mass attenuation coefficients[15] of b) La, Gd, Lu and c) I, Gd, and Ho plus water shown with the thresholds of the energy bins on the CZT detector for each phantom.

### Energy Bin Settings

For the HC and LC La-Gd-Lu phantoms, the energy bins on the CZT detector were set to 16-39 keV, 39-44 keV, 44-50 keV, 50-56 keV, 56-63 keV, and 63-120 keV to accommodate for the K-edge values of La, Gd, and Lu of 38.9 keV, 50.2 keV, and 63.3 keV, respectively. The intermediate thresholds of 44 keV and 56 keV were chosen such that there were an equal amount of x-rays in each energy bin using the x-ray beam spectrum in Figure 7.2a.

For the HC and LC I-Gd-Ho phantoms, the energy bins were set to 16-33 keV, 33-50 keV, 50-56 keV, 56-63 keV, and 81-120 keV. These were chosen to accommodate the K-edge values of I, Gd, and Ho of 33.2 keV, 50.2 keV, and 55.6 keV, respectively. Table 7.1 summarizes the K-edge energies of each element in the phantoms and the detector energy thresholds used for each acquisition.

Table 7.1: Summary of K-edge energies of each element and detector energy thresholds.

| **Phantom** | La-Gd-Lu | | | I-Gd-Ho | | |
|---|---|---|---|---|---|---|
| **Element** | La | Gd | Lu | I | Gd | Ho |
| **K-edge energy (keV)** | 38.9 | 50.2 | 63.3 | 33.2 | 50.2 | 55.6 |
| **CZT energy thresholds (keV)** | 16, 39, 44, 50, 56, 63, 120 | | | 16, 33, 50, 56, 63, 81, 120 | | |

### 7.3.3 Data Acquisition

For all scans of each phantom, 180 projections were acquired over a 360° continuous rotation at a speed of 1.48 degrees per second about the isocentre. Three rotations were performed in order to image across the entire phantom body 3 cm in diameter. Because the linear motion stages allowed for sub-millimeter accuracy in motion of the detector and x-ray source, stitching of each projection produced from the three 360° rotations together was possible. The x-ray source was running at 120 kVp and 1 mA with a 1 mm focal spot and 1 mm of aluminum filtration. The detector acquired projection data over 0.25 second intervals. The acquisition time for one full rotation of the phantom was 4 minutes, so with three full rotations it took 12 minutes to image the whole phantom.

### 7.3.4 Image Reconstruction

#### PCCT Image Reconstruction

All of the projection data, including the air and dark field scans, were corrected for bad pixel response using nearest-neighbour pixel interpolation [138]. Detector counts in each energy bin were converted into projections $p$ similar to Equation 3.1 but in the following manner:

$$p = -\ln((N - N_{dark})/(N_0 - N_{dark})) \tag{7.1}$$

where $N$ is the detector signal with the phantom, $N_0$ is the detector signal without the phantom, and $N_{dark}$ is the detector signal with no beam. For the different energy bins, the projection data from each detector translation were stitched together to generate projections of the entire phantom. All images underwent ring-artifact corrections using the wavelet-FFT method [141], which used a DB42 wavelet with a third level decomposition and a damping coefficient of 1.2. The CT images were then

reconstructed using the Feldkamp-Davis-Kress (FDK) algorithm[86] with a Hamming filter. The resulting CT images at each energy bin were 129 × 129 pixels in size, and the reconstructed cubic voxel size was 250 $\mu$m. MATLAB (The Mathworks, Natick, MA) was used for data processing and image reconstruction, while Python was used for data analysis.

### K-edge Images

In general, a K-edge image for a given contrast agent can be reconstructed by subtracting the CT image of the energy bin directly above the K-edge from the CT image directly below the K-edge. In this study, the K-edge images were reconstructed using a weighted sum of all energy binned CT images in the following manner:

$$y_X = \sum_{i=1}^{6} w_{Xi}\, a_i \tag{7.2}$$

where $y_X$ is the K-edge image of contrast agent $X$, $a_i$ is the CT image at bin $i$, and $w_{Xi}$ is the weight given to bin $i$. The weight $w_{Xi}$ is a number that is constrained between -1 and 1. The known concentrations of the HC phantoms were used to find the weights using a minimization algorithm, and then applied to the LC phantoms. In this algorithm, the `COBYLA` method[142] was used with an error tolerance of $1 \times 10^{-8}$, bounds of -1 and 1, and 100 maximum iterations to find the weights $w_{Xi}$ that would give the minimum value of $|y_X - u_X|$. The initial guess of weights to initiate the optimization were set manually to obtain the best images. Once the weights were found for the K-edge images of the contrast agents in the HC phantoms, the same weights were applied in Equation 7.2 to form the K-edge images of the contrast agents in the LC phantoms. This was done to validate the weights on an independent phantom scan. All K-edge images were scaled to the 5% contrast in the respective HC phantom, and a single slice for each K-edge image was selected for presentation. Negative values arising from Equation 7.2 subtraction in the zero-contrast vials were set to 0. The minimization algorithm was available in the SciPy Optimize package[93].

### Signal Linearity

The linearity of the contrast agent signal from each vial was assessed by comparing the reconstructed concentrations in each K-edge image to the actual concentration. Error bars for the reconstructed concentration were calculated to be the standard

deviation of the pixels in the ROI. The difference of concentration for each vial was found by subtracting the actual concentration from the reconstructed concentration. The signal and error of 0% contrast was calculated as the average and standard deviation, respectively, of all peripheral zero-contrast vials in both the HC and LC K-edge images. Each data set was fit to a linear function with the y-intercept fixed at zero, and an $R^2$ value using Equation 3.11 was found to assess the goodness of fit. The slope and its associated error of the linear function was found with a curve fit algorithm available in the SciPy Optimize package[93].

#### Root Mean Square Error

We used the root mean square error (RMSE) to quantify the quality of the contrast agent separation. The RMSE in each K-edge image was evaluated for a region of interest (ROI) containing $n$ pixels by the following:

$$RMSE = \sqrt{\frac{\sum_{j=1}^{n}(\hat{y}_j - y_j)^2}{n}} \tag{7.3}$$

where $\hat{y}_j$ and $y_j$ are the expected and measured values, respectively, in pixel $j$ of a K-edge image. Each ROI was centred on a 6 mm-diameter vial and was defined as a 4 mm-diameter circle. The expected value in the non-zero contrast vials should be equal to the concentration of the contrast agent. The expected value in each of the zero-contrast ROIs should be 0, and a high RMSE value should indicate a large amount of cross contamination from these vials. The calculated RMSE for the ROI over the middle water vial was omitted due to ring artifacts that were found to obscure the signal.

### 7.3.5 Dose Estimation

To estimate the dose of the PCCT scan, a 3 cm-diameter circle was cut out of a sheet of Gafchromic® EBT3 film (Ashland Advanced Materials, Bridgewater, NJ) and irradiated at isocentre between two 3 cm-diameter cylindrical phantoms with water vials using the same imaging setup. The calibration curve was generated using ten films irradiated to doses between 0.2 Gy and 8 Gy according to the procedure outlined in Breitkreutz et al. (2020) [73] using an x-ray tube voltage of 120 kVp with 1 mm Al filtration. Irradiated films were scanned 24 hours after exposure with an EPSON® 10000XL flatbed scanner (Epson America, Long Beach, CA) at a resolution

of 200 dots per inch, and FilmQA pro® (Ashland Advanced Materials, Bridgewater, NJ) was used to analyze the films using triple-channel dosimetry. The phantom dose was estimated by calculating the optical density in a 2 cm × 2 cm region in the middle of the film. The imaging dose was calculated from the proportion of the actual beam-on time for a 0.25 s acquisition.

## 7.4 Results

### 7.4.1 K-edge Images

Figure 7.3 shows the results of the K-edge subtraction technique for La, Gd, and Lu, respectively for the HC and LC phantoms. Figure 7.4 shows the results of the K-edge subtraction technique for I, Gd, and Ho, respectively. The weights $w_i$ from Equation 7.2 used for K-edge reconstruction of the La-Gd-Lu and I-Gd-Ho phantoms are shown in Table 7.2 and 7.3, respectively. Both La and Lu, each having a difference in $Z$ of 7 from Gd, stood out from Gd in the K-edge images. There was good contrast agent discrimination for all vials in each K-edge image of the LC and HC phantoms except the 0.5% vial was difficult to resolve for Lu. There was some false signal in the middle of the Lu image due to ring artifacts in the CT images and the narrow energy bins set by the detector. The I K-edge images in Figure 7.4a,d had excellent contrast agent discrimination. As shown in Figure 7.4b,e for Gd and Figure 7.4c,f for Ho, these contrasts with a difference in $Z$ of 3 were discriminated from each other. Some false signal was evident in and around the middle water vial in these Ho and Gd K-edge images, likely due to ring artifacts that were present in the CT images.

Table 7.2: Weights of energy-binned CT images to form La-Gd-Lu phantom K-edge images.

| Contrast Agent | $w_1$ | $w_2$ | $w_3$ | $w_4$ | $w_5$ | $w_6$ |
|---|---|---|---|---|---|---|
| La | -0.740 | 0.933 | 0.005 | 0.081 | -0.016 | -0.125 |
| Gd | 0.011 | 0.012 | -0.975 | 0.980 | -0.005 | 0.034 |
| Lu | -0.030 | -0.029 | 0.031 | 0.098 | -1.105 | 0.967 |

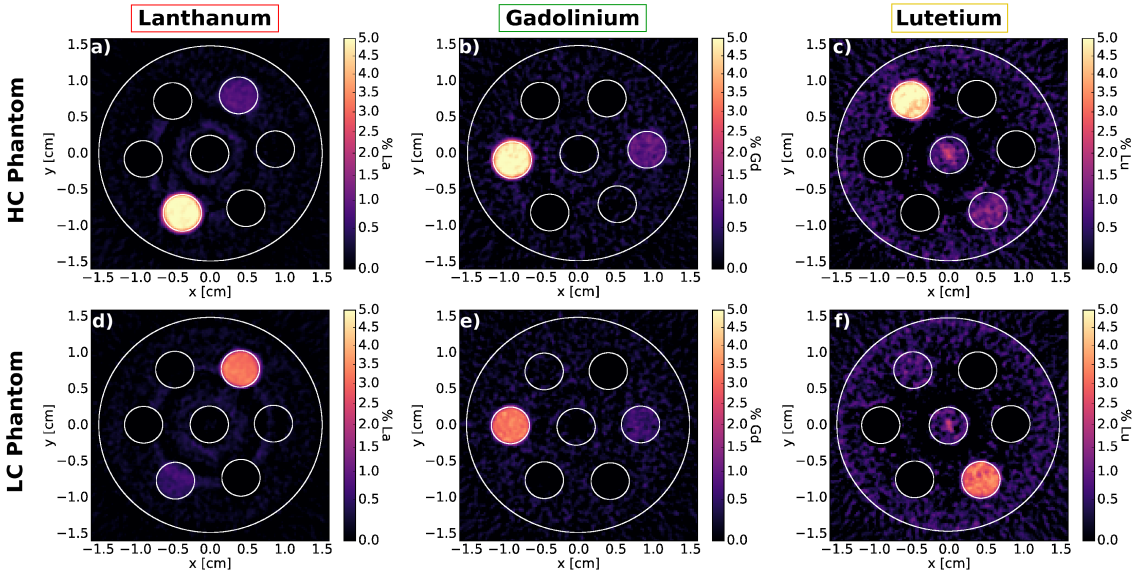


Figure 7.3: K-edge images of the high and low concentration La-Gd-Lu phantoms showing a,d) La, b,e) Gd, and c,f) Lu contrast.

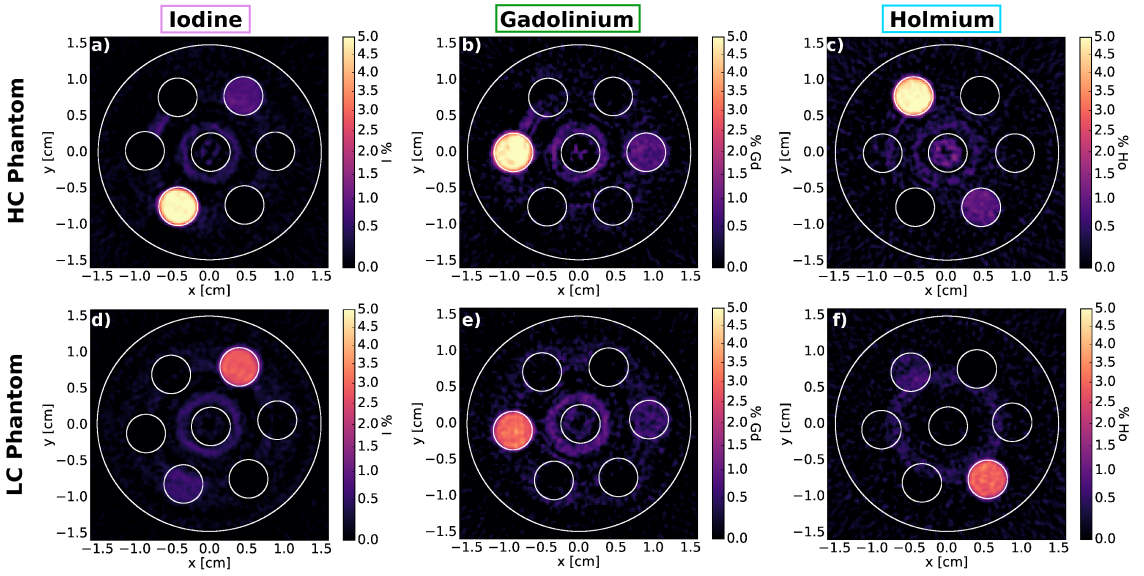


Figure 7.4: K-edge images of the high and low concentration I-Gd-Ho phantoms showing a,d) I, b,e) Gd, and c,f) Ho contrast.

Table 7.3: Weights of binned CT images to form I-Gd-Ho phantom K-edge images.

| Contrast Agent | $w_1$ | $w_2$ | $w_3$ | $w_4$ | $w_5$ | $w_6$ |
|---|---|---|---|---|---|---|
| I | -0.753 | 0.984 | -0.034 | 0.088 | -0.129 | 0.002 |
| Gd | -0.723 | -0.011 | 0.949 | -0.019 | 0.039 | 0.024 |
| Ho | 0.006 | 0.058 | -0.956 | 0.956 | 0.007 | -0.013 |

### 7.4.2 Evaluation of K-edge images

#### Reconstructed Concentration

The reconstructed versus actual concentration of each contrast agent is plotted in Figure 7.5a-b for the La-Gd-Lu and I-Gd-Ho phantoms, respectively. The slopes of each data set were 1.009, 1.019, and 1.017 for La, Gd, and Lu and 0.972, 0.995, and 0.986 for I, Gd, and Ho, respectively. The $R^2$ values were 0.996, 0.997, and 0.999 for La, Gd, and Lu and 0.996, 0.997, and 0.997 for I, Gd, and Ho, respectively. The difference between the reconstructed and actual concentration in both La-Gd-Lu and I-Gd-Ho phantoms did not exceed 0.25% for all vials.

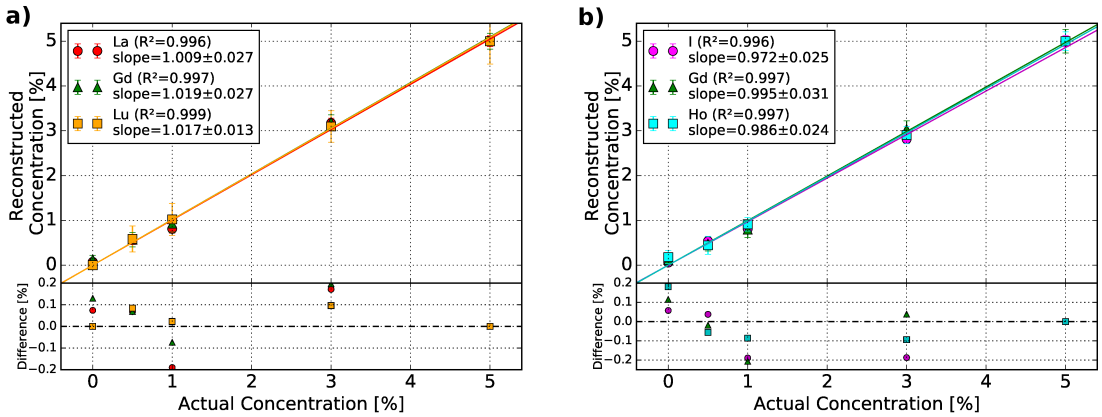


Figure 7.5: Reconstructed vs. actual concentration of each contrast agent in the a) La-Gd-Lu and b) I-Gd-Ho phantoms. The slope and the $R^2$ value of the fitted data is shown in the legend. The subplot shows the difference between the reconstructed and actual concentration.

#### Root Mean Square Error

A summary of RMSE values of all vials for each K-edge image (Figures 7.3 and 7.4) is shown in Table 7.4 and 7.5 for the La-Gd-Lu and I-Gd-Ho phantoms, respectively.

Table 7.4: RMSE of each vial in all K-edge images of the La-Gd-Lu phantom. The RMSE of each vial of contrast agent in its corresponding K-edge image is shown in bold, unbolded values are from zero-contrast vials.

| | Contrast | RMSE of vial signal (%) | | | |
|---|---|---|---|---|---|
| Concentration | | 0.5% | 1% | 3% | 5% |
| La K-edge image | **La** | **0.13** | **0.21** | **0.20** | **0.12** |
| | Gd | 0.08 | 0.02 | 0.00 | 0.00 |
| | Lu | 0.01 | 0.00 | 0.00 | 0.00 |
| Gd K-edge image | La | 0.01 | 0.00 | 0.00 | 0.00 |
| | **Gd** | **0.17** | **0.20** | **0.25** | **0.18** |
| | Lu | 0.12 | 0.10 | 0.00 | 0.00 |
| Lu K-edge image | La | 0.00 | 0.00 | 0.00 | 0.00 |
| | Gd | 0.00 | 0.00 | 0.00 | 0.00 |
| | **Lu** | **0.29** | **0.36** | **0.36** | **0.51** |

Table 7.5: RMSE of each vial in all K-edge images of the I-Gd-Ho phantom. The RMSE of each vial of contrast agent in its corresponding K-edge image is shown in bold, unbolded values are from zero-contrast vials.

| | Contrast | RMSE of vial signal (%) | | | |
|---|---|---|---|---|---|
| Concentration | | 0.5% | 1% | 3% | 5% |
| I K-edge image | **I** | **0.11** | **0.21** | **0.21** | **0.12** |
| | Gd | 0.04 | 0.03 | 0.00 | 0.00 |
| | Ho | 0.04 | 0.00 | 0.00 | 0.00 |
| Gd K-edge image | I | 0.06 | 0.05 | 0.03 | 0.03 |
| | **Gd** | **0.17** | **0.27** | **0.19** | **0.26** |
| | Ho | 0.06 | 0.05 | 0.04 | 0.15 |
| Ho K-edge image | I | 0.10 | 0.04 | 0.00 | 0.00 |
| | Gd | 0.12 | 0.10 | 0.18 | 0.27 |
| | **Ho** | **0.21** | **0.17** | **0.21** | **0.21** |

In the case of the 0.5% and 1% vials in the La-Gd-Lu phantoms the RMSE values were 0.13% and 0.21% for La, 0.17% and 0.20% for Gd, and 0.29% and 0.36% for the Lu K-edge images. For the 0.5% and 1% vials in the I-Gd-Ho phantoms the RMSE values were 0.11% and 0.21% for I, 0.17% and 0.27% for Gd, and 0.21% and 0.17% for the Ho K-edge images.

The RMSE values of the zero-contrast vials are also summarized in Tables 7.4 and 7.5. For the La-Gd-Lu phantom, the highest RMSE values for the La K-edge image from Gd and Lu vials were 0.02% and 0.00% for the HC phantom and 0.08% and 0.01% for the LC phantom, respectively. The highest RMSE values for the Gd K-edge image from La and Lu vials were 0.00% and 0.10% for the HC phantom and

0.01% and 0.12% for the LC phantom, respectively. The RMSE values for the Lu K-edge image from La and Gd vials were all 0.00% for both the HC and LC phantoms. For the I-Gd-Ho phantom, the highest RMSE values for the I K-edge image from Gd and Ho were 0.03% and 0.0% for the HC phantom and 0.04% and 0.04% for the LC phantom, respectively. The highest RMSE values for the Gd K-edge image from I and Ho vials were 0.05% and 0.15% for the HC phantom and 0.06% and 0.06% for the LC phantom, respectively. The RMSE values for the Ho K-edge image from I vials were 0.04% for the HC phantom and 0.10% for the LC phantom, respectively. The maximum RMSE value of all zero-contrast vials was 0.27% for the Ho K-edge image from the 5% Gd vial, and was 0.18% from the 3% Gd vial.

## 7.5 Discussion

We have demonstrated simultaneous K-edge imaging of high-$Z$ contrast agent triplets, five in total, of varying concentration among four 3D-printed small animal phantoms using a CZT photon-counting detector. For the 3% and 5% concentrations, all contrast agents were detectable in the K-edge images. The signal of the 0.5% vials were reconstructed to within their associated error bars as evident in Figure 7.5 for all contrast agents studied, albeit difficult to detect by eye in their K-edge images. In the energy-binned CT images, there were not only ring artifacts due to pixel instability, but also other streaking artifacts due to the multiple detector position data stitching. These artifacts then propagate from the binned CT images to the K-edge images in Figures 7.3 and 7.4 and decrease image quality. The streaking artifacts were likely caused by the data acquisition timing between multiple detector positions, rather than the precision of the detector positions. Human error was introduced when attempting to start the data acquisition at the exact same time between detector translations, and further timing error by computer lag may have caused variance in the data saving time per acquisition. Since three translations were used to cover the extent of the phantom, a larger active area of the CZT detector that fully covers the data set would reduce both the streaking artifacts and the total acquisition time by a factor of three to 4.5 minutes. A larger active area would also remove the need for timing accuracy of the data acquisition.

The CZT detector, given the 120 kVp spectrum and the set energy bins, was able to discriminate three contrast agents in the La-Gd-Lu phantom with K-edges 11 keV apart. In addition, there was minimal cross-contamination in the peripheral

vials in the K-edge images presented in Figure 7.3. The CZT detector was able to discriminate three contrast agents in the I-Gd-Ho phantom, two of which had a difference in K-edges of 5.4 keV. The false signal present in the Gd and Ho K-edge images in Figure 7.4 was likely caused by the energy resolution of the detector (6-9 keV) considering the difference in K-edge energy between Gd and Ho of 5.4 keV. Since the FWHM of the 59.5 keV $^{241}$Am gamma ray peak was equal to 8.9 keV, two K-edges a minimum of half the FWHM apart (4.5 keV) near this gamma ray peak energy could be considered as partially resolved in the reconstructed K-edge images. The choice of 1 mm Al beam filtration, while soft for many preclinical systems, was chosen in this study as thicker beam filtration generally leads to noisier K-edge images of lanthanide contrast agents[143].

### 7.5.1 Signal Linearity

For most of the vials, Figure 7.5 demonstrates that the signal in each K-edge image is proportional to the concentration. The $R^2$ values for each data set were above 0.99, suggesting good linearity. This is also supported by the slopes of each linear fit being equal to one within error, except in the cases of Lu and I based on the slope error. The signal in the Lu vials in Figure 7.3c,f especially was degraded by the ring artifacts, which may affect the signal linearity.

The signal in each of the 0.5% and 1% vials were more susceptible to degradation by the ring artifacts in the K-edge images. The values of the RMSE in these non-zero contrast vials varied by no more than a factor of 2 compared to the 3% and 5% vials, however relative to the actual concentration the RMSE values are drastically higher for lower concentration vials. This suggests the ring artifacts prevent our CZT detector from reconstructing biologically relevant concentrations of contrast agents of $< 0.1\%$[144, 140] unless a more appropriate ring-artifact correction algorithm was devised. It is evident that the peripheral ring artifacts interfere with the Lu (Figure 7.3c,f) vials in their respective K-edge images, as the RMSE values are up to four times higher than the RMSE values of the lower-$Z$ contrast agents with similar concentration. The ring artifacts disrupting the Lu vials in the Lu K-edge images were likely inflating those RMSE values compared to the other contrast agents in the La-Gd-Lu phantom. The same effect was apparent in the Gd vials in the Gd K-edge image of the HC I-Gd-Ho phantom (Figure 7.4c).

### 7.5.2 Cross-contamination

As summarized in Table 7.4, the RMSE of the zero-contrast vials was found to be low ($< 0.12\%$) for the La and Lu K-edge images, in particular. All zero-contrast RMSE values for the Lu K-edge images were 0.00%; this is because in the peripheral zero-contrast ROIs, all values were negative, meaning no Lu signal was present in the La or Gd vials. The same is true in the case of all 3% and 5% zero-contrast vials in the La and Gd K-edge images, respectively. The negative pixel values in each zero-contrast ROI were set to 0.

As summarized in Table 7.5, the RMSE values of the 3% and 5% Gd and Ho vials in the I K-edge image were all 0, as described above. The abnormally-high RMSE of 0.18% and 0.27% in the 3% and 5% Gd vials, respectively, in the HC Ho K-edge image (Figure 7.4c) suggests the effect of the ring artifacts increasing the signal in the Ho vials. This effect is more apparent for higher concentration Gd vials, as evidenced by the lower RMSE values of 0.12% and 0.10% from the 0.5% and 1% Gd vials in the Ho K-edge images. Additionally, the next highest RMSE value of 0.15% was from the 5% Ho vial in the HC Gd K-edge image. These high RMSE values of Gd and Ho vials in each other's K-edge images may also be due to the close difference in K-edge energies between Gd and Ho (5.4 keV), compared to the energy response of the CZT detector (6-9 keV). Charge sharing from multiple pixel readout has been shown to account for a degradation in energy resolution[145]. For the high-flux detector used in this study under typical operating condition (high voltage of 1000 V), we have calculated based on the previous characterization work[146, 147] that about 40% of photons undergo charge-sharing events that lead to spectral distortion. Fortunately, the detector has built-in anti-charge sharing capability[148, 149] that rejects those events and only single count events were analyzed in this study. In this mode of operation, most of the photons that undergo the charge-sharing effect were rejected.

Ring artifacts were especially concentrated in the middle of the HC and LC Lu K-edge images (Figure 7.3c,f) and the HC Ho K-edge image (Figure 7.4c). This was the reason for excluding the middle water vial in the RMSE calculations, as no meaningful analysis would be possible.

The weighted summation of the CT images of different energy bins to reconstruct each K-edge image utilized the entire PCCT data. Basis material decomposition, as demonstrated in many other PCCT studies using preclinical scanners[150, 137, 140, 135, 138], also uses the entire PCCT data. This method may alleviate some cross-

contamination between contrast agents and thus decrease the RMSE of each vial. However, one benefit of K-edge imaging as opposed to basis material composition is that the mass attenuation coefficient is very similar between contrast agents with similar $Z$, except for the discontinuity at the K-edge energy. The energy threshold windows on photon-counting detectors can be set arbitrarily on either side of the K-edge to hone in on the difference of attenuation to maximize the signal. However, beam hardening is an issue for clinical translation that cannot be ignored when imaging human-sized objects. The choice of energy bin thresholds in this study could be better optimized by taking into account beam hardening. In addition, a follow-up study has found that for our current table-top PCCT imaging setup, the optimal energy bin thresholds should be $\pm$10 keV from the K-edge energy of Gd to maximize K-edge contrast-to-noise ratio when imaging only Gd contrast[143]. The present study used energy thresholds that were at least 6 keV apart to form Gd K-edge images since multiple contrast agents were imaged and therefore the threshold choice was limited. For the above reasons, this work should be considered as preliminary.

### 7.5.3 Comparison with Previous PCCT Studies

The prototype CT imaging system from the Schlomka *et al.* (2008) [30] study demonstrated the feasibility of PCCT imaging for I and Gd contrast agents between 0.4% and 2% concentration by weight embedded in calcium. This is a similar but lower range in concentration than our 0.5% - 3% solutions, however some difficulty in separating the two contrast agents at low concentration was apparent in the Schlomka *et al.* (2008) study. Their imaging system used a linear CdTe detector array of pixel pitch 0.4 mm and pixel size of approximately 250 $\mu$m. For a current exposure of 11.3 mAs they could not accurately reconstruct 0.3% I and 0.4% Gd. This is compared to the low RMSE (0.11%) of our reconstructed 0.5% I vial in the I-Gd-Ho phantom and higher RMSE (0.17% and 0.17%) of the 0.5% Gd vials in the La-Gd-Lu and I-Gd-Ho phantoms, respectively. These particular vials were accurately reconstructed according to Figure 7.5, with an absolute difference of less than 0.1%. The difference in the reconstruction accuracy of these contrast agents can be attributed to the larger 8 cm diameter phantom containing slightly larger diameter contrast agent inserts of 8 mm and the difference in imaging setup as outlined above.

The PCCT imaging system from the Si-Mohamed *et al.* (2018)[128] study used a high-powered unfiltered 120 kVp x-ray source which could reconstruct I and Gd

concentrations with a slope of 1.04 and 0.98 for a linear fit with an $R^2$ of 0.99 and 0.98, respectively, using a 400 $\mu$m $\times$ 400 $\mu$m $\times$ 250 $\mu$m voxel grid. In addition, the RMSE value of their Gd-only image from I vials was 0.33%. This is to compare with our Gd $R^2$ value of 0.997 and slope values of 1.019 and 0.995 for both the La-Gd-Lu and I-Gd-Ho phantoms, and our I $R^2$ value of 0.996 and slope of 0.972 with a smaller reconstructed cubic voxel size of 250 $\mu$m. Our RMSE of the Gd K-edge image from I vials only ranged between 0.03% and 0.06%, meaning our Gd K-edge images suffered from less cross-contamination from I vials than in Si-Mohamed *et al.* (2018). Aside from the larger phantom size with a quoted CT dose index of 0.74 mGy and larger vial size, the energy thresholds on the prototype photon-counting detector used in the Si-Mohamed *et al.* (2018) study were optimized for each of the separate scans of each contrast agent and differed from the energy thresholds used in our experiment.

The Panta *et al.* (2018) [137] study used material basis decomposition to image I, Gd, and gold simultaneously using a preclinical CdTe-Medipix3RX photon-counting detector with a pixel pitch of 110 $\mu$m and four optimized energy bins. Their x-ray exposure was 118 kVp, 27 $\mu$A, and 0.12 seconds per projection. Using an ordered-subset expectation maximization (OSEM) iterative image reconstruction and basis material decomposition to reconstruct images with a cubic voxel size of 180 $\mu$m, they were able to identify 0.2% Gd solutions and 0.9% I solutions by weight in the K-edge images. According to Figure 7.5, our imaging system underestimated the concentration of the 1% I with a difference of 0.2%, however the 0.5% Gd vials in the LC La-Gd-Lu and I-Gd-Ho phantoms were reconstructed accurately with differences of less than 0.1%. These results suggest that our imaging system is consistent with Panta *et al.* (2018) when imaging similar concentrations of Gd. The difference in the number of energy bins, the detector type, and the reconstructed voxel size may account for some differences in the image quality between our study and Panta *et al.* (2018).

To our knowledge, La, Lu, and Ho contrast agents have not been imaged previously using PCCT. Ytterbium and hafnium are similar novel contrast agents also belonging to the lanthanide group and have been imaged with PCCT. The Pan *et al.* (2012)[134] study uses PCCT to image ytterbium ($Z$ = 70, K-edge energy = 61.3 keV) nanoparticulates *in vivo* with a 130 kVp x-ray beam operating at 50 $\mu$A in 72 seconds. With their CZT detector using six energy thresholds on the preclinical imaging system, Pan *et al.* (2012) was able to reconstruct a single slice image of ytterbium nanoparticulates using basis material decomposition at a concentration of 0.01% by

weight. This same concentration was injected into a mouse, and a fraction of the concentration in the heart was detectable with a reconstructed pixel size of 100 $\mu$m. The 0.5% Lu vial ($Z = 71$, K-edge energy = 63.3 keV) in our LC La-Gd-Lu phantom was visible in the K-edge image and had a difference of less than 0.1% according to Figure 7.5, but its RMSE is quite high at 0.29%. While a direct comparison is difficult to perform, the difference in visibility can be attributed to the need of energy bin optimization and different reconstruction methods when imaging Lu simultaneously with other contrast agents.

In our setup employing a continuous x-ray beam, the imaging dose was 116 mGy over a total scan time of 12 min. This setup has an acceptable imaging time but relatively high imaging dose for scanning small animals under anesthesia[103]. The CZT detector acquired projection images in 0.25 second periods for image reconstruction. Since the beam operated continuously the total dose delivered to each phantom per phantom rotation was 624 mGy. The imaging dose could be decreased by employing a pulsed beam synchronized with the detector acquisition and with a 25% duty cycle. Alternatively, the rotation speed could be increased by a factor of four, which could result in image blurring due to motion.

## 7.6 Conclusions

We have simultaneously imaged three contrast agents in a small animal-sized phantom; the clinically-relevant I and Gd in combination with novel lanthanide contrast agents such as La, Lu, and Ho. This was achieved using weighted K-edge subtraction imaging with a CZT detector with six energy bins capable of sustaining high count rates. This first demonstration of multiplexed PCCT imaging of similar-$Z$ contrast agents, with a difference of $Z$ as low as 3 and K-edge energy as low as 5.4 keV, on a table-top imaging system could lead to improved disease diagnosis with novel contrast agents.

# Chapter 8

# Design of a Combined X-ray Fluorescence Computed Tomography and Photon-Counting CT Table-top Imaging System

## 8.1 Summary

Our table-top imaging system is capable of both XFCT and PCCT, whose data can be simultaneously acquired. The design of both XFCT and PCCT portions of the imaging system were chosen based on our previous studies. The following experiment evaluates the performance of imaging Gd and Au solutions together, either mixed or separated in a small animal phantom and in mice, using pencil beam XFCT, pencil beam PCCT, and cone beam PCCT[151].

## 8.2 Introduction

Computed Tomography (CT) is a widely-used form of anatomical imaging which typically uses polyenergetic x-rays to produce single-channel images. Many generations of CT scanners, such as pencil beam and cone beam geometries, have been developed for a wide range of clinical and industrial applications over the last 50 years[22]. Conventional CT uses energy-integrating detectors to reconstruct images in the form of attenuation maps which offer high contrast structural information. However, the attenuation maps are material and energy dependent, and the energy-integrating nature of the detectors can lead to the reduced ability to distinguish certain materials in a conventional CT image. This poses a problem with the growing use of contrast agents in the clinic to aid in disease diagnosis and structure enhancement.

Dual-energy CT (DECT) most commonly uses two diagnostic x-ray tube energies

to create high- and low-energy attenuation maps in an effort to recognize two distinct materials which may have similar contrast in a conventional CT image. While clinically useful in most contexts, DECT may result in longer imaging times, higher imaging doses, and costly equipment. There is also a growing need to quantitatively image contrast agents in preclinical settings for certain applications such as radiotherapy enhancement using gold nanoparticles (AuNPs)[10] and combined CT and magnetic resonance imaging[7] using gadolinium (Gd) contrast[152].

Advancements in photon counting detector development has made photon-counting CT (PCCT) possible[28, 29]. In photon-counting detectors, detected x-rays are counted and their energies are sorted by analyzing the pulse heights generated in the semiconductor layer. PCCT imaging can distinguish high-atomic number *(Z)* materials by setting appropriate detector energy bins above and below the K-edges of each material. In DECT imaging, a similar effect is achieved by selecting appropriate x-ray tube voltages on either side of a K-edge for one material when two x-ray beams of different energies are used[25]. Compared to DECT, the main advantage of PCCT when combined with K-edge imaging is the ability to discern multiple high-$Z$ contrast agents from structures such as bone or other contrast agents, which would be difficult to resolve in a conventional CT images[30, 115]. PCCT also resolves some disadvantages associated with DECT as described above in terms of imaging time and dose. In one study, gold (Au) and platinum contrast were distinct from two types of bone material with similar CT numbers in a K-edge subtracted CT image using kilovoltage pencil beam xrays[52]. Using basis material decomposition, PCCT can also distinguish between different high-$Z$ contrast agents[137, 138, 128] as well as from low-$Z$ tissue-equivalent material[153, 154]. The development of high-flux photon-counting detectors have caused PCCT to rapidly develop in recent years[33], but it is still limited by cost of large-scale production[34].

X-ray fluorescence CT (XFCT) is a form of molecular imaging that detects scattered x-rays to reconstruct quantitative images of contrast such as AuNPs[42, 54]. XFCT is capable of identifying low concentrations of contrast agents such as AuNPs, with Gd gaining recent interest for *in vivo* XFCT imaging[40]. Simultaneous imaging of multiple contrast agents, or multiplexed, XFCT has been demonstrated for elements including Au, Gd, and barium, provided the fluorescent x-ray energies are sufficiently resolved[45]. However, scatter and attenuation of fluorescent x-rays in *in vivo* imaging remain a problem in XFCT; many scatter- and attenuation-correction algorithms have been devised to improve the achievable sensitivity[46, 43]. In addition,

while pencil beam XFCT results in long imaging times, collimators for fan beam or cone beam XFCT have shown to compromise the image quality when imaging AuNPs in exchange for faster imaging times[95, 41, 108]. Detecting fluorescent x-rays from AuNPs at high scattering angles relative to the incident pencil beam improved AuNP imaging sensitivity of XFCT images compared to lower scattering angles due to the energy of the detected Compton-scattered x-rays [47, 39], however the imaging time was prohibitively long for small animal imaging. Due to these factors, XFCT is largely confined to small animal imaging or imaging at shallow depths[59].

PCCT faces less obstacles in clinical translation than XFCT, as it can image at depth, with several PCCT imaging systems having studied many applications[123, 122, 120]. However, XFCT has been shown to have better imaging sensitivity than K-edge PCCT at sub-percentage concentrations of AuNPs[53]. When considering the application of imaging AuNPs, the AuNP concentrations range from as low as 0.001%[12] to as high as 0.7%[10], making AuNP detection an attractive application for XFCT. To leverage the benefits of both XFCT and PCCT, in particular the shallow high-sensitivity imaging from XFCT and at-depth material discrimination from PCCT, we propose the design of a combined XFCT and PCCT table-top imaging system capable of simultaneous pencil beam data acquisition. Many hybrid imaging systems have been developed; examples include spectral CT combined with micro-CT to enable both high spectral resolution and high spatial resolution[127] and XFCT combined with transmission CT to allow for molecular imaging of AuNPs with anatomical information[155]. Another cone beam table-top imaging system capable of combined XFCT and K-edge PCCT is under development that uses two cadmium zinc telluride (CZT) photon-counting detectors for each imaging modality[156]. Our table-top imaging system used two cadmium telluride (CdTe) spectrometers and a high-flux CZT photon-counting detector. The CdTe spectrometers were optimized to balance imaging sensitivity and detector pileup for XFCT, and the photon-counting detector was capable of both K-edge PCCT imaging and energy-integrating transmission CT to image Gd and Au contrast agents. We evaluated the image quality of Gd and Au contrast in a small animal phantom for both XFCT and K-edge PCCT in a pencil beam geometry compared to K-edge PCCT in a cone beam geometry, as well as assessed the accuracy of reconstruction between pure and mixed contrast agents. In addition, we scanned three mice injected with Gd and Au contrast agents and reconstructed preliminary mouse images.

## 8.3 Materials and Methods

### 8.3.1 Imaging Setup

The imaging setup for pencil beam acquisition (Figure 8.1a) consisted of an x-ray tube, a CZT photon-counting detector, two CdTe spectrometers, a linear motion stage, and a rotation stage. The imaging setup for cone beam acquisition (Figure 8.1b) included the x-ray tube, a CZT photon-counting detector, a linear motion stage, and a rotation stage. The MRX-160/22 X-ray tube (Comet Technologies, Flamatt, Switzerland) and the CZT detector were mounted on the M-IMS300V and M-IMS600LM motion stages, and the phantom was placed on a RVS80CC rotation stage (Newport Corporation, Irvine, CA USA). The CZT photon-counting detector was placed 11 cm from the isocentre opposite the x-ray tube. The CdTe spectrometers, labelled as #1 and #2 in Figure 8.1a, were placed 8 cm from the isocentre at an angle shown in Figure 8.1a such that x-rays would be Compton-scattered at lower energies and thus increase the detector sensitivity to Au fluorescent x-rays[39]. Small lead (Pb) sheets were draped over the CdTe crystal as shielding in an effort to minimize scatter from the incident x-ray beam and reduce the count rate on the CdTe spectrometers. The rotation stage and both CdTe spectrometers were mounted on another motion stage which enabled translation perpendicular to the incident beam. This arrangement kept the distance between each CdTe spectrometer and the centre of the phantom constant at 8 cm [59]. The entire setup was mounted on an optical table.

Each mouse and phantom were imaged using a pencil or cone beam CT geometry. For the pencil beam geometry the x-ray beam was collimated with a 0.4 mm-diameter tungsten collimator such that the beam size was 1 mm at the isocentre. The x-ray tube was placed 20 cm from the isocentre in this geometry, which was as close as possible to reduce the beam divergence while minimizing the pile-up in the CdTe spectrometers. For the cone beam geometry, the x-ray beam was collimated with lead such that the beam area at the isocentre was 36.6 mm in width and 13.7 mm in height. In order for the beam to completely cover the phantom, the x-ray tube was placed 32 cm from the isocentre in this geometry. The cone beam energy spectrum shown in Figure 8.2a was simulated using an existing Monte Carlo model of the x-ray tube [73].

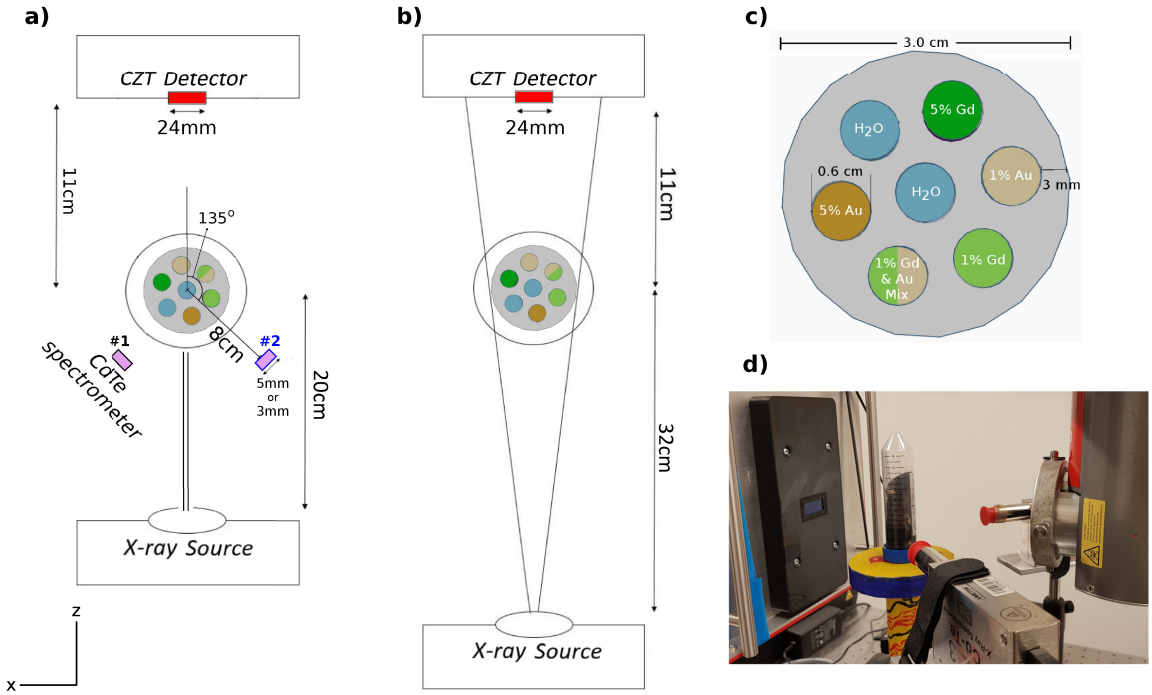


Figure 8.1: Schematic diagrams showing the a) pencil beam and b) cone beam setups, as well as the c) phantom. Diagrams are not to scale. d) Photo of the pencil beam setup for mouse imaging, without lead shielding on the CdTe spectrometers.

### Phantom

The 3D-printed phantom (Figure 8.1c) used in this study was 3 cm in diameter, 2.5 cm in height, and made of solid polyactic acid (PLA) of density 1.25 g/cm$^3$ (Conceptualize CAD & Print, Victoria, BC Canada). Seven 6 mm-diameter holes were built into the phantom to accommodate 0.2 mL Flat Cap PCR tubes (Fisher Scientific, Ottawa, ON Canada), which are referred to as vials. Four of these vials contained Gd and Au contrast agents whose concentrations were 1% and 5% by weight. One vial contained a mixture of 1% Gd and 1% Au of equal volume, with the rest of the vials containing deionized water. The Gd and Au contrast agents used were gadolinium (III) chloride hexahydrate with a purity of 99.999% (Sigma-Aldrich, Oakville, ON Canada) and gold (III) chloride solution (GG3CS-25.4-100 Lot AUY03-7077, Nanopartz Inc., Loveland, CO USA), both of which were diluted to the appropriate concentrations in deionized water.

### Mice

Three freshly-euthanized mice originally used for unrelated research each with a weight of 32 g, 26 g, and 20 g were obtained for this study with ethics approval. The 32 g, 26 g, and 20 g mouse were each injected post-mortem with 0.2 mL of 5% Gd, 5% Au, and a mixture of 5% Gd and Au solutions, respectively, in the upper torso region. These mice are referred to as the Gd-only, Au-only, and mixed Gd/Au mice, respectively. The mixture solution was prepared by mixing 0.1 mL each of 5% Gd and 5% Au solutions together before injection. Each mouse was then placed in 50 mL test tubes (Fisher Scientific, Ottawa, ON Canada) which were 2.5 cm in diameter.

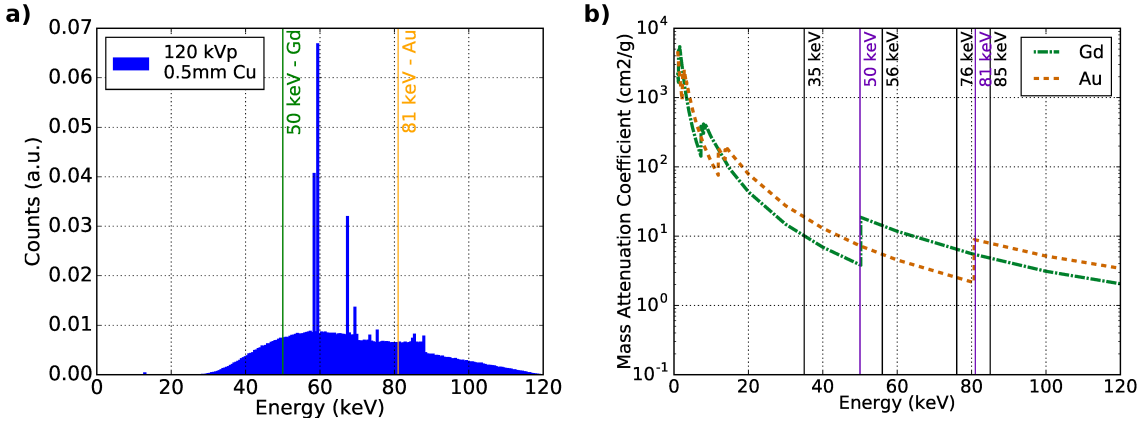


Figure 8.2: a) Monte Carlo-generated 120 kVp x-ray beam spectrum filtered with 0.5 mm Cu from the x-ray tube, with K-edge energies of 50 keV and 81 keV for Gd and Au, respectively. b) Mass attenuation coefficients of Gd and Au with set energy bins on the CZT detector.

## 8.3.2 Detectors

### Spectrometers

Each X-123CdTe spectrometer (Amptek Inc., Bedford, MA, USA) was a complete integrated system consisting of the XR-100CdTe detector and preamplifier, a DP5 digital pulse processor and multi-channel analyzer, and a PC5 power supply. The spectrometer had a single-pixel CdTe crystal with 1 mm thickness capable of count rates up to $2 \times 10^5$ counts per second. A CdTe crystal size of (5×5) mm$^2$ was used to image the phantom, while a crystal size of (3×3) mm$^2$ was used to image each mouse. Each CdTe spectrometer was calibrated to the 81 keV peak of the

$^{133}$Ba gamma spectrum, and the measured energy resolution of each spectrometer was 900 eV for the (5×5) mm$^2$ crystal and 800 eV for the (3×3) mm$^2$ crystal at 81 keV[59]. The multi-channel analyzer had 1024 channels for data acquisition, which were rebinned post-acquisition so that there were 256 energy bins with an energy bin width of 0.6 keV. The settings on each CdTe spectrometer were the following: rise-time discrimination off, peak time of 3.2 $\mu$s, flat top width of 0.4 $\mu$s, slow threshold of 2.929%, total gain of 9.000×, and pile-up rejection on.

#### Photon-counting Detector

The photon-counting detector (Redlen Technologies, Saanichton, BC) consisted of a CZT sensor and integrated readout electronics. The CZT sensor consisted of two adjacent modules each (8×12) mm$^2$ in size with a 2 mm-thick crystal with a total active area of (8×24) mm$^2$. Each module on the CZT sensor had 864 individual pixels (24×36) with a pixel pitch of 330 $\mu$m, and a pixel count variability of <10%. The detector energy resolution of 8.9 keV was measured by the manufacturer by calculating the full width at half maximum (FWHM) of the 59.5 keV gamma ray peak of a $^{241}$Am spectral sweep. The sensor operated at 250 Mcps/mm$^2$ without any signs of polarization [33] and was connected to a high-speed photon counting Application Specific Integrated Circuit (ASIC) that operated at rates up to 62.5 Mcps per channel. The energies of the incident x-rays onto the sensor were sorted into six energy bins, which were adjustable in the 16-200 keV energy range. The mass attenuation coefficients of Gd and Au and the energy bin thresholds for both pencil beam and cone beam imaging are shown in Figure 8.2b. The energy bins on the CZT detector were set to 35, 50, 56, 76, 81, 85, and 120 keV to accommodate for the K-edge values of Gd and Au of 50.2 keV and 80.7 keV, respectively. The other thresholds were chosen to equalize the number of photons in each energy bin based on the x-ray beam spectrum in Figure 8.2a.

### 8.3.3 Data Acquisition

For both pencil and cone beam acquisitions, the x-ray source operated at 120 kVp and 2 mA with a 0.4 mm focal spot in IEC and 0.5 mm of copper (Cu) filtration. The method of data acquisition for phantom imaging was identical to that of the mice. The cone beam data acquisition for each mouse was acquired immediately post-injection of each contrast solution on the same day. The pencil beam data acquisition for each

mouse was acquired approximately 1 day, 2 days, and 3 days after contrast agent injection for the mixed Gd/Au, Au-only, and Gd-only mouse, respectively.

#### Pencil Beam

The pencil beam acquisition was performed with a stationary source and detector and a rotating/translating phantom. For each angle, 33 projections were acquired over a continuous translation at a speed of 0.095 mm per second. The CdTe spectrometers and the CZT detector simultaneously acquired projection data during 8 and 10 second intervals, respectively. This was repeated using 30 angles in 12° steps. The acquisition time for one full translation was 5.8 minutes, and the total time to image the phantom was 174 minutes.

#### Cone Beam

The cone beam acquisition was performed with a stationary source and detector and a rotating phantom. 180 projections were acquired over a 360° continuous rotation at a speed of 1.49 degrees per second. Three rotations were performed at different CZT detector positions in order to image across the entire phantom and mouse bodies. The detector acquired projection data during 1 second intervals. The acquisition time for one full rotation of the phantom was 4 minutes, so with three full rotations it took 12 minutes to image the phantom. No XFCT data were acquired in the cone beam geometry.

### 8.3.4 Image Reconstruction

All reconstructed images were calibrated to the 5% concentration in the phantom. MATLAB (The Mathworks, Natick, MA) and Python were used for data processing and image reconstruction of cone beam and pencil beam images, respectively, while Python was used for data analysis of all images.

#### XFCT Image Reconstruction

X-ray spectra were collected in each CdTe spectrometer during the pencil beam acquisition (Figure 8.3). To reconstruct Gd XFCT images, the fluorescent x-rays $K_{\alpha 1}$ (43.0 keV), $K_{\alpha 2}$ (42.3 keV), and $K_{\beta 1}$ (48.7 keV) were interpreted as signal, with the $K_{\beta 1}$ x-ray having a tolerance of $\pm$ 0.5 keV to define the fluorescent region. However,

the Gd $K_{\alpha 1}$ and $K_{\alpha 2}$ fluorescent peaks in each spectrum were not distinguishable, so the average energy of 42.65 keV was treated as one fluorescent peak with a tolerance of $\pm$ 1.0 keV to define this fluorescent region. The net number of Gd fluorescent x-rays in a fluorescent region was estimated by finding the average number of counts in neighbouring 0.5 keV or 1 keV regions from either side of the fluorescent region, then subtracting this value from the number of counts in the fluorescent region. To reconstruct Au XFCT images, the fluorescent x-rays $K_{\alpha 1}$ (68.8 keV), $K_{\alpha 2}$ (67.0 keV), and $K_{\beta 1}$ (78.0 keV) were interpreted as signal with $\pm$ 0.5 keV to define the fluorescent region for each. The net number of Au fluorescent x-rays in a fluorescent region was estimated in the same way as for Gd above, except the neighbouring regions were all 0.5 keV. The total number of fluorescent x-rays was found by summing the number of Gd or Au fluorescent x-rays for each type, and repeated over 33 translations and 30 rotations to form a sinogram corresponding to each of the two CdTe spectrometers. Negative values in the sinograms were set to zero. The two sinograms for each CdTe spectrometer were added together, and both Gd and Au XFCT images were reconstructed using an inverse radon transform with the default ramp filter. The resulting XFCT images were 33 $\times$ 33 pixels with a voxel size of (1 mm)$^3$.

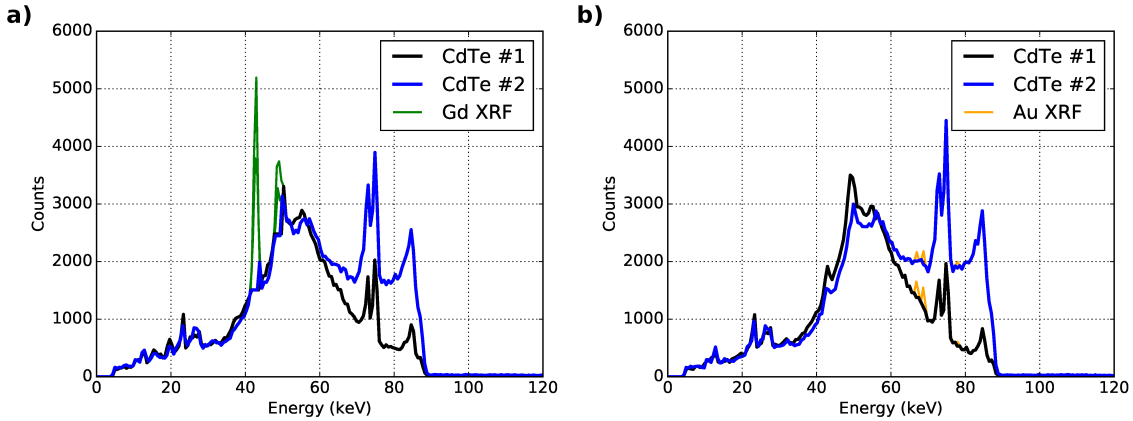


Figure 8.3: X-ray spectra from the phantom as detected on the left and right CdTe spectrometers showing the maximum a) Gd and b) Au x-ray fluorescence (XRF) at different translation and rotation steps.

### PCCT Image Reconstruction

Before reconstructing the pencil and cone beam PCCT images, each projection scan was corrected for non-uniform pixel response using nearest-neighbour pixel interpo-

lation [138]. Detector counts were converted into projections $p$ by the following:

$$p = -\ln((N - N_{dark})/(N_0 - N_{dark})) \tag{7.1}$$

where $N$ is the number of counts with the phantom, $N_0$ is the number of counts without the phantom, and $N_{dark}$ is the number of counts without the x-ray beam.

**Pencil Beam** A $4 \times 4$ square pixel region on the CZT detector with the highest number of counts $N_0$ was selected for data acquisition. The counts in this region were summed to equal $N$, $N_0$, and $N_{dark}$ in Equation 7.1 to form a projection for a given translation and rotation. These projections formed a sinogram for each energy bin with 33 translation and 30 rotation steps. The PCCT images were reconstructed using an inverse Radon transform with a ramp filter. Similar to the XFCT images, the resulting pencil beam PCCT images at each energy bin were $33 \times 33$ pixels with a voxel size of $(1\text{ mm})^3$.

**Cone Beam** For each of the six energy bins and the energy-integrated bin, the projection data from each of the three detector translations were manually combined to generate a set of three-dimensional projections of the entire phantom. Ring artifact corrections were performed on the projections using the wavelet-FFT method [141] to suppress stripe artifacts appearing in the projections along each dimension. This method used a DB42 wavelet with a second level decomposition and a damping coefficient of 1.2 in the fixed pixel column dimension and a first level decomposition and damping coefficients of 0.5 and 2.4 in the fixed rotation and pixel row dimensions, respectively. The PCCT images were then reconstructed using the Feldkamp-Davis-Kress (FDK) algorithm[86] with a Hamming filter. The resulting cone beam PCCT images at each energy bin were $123 \times 123$ pixels and the reconstructed voxel size was 250 $\mu$m.

### K-edge Images

For both pencil and cone beam acquisitions, the K-edge PCCT images for Gd and Au were reconstructed by subtracting the PCCT image of the energy bin directly below the K-edge from the PCCT image directly above the K-edge in each axial CT slice of the phantom. To form Gd K-edge images, the 35-50 keV PCCT image was subtracted from the 50-56 keV PCCT image. To form Au K-edge images, the 76-81

keV PCCT image was subtracted from the 81-85 keV PCCT image.

### 8.3.5 Image Analysis

#### Accuracy of Reconstructed Concentration

The reconstructed concentration of each phantom vial of the Gd and Au images was compared with the actual prepared concentration for a region of interest (ROI) centered on each vial. The signal in the peripheral water vial in the phantom was interpreted as 0% Gd and 0% Au. The reconstructed concentration of the 5% Gd and Au vials were defined to be equal to the actual concentration due to the image calibration applied in this work.

#### Contrast-to-Noise Ratio

The contrast to noise ratio (CNR) and its associated error $\mathrm{CNR}_{\mathrm{err}}$ in each phantom image was evaluated for an ROI by the following:

$$\mathrm{CNR} = \frac{\mu_{\mathrm{ROI}} - \mu_{\mathrm{water}}}{\sigma_{\mathrm{phantom}}} \tag{3.9}$$

$$\mathrm{CNR}_{\mathrm{err}} = \frac{\sqrt{\sigma^2_{\mathrm{ROI}} + \sigma^2_{\mathrm{water}}}}{\sigma_{\mathrm{phantom}}} \tag{8.1}$$

where $\mu_{\mathrm{ROI}}$ and $\sigma_{\mathrm{ROI}}$ are the mean and standard deviation of the ROI for each contrast agent, respectively, $\mu_{\mathrm{water}}$ and $\sigma_{\mathrm{water}}$ are the mean and standard deviation of the ROI for the water vial, respectively, and $\sigma_{\mathrm{phantom}}$ is the standard deviation placed in the plastic phantom. The ROI representing the phantom was a 30 mm-diameter circle over the entire phantom body excluding the vials. The imaging sensitivity of a contrast agent was based on the Rose criterion, which was defined as the concentration at which CNR was equal to 5[91].

#### CT Number Analysis

In both pencil and cone beam acquisitions, energy-integrated CT images were reconstructed with the data in the energy-integrated bin on the CZT detector. The energy-integrated CT images were normalized to CT number in Hounsfield units

(HU) in the following manner:

$$\text{CT number}_\text{i} = 1000\frac{\mu_i - \mu_{\text{H}_2\text{O}}}{\mu_{\text{H}_2\text{O}} - \mu_{\text{air}}} \tag{3.8}$$

where $\mu$ is the attenuation in image pixel $i$, $\mu_{\text{H}_2\text{O}}$ is the average attenuation in the ROI of the water vial, and $\mu_{\text{air}}$ is the attenuation of air. Vial CT numbers in the pencil beam and cone beam images were compared.

#### Preliminary Mouse Images

For each of the pencil beam XFCT, pencil beam K-edge PCCT, and cone beam K-edge PCCT mouse images, the contrast was quantified in two different ways: average concentration in a select ROI and maximum concentration in an organ.

The average reconstructed concentration was evaluated for select ROIs in which a high amount of Gd or Au contrast was concentrated in each of the K-edge PCCT images. In the case of the mixed Gd/Au mouse images, two ROIs were identified for each of Gd and Au contrast.

The lungs were contoured in each of the Gd-only and the Au-only cone beam CT mouse images. The lungs in the mixed Gd/Au cone beam CT mouse image were not visible, so instead the heart was contoured in this image. The maximum reconstructed concentration in the contoured organs was found by taking the maximum value of the Gd or Au concentration in the contoured organ regions.

### 8.3.6 Dose

To estimate the phantom imaging dose, a cylindrical water phantom was simulated in TOPAS [69], a GEANT-4 based Monte Carlo software package, in the same setup according to Figure 8.1a-b for pencil and cone beam geometry, respectively. The relevant physics modules "g4em-standard_opt4", "g4decay", "g4ion-binarycascade", "g4stopping", and "g4em-extra" were used in the simulation, as well as the modeling of fluorescence, Auger electrons, and particle-induced x-ray emission[96]. The simulation output was the dose per primary electron in a central slice of the phantom, which was converted to the actual phantom dose using the imaging time and current.

## 8.4 Results

The Gd images for pencil beam XFCT, pencil beam K-edge PCCT, and cone beam K-edge PCCT are shown in Figure 8.4a-c, respectively. The amount of noise in these images, calculated as the standard deviation in the phantom body ROI, was 0.14%, 0.17%, and 0.16% Gd, respectively.

The Au images for pencil beam XFCT, pencil beam K-edge PCCT, and cone beam K-edge PCCT are shown in Figure 8.4d-f, respectively. The amount of noise in these images, calculated as the standard deviation in the phantom body ROI, was 0.61%, 0.16%, and 0.30%, respectively.

In general, the spatial resolution of the cone beam images was much better than the pencil beam images as expected due to the pixel sizes. Mild streak artifacts were present in the pencil beam XFCT and K-edge PCCT images. The imaging doses for the pencil beam XFCT, pencil beam K-edge PCCT, and cone beam K-edge PCCT images were 680 mGy, 850 mGy, and 250 mGy, respectively.

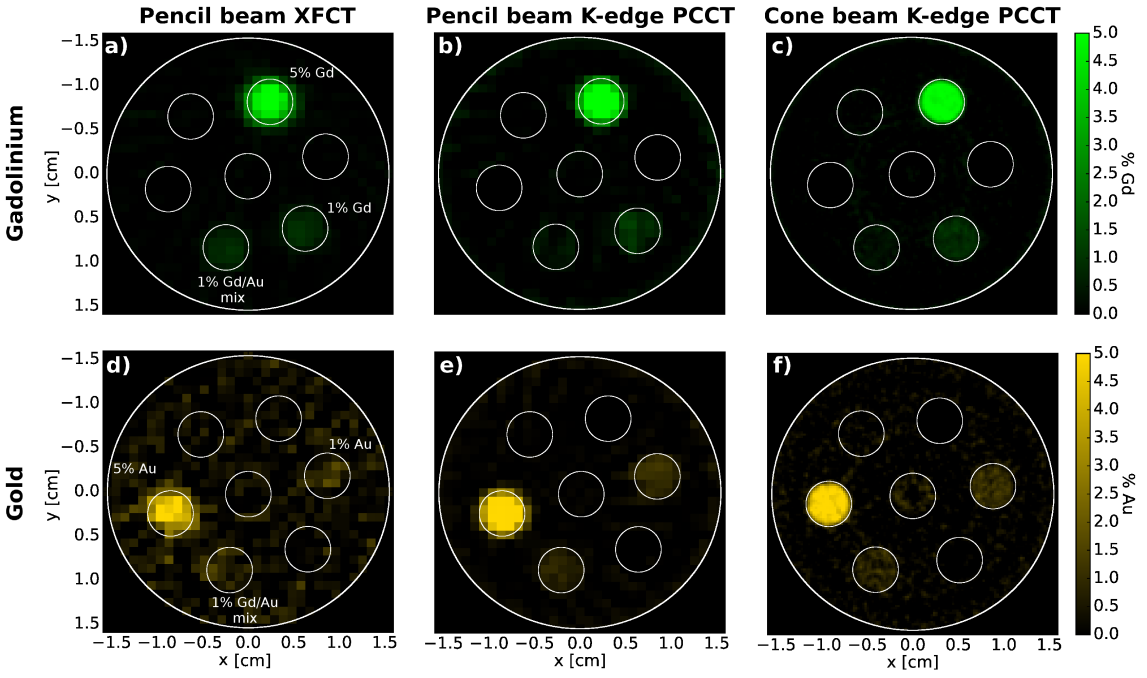


Figure 8.4: All contrast images of a-c) Gd and d-f) Au. a,d) Pencil beam XFCT images. b,e) Pencil beam K-edge PCCT images. c,f) Cone beam K-edge PCCT images.

### 8.4.1 Reconstructed Concentration

The reconstructed concentrations of each vial in the Gd and Au images are summarized in Table 8.1. Of the Gd images, the 0% and 1% Gd vials were reconstructed within one standard deviation, except in the case of the 1% Gd vial in the cone beam K-edge PCCT image (Figure 8.4c). None of the images could reconstruct the mixed 1% Gd vial within error. Of the Au images, all vials were reconstructed within error except for the mixed 1% Au vial in both K-edge PCCT images (Figure 8.4e-f).

Table 8.1: Reconstructed concentration of each vial.

| Vial | Reconstructed concentration (%) ± Absolute error | | |
|---|---|---|---|
| | Pencil beam XFCT | Pencil beam K-edge PCCT | Cone beam K-edge PCCT |
| 0% Gd | 0.03 ± 0.10 | 0.00 ± 0.10 | 0.00 ± 0.12 |
| 1% Gd | 0.86 ± 0.16 | 0.87 ± 0.25 | 0.84 ± 0.13 |
| 1% Gd mixed | 0.81 ± 0.16 | 0.31 ± 0.15 | 0.30 ± 0.11 |
| 0% Au | 0.10 ± 0.79 | 0.00 ± 0.10 | 0.00 ± 0.30 |
| 1% Au | 0.99 ± 0.65 | 1.01 ± 0.23 | 1.04 ± 0.20 |
| 1% Au mixed | 0.92 ± 0.55 | 0.71 ± 0.19 | 0.69 ± 0.26 |

### 8.4.2 CNR Evaluation

The CNR results for each vial are summarized in Figure 8.5 for Gd and Au images, respectively. The pencil beam XFCT images had the highest CNR values of the 1% and 5% Gd vials of 6.0 and 36.0, respectively (Figure 8.5a). The CNR values of the 1% and 5% Gd vials in Figure 8.5a were independent of the imaging method because the error bars overlap. The CNR of the mixed 1% Gd vial in the XFCT image was 5.7, which was within the error bar of the pure 1% Gd vial CNR in the XFCT image. However, for the pencil and cone beam K-edge PCCT images, the CNR values of the

mixed 1% Gd vial were lower at 2.0 and 1.9, respectively. The Rose criterion failure of these vials was due to the inaccuracy in concentration evaluation from Table 8.1. The Gd imaging sensitivity for XFCT, pencil beam K-edge PCCT, and cone beam K-edge PCCT was 0.75%, 0.81%, and 0.79%, respectively.

The CNR values of the 1% and 5% Au vials in Figure 8.5b were the highest in the pencil beam K-edge PCCT image at 6.1 and 30.3, respectively. The CNR of the mixed 1% Au vial was lower than the pure 1% Au vial among the three Au images, although the difference was not as pronounced compared to Gd. Only the 5% Au vial for all Au images and the 1% Au vial in the pencil beam K-edge PCCT image satisfied the Rose criterion, as noise is prevalent in both of the Au XFCT and cone beam K-edge PCCT images. The Au imaging sensitivity for XFCT, pencil beam K-edge PCCT, and cone beam K-edge PCCT was 2.97%, 0.82%, and 1.51%, respectively.

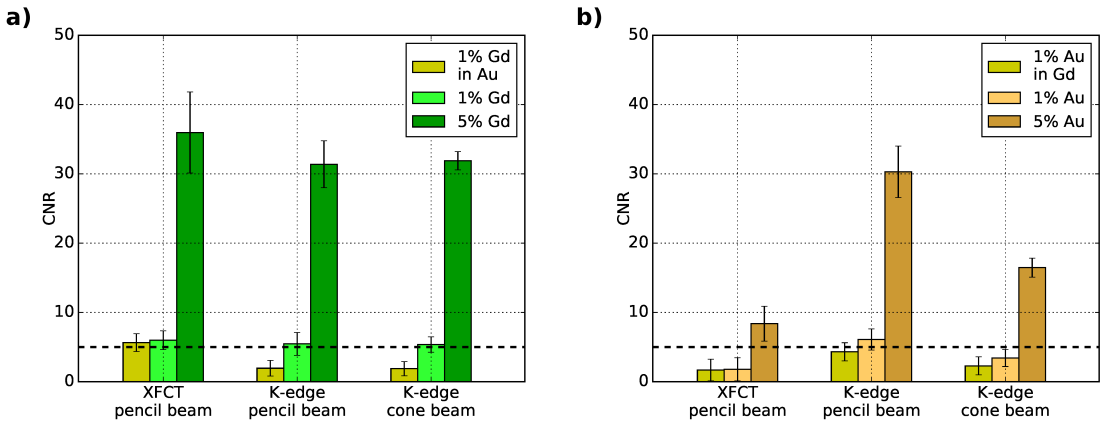


Figure 8.5: CNR of contrast vials in a) Gd and b) Au images for pencil beam XFCT and K-edge PCCT, and cone beam K-edge PCCT.

### 8.4.3 Energy-Integrated CT Images

The energy-integrated CT images for the pencil and cone beam acquisitions are shown in Figure 8.6. The spatial resolution of the pencil beam CT image (Figure 8.6a) is limited by the number of translations, however most vials are clearly distinguished. The high spatial resolution from the CZT detector is evident in the cone beam CT image (Figure 8.6b), however ring artifacts are present that disrupt the contrast of the middle water vial.

Table 8.2 compares the CT numbers for the pencil and cone beam CT images for each vial. All CT numbers for each vial are consistent between the pencil beam and

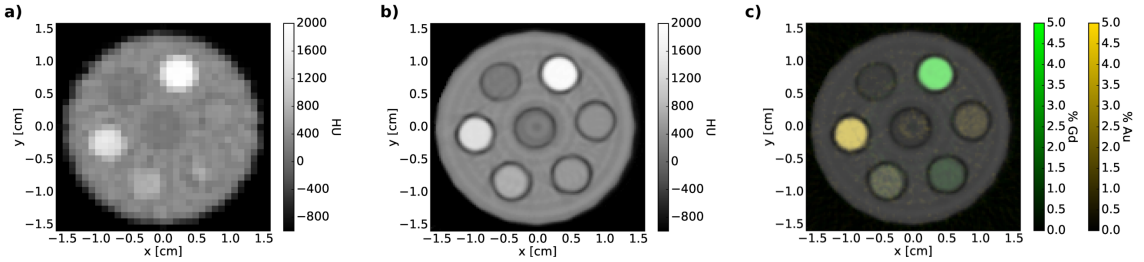


Figure 8.6: a) Pencil beam and b) cone beam CT images normalized to HU. c) Overlay image of cone beam CT and K-edge PCCT images of Gd and Au.

the cone beam CT images, however the standard deviation associated with the CT number in the pencil beam CT image was relatively large. This is in part due to the low number of pixels in each ROI relative to the vial size in this image, as well as artifacts caused by partial volume, streaks, and continuous motion during acquisition.

Table 8.2: CT number of each vial.

| | CT number (HU) ± Absolute error (HU) | | | | | |
|---|---|---|---|---|---|---|
| Vial | Water | 1% Gd | 5% Gd | 1% Au | 5% Au | 1% Gd/Au Mix |
| Pencil beam CT | 0 ± 58 | 317 ± 132 | 1898 ± 200 | 240 ± 86 | 1236 ± 159 | 554 ± 80 |
| Cone beam CT | 0 ± 19 | 329 ± 20 | 1881 ± 21 | 257 ± 19 | 1254 ± 26 | 578 ± 26 |

### 8.4.4 Preliminary Mouse Images

The pencil beam CT, K-edge PCCT, and XFCT images of the three mice are shown in Figure 8.7. The contrast distribution in all K-edge PCCT images (Figures 8.7a-c) are consistent with the higher HU in the respective energy-integrated CT images evidenced in the overlay images (Figures 8.7g-i). Streak artifacts are prominent in these images, however, likely due to the limited number of rotations used in the pencil beam geometry. The Gd distribution in the Gd-only mouse XFCT image (Figure 8.7j) and the mixed Gd/Au mouse XFCT image (Figure 8.7l) largely resemble the Gd distribution in their respective K-edge PCCT images (Figures 8.7d,f). However, the XFCT images in the Au-only mouse (Figure 8.7k) and mixed Gd/Au mouse (Figure 8.7l) are too noisy to depict the Au distribution.

The cone beam CT and K-edge PCCT images for the three mice are shown in Figure 8.8. The cone beam acquisition has the obvious benefit of higher spatial

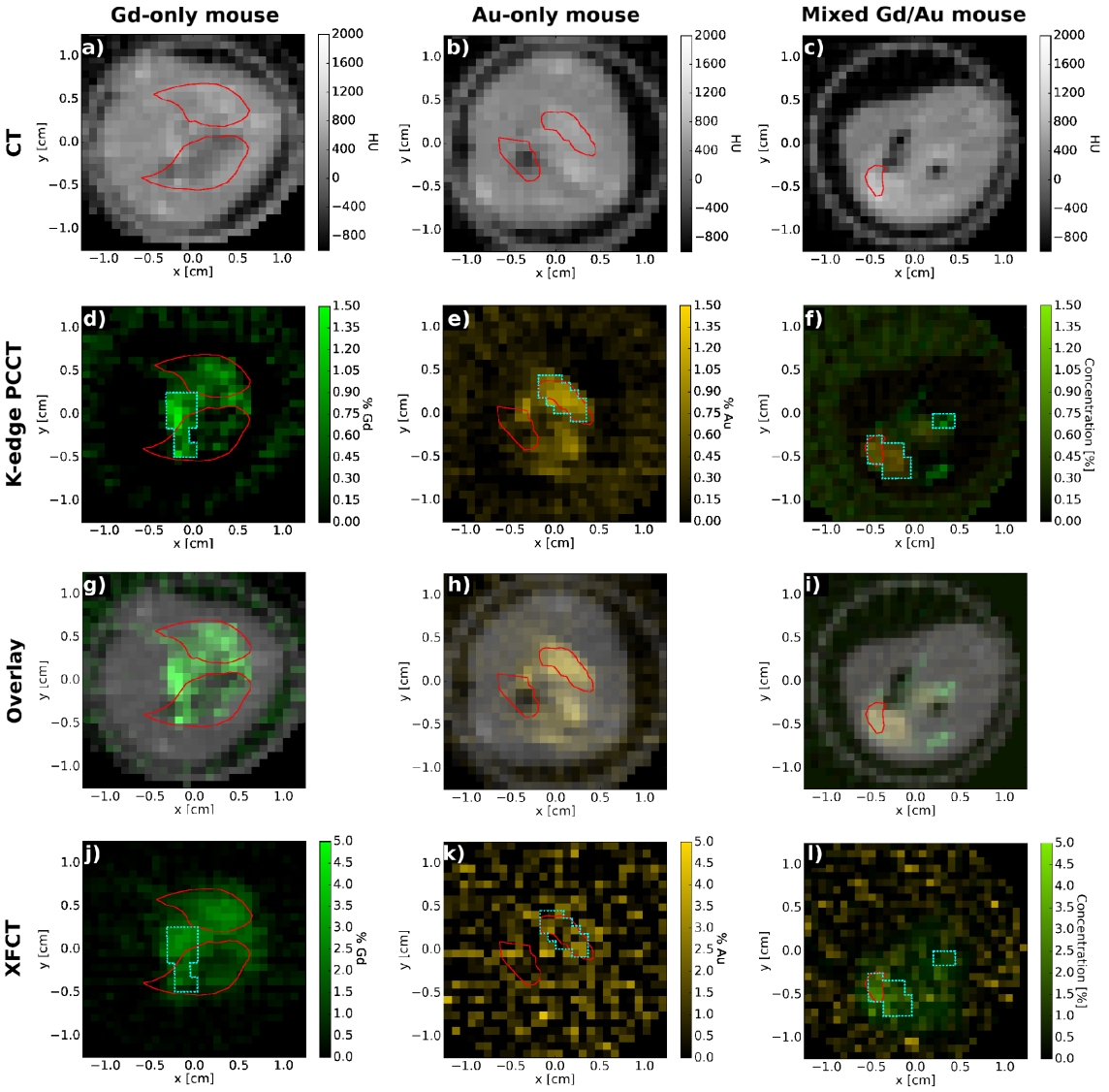


Figure 8.7: a-c) Energy-integrated CT images, d-f) K-edge PCCT images and their respective g-i) overlay images, and j-l) XFCT images of the Gd-only (left), Au-only (middle), and mixed Gd/Au (right) mice scanned with a pencil beam geometry. Red solid lines delineate the lungs in the Gd-only and Au-only mice and the heart in the mixed Gd/Au mouse. Cyan dashed lines in each K-edge PCCT and XFCT images outline an ROI containing a high amount of contrast.

resolution as shown in the energy-integrated CT images (Figures 8.8a-c) compared to the pencil beam acquisition (Figures 8.7a-c). In addition, the overlay images in Figures 8.8g-i depict the coincidence between the contrast distribution in the K-edge PCCT images with the higher HU values in the energy-integrated CT images.

Ring artifacts are evident in all of the K-edge PCCT images (Figures 8.8d-f) but most notably in the Au-only mouse image. Despite the ring artifacts, the contrast distribution in the Gd-only and Au-only K-edge PCCT images (Figures 8.8d,e) is quite clear compared to the mixed Gd/Au K-edge PCCT image in Figure 8.8f.

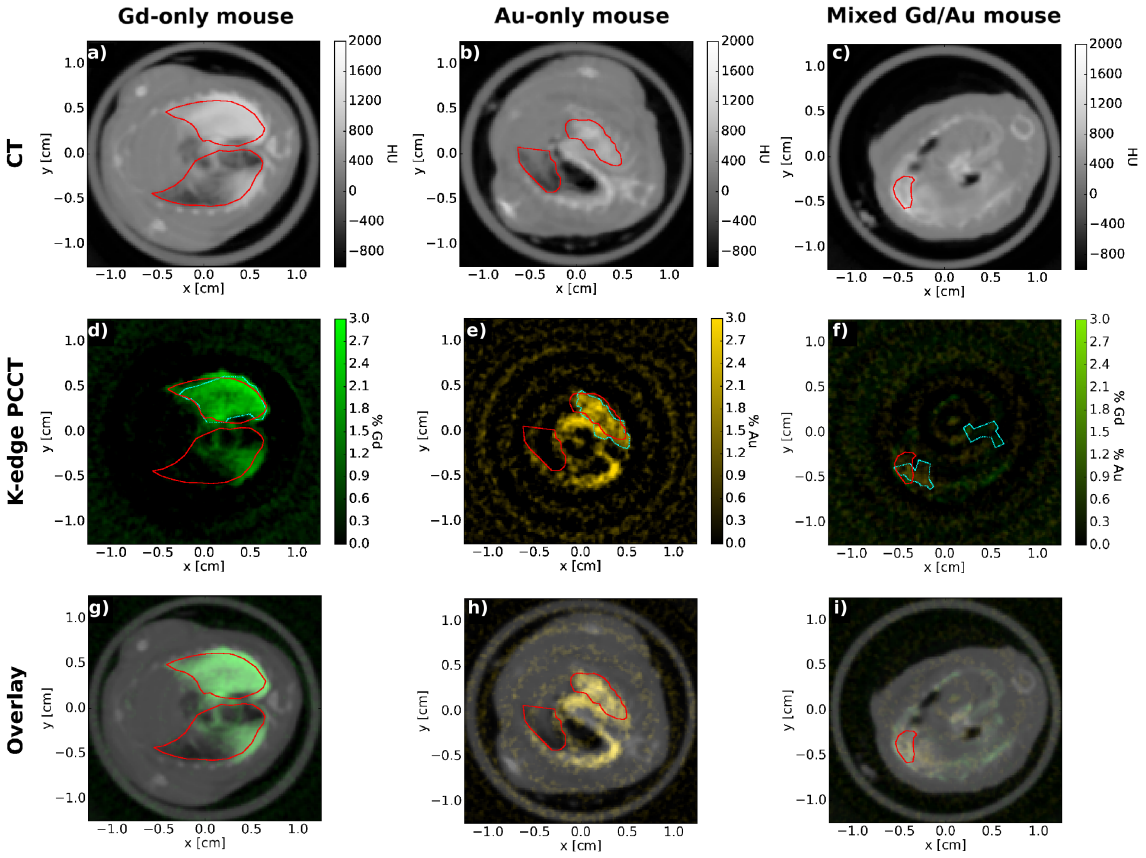


Figure 8.8: a-c) Energy-integrated CT images, d-f) K-edge PCCT images and their respective g-i) overlay images of the Gd-only (left), Au-only (middle), and mixed Gd/Au (right) mice scanned with a cone beam geometry. Red solid lines delineate the lungs in the Gd-only and Au-only mice and the heart in the mixed Gd/Au mouse. Cyan dashed lines in each K-edge PCCT image outline an ROI containing a high amount of contrast.

Table 8.3 summarizes the average reconstructed concentration in a selected ROI as well as the maximum concentration in a single voxel within a selected organ of Gd and Au contrast in all mouse images. Across the Gd-only and mixed Gd/Au mice, the pencil beam XFCT images reconstructed a higher concentration of Gd compared to the pencil beam K-edge PCCT images. Even though an equal concentration of Gd and Au contrast were injected into the mixed Gd/Au mouse, both the maximum

and average reconstructed concentrations of Au were higher than that of Gd across the pencil and cone beam K-edge PCCT images of the mixed Gd/Au mouse. The reconstructed concentration values of Au in the XFCT images were inconclusive given the large amount of noise in these images.

Table 8.3: Average and maximum reconstructed concentrations of contrast in mouse images within selected ROIs and organs, respectively.

| Mouse | Contrast Agent | Average reconstructed concentration in ROI (%) | | | Maximum reconstructed concentration in organ (%) | | |
|---|---|---|---|---|---|---|---|
| | | Pencil beam XFCT | Pencil beam K-edge PCCT | Cone beam K-edge PCCT | Pencil beam XFCT | Pencil beam K-edge PCCT | Cone beam K-edge PCCT |
| Gd-only | Gd | 1.96 | 0.80 | 1.98 | 2.68 | 1.19 | 2.89 |
| Mixed Gd/Au | Gd | 1.55 | 0.56 | 0.41 | 2.97 | 0.46 | 0.71 |
| Au-only | Au | 1.60 | 0.90 | 1.88 | 3.46 | 1.06 | 3.47 |
| Mixed Gd/Au | Au | 1.90 | 0.92 | 1.18 | 3.29 | 1.24 | 2.01 |

## 8.5 Discussion

We designed a table-top imaging system that was able to simultaneously image a 3D-printed small animal phantom filled with two contrast agents using XFCT, K-edge PCCT, and energy-integrated CT imaging. We performed simultaneous XFCT, K-edge PCCT, and energy-integrated CT imaging of pure and mixed concentrations of Gd and Au using a pencil beam geometry. We also demonstrated K-edge PCCT and energy-integrated CT imaging using a cone beam geometry.

Based on phantom data presented in Figure 8.5, XFCT imaging is best for imaging Gd solutions, and pencil beam PCCT imaging is best for imaging Au solutions. This applies to Gd and Au in a mixture, however with a penalty of decreased CNR and lowered reconstruction accuracy. Cone beam PCCT imaging has a negligible decrease in CNR for Gd solutions or a factor of 2 decrease in CNR for Au solutions compared to pencil beam PCCT imaging, however with the benefit of higher spatial resolution and faster imaging time critical for small animal imaging. When imaging Gd and Au present in a mixture, XFCT overall had the best reconstruction accuracy. However, the vials in the Au XFCT image had low CNR values due to noise from scattered x-rays.

Our table-top imaging system acquired simultaneous XFCT and K-edge PCCT images of euthanized mice injected with Gd and Au contrast using a pencil beam geometry, as well as K-edge and energy-integrated CT imaging using a cone beam

geometry. However, a major limitation was that the accuracy of the Gd and Au concentration in each mouse is unknown, and the energy-integrated CT images only provide limited information of where contrast solution actually exists in the mouse since solution was injected in the general upper thoracic region of each mouse. These mouse results were consistent with the phantom results in terms of expected image quality between XFCT and K-edge PCCT images, and the general trend of diminished contrast signal in K-edge PCCT images of the mixed Gd/Au solution. The presented cone beam images in Figure 8.8 all depict the image slice which had a high amount of contrast signal. The pencil beam geometry attempted to image this same cone beam slice 1 to 3 days post injection, however in that time the contrast solutions may have moved around inside the mouse due to gravity or handling and not have a consistent concentration between slices. In addition, mouse anatomy postmortem can be greatly affected due to organ relaxation, oxygen loss, and small changes in body mass due to secondary flaccidity, which makes the comparison between pencil beam and cone beam K-edge PCCT images limited[157]. Overall, these limitations render these results as preliminary.

### 8.5.1 XFCT

All contrast vials were visible in the Gd XFCT image (Figure 8.4a). The Gd signal in the XFCT image was quite strong compared to Au from Figure 8.3 because there were more x-rays above the K-edge of Gd (50.2 keV) than the K-edge of Au (80.7 keV) in the beam, which were capable of inducing fluorescent x-rays. The energy of the Au fluorescent x-rays were similar to that of Pb, which would have been induced from the shielding near the CdTe spectrometers to interfere with the Au signal. In addition, in Figure 8.3 there was a high amount of background counts in the CdTe #2 spectrum compared to CdTe #1 above 60 keV. At extreme translation positions, the Pb fluorescent x-rays interfered with the $K_{\beta 1}$ Au fluorescent x-rays. Both spectra in Figure 8.3 were taken at pencil beam positions near CdTe #2. The disparity between the amount of Compton scattered x-rays from the Pb shielding and the CdTe spectrometers is due to the different amount of Pb on each CdTe spectrometer; there was less Pb draped over CdTe #1 than CdTe #2.

### 8.5.2 K-edge PCCT

The pencil beam K-edge PCCT images showed visible pure 1% and 5% Gd and Au vials in their respective images in Figure 8.4b,e. The 1% Gd and Au vials were accurately reconstructed in these images, however the mixed 1% Gd and Au vials were below the actual concentration. The same was true with the Gd and Au cone beam K-edge PCCT images (Figure 8.4c,e). The ability to reconstruct mixed contrast agents may be limited by the simple K-edge subtraction used in reconstruction since the Gd and Au linear attenuation coefficients in the 1% mixed vial are additive and thus directly affect the contrast in the K-edge PCCT images. In the mixed 1% vial based on Figure 8.2b, subtracting the 35-50 keV bin from the 50-56 keV bin will result in the positive signal from the Gd K-edge combined with the negative signal from the Au attenuation curve, and vice versa when subtracting the 76-81 keV bin from the 81-85 keV bin. Since the difference in attenuation of Gd in the Au K-edge PCCT images is smaller than for Au in the Gd K-edge PCCT images, this effect is greater in the Gd K-edge PCCT images with the reconstructed concentration in the mixed 1% vial being as low as 0.30% compared to as low as 0.69% in the Au K-edge PCCT images.

### 8.5.3 Table-top Imaging System Design

In the design of the table-top imaging system, the CdTe spectrometers were placed at a backscattered angle of 135° 8 cm away from the phantom centre to optimize the sensitivity of the Au fluorescent x-rays[39] and minimize the detector pile-up in the CdTe spectrometers during imaging[59] in combination with the Pb shielding. Other design considerations included the x-ray beam and CZT detector energy thresholds based on the contrast agents in the phantom. The choice of the x-ray beam filtration was based on having enough x-rays above the K-edges of Gd and Au to induce fluorescence while having enough x-rays below the K-edge of Gd for an equal amount of x-rays in each energy bin to perform K-edge subtraction. As shown in Figure 8.2a, using 0.5 mm of Cu to filter the x-ray beam resulted in x-ray energies greater than 30 keV necessary to populate the lowest energy bin. Using filters with lower atomic number such as Al would have resulted in lower CNR for the Au XFCT image, and the lower energy x-rays would only contribute to the imaging dose[143]. However, Al filtration would allow for imaging contrast agents with lower atomic number such as iodine, as the CZT energy thresholds would need to be set to lower energies to

accommodate the lower K-edge energy.

The imaging doses for the pencil beam XFCT and K-edge PCCT images were different (680 mGy and 850 mGy, respectively) despite their concurrent data acquisition. This is due to the different data saving times in the photon-counting detector and each spectrometer of approximately 0.5 seconds and 2.5 seconds, respectively, which affected their acquisition time per projection. These imaging doses are too high for small animal imaging[103]. The imaging dose of 250 mGy for the cone beam K-edge PCCT was about 3 times less than that of the pencil beam K-edge PCCT likely in part due to the larger distance between the isocentre and the x-ray tube focal spot in the cone beam geometry (32 cm) compared to the pencil beam geometry (20 cm). Increasing this distance in the pencil beam geometry would decrease the spatial resolution of the resulting images as the beam size at the isocentre would increase. As 250 mGy is still too large of a dose for small animal imaging, reducing the acquisition time or further optimization of the table-top setup would lead to dose reduction. Further avenues for cone beam optimization include a larger CZT detector array to minimize geometric artifacts, as well as an alternative method of energy calibration of the CZT detector compared to the K-edge method that was used by the manufacturer.

### 8.5.4 Comparison with Other Studies

The simultaneous K-edge and x-ray fluorescence CT imaging (SKYFI) setup from Li *et al.* (2016) was theoretically capable of synchronized cone beam XFCT and K-edge PCCT using two CZT photon-counting detectors perpendicular to the beam to detect fluorescent x-rays with a pinhole collimator and another CZT photon-counting detector array against the incident beam for K-edge PCCT[156]. Only simulation results were presented in the Li *et al.* (2016) study of imaging AuNPs with concentrations ranging from 0.1% to 5% by weight in a 3.5 cm-diameter water phantom. The cone beam XFCT imaging sensitivity of AuNPs was 0.1%, where a CNR of 5 was met with 10 s collection time, and the cone beam K-edge PCCT imaging sensitivity of AuNPs was roughly the same. These sensitivities are better than that of our pencil beam XFCT Au sensitivity of 2.97% and cone beam K-edge PCCT Au sensitivity of 1.51%, as our results are experimental. There is also a difference in setup in terms of scanning geometry, detector type, beam filtration, reconstruction method, and phantom design. There was also no mention of dose in the Li *et al.* (2016) study. The addition of a detector array with ample collimation would enable cone beam XFCT

on our table-top imaging system.

The pencil beam XFCT imaging setup of Au in the Ahmad *et al.* (2015) study was able to detect 0.5% Au with one CdTe spectrometer at a backscattered angle of 145° measured from the beam axis[39]. Only the Au $K_{\beta 1}$ fluorescent x-rays contributed to the XFCT image at this detector angle. The phantom in the Ahmad *et al.* (2015) study was twice the diameter of our phantom with vial sizes of 2 cm in diameter. However, the XFCT imaging dose in Ahmad *et al.* (2015) was 14.2 mGy compared to our XFCT imaging dose of 680 mGy. Our CdTe spectrometers detected $K\alpha_1$, $K\alpha_2$, and $K\beta_1$ Au fluorescent x-rays with no scatter or attenuation correction, and XFCT images were reconstructed with FBP rather than with an iterative reconstruction method. The 120 kVp beam in Ahmad *et al.* (2015) was heavily filtered with 1 mm Pb, whereas our filtration of 0.5 mm Cu was optimal for imaging both Gd and Au with XFCT and K-edge PCCT. The Gd sensitivity of attenuation- and scatter-corrected cone beam XFCT in the Zhang *et al.* (2019) study was 0.18% in a 5 cm PMMA phantom with 11 mm vials[40]. This is in comparison with our Gd sensitivity of 0.75% for our pencil beam XFCT. Both imaging setups are different in imaging geometry, reconstruction method, XFCT detectors, and beam energy. The XFCT imaging dose in Zhang *et al.* (2019) was 455 mGy to the centre of the phantom.

Multiplexed pencil beam XFCT of Au, Gd, and barium was achieved in the Kuang *et al.* (2013) study, which detected 2% Au and Gd by weight in a 3.5 cm-diameter water phantom[45]. The imaging sensitivity of Au and Gd with the imaging setup in Kuang *et al.* (2013) was 0.25% and 0.00078%, respectively, for an imaging dose of 770 mGy. Their XFCT imaging setup was able to isolate the Au, Gd, and barium in the 2% mixture vial, similar to what we achieved with our 1% Gd and Au mixture. The x-ray beam used in Kuang *et al.* (2013) was 150 kVp with a mixture of Pb, Al, and Cu filtration, and the XFCT images were reconstructed with an iterative reconstruction method.

The PCCT imaging system from Si-Mohamed *et al.* (2018) used a 120 kVp x-ray beam in 1-second rotations which could detect 1% Gd and Au with a CNR of 31.1 and 28.0, respectively, with a pixel size of 400 $\mu$m[128]. In comparison, our cone beam K-edge PCCT CNR values of 1% Gd and Au were 5.4 and 3.4, respectively, for a reconstructed voxel size of 250 $\mu$m. The x-ray tube in the Si-Mohamed *et al.* (2018) study had a tube current of 10 mA - 100 mA, which is much higher than the 2 mA tube current we used with 0.5 mm Cu filtration and may explain the higher CNR values. In Si-Mohamed *et al.* (2018), the CNR of 1% Gd and Au in the presence of

each other was 16.7 and 13.7, respectively, in comparison with our mixed 1% Gd and Au CNR values of 1.9 and 2.3, respectively, for cone beam K-edge PCCT. The Si-Mohamed *et al.* (2018) study also demonstrated the reduction of CNR when imaging mixed Gd and Au compared with pure Gd and Au using PCCT. Aside from the larger 13 cm-diameter phantom and larger vial sizes of diameter 1.5 cm, the energy thresholds on the prototype photon-counting detector used in the Si-Mohamed *et al.* (2018) study were optimized for each of the separate scans of pure and mixed Gd and Au, which were reconstructed using basis material decomposition and free from ring artifacts. Our energy thresholds were chosen to optimize a simultaneous XFCT and PCCT scan using K-edge subtraction.

## 8.6 Conclusions

We demonstrated simultaneous pencil beam XFCT, K-edge PCCT, and energy-integrated CT of a small animal phantom containing vials of Gd and Au. We also showed preliminary images of three euthanized mice each injected with Gd only, Au only, and a mixture of Gd and Au solutions. The design of this table-top imaging system was enabled by two CdTe spectrometers and a high-flux CZT photon-counting detector. The pencil beam geometry allowed for implementation of XFCT, which was able to better reconstruct mixed concentrations of 1% Gd and Au than pencil or cone beam K-edge PCCT. Our imaging system was capable of PCCT using a cone beam geometry. Cone beam PCCT enabled K-edge PCCT of Gd and Au at high spatial resolution and lower imaging time compared to pencil beam, however imaging sensitivity of Au was lower for the cone beam geometry. The reduction of imaging dose, scatter and attenuation correction, and implementing a larger detector array to enable cone beam XFCT will be the focus of future development.

# Chapter 9

# Conclusions

Contrast agents such as iodine and gadolinium are frequently used to aid in disease diagnosis using CT or MRI, respectively. Novel contrast agents in the lanthanide group and AuNPs have promising utility in small animal imaging and in the clinic; for instance AuNPs are of interest as radio-sensitizers for cancer treatment during radiation therapy. The ability to detect contrast agents when inside a phantom, small animal, or patient with innovative medical imaging techniques is crucial for their intended purpose.

XFCT has progressed into a promising imaging modality for detecting trace amounts of contrast agent for small animal imaging. The efficiency of fluorescent x-ray detection and attenuation of the excitation beam and fluorescent x-rays are factors contributing to the long scan time of XFCT and thus limit the expansion of XFCT to the clinic. However, it is known that K-shell XFCT can detect lower concentrations of AuNPs compared to energy-integrated CT and K-edge PCCT, and L-shell XFCT can further lower the minimum detectable concentration of AuNPs due to the higher interaction probability of low energy x-rays producing more L-shell fluorescent x-rays.

X-ray PCCT is capable of producing multicoloured CT images with energy-resolving photon counting detectors. Several preclinical x-ray scanners capable of PCCT have successfully produced maps of contrast agents such as iodine, gadolinium, and gold, which is powerful for disease diagnosis. Clinical translation of PCCT has been limited by the low energy resolution and low maximum count rate on many photon counting detectors, which are not appropriate for high-flux conditions demanded by clinical CT.

As a top-level summary of this dissertation, we have presented a design for a table-top x-ray system for small animal imaging capable of detecting contrast agents

in phantoms and in mice using both XFCT and PCCT. We showed in Monte Carlo simulations that XFCT induced by x-rays resulted in the best image quality of AuNPs and is the most practical, but XFCT can be promising for detecting AuNPs for electron and proton beam therapy using x-ray fluorescence techniques. Another series of Monte Carlo simulations documented the expected CNR for different arrangements of eight spectrometers for pencil beam XFCT imaging of AuNPs, which was directly applicable for designing the XFCT portion of the table-top system capable of faster imaging time. In another set of Monte Carlo simulations, we found an optimal collimator arrangement for faster XFCT imaging of AuNPs with minimal compromise in AuNP sensitivity should the table-top system be further modified to perform sheet beam or cone beam XFCT. An experimental PCCT study demonstrated the ability to image multiple lanthanide contrast agents in a single scan, with minimal cross contamination in particular between elements close together in $Z$. These studies led up to the design of our XFCT and PCCT system, which could image both Gd and Au solutions. Our hybrid table-top system offers high-sensitivity and at-depth imaging of contrast agents characteristic of XFCT and PCCT, respectively, with the added benefit of CT providing anatomical information enabled by integrating the PCCT data. For imaging multiple contrast agents at once, we have demonstrated the need for XFCT to accurately reconstruct spatially-coincident contrast agents compared to K-edge subtraction imaging. The presented work in this dissertation for our table-top system is currently suitable for preclinical applications, as the attenuation of fluorescent x-rays in large objects prohibits clinical translation of XFCT at this time. However, the photon-counting detector employed on this system is capable of sustaining high-flux conditions typical of clinical CT imaging; further detector development may result in routine clinical use of PCCT for detecting contrast agents.

The next section will summarize the presented work in this dissertation on a chapter by chapter basis.

## 9.1 Summary

**Chapter 1** motivated the use of contrast agents in medical imaging, and introduced the relevant particle interactions underlying the physics behind the concepts of CT, XFCT, and PCCT.

**Chapters 2 and 3** laid the foundations of the materials and methods used in this research. A review of x-ray generation and detection, Monte Carlo methods,

and film dosimetry was introduced in the former chapter, and a detailed description of the process from data acquisition to image reconstruction to image analysis was outlined in the latter chapter. The first three chapters are crucial in understanding the research presented in this dissertation.

In **Chapter 4** we documented the expected CNR per unit phantom dose in K-shell and L-shell XFCT images of AuNPs for a variety of excitation beams using Monte Carlo simulations. These excitation beams included 81 keV and 5 MeV photon, 220 kVp and 6 MV photon, 10 MeV and 100 MeV electron, and 100 MeV and 250 MeV proton pencil beams incident on a 2.5 cm- and 5 cm-diameter water phantoms. The best image overall was L-shell XFCT produced by 81 keV photon beams with a AuNP sensitivity of 0.003%, with 220 kVp photon beams only having a slight decrease in AuNP sensitivity at 0.1% when imaging the 2.5 cm-diameter phantom for a dose of 30 mGy. In addition, K-shell XFCT images of the 5 cm-diameter phantom induced by 100 MeV electron beams and L-shell XFCT images of the 2.5 cm-diameter phantom induced by 100 MeV proton beams had AuNP sensitivities of 0.49% and 0.28%, respectively, for a dose of 30 mGy. These results suggest that x-ray fluorescence techniques may be a feasible option for onboard imaging of AuNP-enhanced radiotherapy, as these AuNP sensitivities were within the range of biological relevance. Since x-ray tubes are readily available to produce photon beams for XFCT imaging with good CNR per unit dose, polyenergetic photon beams were chosen as the main radiation source for our table-top imaging system for small animal imaging purposes out of feasibility.

We have shown in **Chapter 5** that the collimator geometry can affect the AuNP imaging sensitivity for both K-shell and L-shell XFCT induced by a sheet beam of monoenergetic x-rays in Monte Carlo simulations. Out of the three collimator geometries presented, the parallel collimator was able to detect the lowest sensitivity of AuNPs in a 2 mm-diameter vial of 0.08% and 0.09% for K-shell and L-shell XFCT imaging, respectively, for an acceptable imaging dose of 30 mGy. This AuNP sensitivity was similar to that achievable with a pencil beam geometry for the same imaging dose, but with the added benefit of a 55-fold reduction of imaging time. This reduction of imaging time addresses a major limitation in table-top XFCT imaging systems.

In **Chapter 6** we modeled the data acquisition of our eight available spectrometers in Monte Carlo simulations to find the arrangement that optimizes AuNP sensitivity for pencil beam K-shell and L-shell XFCT imaging. In addition we documented the tradeoff of active area and energy resolution for our CdTe spectrometers, assessed

the data acquisition strategy of stationary vs. moving spectrometers, and varied the depth of AuNP vials in the phantom to evaluate the efficacy of K-shell and L-shell XFCT. A backscattered grid spectrometer arrangement was found to be the optimal arrangement with the lowest minimum concentration of AuNP detectable of 0.055% for K-shell XFCT and 0.095% for L-shell XFCT, though the spectrometer arrangement was not a significant factor for AuNP sensitivity in L-shell XFCT. Our table-top system will be best suited for imaging shallow, subcutaneous AuNPs using L-shell XFCT and imaging deep, orthotopic AuNPs using K-shell XFCT. These simulated results have helped in the design of our table-top x-ray imaging system.

**Chapter 7** is our first experimental study in which we have simultaneously imaged three contrast agents in a small animal-sized phantom with PCCT. We introduced a "weighted" K-edge subtraction algorithm to reconstruct contrast agent maps using a high-flux photon counting detector. The contrast agents that were studied included the clinically-relevant I and Gd in combination with novel lanthanide contrast agents such as La, Lu, and Ho at varying concentrations in each vial. Each contrast agent was reconstructed with excellent signal linearity with a difference between reconstructed and actual concentration of no more than 0.25%. In particular we could image Gd and Ho separately when in the same phantom with minimal cross contamination of RMSE $< 0.27\%$ in zero contrast vials; remarkably the atomic numbers of Gd and Ho were 64 and 67, and their K-edge energies were 50.2 keV and 55.6 keV, respectively. This demonstration on a cone beam table-top imaging system could lead to improved disease diagnosis with novel contrast agents.

**Chapter 8** describes the design of a table-top x-ray imaging system capable of simultaneous XFCT and PCCT imaging of 1% and 5% Gd and Au solutions in a phantom and in mice. This was achieved using a high-flux CZT photon-counting detector and two CdTe spectrometers to detect K-shell fluorescent x-rays in a pencil beam geometry, and only PCCT images were reconstructed in a cone beam geometry. When imaging 1% pure and mixed Gd solution, using pencil beam XFCT resulted in the highest CNR of 6.0 and 5.7, compared to pencil beam (CNR of 5.4 and 2.0) and cone beam PCCT (CNR of 5.2 and 1.9), respectively. When imaging 1% pure and mixed Au solution, using pencil beam PCCT resulted in the highest CNR of 6.1 and 4.2 compared to the noisy pencil beam XFCT and cone beam PCCT (CNR of 3.0 and 2.1), respectively, with only a modest decrease in CNR if Au was mixed with Gd. Accurately reconstructing concentrations of Gd when mixed with Au has been identified as a benefit of XFCT over K-edge PCCT. Going ahead with cone

beam PCCT imaging, however, would greatly increase the imaging time and spatial resolution with a minor decrease in CNR compared to pencil beam XFCT and PCCT imaging of Gd and Au solutions, respectively.

Finally, **Chapter 9** brings this dissertation to a close with a summary of the research presented above and a discussion of future work to further develop the table-top x-ray imaging system. I believe this research has contributed in developing novel imaging methods for improving contrast agent detection for disease diagnosis.

## 9.2 Future Work

This research dissertation has laid the groundwork for the design of our table-top x-ray imaging system, which is capable of simultaneous pencil beam XFCT and PCCT imaging. There are plenty of projects to further develop the table-top system.

The research presented in Chapter 6 introduced the stripping method as an algorithm for correcting detector response. This helped improve the number of detected fluorescent x-ray counts in each spectrometer of the XFCT simulations. The stripping method could be applied to the spectrometer data from experimental XFCT scans, or more ambitiously, to the photon-counting detector data for each pixel. The photon counting detector in this research is capable of sustaining high photon fluxes of 2.5 $\times 10^8$ cps, but comes at a cost of charge sharing between pixels that degrade the image quality. Even though the photon counting detector does have a charge sharing discrimination setting enabled, it is not perfect. The XCITE lab, together with Redlen Technologies, will investigate the effect of pulse width on resulting K-edge images in conjunction with a group at Ryerson University who is working on a comprehensive charge-sharing correction algorithm that will improve x-ray detection efficiency and the resulting image quality.

The XCITE lab, at time of writing, will obtain a new CZT photon-counting detector that is 20 cm wide and 1 cm in height, which is quite the improvement compared to the current detector with a width of only 2.4 cm. This removes the need for detector translations during cone beam PCCT data acquisition of the small animal phantom, which will thus reduce the acquisition time by a factor of three. This opens up many doors towards dynamic imaging to simulate a baggage scan, or imaging larger objects for PCCT such as rat-, dog-, or human-sized phantoms. A larger pixelated photon-counting detector could also be repurposed as a XFCT detector with the appropriate collimation. A multi-pinhole collimator such as the one introduced in Chapter 5 could

be manufactured to fit over each pixel or aggregation of pixels. Alternatively, using a single pinhole collimator[43] is a simpler design but would reduce the number of detected fluorescent x-rays for constant dose compared to a multi-pinhole collimator. Using a photon-counting detector compared to a spectrometer to detect fluorescent x-rays would mean a compromise in energy resolution of 8.9 keV at 60 keV compared to 900 eV at 81 keV for the 25 $mm^2$ CdTe spectrometer, so would be limited to detecting only K-shell fluorescent x-rays from high-$Z$ contrast agents within a specific energy range set on the detector. This setup could enable fan beam XFCT of small animal phantoms with a faster acquisition time than the current pencil beam strategy on our table-top imaging system.

The combined XFCT and PCCT table-top x-ray imaging system presented in **Chapter 8** will need further optimization based on the desired contrast agents. Parameters such as the energy bin thresholds on the photon counting detector should be optimized based on the CNR of the K-edge images, rather than the expected x-ray fluence. The x-ray tube energy and filtration is another important parameter of the imaging system that should be optimized based on the CNR and imaging dose. Parameter optimization for PCCT has been studied for gold and some lathanide contrast agents[143], but not yet for a combined XFCT and PCCT imaging system. The XFCT portion of the table-top imaging system only used two CdTe spectrometers. The XFCT imaging sensitivity could be further improved by the use of all eight spectrometers available in the lab for combined K-shell and L-shell XFCT. The attenuation correction that was developed for iterative reconstruction could be used to reconstruct better XFCT images compared to those reconstructed using FBP.

Currently our contrast agent images are reconstructed using some form of K-edge subtraction imaging from the PCCT data. Other PCCT scanners use a basis material decomposition algorithm to reconstruct contrast agent images as well as calcium[138, 144, 154]. Implementing a similar algorithm to our PCCT data would allow for a more fair comparison between our images and other PCCT images, and possibly improve the imaging sensitivity. Based on the results of Chapter 8, it is also worth investigating PCCT imaging of contrast agents that are mixed together; the use of multiple contrasts in possible clinical scenarios such as colonography[123] and abdominal perfusion imaging[122] may involve some spatial overlap between them.

Lastly, the imaging doses reported throughout the experimental work throughout this dissertation are too high even for small animal imaging. There is room for exploration of dose reduction techniques to render our table-top x-ray imaging system

feasible for imaging of small animals under anesthesia within an acceptable time frame. This may involve reducing the beam current on the x-ray tube or decreasing the data acquisition time, but at the expense of decreasing CNR. Optimizing the filtration of the incident x-ray beam may help in dose reduction by removing lower energy x-rays.

# Bibliography

[1] Darren R Brenner, Hannah K Weir, Alain A Demers, Larry F Ellison, Cheryl Louzado, Amanda Shaw, Donna Turner, Ryan R Woods, and Leah M Smith. Projected estimates of cancer in Canada in 2020. *Cmaj*, 192(9):E199–E205, 2020.

[2] Ukihide Tateishi, Hiroshi Nishihara, Satoshi Watanabe, Toshiaki Morikawa, Kazuhiro Abe, and Kazuo Miyasaka. Tumor angiogenesis and dynamic CT in lung adenocarcinoma: radiologic–pathologic correlation. *Journal of computer assisted tomography*, 25(1):23–27, 2001.

[3] B Wintersperger, T Jakobs, P Herzog, S Schaller, K Nikolaou, C Suess, C Weber, M Reiser, and C Becker. Aorto-iliac multidetector-row CT angiography with low kv settings: improved vessel enhancement and simultaneous reduction of radiation dose. *European radiology*, 15(2):334–341, 2005.

[4] Xuemei Hu, Liya Ma, Jinhua Zhang, Zhen Li, Yaqi Shen, and Daoyu Hu. Use of pulmonary CT angiography with low tube voltage and low-iodine-concentration contrast agent to diagnose pulmonary embolism. *Scientific Reports*, 7(1):1–8, 2017.

[5] Claudia Calcagno, Sarayu Ramachandran, Antoine Millon, Philip M Robson, Venkatesh Mani, and Zahi Fayad. Gadolinium-based contrast agents for vessel wall magnetic resonance imaging (MRI) of atherosclerosis. *Current cardiovascular imaging reports*, 6(1):11–24, 2013.

[6] C Saade, R Bou-Fakhredin, David Mark Yousem, K Asmar, L Naffaa, and F El-Merhi. Gadolinium and multiple sclerosis: vessels, barriers of the brain, and glymphatics. *American Journal of Neuroradiology*, 39(12):2168–2176, 2018.

[7] David S Gierada and Kyongtae T Bae. Gadolinium as a CT contrast agent: assessment in a porcine model. *Radiology*, 210(3):829–834, 1999.

[8] Keika Ose, Tomoki Doue, Kan Zen, Mitsuyoshi Hadase, Takahisa Sawada, Akihiro Azuma, and Hiroaki Matsubara. Gadolinium as an alternative to iodinated contrast media for x-ray angiography in patients with severe allergy. *Circulation Journal*, 69(4):507–509, 2005.

[9] Devika B Chithrani, Salomeh Jelveh, Farid Jalali, Monique van Prooijen, Christine Allen, Robert G Bristow, Richard P Hill, and David A Jaffray. Gold nanoparticles as radiation sensitizers in cancer therapy. *Radiation research*, 173(6):719–728, 2010.

[10] James F Hainfeld, Daniel N Slatkin, and Henry M Smilowitz. The use of gold nanoparticles to enhance radiotherapy in mice. *Physics in Medicine & Biology*, 49(18):N309, 2004.

[11] Priyanka Singh, Santosh Pandit, VRSS Mokkapati, Abhroop Garg, Vaishnavi Ravikumar, and Ivan Mijakovic. Gold nanoparticles in diagnostics and therapeutics for human cancer. *International journal of molecular sciences*, 19(7):1979, 2018.

[12] Nikolai Khlebtsov and Lev Dykman. Biodistribution and toxicity of engineered gold nanoparticles: a review of in vitro and in vivo studies. *Chemical Society Reviews*, 40(3):1647–1671, 2011.

[13] RC Murty. Effective atomic numbers of heterogeneous materials. *Nature*, 207(4995):398–399, 1965.

[14] Harold Elford Johns and John Robert Cunningham. The physics of radiology. 1983.

[15] John H Hubbell and Stephen M Seltzer. Tables of x-ray mass attenuation coefficients and mass energy-absorption coefficients 1 kev to 20 Mev for elements Z = 1 to 92 and 48 additional substances of dosimetric interest. Technical report, National Inst. of Standards and Technology-PL, Gaithersburg, MD, United States Department of Commerce, Technology Administration, National Institute of Standards and Technology, 1996, updated 2004 Jul.

[16] Oskar Klein and Yoshio Nishina. The scattering of light by free electrons according to Dirac's new relativistic dynamics. *Nature*, 122(3072):398–399, 1928.

[17] Lise Meitner. Über die entstehung der $\beta$-strahl-spektren radioaktiver substanzen. *Zeitschrift für Physik*, 9(1):131–144, 1922.

[18] Frank Herbert Attix. *Introduction to radiological physics and radiation dosimetry*. John Wiley & Sons, 2008.

[19] Sven AE Johansson and Thomas B Johansson. Analytical application of particle induced x-ray emission. *Nuclear Instruments and Methods*, 137(3):473–516, 1976.

[20] Bernard Gottschalk. Physics of proton interactions in matter. *Proton Therapy Physics*, pages 19–60, 2012.

[21] Godfrey N Hounsfield. Computerized transverse axial scanning (tomography): Part 1. Description of system. *The British journal of radiology*, 46(552):1016–1022, 1973.

[22] Willi A Kalender. X-ray computed tomography. *Physics in Medicine & Biology*, 51(13):R29, 2006.

[23] Do Hyung Lee, Young Hen Lee, Hyung Suk Seo, Ki Yeol Lee, Sang-il Suh, Inseon Ryoo, Sung-Hye You, Byungjun Kim, and Kyung-Sook Yang. Dual-energy CT iodine quantification for characterizing focal thyroid lesions. *Head & neck*, 41(4):1024–1031, 2019.

[24] Jessica G Zarzour, Desmin Milner, Roberto Valentin, Bradford E Jackson, Jennifer Gordetsky, Janelle West, Soroush Rais-Bahrami, and Desiree E Morgan. Quantitative iodine content threshold for discrimination of renal cell carcinomas using rapid kV-switching dual-energy CT. *Abdominal Radiology*, 42(3):727–734, 2017.

[25] Thorsten R. C. Johnson, Bernhard Krauß, Martin Sedlmair, Michael Grasruck, Herbert Bruder, Dominik Morhard, Christian Fink, Sabine Weckbach, Miriam Lenhard, Bernhard Schmidt, Thomas Flohr, Maximilian F. Reiser, and Christoph R. Becker. Material differentiation by dual energy CT: initial experience. *European Radiology*, 17(6):1510–1517, Jun 2007.

[26] Jerrold T Bushberg and John M Boone. *The essential physics of medical imaging*. Lippincott Williams & Wilkins, 2011.

[27] Alvin C Silva, Brian G Morse, Amy K Hara, Robert G Paden, Norio Hongo, and William Pavlicek. Dual-energy (spectral) CT: applications in abdominal imaging. *Radiographics*, 31(4):1031–1046, 2011.

[28] Robert E Alvarez and Albert Macovski. Energy-selective reconstructions in x-ray computerised tomography. *Physics in Medicine & Biology*, 21(5):733, 1976.

[29] E Roessl and R Proksa. K-edge imaging in x-ray computed tomography using multi-bin photon counting detectors. *Physics in Medicine & Biology*, 52(15):4679, 2007.

[30] JPea Schlomka, E Roessl, R Dorscheid, S Dill, G Martens, T Istel, C Bäumer, C Herrmann, R Steadman, G Zeitler, et al. Experimental feasibility of multi-energy photon-counting K-edge imaging in pre-clinical computed tomography. *Physics in Medicine & Biology*, 53(15):4031, 2008.

[31] Jeffrey F Marsh, Steven M Jorgensen, David S Rundle, Andrew J Vercnocke, Shuai Leng, Philip H Butler, Cynthia H McCollough, and Erik L Ritman. Evaluation of a photon counting Medipix3RX cadmium zinc telluride spectral x-ray detector. *Journal of Medical Imaging*, 5(4):043503, 2018.

[32] Nigel G Anderson and Anthony P Butler. Clinical applications of spectral molecular imaging: potential and challenges. *Contrast media & molecular imaging*, 9(1):3–12, 2014.

[33] K Iniewski. CZT sensors for Computed Tomography: from crystal growth to image quality. *Journal of Instrumentation*, 11(12):C12034, 2016.

[34] Shuai Leng, Michael Bruesewitz, Shengzhen Tao, Kishore Rajendran, Ahmed F Halaweish, Norbert G Campeau, Joel G Fletcher, and Cynthia H McCollough. Photon-counting detector CT: System design and clinical applications of an emerging technology. *RadioGraphics*, 39(3):729–743, 2019.

[35] Mahdieh Moghiseh, Chiara Lowe, John G Lewis, Dhiraj Kumar, Anthony Butler, Nigel Anderson, and Aamir Raja. Spectral photon-counting molecular imaging for quantification of monoclonal antibody-conjugated gold nanoparticles targeted to lymphoma and breast cancer: an in vitro study. *Contrast media & molecular imaging*, 2018, 2018.

[36] P. Boisseau and L. Grodzins. Fluorescence tomography using synchrotron radiation at the NSLS. *Hyperfine Interactions*, 33(1):283–292, Mar 1987.

[37] A Simionovici, M Chukalina, Ch Schroer, M Drakopoulos, A Snigirev, I Snigireva, B Lengeler, K Janssens, and F Adams. High-resolution x-ray fluorescence microtomography of homogeneous samples. *IEEE Transactions on Nuclear Science*, 47(6):2736–2740, 2000.

[38] Nivedh Manohar, Francisco J Reynoso, and Sang Hyun Cho. A benchtop cone-beam x-ray fluorescence computed tomography (XFCT) system with a high-power x-ray source and transmission CT imaging capability. *Medical physics*, 45(10):4652–4659, 2018.

[39] Moiz Ahmad, Magdalena Bazalova-Carter, Rebecca Fahrig, and Lei Xing. Optimized detector angular configuration increases the sensitivity of x-ray fluorescence computed tomography (XFCT). *IEEE Transactions on Medical Imaging*, 34(5):1140–1147, 2015.

[40] Siyuan Zhang, Liang Li, Jiayou Chen, Zhiqiang Chen, Wenli Zhang, and Hongbing Lu. Quantitative imaging of Gd nanoparticles in mice using benchtop cone-beam x-ray fluorescence computed tomography system. *International journal of molecular sciences*, 20(9):2315, 2019.

[41] Bernard L Jones and Sang Hyun Cho. The feasibility of polychromatic cone-beam x-ray fluorescence computed tomography (XFCT) imaging of gold nanoparticle-loaded objects: a Monte Carlo study. *Physics in Medicine & Biology*, 56(12):3719–3730, 2011.

[42] K Ricketts, Andrea Castoldi, Chiara Guazzoni, Cigdem Ozkan, C Christodoulou, AP Gibson, and GJ Royle. A quantitative x-ray detection system for gold nanoparticle tumour biomarkers. *Physics in Medicine & Biology*, 57(17):5543–5555, 2012.

[43] Wei Fang, Liang Li, and Siyuan Zhang. Fan-beam x-ray fluorescence computed tomography (XFCT) with gold nanoparticles. In *2017 IEEE Nuclear Science Symposium and Medical Imaging Conference (NSS/MIC)*, pages 1–4. IEEE, 2017.

[44] Seongmoon Jung, Wonmo Sung, and Sung-Joon Ye. Pinhole x-ray fluorescence imaging of gadolinium and gold nanoparticles using polychromatic x-rays: a Monte Carlo study. *International Journal of Nanomedicine*, 12:5805, 2017.

[45] Yu Kuang, Guillem Pratx, Magdalena Bazalova, Bowen Meng, Jianguo Qian, and Lei Xing. First demonstration of multiplexed x-ray fluorescence computed tomography (XFCT) imaging. *IEEE transactions on medical imaging*, 32(2):262–267, 2012.

[46] Don Vernekohl, Stratis Tzoumas, Wei Zhao, and Lei Xing. Polarized X-ray excitation for scatter reduction in X-ray fluorescence computed tomography. *Medical physics*, 2018.

[47] Moiz Ahmad, Magdalena Bazalova, Liangzhong Xiang, and Lei Xing. Order of magnitude sensitivity increase in x-ray fluorescence computed tomography (XFCT) imaging with an optimized spectro-spatial detector configuration: theory and simulation. *IEEE Transactions on Medical Imaging*, 33(5):1119–1128, 2014.

[48] Bernard L Jones, Nivedh Manohar, Francisco Reynoso, Andrew Karellas, and Sang Hyun Cho. Experimental demonstration of benchtop x-ray fluorescence computed tomography (XFCT) of gold nanoparticle-loaded objects using lead- and tin-filtered polychromatic cone-beams. *Physics in Medicine & Biology*, 57(23):N457, 2012.

[49] Wenxiang Cong, Haiou Shen, Guohua Cao, Hong Liu, and Ge Wang. X-ray fluorescence tomographic system design and image reconstruction. *Journal of X-ray science and technology*, 21(1):1–8, 2013.

[50] Geng Fu, Ling-Jian Meng, Peter Eng, Matt Newville, Phillip Vargas, and Patrick La Riviere. Experimental demonstration of novel imaging geometries for x-ray fluorescence computed tomography. *Medical physics*, 40(6Part1):061903, 2013.

[51] Tenta Sasaya, Naoki Sunaguchi, Kazuyuki Hyodo, Tsutomu Zeniya, and Tetsuya Yuasa. Multi-pinhole fluorescent x-ray computed tomography for molecular imaging. *Scientific reports*, 7(1):5742, 2017.

[52] Magdalena Bazalova, Yu Kuang, Guillem Pratx, and Lei Xing. Investigation of X-ray fluorescence computed tomography (XFCT) and K-edge imaging. *IEEE Transactions on Medical Imaging*, 31(8):1620–1627, 2012.

[53] Peng Feng, Wenxiang Cong, Biao Wei, and Ge Wang. Analytic comparison between x-ray fluorescence CT and K-edge CT. *IEEE Transactions on Biomedical Engineering*, 61(3):975–985, 2013.

[54] Nivedh Manohar, Francisco J Reynoso, and Sang Hyun Cho. Experimental demonstration of direct L-shell x-ray fluorescence imaging of gold nanoparticles using a benchtop x-ray source. *Medical physics*, 40(8):080702, 2013.

[55] Magdalena Bazalova-Carter, Moiz Ahmad, Lei Xing, and Rebecca Fahrig. Experimental validation of L-shell x-ray fluorescence computed tomography imaging: phantom study. *Journal of Medical Imaging*, 2(4):043501, 2015.

[56] Magdalena Bazalova-Carter. The potential of L-shell X-ray fluorescence CT (XFCT) for molecular imaging. *The British Journal of Radiology*, 88(1055):20140308, 2015. PMID: 26204972.

[57] A Thompson, D Attwood, E Gullikson, M Howells, K-J Kim, J Kirz, J Kortright, I Lindau, Y Liu, P Pianetta, A Robinson, J Scofield, J Underwood, G Williams, and W Winick. *X-Ray Data Booklet*. Berkeley, CA: Lawrence Berkeley National Laboratory, 2009.

[58] Robert Redus. Charge trapping in XR-100T-CdTe cadmium telluride detectors application note (ANCZT-2 Rev. 3). Available at https://www.amptek.com/internal-products/charge-trapping-in-xr-100t-cdte-cadmium-telluride-detectors-application-note (2020/07/17).

[59] CAS Dunning and M Bazalova-Carter. Optimization of a table-top x-ray fluorescence computed tomography (XFCT) system. *Physics in Medicine & Biology*, 63(23):235013, 2018.

[60] Stephen M Seltzer. Calculated response of intrinsic germanium detectors to narrow beams of photons with energies up to ∼300 keV. *Nuclear Instruments and Methods in Physics Research*, 188(1):133–151, 1981.

[61] Martin J Willemink, Mats Persson, Amir Pourmorteza, Norbert J Pelc, and Dominik Fleischmann. Photon-counting CT: technical principles and clinical prospects. *Radiology*, 289(2):293–312, 2018.

[62] Dean Karlen. *PHYS 515 course notes*. University of Victoria, 2015.

[63] Sea Agostinelli, John Allison, K al Amako, John Apostolakis, H Araujo, P Arce, M Asai, D Axen, S Banerjee, G 2 Barrand, et al. GEANT4a simulation toolkit. *Nuclear Instruments and Methods in Physics Research Section A: Accelerators, Spectrometers, Detectors and Associated Equipment*, 506(3):250–303, 2003.

[64] Christina Zacharatou Jarlskog and Harald Paganetti. Physics settings for using the Geant4 toolkit in proton therapy. *IEEE Transactions on nuclear science*, 55(3):1018–1025, 2008.

[65] Herman Kahn. Applications of Monte Carlo. Technical report, RAND Corp., Santa Monica, Calif., 1954.

[66] DE Raeside. An introduction to Monte Carlo methods. *American Journal of Physics*, 42(1):20–26, 1974.

[67] TT Böhlen, F Cerutti, MPW Chin, Alberto Fassò, Alfredo Ferrari, PG Ortega, Andrea Mairani, Paola R Sala, G Smirnov, and V Vlachoudis. The FLUKA code: developments and challenges for high energy and medical applications. *Nuclear data sheets*, 120:211–214, 2014.

[68] A Ferrari, PR Sala, A Fassò, and J Ranft. FLUKA: a multi-particle transport code. CERN Yellow Report 2005-10. Technical report, INFN/TC_05/11, SLAC, 2005.

[69] Joseph Perl, Jungwook Shin, Jan Schümann, Bruce Faddegon, and Harald Paganetti. TOPAS: An innovative proton Monte Carlo platform for research and clinical applications. *Medical physics*, 39(11):6818–6837, 2012.

[70] Joost Mathijs Verburg, Clemens Grassberger, Stephen Dowdell, Jan Schuemann, Joao Seco, and Harald Paganetti. Automated Monte Carlo simulation of proton therapy treatment plans. *Technology in cancer research & treatment*, 15(6):NP35–NP46, 2016.

[71] I Kawrakow and D W O Rogers. The EGSnrc code system: Monte Carlo simulation of electron and photon transport. *NRCC Report PIRS-701 (Ottawa: NRCC)*, 2006.

[72] D W O Rogers, B Walters, and I Kawrakow. BEAMnrc users manual. *NRCC Report PIRS-0509 (Ottawa: NRCC)*, 2006.

[73] Dylan Y Breitkreutz, Nolan M Esplen, Michael D Weil, and Magdalena Bazalova-Carter. Experimental demonstration of the skin sparing ability of a proof-of-principle kilovoltage arc therapy system. *Medical physics*, Under review, 2020.

[74] Iwan Kawrakow, DWO Rogers, and BRB Walters. Large efficiency improvements in BEAMnrc using directional bremsstrahlung splitting: directional bremsstrahlung splitting. *Medical physics*, 31(10):2883–2898, 2004.

[75] Sang Chul Lee, Ho Kyung Kim, In Kon Chun, Myung Hye Cho, Soo Yeol Lee, and Min Hyoung Cho. A flat-panel detector based micro-CT system: performance evaluation for small-animal imaging. *Physics in Medicine & Biology*, 48(24):4173, 2003.

[76] Lucien Pages, Evelyne Bertel, Henri Joffre, and Laodamas Sklavenitis. Energy loss, range, and bremsstrahlung yield for 10-kev to 100-Mev electrons in various elements and chemical compounds. *Atomic Data and Nuclear Data Tables*, 4:1–27, 1972.

[77] Cynthia H McCollough, Jerrold T Bushberg, Joel G Fletcher, and Laurence J Eckel. Answers to common questions about the use and safety of CT scans. In *Mayo Clinic Proceedings*, volume 90, pages 1380–1392. Elsevier, 2015.

[78] Christopher Daniel Johnstone and Magdalena Bazalova-Carter. MicroCT imaging dose to mouse organs using a validated Monte Carlo model of the small animal radiation research platform (SARRP). *Physics in Medicine & Biology*, 63(11):115012, 2018.

[79] Nobuyuki Miyahara, Toshiaki Kokubo, Yukihiro Hara, Ayuta Yamada, Takafumi Koike, and Yoshinori Arai. Evaluation of x-ray doses and their corresponding biological effects on experimental animals in cone-beam micro-CT scans (R-mCT2). *Radiological physics and technology*, 9(1):60–68, 2016.

[80] Ashland Advanced Materials. *Gafchromic® EBT3 Specification and User Guide*. Retrieved 5 August 2020.

[81] Cheryl Duzenli. *Radiation dosimetry measurement techniques in radiation therapy*. BC Cancer Agency – Vancouver, 2015.

[82] James A Sorenson, Michael E Phelps, et al. *Physics in nuclear medicine*. Grune & Stratton New York, 1987.

[83] Johann Radon. On the determination of functions from their integral values along certain manifolds. *IEEE transactions on medical imaging*, 5(4):170–176, 1986.

[84] Steven W Smith et al. The scientist and engineer's guide to digital signal processing. 1997.

[85] Stéfan van der Walt, Johannes L. Schönberger, Juan Nunez-Iglesias, François Boulogne, Joshua D. Warner, Neil Yager, Emmanuelle Gouillart, Tony Yu, and the scikit-image contributors. scikit-image: image processing in Python. *PeerJ*, 2:e453, 6 2014.

[86] Lee A Feldkamp, LC Davis, and James W Kress. Practical cone-beam algorithm. *Journal of the Optical Society of America*, 1(6):612–619, 1984.

[87] Kyungsang Kim. 3d Cone beam CT (CBCT) projection backprojection FDK, iterative reconstruction Matlab examples. *MATLAB Central File Exchange*, 2020.

[88] Lawrence A Shepp and Yehuda Vardi. Maximum likelihood reconstruction for emission tomography. *IEEE Transactions on Medical Imaging*, 1(2):113–122, 1982.

[89] Murali Ravi, Angu Sewa, TG Shashidhar, and Siva Sankara Sai Sanagapati. FPGA as a hardware accelerator for computation intensive maximum likelihood expectation maximization medical image reconstruction algorithm. *IEEE Access*, 7:111727–111735, 2019.

[90] Magdalena Bazalova, Moiz Ahmad, Guillem Pratx, and Lei Xing. L-shell x-ray fluorescence computed tomography (XFCT) imaging of Cisplatin. *Physics in Medicine & Biology*, 59(1):219–232, 2014.

[91] Albert Rose. *Vision: Human and Electronic*. New York, NY: Plenum, 1973.

[92] Siyuan Zhang, Liang Li, Ruizhe Li, and Zhiqiang Chen. Full-field fan-beam x-ray fluorescence computed tomography system design with linear-array detectors and pinhole collimation: a rapid Monte Carlo study. *Optical Engineering*, 56(11):113107, 2017.

[93] Pauli Virtanen, Ralf Gommers, Travis E. Oliphant, Matt Haberland, Tyler Reddy, David Cournapeau, Evgeni Burovski, Pearu Peterson, Warren Weckesser, Jonathan Bright, Stéfan J. van der Walt, Matthew Brett, Joshua Wilson, K. Jarrod Millman, Nikolay Mayorov, Andrew R. J. Nelson, Eric Jones, Robert Kern, Eric Larson, CJ Carey, İlhan Polat, Yu Feng, Eric W. Moore, Jake Vand erPlas, Denis Laxalde, Josef Perktold, Robert Cimrman, Ian Henriksen, E. A. Quintero, Charles R Harris, Anne M. Archibald, Antônio H. Ribeiro, Fabian Pedregosa, Paul van Mulbregt, and SciPy 1. 0 Contributors. SciPy 1.0: Fundamental Algorithms for Scientific Computing in Python. *Nature Methods*, 17:261–272, 2020.

[94] Chelsea AS Dunning and Magdalena Bazalova-Carter. X-ray fluorescence computed tomography induced by photon, electron, and proton beams. *IEEE transactions on medical imaging*, 38(12):2735–2743, 2019.

[95] Chelsea A. S. Dunning and Magdalena Bazalova-Carter. Sheet beam x-ray fluorescence computed tomography (XFCT) imaging of gold nanoparticles. *Medical Physics*, 45(6):2572–2582, 2018.

[96] Sven AE Johansson, John L Campbell, Klas G Malmqvist, James D Winefordner, et al. *Particle-induced X-ray emission spectrometry (PIXE)*, volume 133. John Wiley & Sons, 1995.

[97] Magdalena Bazalova-Carter, Moiz Ahmad, Taeko Matsuura, Seishin Takao, Yuto Matsuo, Rebecca Fahrig, Hiroki Shirato, Kikuo Umegaki, and Lei Xing. Proton-induced x-ray fluorescence CT imaging. *Medical physics*, 42(2):900–907, 2015.

[98] Jerimy C Polf, Lawrence F Bronk, Wouter HP Driessen, Wadih Arap, Renata Pasqualini, and Michael Gillin. Enhanced relative biological effectiveness of proton radiotherapy in tumor cells with internalized gold nanoparticles. *Applied physics letters*, 98(19):193702, 2011.

[99] Magdalena Bazalova-Carter, Bradley Qu, Bianey Palma, Björn Hårdemark, Elin Hynning, Christopher Jensen, Peter G Maxim, and Billy W Loo. Treatment planning for radiotherapy with very high-energy electron beams and comparison of VHEE and VMAT plans. *Medical physics*, 42(5):2615–2625, 2015.

[100] Emil Schüler, Kjell Eriksson, Elin Hynning, Steven L Hancock, Susan M Hiniker, Magdalena Bazalova-Carter, Tony Wong, Quynh-Thu Le, Billy W Loo, and Peter G Maxim. Very high-energy electron (VHEE) beams in radiation therapy; Treatment plan comparison between VHEE, VMAT, and PPBS. *Medical physics*, 44(6):2544–2555, 2017.

[101] Radhe Mohan, Chen Chui, and Leon Lidofsky. Energy and angular distributions of photons from medical linear accelerators. *Medical physics*, 12(5):592–597, 1985.

[102] Donald L Snyder, Michael I Miller, Lewis J Thomas, and David G Politte. Noise and edge artifacts in maximum-likelihood reconstructions for emission tomography. *IEEE Transactions on Medical Imaging*, 6(3):228–238, 1987.

[103] John M Boone, Orlando Velazquez, and Simon R Cherry. Small-animal x-ray dose from micro-CT. *Molecular imaging*, 3(3):15353500200404118, 2004.

[104] A Tomal, DM Cunha, M Antoniassi, and ME Poletti. Response functions of Si (Li), SDD and CdTe detectors for mammographic x-ray spectroscopy. *Applied Radiation and Isotopes*, 70(7):1355–1359, 2012.

[105] Magdalena Bazalova-Carter, Michael Liu, Bianey Palma, Michael Dunning, Doug McCormick, Erik Hemsing, Janice Nelson, Keith Jobe, Eric Colby, Albert C Koong, et al. Comparison of film measurements and Monte Carlo simulations of dose delivered with very high-energy electron beams in a polystyrene phantom. *Medical physics*, 42(4):1606–1613, 2015.

[106] Shanghai Jiang, Peng He, Luzhen Deng, Mianyi Chen, and Biao Wei. Monte carlo simulation for polychromatic x-ray fluorescence computed tomography with sheet-beam geometry. *International journal of biomedical imaging*, 2017, 2017.

[107] Qingkai Huo, Tetsuya Yuasa, Takao Akatsuka, Tohoru Takeda, Jin Wu, Kazuyuki Hyodo, F Avraham Dilmanian, et al. Sheet-beam geometry for in

vivo fluorescent x-ray computed tomography: proof-of-concept experiment in molecular imaging. *Optics letters*, 33(21):2494–2496, 2008.

[108] Ling Jian Meng, Nan Li, and Patrick J La Riviere. X-ray fluorescence emission tomography (XFET) with novel imaging geometries–a Monte Carlo study. *IEEE transactions on nuclear science*, 58(6):3359–3369, 2011.

[109] A Groll, J George, P Vargas, PJ La Riviere, and Ling Jian Meng. Element mapping in organic samples utilizing a benchtop x-ray fluorescence emission tomography (XFET) system. *IEEE transactions on nuclear science*, 62(5):2310–2317, 2015.

[110] R Ballabriga, M Campbell, E Heijne, X Llopart, L Tlustos, and Winnie Wong. Medipix3: A 64 k pixel detector readout chip working in single photon counting mode with improved spectrometric performance. *Nuclear Instruments and Methods in Physics Research Section A: Accelerators, Spectrometers, Detectors and Associated Equipment*, 633:S15–S18, 2011.

[111] Don Vernekohl, Moiz Ahmad, Garry Chinn, and Lei Xing. Feasibility study of Compton cameras for x-ray fluorescence computed tomography with humans. *Physics in Medicine & Biology*, 61(24):8521–8540, 2016.

[112] T. Edmond Hui, Darrell R. Fisher, Joseph A. Kuhn, Lawrence E. Williams, Cynthia Nourigat, Christopher C. Badger, Barbara G. Beatty, and J. David Beatty. A mouse model for calculating cross-organ beta doses from yttrium-90-labeled immunoconjugates. *Cancer*, 73(S3):951–957, 1994.

[113] Koji Maeda, Masao Matsumoto, and Akira Taniguchi. Compton-scattering measurement of diagnostic x-ray spectrum using high-resolution Schottky CdTe detector. *Medical Physics*, 32(6):1542–1547, 2005.

[114] Magdalena Bazalova and Frank Verhaegen. Monte Carlo simulation of a computed tomography x-ray tube. *Physics in Medicine & Biology*, 52(19):5945–5955, 2007.

[115] Chelsea AS Dunning, Jericho OConnell, Spencer M Robinson, Kevin J Murphy, Adriaan L Frencken, Frank CJM van Veggel, Kris Iniewski, and Magdalena

Bazalova-Carter. Photon-counting computed tomography of lanthanide contrast agents with a high-flux 330-$\mu$m-pitch cadmium zinc telluride detector in a table-top system. *Journal of Medical Imaging*, 7(3):033502, 2020.

[116] Naoki Takahashi, Robert P Hartman, Terri J Vrtiska, Akira Kawashima, Andrew N Primak, Oleksandr P Dzyubak, Jayawant N Mandrekar, Joel G Fletcher, and Cynthia H McCollough. Dual-energy CT iodine-subtraction virtual unenhanced technique to detect urinary stones in an iodine-filled collecting system: a phantom study. *American Journal of Roentgenology*, 190(5):1169–1173, 2008.

[117] Sven F Thieme, Thorsten RC Johnson, Christopher Lee, Justin McWilliams, Christoph R Becker, Maximilian F Reiser, and Konstantin Nikolaou. Dual-energy CT for the assessment of contrast material distribution in the pulmonary parenchyma. *American Journal of Roentgenology*, 193(1):144–149, 2009.

[118] Juergen Fornaro, Sebastian Leschka, Dennis Hibbeln, Anthony Butler, Nigel Anderson, Gregor Pache, Hans Scheffel, Simon Wildermuth, Hatem Alkadhi, and Paul Stolzmann. Dual-and multi-energy CT: approach to functional imaging. *Insights into Imaging*, 2(2):149–159, 2011.

[119] Cynthia H McCollough, Shuai Leng, Lifeng Yu, and Joel G Fletcher. Dual-and multi-energy CT: principles, technical approaches, and clinical applications. *Radiology*, 276(3):637–653, 2015.

[120] Amir Pourmorteza, Rolf Symons, Veit Sandfort, Marissa Mallek, Matthew K Fuld, Gregory Henderson, Elizabeth C Jones, Ashkan A Malayeri, Les R Folio, and David A Bluemke. Abdominal imaging with contrast-enhanced photon-counting CT: first human experience. *Radiology*, 279(1):239–245, 2016.

[121] Rolf Symons, Amir Pourmorteza, Veit Sandfort, Mark A Ahlman, Tracy Cropper, Marissa Mallek, Steffen Kappler, Stefan Ulzheimer, Mahadevappa Mahesh, Elizabeth C Jones, et al. Feasibility of dose-reduced chest CT with photon-counting detectors: initial results in humans. *Radiology*, 285(3):980–989, 2017.

[122] Rolf Symons, Bernhard Krauss, Pooyan Sahbaee, Tyler E Cork, Manu N Lakshmanan, David A Bluemke, and Amir Pourmorteza. Photon-counting CT for simultaneous imaging of multiple contrast agents in the abdomen: an in vivo study. *Medical physics*, 44(10):5120–5127, 2017.

[123] Daniela Muenzel, Daniel Bar-Ness, Ewald Roessl, Ira Blevis, Matthias Bartels, Alexander A Fingerle, Stefan Ruschke, Philippe Coulon, Heiner Daerr, Felix K Kopp, et al. Spectral photon-counting CT: Initial experience with dual–contrast agent K-edge colonography. *Radiology*, 283(3):723–728, 2016.

[124] Nigel G. Anderson and Anthony P. Butler. Clinical applications of spectral molecular imaging: Potential and challenges. *Contrast Media and Molecular Imaging*, 9(1):3–12, 2014.

[125] Alvin C. Silva, Brian G. Morse, Amy K. Hara, Robert G. Paden, Norio Hongo, and William Pavlicek. Dual-energy (spectral) CT: Applications in abdominal imaging. *RadioGraphics*, 31(4):1031–1046, 2011. PMID: 21768237.

[126] Katsuyuki Taguchi. Imaging technologies and potential clinical applications of photon-counting x-ray computed tomography. In *Radiation Detectors for Medical Imaging*, pages 149–168. CRC Press, 2015.

[127] James Bennett, Alex MT Opie, Qiong Xu, Hengyong Yu, Michael F Walsh, Anthony PH Butler, Phillip Butler, Guohua Cao, Aaron Mohs, and Ge Wang. Hybrid spectral micro-CT: system design, implementation, and preliminary results. *IEEE Trans. Biomed. Engineering*, 61(2):246–253, 2014.

[128] Salim Si-Mohamed, Daniel Bar-Ness, Monica Sigovan, Valérie Tatard-Leitman, David P Cormode, Pratap C Naha, Philippe Coulon, Lucie Rascle, Ewald Roessl, Michal Rokni, et al. Multicolour imaging with spectral photon-counting CT: a phantom study. *European radiology experimental*, 2(1):34, 2018.

[129] Sebastian Feuerlein, Ewald Roessl, Roland Proksa, Gerhard Martens, Oliver Klass, Martin Jeltsch, Volker Rasche, Hans-Juergen Brambs, Martin HK Hoffmann, and Jens-Peter Schlomka. Multienergy photon-counting K-edge imaging: potential for improved luminal depiction in vascular imaging. *Radiology*, 249(3):1010–1016, 2008.

[130] Melanie S Joy, William F Finn, LAM-302 Study Group, et al. Randomized, double-blind, placebo-controlled, dose-titration, phase III study assessing the efficacy and tolerability of lanthanum carbonate: a new phosphate binder for the treatment of hyperphosphatemia. *American Journal of Kidney Diseases*, 42(1):96–107, 2003.

[131] Ron R Allison and Claudio H Sibata. Oncologic photodynamic therapy photosensitizers: a clinical review. *Photodiagnosis and photodynamic therapy*, 7(2):61–75, 2010.

[132] Xinghua Zhang, Barbara Blasiak, Armando J Marenco, Simon Trudel, Boguslaw Tomanek, and Frank CJM van Veggel. Design and regulation of $NaHoF_4$ and $NaDyF_4$ nanoparticles for high-field magnetic resonance imaging. *Chemistry of Materials*, 28(9):3060–3072, 2016.

[133] Paul F FitzGerald, Robert E Colborn, Peter M Edic, Jack W Lambert, Andrew S Torres, Peter J Bonitatibus Jr, and Benjamin M Yeh. CT image contrast of high-Z elements: phantom imaging studies and clinical implications. *Radiology*, 278(3):723–733, 2015.

[134] Dipanjan Pan, Carsten O Schirra, Angana Senpan, Anne H Schmieder, Allen J Stacy, Ewald Roessl, Axel Thran, Samuel A Wickline, Roland Proska, and Gregory M Lanza. An early investigation of ytterbium nanocolloids for selective and quantitative multicolor spectral CT imaging. *ACS nano*, 6(4):3364–3370, 2012.

[135] Fatemeh Ostadhossein, Indu Tripathi, Lily Benig, Denae LoBato, Mahdieh Moghiseh, Chiara Lowe, Aamir Raja, Anthony Butler, Raj Panta, Marzieh Anjomrouz, et al. Multi-color delineation of bone microdamages using ligand-directed sub-5 nm hafnia nanodots and photon counting CT imaging. *Advanced Functional Materials*, 2019.

[136] H Ghadiri, Mohammad Reza Ay, MB Shiran, H Soltanian-Zadeh, and Habib Zaidi. K-edge ratio method for identification of multiple nanoparticulate contrast agents by spectral CT imaging. *The British journal of radiology*, 86(1029):20130308, 2013.

[137] RK Panta, Stephen T Bell, JL Healy, R Aamir, CJ Bateman, M Moghiseh, APH Butler, and NG Anderson. Element-specific spectral imaging of multiple contrast agents: a phantom study. *Journal of Instrumentation*, 13(02):T02001, 2018.

[138] Mahdieh Moghiseh, Raja Aamir, Raj K Panta, Niels de Ruiter, A Chernoglazov, JL Healy, AP Butler, and NG Anderson. Discrimination of multiple high-Z

materials by multi-energy spectral CT–a phantom study. *JSM Biomed Imaging Data Pap*, 61:1007, 2016.

[139] Jack F Butler, Stan J Friesenhahn, Clinton L Lingren, Boris A Apotovsky, F Patrick Doty, William L Ashburn, and William P Dillon. $Cd_{1-x}Zn_xTe$ detector imaging array. In *Medical Imaging 1993: Physics of Medical Imaging*, volume 1896, pages 30–38. International Society for Optics and Photonics, 1993.

[140] Salim Si-Mohamed, Valérie Tatard-Leitman, Alexis Laugerette, Monica Sigovan, Daniela Pfeiffer, Ernst J Rummeny, Philippe Coulon, Yoad Yagil, Philippe Douek, Loic Boussel, et al. Spectral photon-counting computed tomography (SPCCT): in-vivo single-acquisition multi-phase liver imaging with a dual contrast agent protocol. *Scientific reports*, 9(1):8458, 2019.

[141] Beat Münch, Pavel Trtik, Federica Marone, and Marco Stampanoni. Stripe and ring artifact removal with combined wavelet–Fourier filtering. *Optics express*, 17(10):8567–8591, 2009.

[142] Michael JD Powell. A direct search optimization method that models the objective and constraint functions by linear interpolation. In *Advances in optimization and numerical analysis*, pages 51–67. Springer, 1994.

[143] Devon Richtsmeier, Chelsea AS Dunning, Kris Iniewski, and Magdalena Bazalova-Carter. Multi-contrast K-edge imaging on a bench-top photon-counting CT system: Acquisition parameter study. *arXiv preprint arXiv:2009.09118*, 2020.

[144] David P Cormode, Salim Si-Mohamed, Daniel Bar-Ness, Monica Sigovan, Pratap C Naha, Joelle Balegamire, Franck Lavenne, Philippe Coulon, Ewald Roessl, Matthias Bartels, et al. Multicolor spectral photon-counting computed tomography: in vivo dual contrast imaging with a high count rate scanner. *Scientific reports*, 7(1):4784, 2017.

[145] Jae Cheon Kim, Stephen E Anderson, Willy Kaye, Feng Zhang, Yuefeng Zhu, Sonal Joshi Kaye, and Zhong He. Charge sharing in common-grid pixelated CdZnTe detectors. *Nuclear Instruments and Methods in Physics Research Section A: Accelerators, Spectrometers, Detectors and Associated Equipment*, 654(1):233–243, 2011.

[146] MC Veale, SJ Bell, DD Duarte, A Schneider, P Seller, MD Wilson, and K Iniewski. Measurements of charge sharing in small pixel CdTe detectors. *Nuclear Instruments and Methods in Physics Research Section A: Accelerators, Spectrometers, Detectors and Associated Equipment*, 767:218–226, 2014.

[147] B Thomas, MC Veale, MD Wilson, P Seller, A Schneider, and K Iniewski. Characterisation of Redlen high-flux CdZnTe. *Journal of Instrumentation*, 12(12):C12045, 2017.

[148] Kris Iniewski, Matthew C Veale, and Magdalena Bazalova-Carter. High-flux CZT for new frontiers in computed tomography (CT), non-destructive testing (NDT) and high-energy physics. Presentation at IEEE Nuclear Science Symposium and Medical Imaging Conference, Manchester, 2019.

[149] Kris Iniewski, Conny Hansson, Elmaddin Guliyev, Georgios Prekas, and Michael Ayukawa. Performance characteristics of 250+ Mcps/mm$^2$ CZT detector module for spectral computed tomography. Presentation at Workshop on Medical Applications of Spectroscopic X-ray Detectors, CERN, 2019.

[150] Mats Persson, Ben Huber, Staffan Karlsson, Xuejin Liu, Han Chen, Cheng Xu, Moa Yveborg, Hans Bornefalk, and Mats Danielsson. Energy-resolved CT imaging with a photon-counting silicon-strip detector. *Physics in Medicine & Biology*, 59(22):6709, 2014.

[151] CAS Dunning and M Bazalova-Carter. Design of a combined x-ray fluorescence computed tomography (CT) and photon-counting CT table-top imaging system. *Journal of Instrumentation*, 15(06):P06031, 2020.

[152] Christophe Alric, Jacqueline Taleb, Géraldine Le Duc, Céline Mandon, Claire Billotey, Alice Le Meur-Herland, Thierry Brochard, Francis Vocanson, Marc Janier, Pascal Perriat, et al. Gadolinium chelate coated gold nanoparticles as contrast agents for both x-ray computed tomography and magnetic resonance imaging. *Journal of the American Chemical Society*, 130(18):5908–5915, 2008.

[153] Raj Kumar Panta, Anthony PH Butler, Philip H Butler, Niels JA de Ruiter, Stephen T Bell, Michael F Walsh, Robert MN Doesburg, Alexander I Chernoglazov, Brian P Goulter, Pierre Carbonez, et al. First human imaging with MARS photon-counting CT. In *2018 IEEE Nuclear Science Symposium*

*and Medical Imaging Conference Proceedings (NSS/MIC)*, pages 1–7. IEEE, 2018.

[154] Tyler E Curtis and Ryan K Roeder. Quantification of multiple mixed contrast and tissue compositions using photon-counting spectral computed tomography. *Journal of Medical Imaging*, 6(1):013501, 2019.

[155] Luzhen Deng, Selcuk Yasar, Md Foiez Ahmed, Sandun Jayarathna, Peng Feng, Biao Wei, Srinivasan Vedantham, Andrew Karellas, and Sang Hyun Cho. Investigation of transmission computed tomography (CT) image quality and x-ray dose achievable from an experimental dual-mode benchtop x-ray fluorescence CT and transmission CT system. *Journal of X-ray science and technology*, 27(3):431–442, 2019.

[156] Liang Li, Ruizhe Li, Siyuan Zhang, and Zhiqiang Chen. Simultaneous x-ray fluorescence and K-edge CT imaging with photon-counting detectors. In *Developments in X-ray Tomography x*, volume 9967, page 99670F. International Society for Optics and Photonics, 2016.

[157] Ryan B Stephens, Krishun H Karau, Christopher J Yahnke, Sara R Wendt, and Rebecca J Rowe. Dead mice can grow–variation of standard external mammal measurements from live and three postmortem body states. *Journal of Mammalogy*, 96(1):185–193, 2015.